Characterizing the deformation response of a unidirectional non-crimp fabric for the development of computational draping simulation models

by

Eleazar Alberto Trejo Sandoval

A thesis

presented to the University of Waterloo

in fulfillment of the

thesis requirement for the degree of

Master of Applied Science

in

Mechanical and Mechatronics Engineering

Waterloo, Ontario, Canada, 2020

Author's Declaration

I hereby declare that I am the sole author of this thesis. This is a true copy of the thesis, including any required final revisions, as accepted by my examiners.

I understand that my thesis may be made electronically available to the public.

Abstract

In several countries around the world, including Canada, government incentives have been put in place to improve the fuel efficiency of vehicles and reduce CO2 emissions. Improvements in composites manufacturing technology, such as high-pressure resin transfer molding and quick curing resins, makes it practical to lightweight through the incorporation of carbon fiber reinforced polymer (CFRP) parts into the body-in-white structure of vehicles. However, the technology has only been realized for small production rates and is currently in the developmental phase towards full automation for high-volume production. Hence, there is a need to developed and calibrate fabric draping simulations models to support this effort and enable the design of CFRP production processes that incorporate cost-effective fabric reinforcement material, such as heavy tow unidirectional non-crimp fabric (UD-NCF). This work aimed to expand the understanding of the forming behaviour of UD-NCFs, within the context of the development of automation capabilities for fabric preforming. The investigation focused on the characterization of the macroscale response of a UD-NCF, including an investigating of associated local deformation mechanisms, to calibrate a macroscale constitutive model and support the development of a computational fabric draping simulation model.

The fabric characterization consisted of a series of experimental tests that measured the fabric in-plane and out-of-plane deformation responses reminiscent of draping operations. The tests were conducted with respect to the carbon fiber (CF) tow longitudinal and transverse directions. The experimental tests conducted were the longitudinal, transverse, and off-axis extension tests; the picture frame test (PFT); the cantilever; and friction sliding test in both material directions. The longitudinal extension and bending stiffness were found to be significantly higher than the respective transverse extension and bending stiffnesses. Also, at low strains, the fabric transverse extension stiffness was found to be negligible until crimping in the transverse glass fibers was removed. Regarding the fabric friction response, the coefficients of friction were higher on the stitching fabric side and when sliding occurred in the longitudinal fabric direction. Also, an investigation of the fabric mesoscale deformation mechanisms revealed the generation of CF tow undulations and intertow gapping, mainly generated by deformation of the stitching, when the fabric was subjected to transverse extension and shear deformations. To address difficulties associated with sliding of the glass fibers at the clamps during extension and PFT testing a clamping design was proposed that fully restrained the glass fibers, while at the same time preventing specimen damage at the grips. 2D DIC was used to study the development of strains in the fabric during all in-plane experimental tests. Challenges associated with fabric surface texturization and strain measurements through digital image correlation were investigated and addressed to improve the optical strain analysis. A surface texturization technique with an oil-based paint was implemented in all tests as it created high contrast speckle patterns on the fabric surface and the least amount of fabric deformation interference when compared with two other surface texturization techniques.

Using the experimental results, a macroscale material model, chosen from the existing material model library available in the commercial finite element software LS-DYNA® was calibrated to simulate forming operations. The material model was calibrated for in-plane and out-of-plane deformation modes in accordance with the experimental tests conducted. The material model parameters were identified by simulating the experimental tests conducted during the fabric characterization process and an iterative inverse parameter identification approach until a good correlation was obtained between the numerical simulations and the corresponding physical tests. In most cases, piecewise linear functions were used to approximate the experimental test data before entering into the material model.

Finally, to validate the calibration of the material model, a single-layer 100-mm diameter hemispherical test with a displacement controlled punch was performed and simulated using the calibrated material model. In addition to the calibrated material model, results from the friction tests were used to define contact boundary conditions in the draping simulation model. A good agreement was obtained between the simulation predictions of macroscopic deformations observed in the fabric, including contour shape and wrinkling, and the experimental results.

Acknowledgements

The work presented in this thesis would not have been possible without the support I received from multiple individuals. I would like to especially thank Professor John Montesano for his mentorship, patience and great professionalism providing me with advice and encouragement throughout the whole process of completing this project. I would also like to acknowledge Professor Clifford Butcher for his guidance in the subject of solid mechanics and the feedback provided for the manuscripts produced by this research. I owe a good deal of appreciation to Dr. Mehdi Ghazimoradi for his assistance in laboratory testing, encouragement and valuable discussions about fabric testing and characterization.

I would also like to express my appreciation to the university laboratory staff: Tom Gawel, Andy Barber, Doug Hirst, and Eckhard Budziarek, for always being available and willing to help. Special thanks to Brock Watson for helping troubleshoot the tensile testing machine on several occasions and coordinating the endless exchanges of camera equipment among multiple students. Also, thanks to Luis Trimiño and Sante DiCecco for completing the SOP training with me and answering all my questions about lab equipment.

Thank you to all the graduate students in the Composites Research Group, specifically Khizar Rouf, Farzad Sharifpour, Pravin Gopal, Zohreh Asaee, Yu Zeng, Ramin Chitsaz, Ben Harvey, Sanaz Hashemi, Devon Hartlen, and Luiz Fonseca for making it fun to come to the office and the good times shared over meals and hangouts.

The support from our sponsors Honda R&D Americas, Laval International, Zoltek Corporation, Hexion Inc., and the Natural Sciences and Engineering Research Council (NSERC) through a CRD Grant is also greatly appreciated.

Most importantly, I would like to thank my wife, Casey Kennedy, for her love and continuous support in these last two years; I would not have been able to complete this work without her.

To my mom and family

Table of Contents

List of Figures

List of Tables

Chapter 1: Introduction

1.1 Research motivation

Recent legislation in the United States, Canada, and Europe [1–4] to economize vehicle fuel consumption and reduce CO_2 emissions have been established for various classes of vehicles, including light duty vehicles (LDV). In response to this initiative, the automotive sector has focused its development efforts for LDVs on improving aerodynamic efficiency, developing new efficient powertrain designs, and optimizing vehicle body-in-white (BIW) structure for weight reduction [5]. Reduction of the vehicle weight, including the BIW structures, is regarded as one of the key factors to improving vehicle fuel economy [6]. An effective approach to vehicle lightweighting is to incorporate high-performance fiber-reinforced plastic (FRP) composite materials into BIW structures [7]. Advantages of FRP materials compared to conventional vehicle BIW structure materials, such as high strength steel and aluminum, include superior specific mechanical properties and improved energy absorbing capabilities [8,9], as shown in Figure 1.1.

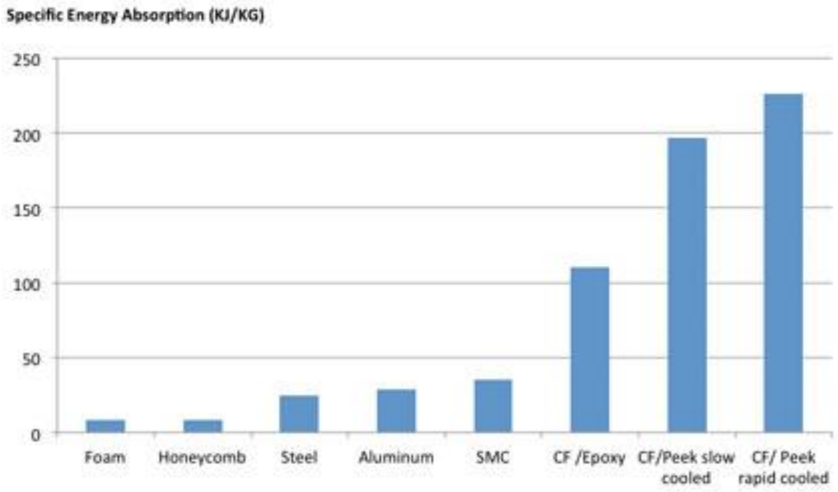

Figure 1.1. Crash energy absorption of CF composites (far right) compared with common engineering materials and structures [10].

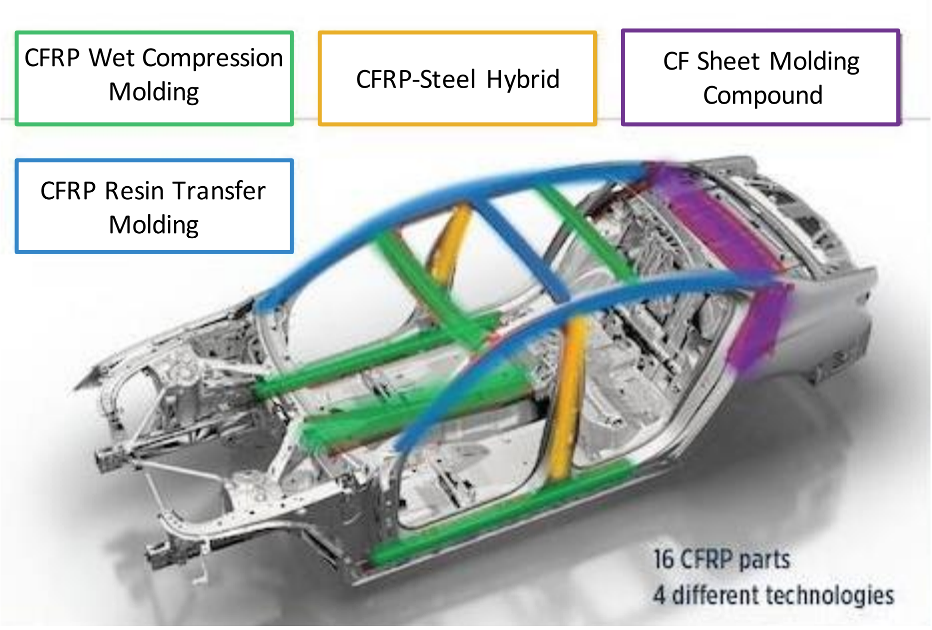

Figure 1.2. Carbon fiber reinforced composites integrated in the chassis of the BMW series 7 [4].

Owing to its superior performance when compared to conventional vehicle BIW structure materials, carbon fiber-reinforced plastic (CFRP) composites have been used in the BIW structures of vehicles. Examples in the marketplace include the BMW 7 Series [4] (Figure 1.2) and the Audi A8 [10]. Despite the advantages of CFRP materials, their adoption in vehicle BIW structures has been limited to luxury vehicles and so-called supercars [11], where the increased material and production costs, and longer processing cycle times typical of CFRP materials can be tolerated. Traditional CFRP composite manufacturing processes such as autoclave curing of prepreg laminates, resin transfer molding (RTM) and compression molding are not conducive to a high-volume production environment. Recent development of new rapid curing resins and low-cost carbon fiber fabrics (e.g., heavy-tow non-crimp fabric (NCFs)), along with processing technologies such as high-pressure RTM (HP-RTM) [12], offer a strong potential for integrating CFRP materials into the BIW structures of high-volume production vehicles by allowing for reductions in cost and time required to fabricate CFRP parts.

Similar to other RTM processes, HP-RTM offers excellent manufacturing benefits such as great impregnation quality and low geometric tolerances [13], while rapid automated fabric handling and pre-forming may enable high-volume manufacturing for composites. Preforming is the first main step in a typical HP-RTM process and consists of placing a stack of reinforcing fabric layers inside a preheated mold where it is formed before resin is injected into the closed mold. During the preforming step a stack of fabric layers may exhibit a variety of defects which can be detrimental to the performance of the CFRP part [14]. These defects are dependent on many factors including the specific architecture of the fabric. Unidirectional non-crimp fabrics (UD-NCFs) which do not contain weaving or knitting patterns, are more susceptible to exhibiting defects during preforming [15]. Although the deformation of reinforcing fabrics have been widely studied to better understand the mechanisms that cause preforming defects, studies of UD-NCF has been limited [14,16]. Characterization of these defects would otherwise be useful for calibration of corresponding computational models that aim to simulate the fabric preforming process. As such, there exists a need to develop a robust computational approach to predict defects associated with the preforming of heavy-tow UD-NCFs, and subsequently map these to computational performance simulation models for improved prediction fidelity.

1.2 Research objectives

Originating from the increasing interest to incorporate CFRPs into LDVs, and to enhance the process capabilities of HP-RTM, the overarching research goal of this project was to develop a robust high fidelity computational approach to predict defects associated with the preforming of heavy-tow UD-NCFs. The main research objectives are summarized as follows:

- Characterize the macroscale response of a heavy-tow UD-NCF when subjected to multiple deformation modes and investigate the corresponding local fabric deformation mechanisms;
- Calibrate a continuum-based material constitutive model using experimental data generated for the UD-NCF;
- Develop and validate a computational fabric draping simulation model.

1.3 Thesis outline

In Chapter 2, a theoretical background and literature review of characterization and modelling of the UD-NCF fabric reinforcement is presented to contextualize this research and to explain existing research limitations and gaps. In Chapter 3, the methods used to test the mechanical response of the fabric are described. In Chapter 4, the numerical methods used to model the fabric material are presented. In Chapter 5, the results of the experimental and computational studies are presented and compared. In Chapter 6, relevant results and findings are discussed. Lastly, conclusions and recommendations are presented in Chapter 8.

Chapter 2: Background and Literature review

In this chapter, the characteristics of fiber-reinforced plastic (FRP) composites, with an emphasis on the reinforcement phase, are reviewed (Section 2.1). Next, an overview of FRP composites manufacturing process methods is presented with an emphasis on HP-RTM and automated fabric preforming (Section 2.2), followed by an introduction of the deformation mechanism present during fabric preforming (Section 2.3). Finally, a literature survey on characterization of fabric reinforcements and numerical draping simulation models is presented in Sections 2.4 and 2.5, respectively.

2.1. Overview of fiber-reinforced plastic composites

FRP composites are heterogeneous materials composed of two distinct phases. High strength and high stiffness fibers constitute the reinforcement phase, while the polymer matrix phase fills the volume around and bonds to the fibers. Designing a high-performance composite part requires an effective combination of the mechanical and chemical properties of the fiber and the matrix to form the most efficient material for its intended application. An optimal fiber/matrix combination with a strong bond between the phases produces an FRP material with enhanced properties compared to the individual constituents; this ability to tailor the composite material is a key advantage compared to homogeneous materials [17].

For FRPs the matrix phase has several roles, including transferring load to the fibers through the fiber/matrix interface, maintaining fibers in their required orientation, protecting the fibers from environmental degradation, and defining the part geometry [18]. The matrix phase is typically either a thermosetting or thermoplastic polymer, with the former more widely used for structural applications. On the other hand, the main role of the reinforcing fibers in structural FRP composites is to support the majority of the load carried by the material. Common fiber types used in structural FRP composites include glass, boron, carbon, and aramid [19]. Several key characteristics of fibers are known to affect mechanical properties and processability of FRPs [18]. For instance, the small diameter of fibers, which contain fewer material microstructural units (graphite crystal sheets) and thus a lower probability of defects when compared to a bulk material, allows for a high fraction of the theoretical strength to be attained. Furthermore, the high aspect ratio (i.e., length/diameter) of fibers results in an increased fiber surface area and bonding interface with the matrix in the FRP material, allowing applied loads to be transferred more effectively to the fibers from the matrix. Finally, a high degree of flexibility (due to the small fiber diameter) and the ability of fibers to withstand bending without fracture increases the capability of handling and forming of a corresponding fabric.

Carbon fibers, which are the focus of this study, are made from one of two precursor materials, namely polyacrylonitrile (PAN) or pitch which is a petroleum by-product [20]. PAN precursors are prefabricated polymer filaments supplied in tow form on a spool and are more cost effective than pitch precursors. As a result, PAN precursors are more widely used to manufacture high-performance carbon fibers. A typical carbon fiber manufacturing process using a PAN precursor is depicted in Figure 2.1. During the first step the precursor filaments are stretched to promote alignment of the polymer molecules along the filament axes prior to heat exposure. The second step (i.e., oxidization) involves heating the filaments to a relatively low temperature in an inert environment to allow for chemical crosslinking between the molecules, while tension is maintained to further improve molecular alignment. The carbonization step exposes the crosslinked filaments to a higher temperature to drive out non-carbon atoms, thus creating carbon fibers with ~92 wt% of carbon. Tension is maintained on the filaments during carbonization to allow the formed graphitic planes to align along the carbon fiber axes. The carbon fibers are then heated to higher temperatures during the graphitization step under tension to further improve the purity of the fibers (~99 wt% of carbon) and graphitic plane alignment, resulting in carbon fibers with high strength and modulus. Sizing is then applied to the 4-7 µm diameter carbon fibers before a group of fibers, called a bundle or tow, is wrapped on a spool. Tows typically consist of 1,000 to 50,000 filaments [18].

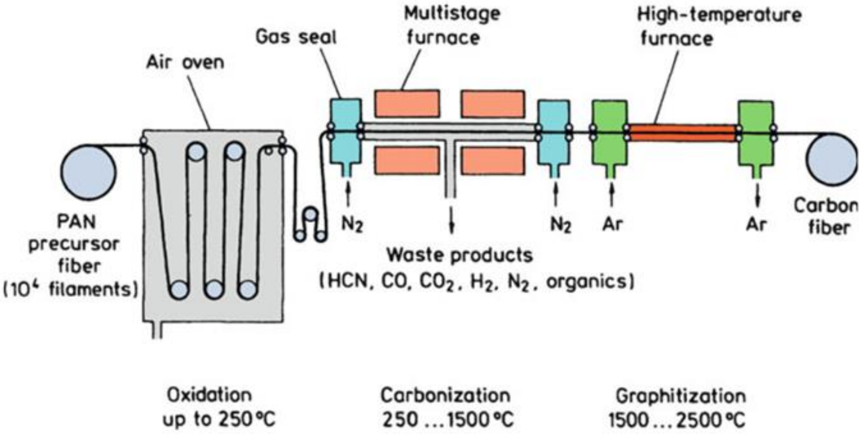

Figure 2.1. Schematic of a typical carbon fiber manufacturing process with a PAN precursor [18].

The reinforcement fibers may be classified as either discontinuous or continuous. Discontinuous fibers can be either short (< 10 mm) or long (> 50 mm) and are often used in FRPs for secondary structural applications. In this case, fiber tows are cut to the desired length for subsequent FRP processing. Composites containing continuous fibers have higher load-bearing capacity than those with discontinuous fibers [21], while also offering improved impact resistance, lower shrinkage, improved surfaced finish, and enhanced dimensional stability [22]. Continuous fibers are also easy to orient during processing, while the orientation of short fibers cannot typically be fully controlled. In most applications, the continuous fibers are oriented along multiple directions (i.e., laminates) to provide improved multidirectional material properties. Continuous fiber tows may be used directly to manufacture composite parts (e.g., wet filament winding or pultrusion processes), to fabricate semi-finished composite materials such as unidirectional tape prepregs, or to create reinforcement fabrics. Fabrics can also be used to fabricate prepregs or used with many different liquid composite molding manufacturing processes to directly fabricate FRP parts (see Section 2.2). There are many types of fabrics used to manufacture FRPs, including woven, multi-axial braided, knitted, and stitched non-crimp fabrics (NCF). Woven fabrics have been used most extensively in industrial applications, however, NCFs have been increasingly used in recent years [23].

Woven fabrics are composed of interlaced fiber tows or yarns that are aligned along two orthogonal directions denoted as warp and weft. Several types of 2D woven fabrics can be produced by weaving the warp and the weft yarns in different patterns. The most common 2D woven fabrics are plain, twill, and satin weave (Figure 2.2). Plain woven fabrics are produced by interlacing the warp and weft threads every time they cross during the weaving process. In twill woven fabrics warp-weft interlacing is shifted based on a specific pattern; for example, a 2x1 twill interlaces every second thread on one side on the fabric and every thread on the other, producing a diagonal mark on the fabric surface [24]. Additionally, 3D woven fabrics are produced by interlacing several layers of 2D woven fabrics with through-thickness fiber yarns. A combination of the properties of the yarns, the weave pattern, and the friction between filaments make such 3D fabrics robust materials [24].

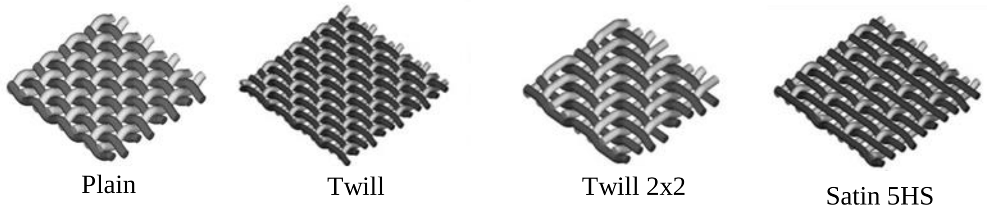

Figure 2.2. Most common woven reinforcement fabrics [24].

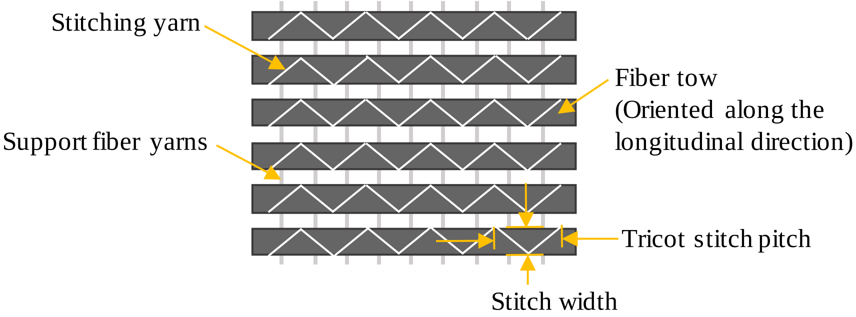

Figure 2.3. Schematic of a unidirectional non-crimp fabric.

Unlike woven fabrics, NCFs do not have interlacing fiber bundles or tows and ideally have no out-of-plane crimping. Instead, fiber tows within a layer of the fabric are evenly spaced and aligned along a single direction, and multiple layers are combined by a stitching process to form a multidirectional NCF. More specifically, unidirectional non-crimp fabrics (UD-NCFs) are comprised of a single layer of aligned fiber tows that are stitched to one another (Figure 2.3). The pattern of the stitching used to connect the fiber tows significantly influences the response of the fabric during FRP part fabrication. Common stitching patterns include pillar, cord, satin, and tricot stitching, shown in Figure 2.3. The tricot stitching pattern follows the direction of the CF tows, crossing the tow twice on every pitch to attach to the previous layer of stitching forming a triangular shape on one face of the fabric. As shown in Figure 2.3, supporting fibers extend transverse to the CF tows lying between the tows and the stitching on the opposite face of the fabric.

UD-NCFs offer several advantages when compared to woven fabrics. Owing to the aligned fiber tows, when subjected to tensile loading UD-NCFs undergo a high stiffness response and do not exhibit the initial low de-crimping stiffness that is characteristic of woven fabrics [25]. Consequently, corresponding composite laminates have improved mechanical properties and energy absorption capabilities [26,27]. Additionally, the simplicity of the architecture of UD-NCFs yields a relatively low fabric manufacturing cost [28]. An important characteristic that impacts the cost of the fabric is the number of filaments per tow, where the cost reduces with increasing number of filaments at the expense of reduced fabric quality. For example, in the aerospace sector where the aim is to fabricate the highest quality structures, tows with 1,000 – 6,000 filaments are generally used while fabrics with 12,000 filaments have also become common [24]. More recently, fabrics with 50,000 filaments per tow, which are known as heavy-tow fabrics, have been used for automotive applications where cost is more critical. For example, heavy-tow UD-NCFs have been used for structural and energy-absorbing components in vehicles [9,29–31].

Despite their excellent mechanical properties and relatively low cost, heavy-tow UD-NCFs may be difficult to handle during processing of FRP components, where the integrity of the fabric architecture can be impacted [32]. Another challenge is the ability to drape the fabric into complex shapes while conserving the fabric architecture and desired fiber orientation. Forming of the fabric is an important step for liquid molding FRP fabrication processes (see Section 2.2). Furthermore, heavy-tow UD-NCFs are composed of multiple discrete constituents which undergo complex interactions when the fabric is deformed, thus characterizing and modeling their response is challenging. Many factors influence the mechanical response of fabrics, such as the fiber properties and the characteristics of the fabric architecture at multiple relevant length scales. Fabrics can be analyzed at three length scales, namely macro, meso, and micro-scale [33], as shown in Figure 2.4 for a UD-NCF containing carbon fiber tows and stitching threads. At the micro-scale, individual carbon fiber filaments in the tows as well as stitching filaments are visible. At the meso-scale, the carbon fiber tows and stitching threads comprise the observed discrete fabric architecture, where deformation of the fabric involves contact and friction forces between the fabric tows and the stitching threads. At the macro-scale, the fabric is perceived as a continuum and homogeneous material where only distinctions in directional properties are considered. These properties are typically incorporated through constitutive relations [34].

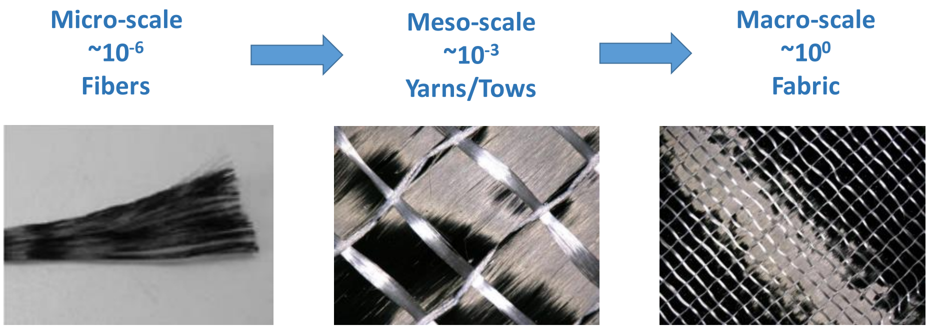

Figure 2.4. Multi-scale nature of a unidirectional non-crimp fabric.

2.2. Manufacturing methods for continuous FRP composites

Manufacturing methods for FRPs can be classified based on the mold type: open, closed and other processes, as shown in Figure 2.5. In open-mold processes the fabric and resin are placed on a single-sided mold before resin curing starts, while in close-mold processes raw materials are placed in a double-sided mold and resin curing takes place under pressure.

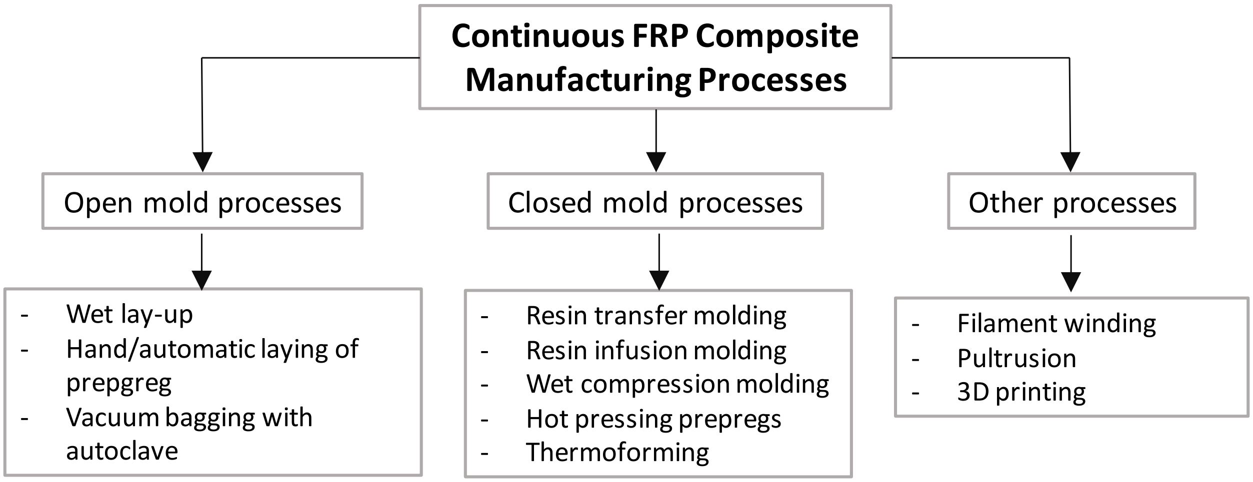

Figure 2.5. Classification of continuous FRP composite manufacturing processes.

Continuous FRP composite manufacturing processes that use liquid resin to impregnate a fabric preform stack in a closed mold are called Liquid Composite Molding (LCM) processes[35]. LCM processes can be used to produce high-quality parts with complex shapes, thus, have become popular in the aerospace and automotive industries. Common LCM processes include resin transfer molding (RTM), resin infusion molding and wet compression molding (Figure 2.5). RTM has become a widely used FRP composite manufacturing process during the past two decades [13,36]. During a typical RTM process, the dry fabric preform is placed in the cavity of a closed mold where premixed molten resin is injected under pressure allowing for wetting of the fabric layers prior to curing and hardening of the near net shape composite part (Figure 2.6). Resin injection typically takes place under low pressures, allowing the displaced air to escape the mold cavity through vents to avoid dry spots and to minimize void formation [37]. RTM cycle times vary from several minutes to hours [38], mainly dependent on part thickness, resin type and processing temperature. Despite the inherently long cycles times, the benefits of the RTM process include the ability to produce high quality geometrically complex parts with tight tolerances and high repeatability. Thus, RTM is regarded as a cost-effective process and has attracted the interest of the automotive industry [18]. However, although the manufacturing process is relatively simple and fabrication is cost-effective, the initial setup cost may be high and parts are limited to small or medium sizes [39].

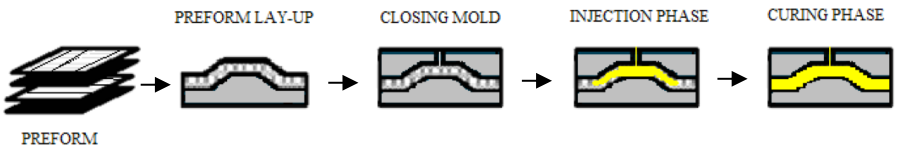

Figure 2.6. Main processing steps during RTM composites manufacturing [40].

To address the limitations of the RTM process, a process variant known as high pressure resin transfer molding (HP-RTM) was recently developed [41]. The main differences with respect to conventional RTM are that highly reactive resin and hardener components are rapidly mixed immediately prior to being injected into the closed mold at high pressures and flow rates using a costly metering unit with a mix head. The resulting high mold cavity pressures require large presses to maintain the tool in a shut and sealed position during resin injection. Notwithstanding, due to rapid resin injection rates and the development of highly reactive fast-curing resins, HP-RTM cycle times are reduced to minutes [12,42], while higher injection pressures lead to improved part surface finish and higher attainable fiber volume fractions.

Despite the feasibility of HP-RTM technology for high volume production applications, further advances must be made to reduce production costs. Automation of the HP-RTM process offers the best opportunity to reduce production costs and further reduce cycle times for high-performance composite parts [43]. Opportunities for automation lie in operations such as dry fabric preforming and handling, as well as demolding and trimming of the cured part (see Figure 2.7 for automated HP-RTM process).. Automation of the fabric preforming process may cause defects that can lead to further problems during the resin infiltration process and ultimately reduced part performance [44]. Common defects observed during fabric preforming are fiber misalignment, out-of-plane wrinkling, and fiber and tow gapping [16]. Owing to the importance of the HP-RTM process fabric preforming step on the quality of an FRP composite part, there is a need to account for the potential defects associated with this process when designing FRP parts for high volume production applications. In particular, fabric draping simulations can be used to predict potential fabric preforming defects or to optimize the preforming process [13].

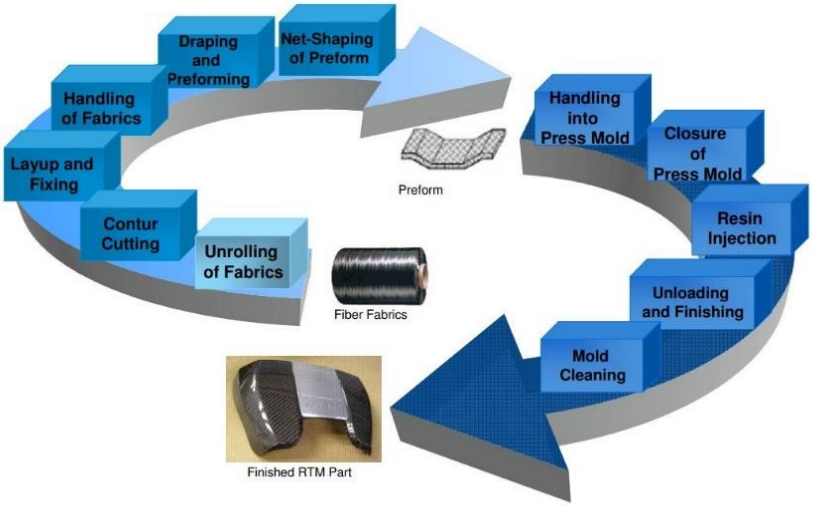

Figure 2.7. Step-by-step sequence of an automated HP-RTM manufacturing process from dry fabric to finish part [13].

2.3. Fabric reinforcement deformation modes during preforming

Characterization of fabric reinforcements is typically performed to calibrate constitutive models required for numerical draping simulations at the macro- [45], meso- [46], and micro- [47] scales, with macroscale material models being favoured for component-level draping simulations. The main goal of the characterization process is to understand the underlying deformation mechanisms that occur during fabric deformation and the effects of individual and combined deformation modes. Incorporating the deformation behaviour of fabrics into numerical draping simulation models requires a detailed characterization of the different fabric deformation modes as well as the interaction between these modes. The macroscopic deformation behaviour of fabrics is dependent on the fabric architecture and the interaction between the corresponding fabric components. During a preforming process, fabrics are primarily subjected to tensile, shear, and bending deformations (see Figure 2.8).

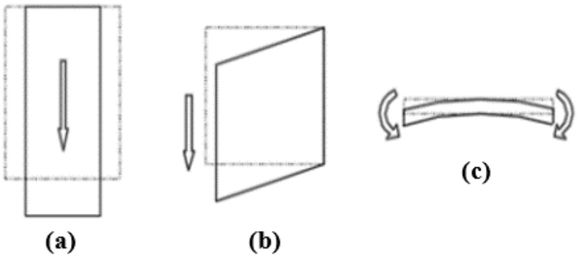

Figure 2.8. Primary modes of deformation of fabric reinforcement during preforming: (a) in-plane tension, (b) in-plane shear, (c) out-of-plane bending.

When modeling biaxial fabrics (fabrics with fibers oriented along the two material directions), the strains in the fiber directions may be considered low given the high stiffness of the fibers [48]. Although this approximation could be challenged for woven fabrics being draped around corners with small radii [24], in most cases strains in the fiber directions can be considered negligible. In contrast, the shear deformation response of fabrics is regarded as the most critical during draping [49–51] (see Figure 2.9). The lower the shear stiffness of a fabric, the more readily the fabric will conform to mold curvatures. If the shear rigidity is not low enough, the fabric will not conform to the mold, and distortion will easily occur. On the other hand, a shear rigidity that is too high could prevent the fabric from forming [52]. In the case of unidirectional fabrics, a low stiffness knitted stitching is the main load-bearing component in the direction orthogonal to the fiber direction, hence, large transverse strains can be reached during draping [48]. Thus, contrary to biaxial fabrics the in-plane deformation modes of UD-NCFs are dominated by transverse extension and shear (Figure 2.9) [48].

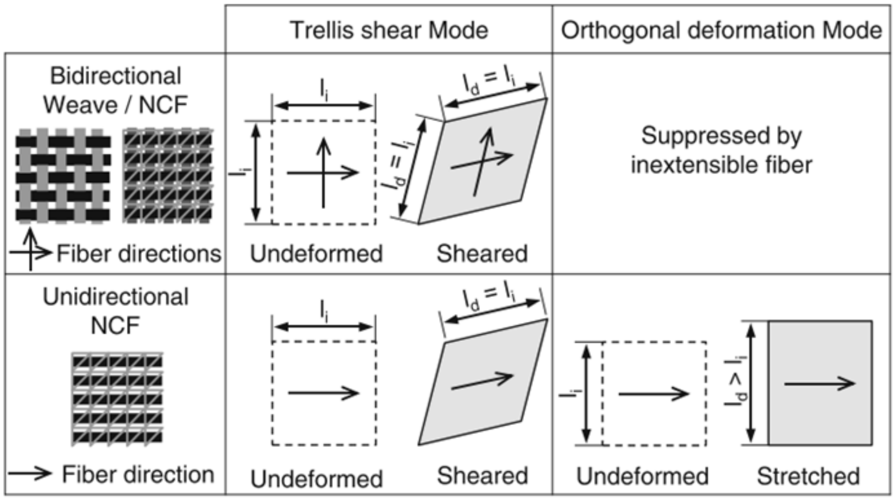

Figure 2.9. Comparison of in-plane deformation modes for bi-axial fabrics and unidirectional fabrics under the assumption of inextensible fibers [48].

The second most relevant deformation mode for woven fabrics is bending. On the positive side, bending enables contouring the fabric around curvatures, however, it could also cause undesirable wrinkling. Fabric fibers are thin structures with extremely small thickness to length ratios; consequently, they are prone to wrinkling. Additionally, the tendency to wrinkle is exacerbated by their fibrous nature, which causes inter-ply sliding and reduces their through-thickness transverse shear stiffness [53,54]. A peculiar characteristic of UD-NCF is the tendency to generate two types of wrinkling modes during forming: macroscopic and mesoscopic wrinkling. Macroscopic wrinkling is primarily instigated by negligible bending stiffness in the transverse direction, creating wrinkles that run parallel to the carbon fiber direction. On the contrary, mesoscopic buckling is induced by tension in the stitching web that creates crimping or undulations in the CF tows [16]. Generally, out-of-plane and in-plane wrinkles are common and undesirable in forming processes. Thus, the identification of forming parameters to prevent wrinkles and preserve the mechanical performance of the reinforcement is critical in composites design [55].

Friction also plays an important role in fabric forming modelling. Inter-tow friction behaviour is of interest in mesoscale models, while inter-ply and ply-tool friction are relevant for macroscale models [56]. For woven fabrics, yarn friction at cross-over point locations is observed during draping, while for UD-NCFs inter-tow and stitching-tow friction is prevalent (Figure 2.10). Even micro-scale kinematic factors, such as fiber rotation during shear deformation, play an important role in fabric deformation behaviour [57].

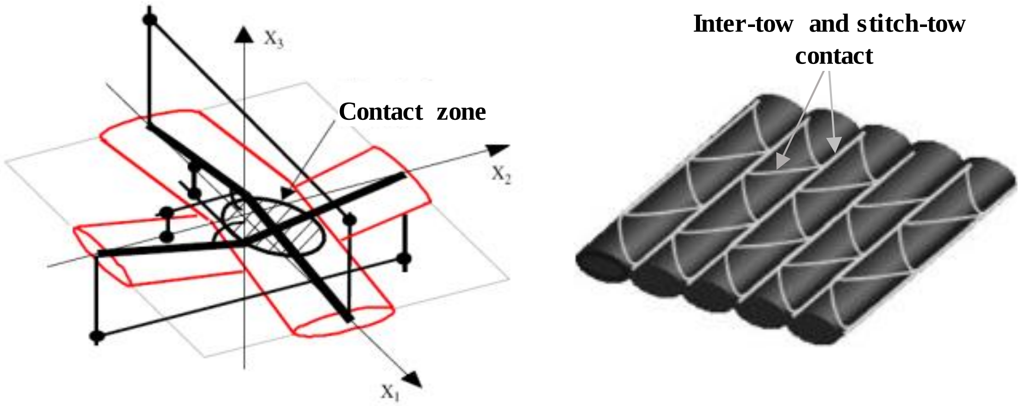

Figure 2.10. (a) Woven fabric cross-over point contact [58] and (b) UD-NCF inter-tow and tow-stitching contact [48].

Although necessary for draping, tensile, shear, and bending deformations may cause defects in the fabric that can be detrimental to the mechanical performance of the final FRP composite part [43,59]. For example, excessive in-plane shear can cause the fabric tows to compact or crimp, introducing local variations in tow orientation or fiber volume fraction [16]. Likewise, in-plane tension deformation of the fabric can cause tow gapping, while out-of-plane bending can cause wrinkling [60]. These defects can also influence the resin infiltration process [43]. In particular, tow gapping can cause variations in local fiber volume fraction which varies the fabric permeability. Fabric regions with a low fiber volume fraction can lead to race tracking during resin infiltration, which in turn could cause voids in the composite part [43,61]. On the other hand, regions with a high fiber volume fraction can limit fiber wetting and reduce fabric permeability, potentially causing dry regions in the composite part.

Although the generation of fabric alterations or defects is practically unavoidable during the preforming process, it is crucial to develop digital tools with defect prediction capabilities that can incorporate distortions generated during the preforming process [43]. An effective draping numerical model would enable the design of preforming processes that control defect generation, fiber volume fraction, and orientation, as well as the final geometric shape of the preform [62]. Therefore, the importance to mechanically characterize fabric reinforcement materials, and friction properties with respect to molds and other fabric layers, to enhance the predictive capabilities of draping defects associated with the preforming processes.

2.4. Characterization of fabric reinforcements

2.4.1. Common fabric characterization tests

There exist no test standards for characterizing reinforcement fabrics; however, a number of tests have been commonly employed to characterize the fabric deformation modes discussed in Section 2.3. For woven fabrics, characterization of the longitudinal and transverse tensile behaviour is conducted by measuring the load response along the direction of the two orthotropic warp and weft axes, as shown in Figure 2.11. Similarly, for UD-NCFs extension tests along or perpendicular to the fabric tow direction have been employed (see Figure 2.3) [16,48].

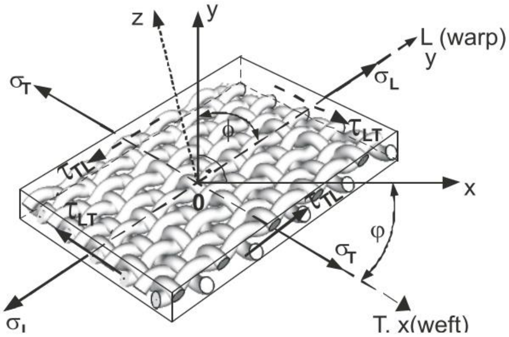

Figure 2.11. Schematic of the warp (longitudinal) and weft (transverse) orthotropic axes of woven fabrics [63].

Two common tests have emerged for characterizing the in-plane shear response of fabrics, namely the picture frame test (PFT) [49–51] and the bias extension test (BET) [16,51,64]. When applied to UD-NCFs, the BET is referred to as the 45º off-axis extension test [16,65]. During the PFT, a tensile force is applied to opposite corners of an initially square frame, causing the frame to deform from a square into a rhomboid, ideally imposing a pure shear stress state on the fabric specimen (Figure 2.12). On the other hand, the 45º off-axis extension test consists of pulling a rectangular piece of fabric, arranged such that the primary fabric axes are initially oriented at a 45° bias from the loading direction. Woven fabrics are known to develop three distinct shear strain regions during a BET, A, B, and C, as seen in Figure 2.13a. Theoretically, if there is no slip between warp and weft yarn, and assuming yarns are inextensible, the deformation in regions A, B, and C, correspond to full, half, and no shear deformations, respectively [51,66]. For UD-NCFs, the fabric is oriented at a 45º bias from the loading direction, producing two shear regions in the fabric: regions D and E, as shown in Figure 2.13 [65].

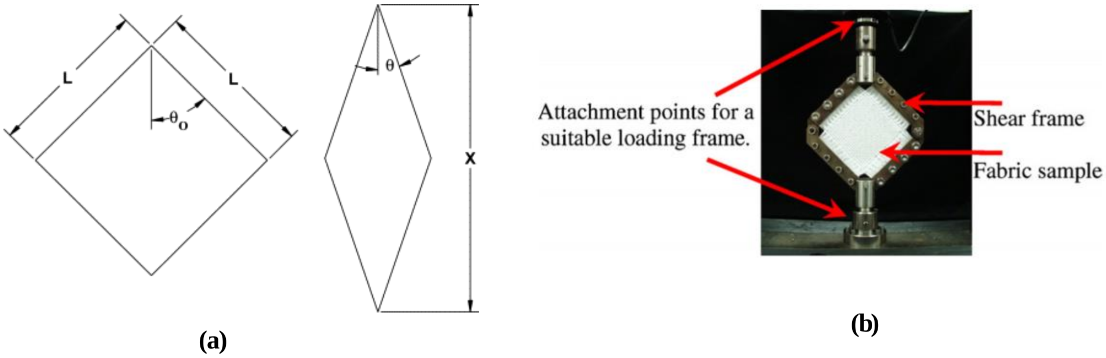

Figure 2.12. Schematic of the deformation kinematics of a fabric specimen during the picture frame test (PFT)[67] and a PFT fixture [68].

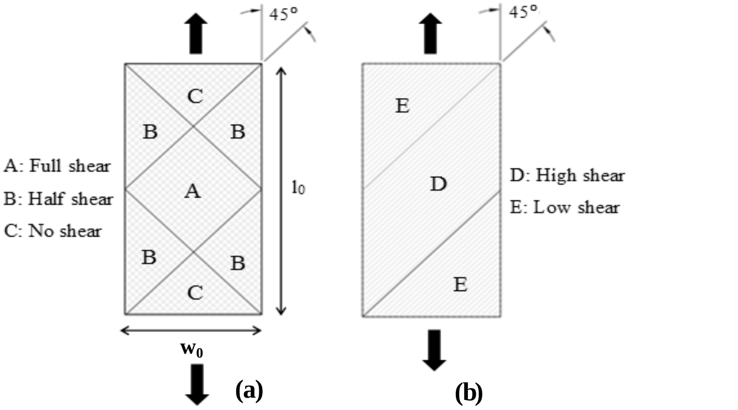

Figure 2.13. Schematics of the (a) bias extension test for woven fabric and (b) the 45° off-axis extension test for UD-NCFs [65].

There are advantages and disadvantages to both the PFT and the 45º off-axis extension test. While the PFT is aimed at subjecting the fabric specimen to a pure shear deformation, it is difficult to impose this condition in a repeatable manner. Hypothetically, the PFT applies homogenous shear deformation throughout the specimen; however, certain assumptions must be met for this hypothesis to be true. First, clamping of the specimen must hold the fabric in a way that prevents slippage and does not introduce pre-tensioning during installation on the test frame. This boundary condition is difficult to achieve, as recognized by Harrison et al. 2004 [51] and Cao et al. [68], and can introduce anomalies in the shear force response since the test setup is highly sensitive to the pre-conditioning or misalignment of the specimen in the frame. Also, overtightening or non-uniform clamping conditions on the PFT specimen can lead to spurious tensile loads within the fabric [69]. Another requirement for a valid PFT is that the specimen must stay aligned with the plane of the frame, i.e. there cannot be out-of-plane deformation [68]. This requirement can be challenging to meet due to the reduction of specimen surface area experienced during the PFT.

Despite the challenges associated with the implementation of the PFT, one advantage is that the deformation imposed on the specimen is similar to that seen during actual fabric forming [51]. However, due to the challenges associated with the PFT, the BET and 45° off-axis extension tests are preferred for the characterization of the shear response of woven and UD-NCFs [16,68,70].

Akin to characterizing the shear response of reinforcement fabrics, characterization of the bending response of fabrics is equally challenging. The bending stiffness of orthotropic fabrics cannot be deduced from the Young’s modulus, as is done for isotropic materials, thus, dedicated tests are required to characterize the macroscopic bending response of fabrics. The cantilever test (Figure 2.14a) has been typically used for capturing the linear bending behaviour of fabrics [60], while the Kawabata bending test (Figure 2.14b) has been used to characterize the nonlinear (or inelastic) bending response of fabrics [29,71]. Non-linearities have been identified in the bending stiffness of reinforcement fabrics, with a tendency for decreased stiffness with increased curvature [71,72]. However, the simplicity of implementation and data interpretation are the main advantages of the cantilever test, and in many cases, an elastic approximation of bending is sufficient for numerical model calibration [16].

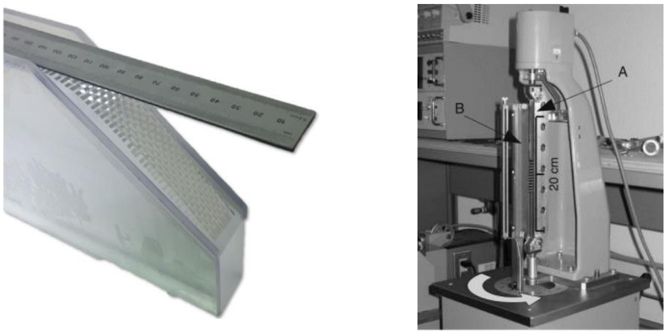

(a) **(b)**

Figure 2.14. (a) Images of a cantilever test used to characterize the bending behaviour of a woven glass fiber fabric [73] and (b) a Kawabata bending test fixture [71].

Characterization of the friction properties of fabrics is also important when for defining the boundary conditions in draping simulation models. The Kawabata surface tester (Figures 2.15a and 2.15b), which was originally developed to measure the surface properties of fabric garment, has been implemented for reinforcement fabrics [74]. In other studies, custom testing apparatus were developed to replicate the fabric forming process conditions [75]. These test apparatuses typically consist of one or two contact surfaces, with a known normal contact force, sliding relative to each other (Figures 2.15c-e).

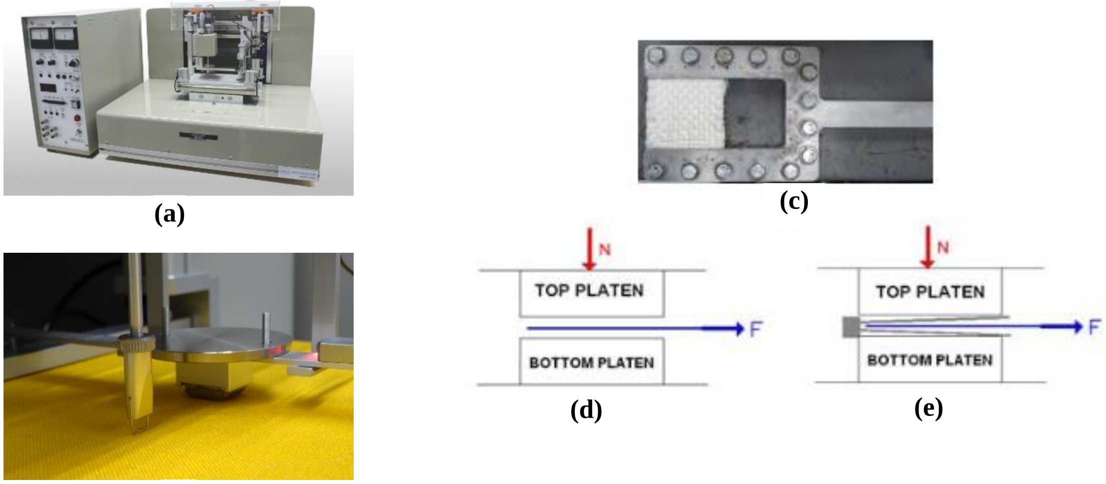

(a)

(b)

(c)

(d)

(e)

Figure 2.15. (a and b) Kawabata surface tester (KES-FB4) machine [76]. (c) Custom fabric holder and schematics of the custom friction test module with a (d) single and (e) double contact surfaces [75].

2.4.2. Fabric characterization studies

A number of researchers have reported the results of studies focused on characterizing the tensile properties of woven fabrics [55,68,77–82]. Jearanaisilawong [79] characterized the tensile properties of a plain woven aramid fabric as well as the fabric constituents (i.e., fibers and yarns). Although Young's modulus remained constant for the fiber, yarn and fabric, the ultimate tensile strength decreased and the strain to failure increased with increasing scale and complexity (i.e., fiber to a fabric) (see Figure 2.16). The different stress-strain behaviours correspond to variations in the deformation mechanisms. For the fabric the most complex tensile response was governed by yarn decrimping, followed by stretching of yarns in the loading direction. Similar findings were reported in References [46,83]. In general, the tensile properties of woven fabrics are governed by the number of yarn crossover points and the associated fiber undulation which are influenced by the weave pattern. For instance, satin woven fabrics exhibit superior tensile properties compared to equivalent plain weave fabrics due to notably fewer yarn crossover points [84].

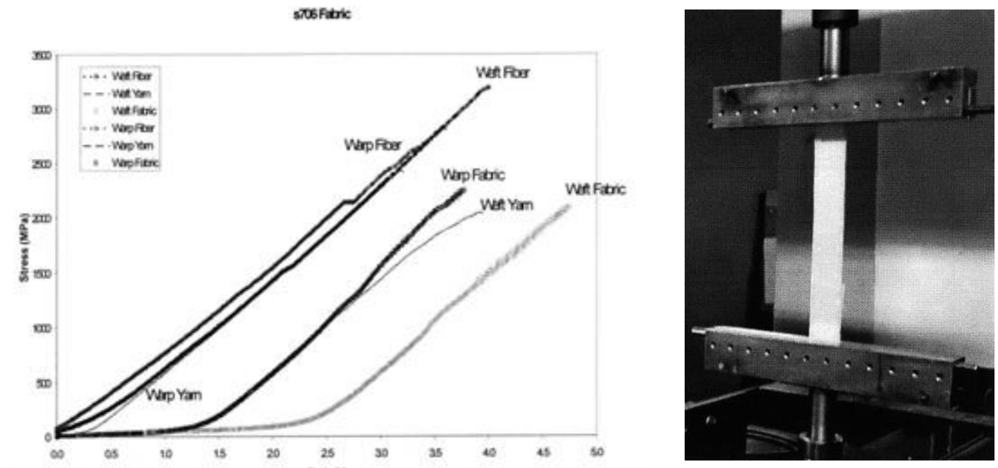

(b)

(a)

Figure 2.16. Tensile test (a) stress-strain response of a woven fabric, yarn and fiber, and (b) tensile test fixture [85].

Characterization of the in-plane shear response of woven fabrics has been the focus of many studies since shear deformation is the primary forming mechanism for draping woven fabrics over double-curved geometries [49,77,80,86–91]. To overcome some of the challenges with the PFT (see Section 2.4.1), some studies considered different configurations of boundary conditions applied to woven fabric specimens. [82] and [92] experimented with removing the weft yarns in the specimen that were adjacent to the clamps, relaxing any pre-tensioning that may have been introduced by the clamping process (see Figure 2.17a). Another PFT variation was introduced by Nosrat-Nezami et al. [93] where needles were used instead of grips to permit yarns to rotate freely during the test (see Figure 2.17b), hence avoiding yarn bending nearby the clamped boundaries. In general, these considerations provided a means to accurately capture the pure shear response of woven fabrics.

When woven fabrics are draped over a double-curved surface, variations in the angle between adjacent perpendicular yarns are a measure of shear deformation or shear angle [93]. The typical macroscale force response of woven fabrics with increasing shear angle is characterized by an s-shape profile with four distinct regions: static friction, dynamic friction, locking and wrinkling, as illustrated in Figure 2.19. When a plain-weave fabric is subjected to large shear angles, the associated macroscopic force response comes from the friction occurring at the crossover points between the warp and the weft yarns, and compression of the yarns, as seen in Figure 2.18. If the shear angle increases further, the compression of the yarns reaches a peak angle that marks the onset of wrinkling; this is called the critical locking angle [84]. In the case that shear deformation is exerted to a pre-tensioned fabric, the material shear stiffness increases as a result of the increased friction dissipation energy at crossover points, prompted by the increased tension in the yarns (see Figure 2. 19) [77].

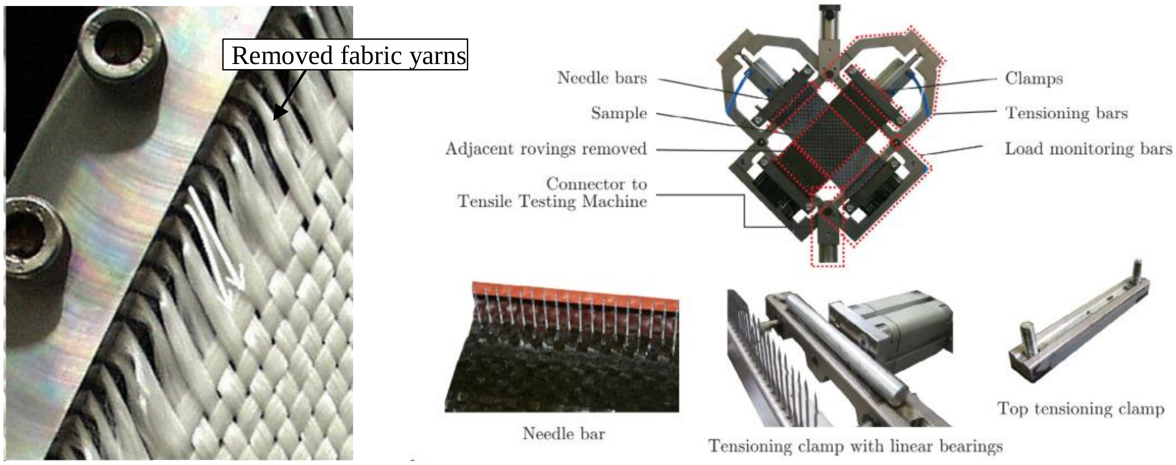

(a) (b)

Figure 2.17. PFT boundary conditions: (a) Bolted clamp with removed transverse yarns [82] and (b) needle bar clamp with linear bearing and tensioner [93].

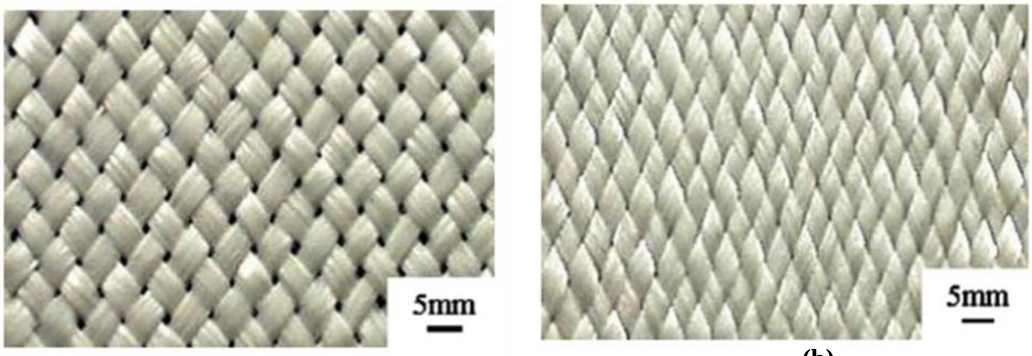

(a) (b)

Figure 2.18. Images of a woven fabric under pure shear at a shear angle of (a) 32º and (b) 50º [82].

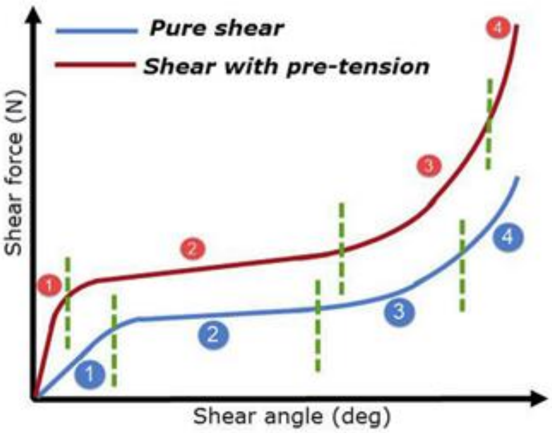

Figure 2.19. Typical shear response of a woven fabric with and without pre-tension identifying the four loading stages. (1) static friction, (2) dynamic friction, (3) locking, and (4) wrinkling [77].

Owing to the fibrous nature and relative motion of fiber yarns during bending, the bending rigidity of woven fabrics is relatively low [54]. Lin et al. [88] studied a four harness satin woven fabric and found that, at least from a mesoscale level point of view, the primary shear deformation mechanism during fabric forming was coupled to bending of yarns [88]. When draping woven fabrics around tight radii, large shear angles tend to increase shear stiffness and decrease bending stiffness, triggering the formation and increasing the size of wrinkles [53,71,72]. Additionally, Bilisik [94] found that the bending rigidity of a single fabric layer depends on linear yarn density, fabric density, and the direction of bending with respect to the warp and weft directions [94].

A number of studies have also investigated the friction properties of woven fabrics [56,87,95], where both inter-yarn (and yarn-surface) friction and inter-ply (and ply-tool) friction have been considered since they are important for calibrating mesoscale and macroscale draping simulation models, respectively. Chakladar et al. [56] investigated the friction reaction of a single tow for different inter-tow angles, reporting a negative correlation between tow angle and friction response. In other words, at a 0º relative orientation between contacting tows, the friction coefficient is maximum, dropping by half as the orientation increases to 90º. Interactions such as fiber bending, migration, and entanglement are responsible for the increase in friction coefficient between parallel tows. Also, the effect of tow size on friction response was found to be marginal [56]. Regarding fabric friction, other factors such as relative fiber orientation, shear angle, and fabric architecture influence the friction response [95]. Nosrat et al. [95] studied woven fabric-fabric and aluminum-fabric friction interaction during forming and found that the friction response increases with shear strain, effectively increasing the friction resistance between layers as shear deformation increases. Allaoui et al. [87] studied the effect of fabric architecture on friction, testing four different types of woven fabrics at varying orientation angles (see Figure 2.20). Consistent with the mesoscale or yarn-level findings by Chakladar et al. [56], Allaoui et al. [87] reported a significant decrease in the average coefficient of friction of plain-weave fabrics when the angle between ply yarns increases. Interestingly, they noticed that on balanced fabrics (such as plain weave), the friction coefficient on fabric-fabric contact is lower for the 0°/90° than for the 0°/0° relative orientation. This finding suggests a level of imbalance in the configuration of the warp and weft yarns during manufacturing of plain weave fabrics. This research also studied two CF unbalanced fabrics with resin powdering, a twill weave and an interlock weave fabric, and found remarkable differences in their kinetic friction responses. During fabric-fabric friction test with 0°/0° relative orientation, the friction coefficients almost double from the twill to the interlock fabric architecture. Friction is sensitive to the fabric architecture, as well as the relative positioning and orientation of fabric/fabric samples. This ultimately reveals that multiple varying friction coefficients, in lieu of a single friction coefficient, are required to accurately simulate a fabric forming operation [56,95].

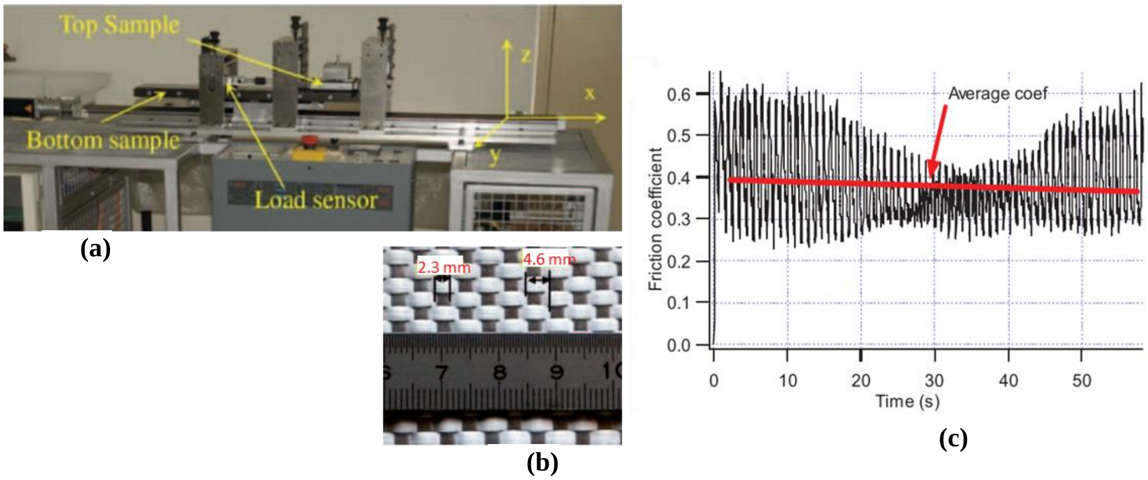

(a)

(b)

(c)

Figure 2.20. (a) Custom friction test module with a displacement controlled sliding surface. (b) Representative plain weave glass fiber sample and corresponding (c) friction coefficient data [87].

More recently, investigations characterizing the behaviour of UD-NCFs have been reported, where the same experimental tests commonly used for woven fabrics have been adopted [16,29]. The longitudinal tensile response of UD-NCFs has been reported to follow a similar trend as observed with woven fabrics (see Figure 2.16a), despite the assumption that tows are ideally non-crimped. This response is characterized by an initial low stiffness behaviour caused by tow decrimping followed by a linear response once the tows are stretched along the loading direction [30]. On the other hand, the transverse tensile response of UD-NCFs is distinct since there are no fiber tows oriented along the fabric transverse direction, and thus the effective fabric stiffness is relatively low in magnitude [16]. Therefore, the transverse response of UD-NCFs, which is dependent on the stitching architecture and the existence of low areal weight transverse supporting fiber yarns, is easily influenced by the specific testing conditions [48]. Senner et al. [48] used a coil specimen (see Figure 2.21) to capture the transverse tensile response of two UD-NCFs by minimizing the specimen edge effects. The normalized force-stretch response is characterized by an initial linear region caused by stretching of the transverse reinforcing yarns and stitching web, followed by a nonlinear response of decreasing stiffness due to successive failure of these components (Figure 2.22) [48].

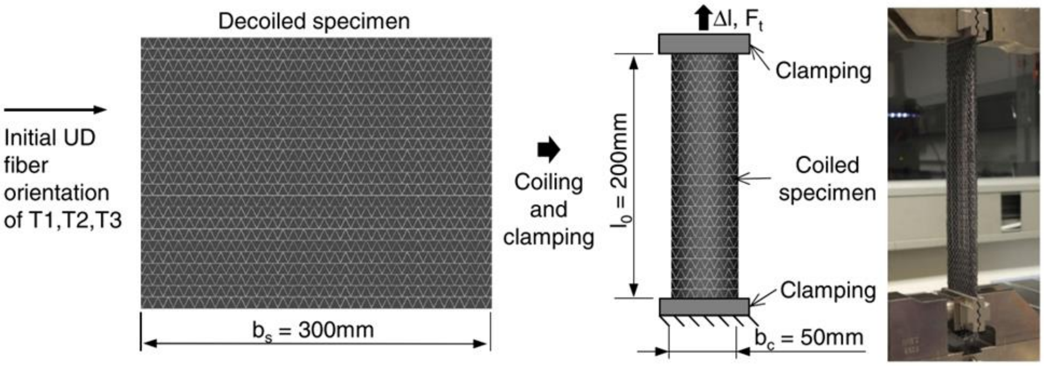

Figure 2.21. UD-NCF transverse tensile characterization test using a coiled specimen [48].

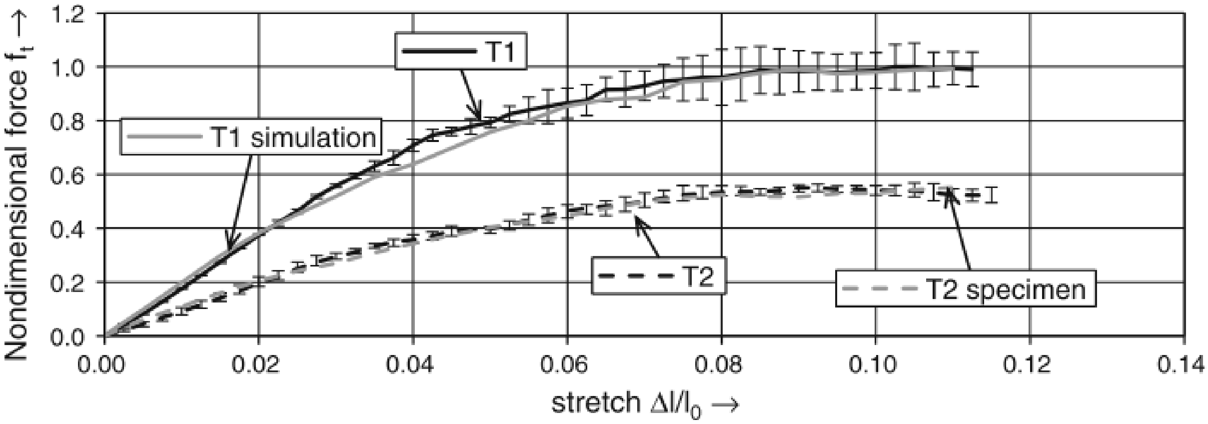

Figure 2.22. Normalized experimental and simulation results of a transverse tensile test for two UD-NCFs. The weight per unit area of T1 is twice that of T2 [48].

The shear response of UD-NCFs has been reported by few researchers to date. In their study, Schirmaier et al. [16] reported that the PFT is not suitable to characterize UD-NCFs because it induces out-of-plane deformations or wrinkling that invalidates the measurement of in-plane shear fabric response. In lieu, it was recommended that a combination of uniaxial off-axis extension tests with multiple biased angles are employed to characterize the shear behaviour of UD-NCFs . The reported shear response from the 45° off-axis extension test gathered by capturing the strain deformation in a region of interest (ROI) in the centre of the specimen, as shown in Figure 2.23a. The resulting deformation within the ROI was a combination of shear, transverse extension and longitudinal compression (see Figure 2.23b). The longitudinal compression was reported to have been caused by undulations in the CF tows. A unique characteristic of UD-NCFs is that the transverse in-plane tension and shear deformation are triggered at low applied force levels, presenting a forming challenge for UD-NCFs because, although shear deformation is desired for draping, transverse tensile strains produce undesirable gaps between the fabric tows [16]. More recently, Pourtier et al. [96] studied the characterization of shear behaviour on fabrics using the 45º off-axis extension test and postulated an alternative simple shear approach for the analysis of NCFs. This research was motivated by the inadequacy of the pure shear deformation analysis to characterize UD-NCFs, as illustrated in Figure 2.24 [97]. The shear angle displacement data for UD-NCF show the 45⁰ off-axis extension test prediction of theoretical shear angle using a pure shear deformation analysis do not correlated with measured experimental values, see Figure 2.24.

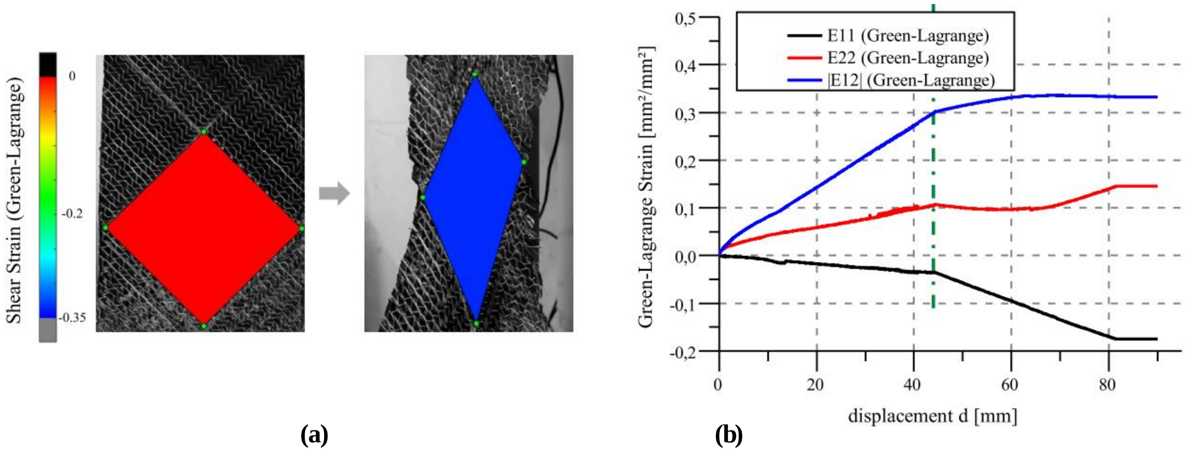

(a) **(b)**

Figure 2.23. (a) 45º off-axis extension test undeformed and deformed shape of the region of interest of a UD-NCF and corresponding homogenized shear (Green-Lagrange) strain level, and (b) homogenized Green-Lagrange material strain components versus global sample displacement [16].

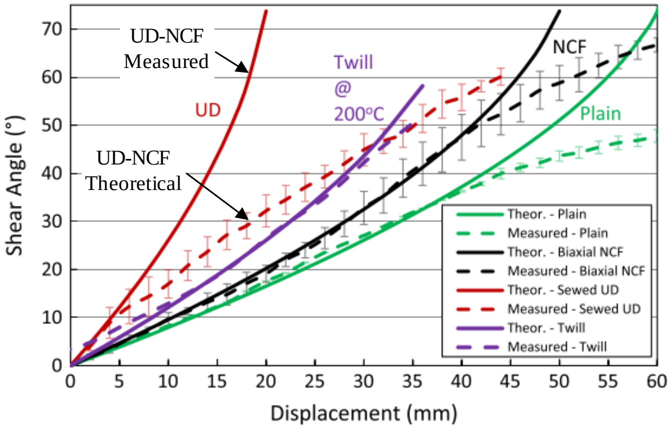

Figure 2.24. Comparison of the 45° off-axis extension test measured and theoretical shear angle calculated using a pure shear approximation approach for four different fabric architectures: plain weave, biaxial NCF, UD-NCF and twill weave [97].

The bending stiffness of UD-NCF is mainly determined by the fabric structure and fiber-fiber, fiber-stitching, and even fiber-binder interactions [98]. The most relevant study characterizing the bending behaviour of UD-NCFs was conducted by [29], where a modified version of the Kawabata bending test was implemented (see Figure 2.25). Timoshenko Beam Theory (TBT) was implemented to predict the bending behaviour in the direction of the fiber tows, obtaining an acceptable agreement with the experimentally measured deflection angles. TBT has the ability to capture transverse shear deformation by allowing independent rotation of the cross-section superimposed with the flexural deformation, as seen in Figure 2.26. In the same study it was found that a UD-NCF with stitched CF tows and transverse supporting GF yarns have a high level of bending anisotropy, with the transverse bending stiffness orders of magnitude lower than the longitudinal bending stiffness. The low magnitude transverse stiffness is attributed to the fact that there are no fiber tows oriented along the transverse direction, as well as the loose nature of the stitching structure and transverse supporting GFs, which are the main load-bearing components in the direction transverse to the carbon fiber tows. In the longitudinal direction, the stitching architecture was also reported to play a crucial role in the bending behaviour of UD-NCF [29]. In general, due to the high level of bending anisotropy draping UD-NCFs over double-curved geometries is difficult to obtain without the potential for generating defects [14]. Galkin et al. [14] found that due to the discrete nature of the UD-NCFs, the bending response in the longitudinal direction is strongly nonlinear and dominated by the through-thickness transverse shear modulus. Likewise, they reported that bending in the longitudinal direction is dominated by through-thickness fiber sliding, and that pre-shearing of the fabric has a negligible influence on bending stiffness.

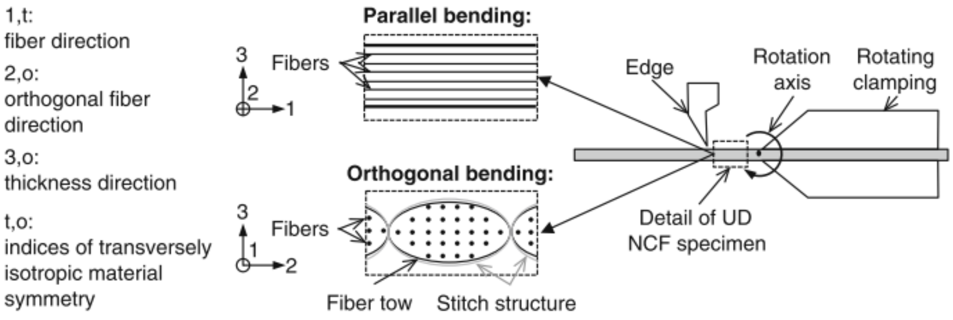

Figure 2.25. Modified version of the Kawabata bending test applied to the parallel (longitudinal) and orthogonal (transverse) direction of UD-NCFs [29].

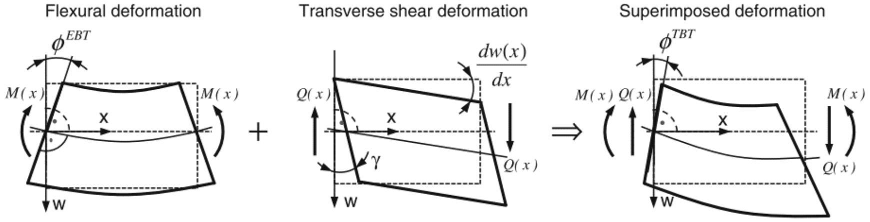

Figure 2.26. Schematic of Timoshenko beam theory superimposition of flexural and transverse shear deformation modes [29].

An important distinction in the shear response of UD-NCFs compared to woven fabric is that a shear angle cannot be defined for UD-NCFs, thus, local fiber volume fraction cannot be estimated based on the shear angle [43]. Also, sliding between UD-NCF layers is another important aspect to consider during multilayer forming. Relative sliding between the layers has an impact on preformed properties such as permeability and handling [59]. More recently, Galkin et al. [14] studied the impact of forming on the local fiber volume fraction of UD-NCFs. They reported that waviness, gapping, and transverse compression of tows due to shearing, are the main reasons for variations in the fiber volume fraction, where the important role of imposed transverse strains was also highlighted. Finally, they pointed out that tow waviness or fiber crimping increases friction during fabric forming [14].

2.4.3. Digital image correlation

Digital image correlation (DIC) is a non-contact optical method used to measure surface deformations. Two-dimensional DIC measures the full-field displacement of a planar surface by capturing variations in a speckle pattern or surface texturization applied on the surface. A high-resolution camera is typically used to capture a series of chronological digital images of the deforming surface [99]. Subsequently, the images are processed by a DIC software that converts them from RGB colour to a greyscale space format [99]. For this reason, it is important to capture clear and highly contrasted images with speckle markings that can be distinctly identified by the system [100]. DIC analysis is initiated by defining a region of interest (ROI) and a subset size. The ROI is divided by the software into a computational grid that is tracked against a reference image. The reference image is by default the first image of the sequence and represents the surface in the un-deformed state. The subset size is user-defined and must be large enough to ensure that it contains a sufficiently distinctive pattern for correlation. A suitable subset size is dependent on the image information content produced by the surface texturization [99].

DIC has been widely adopted for material characterization, including for composite materials [8,101]. However, dry fabrics such as UD-NCF, are challenging materials to study using DIC due to several reasons. First, UD-NCFs may be susceptible to large shear deformations, complicating deformation tracking. Second, the DIC algorithm approximates the heterogeneous surface of the fabric as a continuum. This approximation may introduce uncertainties caused by surface shifting. For example, a particular fiber filament initially on the surface of the fabric may relocate under the fabric surface during deformation, disappearing from the DIC image [102]. The combination of these factors can lead to pattern breakdown and loss of correlation for fabrics during DIC analysis [102]. For these reasons, DIC has not been widely used to characterize reinforcement fabrics. Dridi et al. [103] was able to capture shear strain deformation on plain-woven cotton fabric, obtaining a positive correlation between experimental and theoretical data. Vanclooster et al. [50] used 3D DIC to track deformations during a double dome forming operation applied to a GF woven fabric and reported having image correlation challenges. First, contact of the tool with the fabric damaged the painted surface pattern. Also, around areas of double curvature, DIC analysis failed due to excessive light reflections from the fabric. More recently, Harrison et al. [60] investigated the out-of-plane deformation of a 2x2 twill-weave CF using 3D DIC. They also encountered experimental challenges related to the high reflectivity, as well as a stiffening effect resulting from surface texturization of the fabric. Application of surface patterns to reinforcement fabrics in preparations for DIC analysis is a challenging task [50,60,84,104] that requires the consideration of the fabric material, architecture, surface reflection, and previous surface treatments.

2.4.4. Summary

A review of the current literature has revealed that in general few studies have characterized the deformation response of stitched UD-NCFs. These fabrics have been characterized as having distinct macroscopic and local deformation modes compared to more widely studied woven fabrics, which stems from the distinct fabric architecture in particular the absence of tow crossover points in UD-NCFs. More in-depth characterization is necessary to improve the quality of the calibration data that is used for material constitutive models, and ultimately to increase the fidelity of corresponding fabric draping simulation models. Additionally, there is a requirement to develop standardized testing techniques for UD-NCFs. The same characterization techniques that have been widely used for woven fabrics are not necessarily applicable for UD-NCFs due to the distinct fabric deformation characteristics. Specifically, there is an absence of friction characterization data for UD-NCFs in the literature, while there are also discrepancies regarding the best approach to characterize the fabric shear response. Moreover, few studies have been conducted to characterize the forming behaviour of UD-NCFs for parts with three-dimensional geometries. This would otherwise be critical for developing an improved understanding of the fabric response during preforming, and to provide a means to validate draping simulations. Finally, there is no widely accepted approach for measuring strain in deformed fabrics. DIC has been considered in few studies to date, with no consensus on the best approach for accurately capturing strains in UD-NCFs.

2.5. Simulating draping of fabric reinforcement

The use of simulation tools to predict the deformability of fabric preforms during forming operations is essential for optimizing the manufacturing processes for CFRPs [71]. Modelling the deformability of reinforcement fabrics is challenging due to complex interactions between the fabric components and the multiple length scales in which these components deform (see Section 2.4.2). As discussed in Section 2.1, fabric reinforcements can be analyzed at the micro, meso, and macroscale discretization levels. The approach chosen to model the forming of fabric reinforcements depends on the scale at which the analysis is made. Independent of the modelling approach, the main challenges are to simulate large strains and high levels of anisotropy accurately [59].

Computational predictions of woven cloth deformations were first reported by Mack and Taylor [105] where so-called pin-joint-net models were developed. This modelling approach, also termed the kinematic approach, did not provide any physically meaningful data, such as the deformation loads, and instead was used to approximate the deformed shape of draped fabrics [106]. Although this modeling approach was computationally inexpensive, it neglected the mechanical properties of the fabric material. Mechanical models that use continuum-based finite element methods to capture fabric behaviour have also been developed [107,108]. Among other advantages, mechanical models allow for simulation of the interactions between the fabric and the tooling, significantly increasing the fidelity of models. In recent years, most of the research on fabric draping has focused on mechanics-based simulations rather than on kinematic approaches [59]. Until recently, much of the research efforts had been directed to improving computational speed for solutions, rather than improving the fidelity of draping models [109–111]. More recently, due to the advances in computational processing speeds, the emphasis has shifted towards improving the fidelity of mechanics-based simulations for predicting the onset of defects to assist in the design of semi-automated manufacturing processes [112].

Draping simulation models can be classified as either mesoscale or macroscale numerical models. In mesoscale models the homogenized tows/yarns and the other fabric components are discretized. A suitable mesoscale model must be able to numerically predict the equivalent material behaviour at the macroscale [64,73,113–117]. Alternatively, in macroscale models fabrics are treated as effective continuum materials and the complex internal mechanical behaviours are implicitly captured [29,54,60,62,70,108,113,118–131]. One of the main advantages of mesoscale models is their ability to capture interactions between the tows/yarns, such as transverse yarn compression and crimping, which are difficult to obtain with semi-discrete and continuous models. Also, these models are particularly useful in the study of fabric properties such as permeability and shear behaviour [59]. On the other hand, it is difficult to correctly model out-of-plane bending stiffness and friction interactions with mesoscale models. Also, complexity of mesoscale models is high due to the large number of elements and interactions being simulated. Thus, macroscale models tend to be more computationally efficient and the preferred choice for many applications.

The current state of the art predictive technology for reinforcing fabric aims at predicting not only the deformed net shape, but also the local fiber volume fraction and fiber orientation of a formed shape, to transfer these predictions from draping simulations into resin infiltration simulations [43].

2.5.1. Mesoscale fabric draping simulation models

Lin et al. [114] developed a mesoscale model for a woven fabric, where the homogenized yarns were treated as transversely isotropic materials with non-linear mechanical properties. The model incorporated normal stiffness definitions parallel to the fabric and shear was determined by the interaction between the warp and the weft yarns. The model failed to accurately predict the shear strain of the continuum element in relation to the strains applied to individual yarns. They noted that regardless of how accurately yarn sliding was modelled, the internal stress of the yarn could not be accurately estimated [114].

Another study conducted by Jauffres et al. [46] proposed a mesoscopic material model for forming simulations of woven fabrics. The model implemented truss and beam elements to represent the homogenized yarns, and shell and membrane elements to represent the shearing behaviour. The material model was implemented in two numerical solvers: Abaqus and LS-DYNA, and compared through a hemispherical test simulation. Abaqus shell elements exhibited higher stiffness than LS-DYNA shell elements. Consequently, the simulation punch force response was also higher for Abaqus compared to the LS-DYNA simulation due to the inability of Abaqus to decouple bending and transverse shear from in-plane stiffness [46]. Results from the two software predictions are shown in Figure 2.27b.

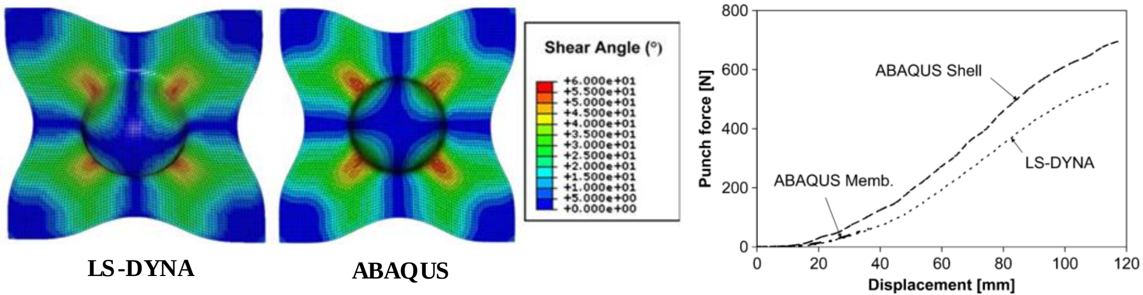

(a) (b)

Figure 2.27. Comparison of (a) shear angle distribution and (b) punch force response from Abaqus and LS-DYNA hemispherical test simulations [46].

Likewise, Cherouat et al., 2013 [115] developed semi-discrete models for woven fabrics using mutually constrained truss, representing the tensile behaviour, and shell elements, representing the shear behaviour of the reinforcement. The mutually constrained elements had their nodes permanently attached to fixed material points. The model was validated using a hemispherical test and was able to predict shear angles (see Figure 2.28), and load-displacement data. The model was not calibrated for bending stiffness, and the impact of the truss and shell elements contribution to the overall mechanical behaviour was not assessed.

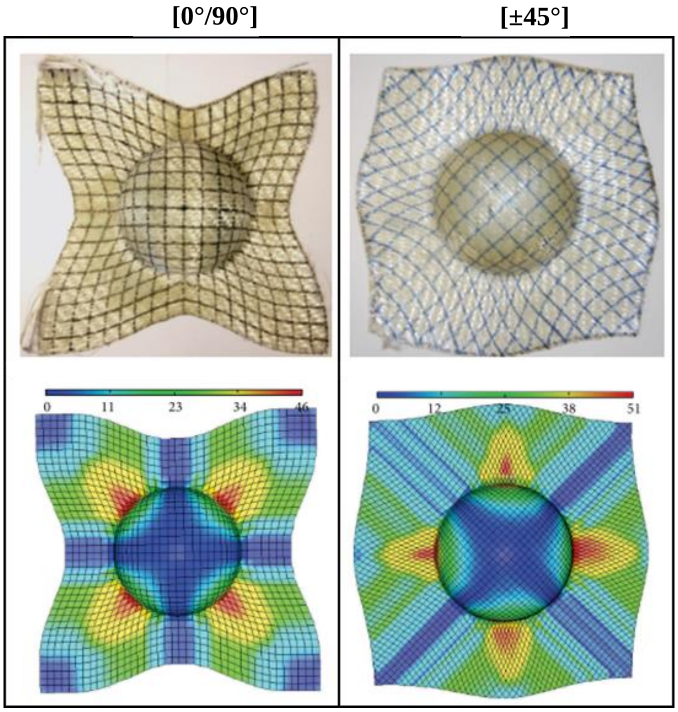

Figure 2.28. Hemispherical test experimental and predicted shape and shear angle data from a model with mutually constrained truss and shell elements published in [115].

Li et al. [64] investigated the in-plane shear behaviour of biaxial carbon non-crimp fabric using biaxial extension and picture frame tests. The study focused on the role that the stitching plays in the overall fabric deformation. The model was implemented in Abaqus explicit, and was discretized with the CF tows represented by rectangular solid elements, while beam elements were used to represent the tricot stitching pattern. A clear advantage of this approach was the ability to predict inter-tow interactions such as fiber slippage, as shown in Figure 2.29. The study found that even though the material tested was a biaxial fabric, which in principle is a balanced fabric, the strained condition of the stitching had a significant influence on the in-plane behaviour of the fabric, resulting in an apparent asymmetrical shear behaviour. Harrison et al. [73] expanded the capability of mesoscale models for NCFs by incorporating independent deformation modes to the stitching. The proposed model discretized the fabric with truss, beam, and membrane elements allowing independent control of axial fiber stiffness, in-plane shear compliance as well as in-plane and out-of-plane flexural moduli (see Figure 2.30). Erol et al. [116] developed and implemented a mesoscale unit cell model for a woven fabric in LS-DYNA® using truss elements. In the model, the tensile and shear behaviours were decoupled. The tensile response was incorporated in the model by aligning the truss elements in the warp and weft directions. In contrast, the shear response, which depends on yarn-to-yarn contact, rotation, sliding and compression, was modelled using a rotational spring location at the cross-over points (see Figure 2.31). Dörr et al., 2017 [117] developed a user-defined model in Abaqus that fully decoupled membrane and bending behaviour of UD-prepreg materials using a combination of membrane and shell elements. The membrane and bending behaviours were both modelled according to Voigt-Kelvin viscoelastic formulation, taking into account the rate dependency of prepregs at process conditions.

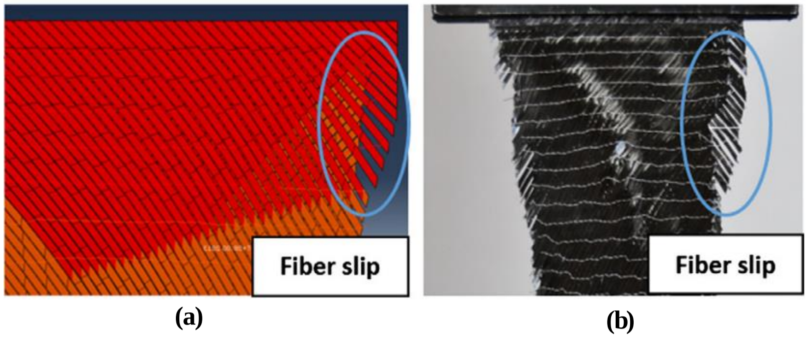

(a) (b)

Figure 2.29. Image of (a) a mesoscale model prediction of inter-tow slippage seen in (b) physical experiments [64].

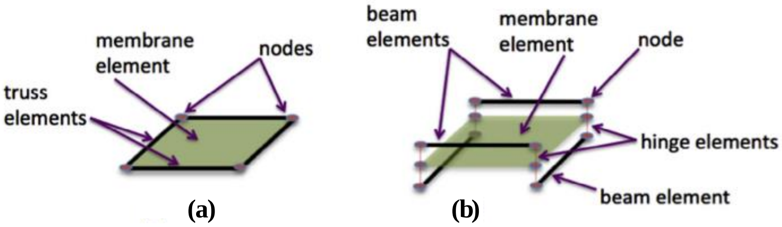

Figure 2.30. Unit cell of (a) a mutually constrained truss and membrane elements and (b) a mutually constrained pantographic beam and membrane mesh proposed by P. Harrison et al., 2016 [73].

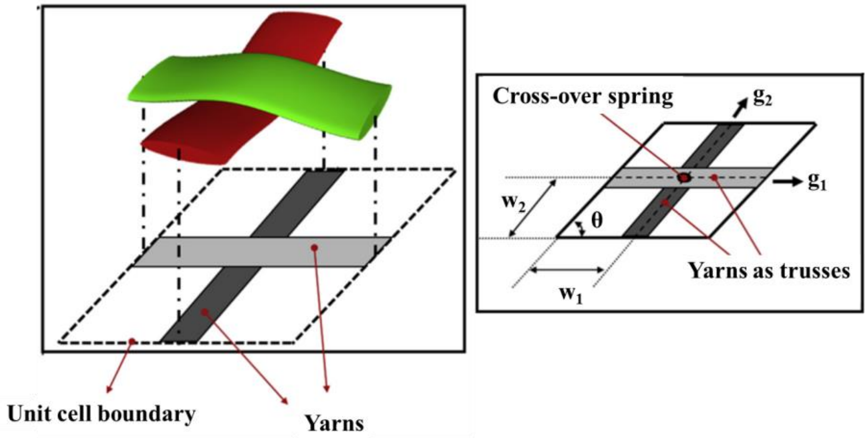

Figure 2.31. Mesoscale representation of a woven fabric using truss elements and rotational springs at cross-over points [116].

2.5.2. Macroscale fabric draping simulation models

Although mesoscale level models are valuable for research purposes, their complexity and high demand for computational resources make them of limited commercial value [129]. This has motivated the development of more computationally efficient macroscale or continuum models for simulating fabric draping. Developing suitable constitutive models for reinforcement fabrics is challenging at best. The first point to consider is that homogenization strategies must be implemented to represent the discrete reinforcement fabric as an effectively homogeneous material at the macroscale, where effective properties are used (see Figure 2.32). The underlying goal of the homogenization process is to postulate a macroscopic constitutive formulation that incorporates details of the fabric constituents at the lower length scales. In some applications, these techniques have proven to be appropriate methods to analyze the behaviour of discrete materials [70,130,132]. In general, there are two methods to develop homogenized constitutive formulations for fabrics. The material may be characterized at the macroscale level and experimentally obtained material properties assigned directly to the constitutive model [60,131]. Alternatively, a mesoscale model may be used to predict the effective material behaviour and then those properties assigned to the constitutive model [113]. Figure 2.33 shows an example of a macroscale draping simulation prediction for a woven fabric.

Furthermore, reinforcement fabrics are orthotropic materials. Many material models have been developed for homogeneous isotropic materials where the Young's and shear moduli are coupled through the Poisson's ratio, as illustrated by Hooke's law in Equation 2.1. This approach is not suitable for reinforcement fabrics [54], where the coupling parameters in the constitutive equation for plane stresses are fabric specific and difficult to ascertain (see Equation 2.2). Also, fabrics exhibit both material and geometric nonlinearities [118,119] as a result of the large deformations that are attainable. The inelastic response of reinforcement fabrics has been represented using numerous types of constitutive models, including hyperelastic [122,123,133], elastoplastic [62,108], and viscoelastic [117,133]. The development of continuum non-orthogonal constitutive models has enabled the representation of the non-linear behaviour of fabrics, while accounting for yarn/tow reorientation during large shear deformations [120].

$$\begin{bmatrix}\sigma_{11}\\ \sigma_{22}\\ \sigma_{12}\end{bmatrix} = \frac{E}{1-\upsilon^2}\begin{bmatrix}1 & \upsilon & 0\\ \upsilon & 1 & 0\\ 0 & 0 & 2(1+\upsilon)\end{bmatrix}\begin{bmatrix}\varepsilon_{11}\\ \varepsilon_{22}\\ 2\varepsilon_{12}\end{bmatrix} \tag{2.1}$$

$$\begin{bmatrix}\sigma_{11}\\ \sigma_{22}\\ \sigma_{12}\end{bmatrix} = \begin{bmatrix}E_1 & ? & ?\\ ? & E_2 & ?\\ ? & ? & G_{12}\end{bmatrix}\begin{bmatrix}\varepsilon_{11}\\ \varepsilon_{22}\\ 2\varepsilon_{12}\end{bmatrix} \tag{2.2}$$

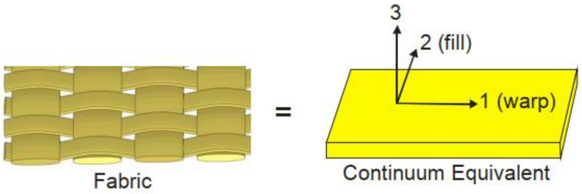

Figure 2.32. Schematic of the continuum equivalent of discrete fabric material [134].

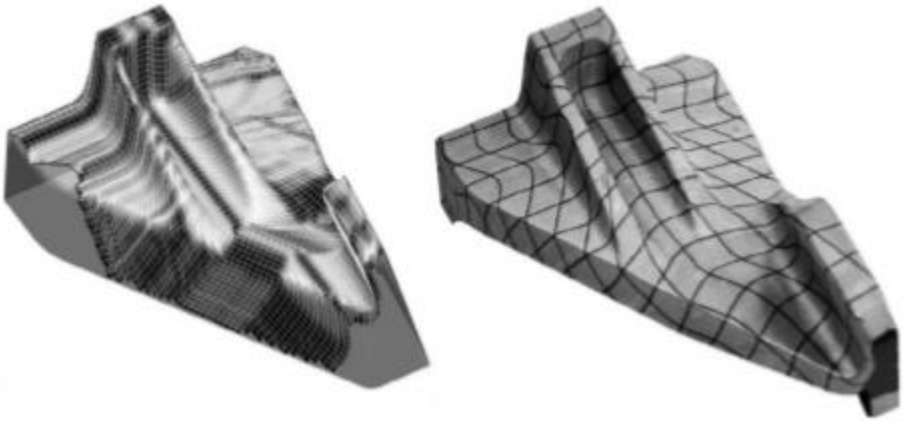

(a) (b)

Figure 2.33. (a) Image of a complex part numerical simulation output and corresponding (b) real preformed part [59].

For performing fabric forming simulations, hyperelastic and hypoelastic constitutive models have been the most widely used. In a hyper-elastic model of a woven fabric, the strain energy is decomposed into the tensile energy in the yarns and the shear energy at crossover points, each of which is determined using curve fitting with uniaxial tensile and shear frame tests [123,126]. Hyperelastic material models have intrinsic material objectivity, making possible the tracking of individual fibers via intrinsic covariant modelling [127]. By contrast, in hypoelastic models, deformation objectivity must be incorporated by application of suitable material frames and transformation laws between a prescribed material frame (e.g., Green-Naghdi's frame) and a fiber parallel frame [108,117,124]. Peng et al. [128] compared a non-orthogonal to an orthogonal hypoelastic constitutive material model, showing that the accuracy of the non-orthogonal model was substantially higher in predicting the boundary profile for a hemispherical test specimen (see Figure 2.34).

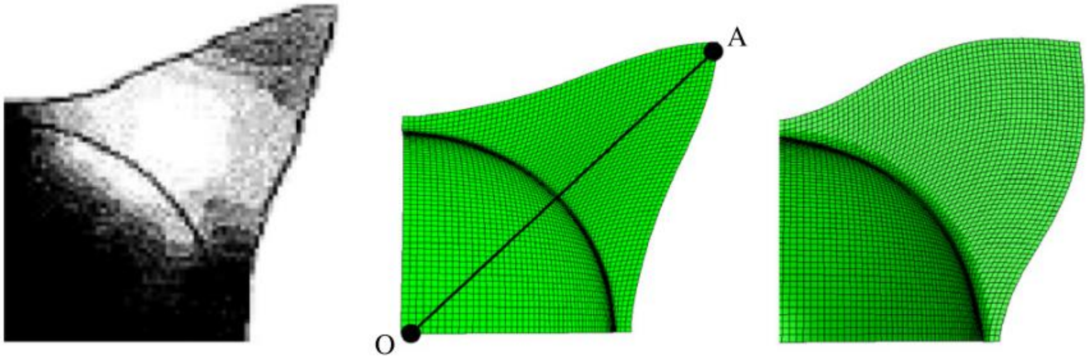

(a) Experiment [28] (b) Nonorthogonal (c) Orthogonal

Figure 2.34. Hemispherical test comparison of a deformed blank between (a) experiment and (b) non-orthogonal and (c) orthogonal simulations [128].

Chen et al. [70] developed a hypo-elastic macroscale model that implemented the non-orthogonal material constitutive equations proposed by Yu [120]. The model was developed as a custom material subroutine to predict the forming behaviour of biaxial fabrics with the aim of tracking the warp and weft yarn direction at the macroscale level. They reported the predicted shear angle distribution to be within 5% of the experimental data from a hemispherical draping test (see Figure 2.35). This study used membrane elements, neglecting the out-of-plane bending deformation of the material.

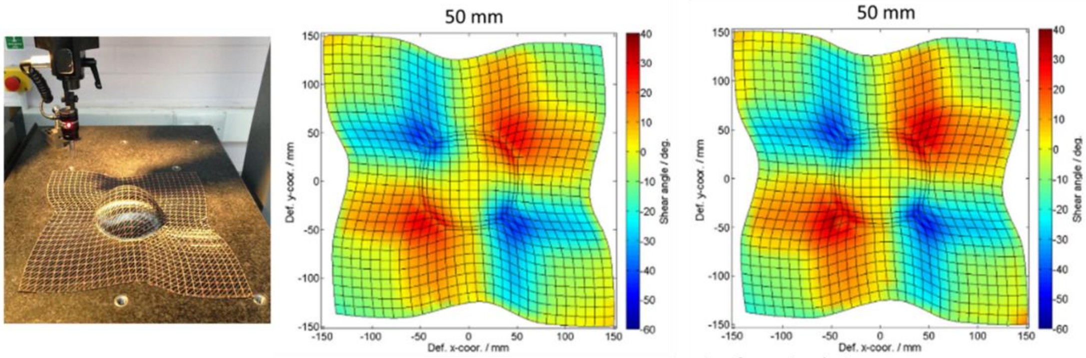

(a) (b) (c)

Figure 2.35. Image of (a) a hemispherical test, and (b) experimental shear angle distribution extracted using a grid strain analysis system, and (c) shear angle distributions from a macroscale numerical simulation [70].

Boisse et al. [132] highlighted some of the shortcomings of fabric models developed within the framework of Cauchy continuum mechanics. They pointed out that this framework is not able to capture fiber slippage and fiber bending stiffness accurately (Figure 2.36). To accommodate deformation discontinuities, they proposed a generalized second gradient theory to complement an orthotropic hyperelastic model, where the strain energy density function was assumed to depend not only on the deformation tensor but also on its gradient [132]. The model was validated with a hemispherical test.

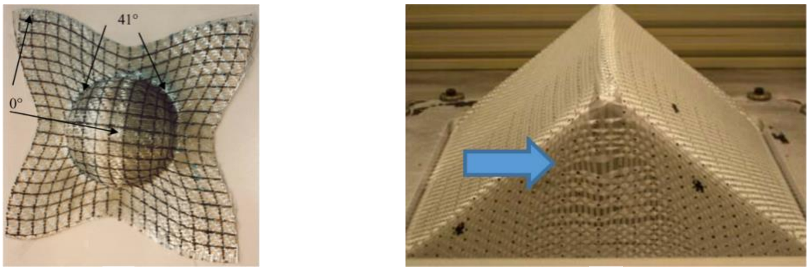

(a) (b)

Figure 2.36. Pictures of (a) a hemispherical test with lines showing material continuity and (b) preforming test with interruptions in fabric continuity [132].

Draping studies of UN-NCFs have received much less attention in the literature compared with woven fabrics and biaxial NCFs [29,62]. Senner 2015 [29] focused on characterizing the bending behaviour of UD-NCF to predict the onset of wrinkle formation during forming using a transversely isotropic hyperelastic constitutive model. The study compared Euler-Bernoulli and Timoshenko beam theories (TBT), adjusting the magnitude of the transverse shear to match experimental results. The model was validated by conducting a draping forming process of a single curvature part (see Figure 2.37). They found the bending stiffness in the transverse direction is negligible and assigned a low value to it in the simulation for numerical stability. Figure 2.37a shows the results of a draping test with the fiber direction aligned with the plane of the page, while in Figure 2.37b, the fibers are aligned perpendicular to the plane of the page. This study demonstrated that the bending behaviour of UD-NCF differs significantly from that of continuous materials.

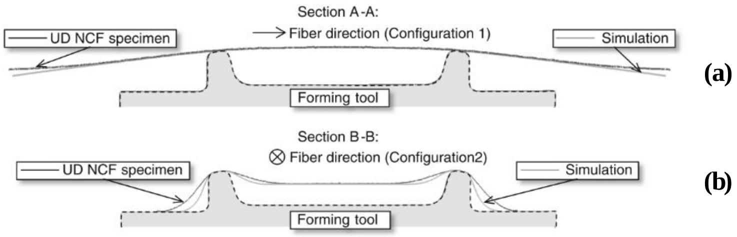

Figure 2.37. Experimental and simulation results of unidirectional non-crimp fabric forming operation over a single curvature shape with the fibers aligned (a) parallel and (b) perpendicular to the plane of the page [29].

A more comprehensive study of the deformation mechanism of UD-NCF for draping modelling was conducted by Schirmaier et al., 2017 [62]. They implemented a hypoelastic material constitutive model that superimposed longitudinal tensile and shear deformation with transverse in-plane deformation. In addition to non-orthogonal and nonlinear in-plane strains (ε_1 and ε_2), this model incorporated a third measurement of plane strain perpendicular to the carbon fiber tows ($\varepsilon_\perp$), as seen in Figure 2.38 In-plane behaviour was assumed to be elasto-plastic while bending behaviour was assumed to be elastic with distinct definitions in the longitudinal and transverse material directions. Their proposed model was parametrized via simulations of off-axis extension tests, and validated with preforming simulations of a hemispherical test and typical automotive component (light pod), shown in Figure 2.39. The model was able to make estimations of fiber orientation, tow gapping, macroscopic wrinkling and contour shape. However, it was unable to predict discrete localized features, such as fiber and tow undulations and bending of individual carbon fiber tows.

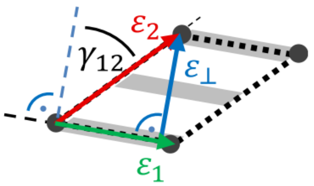

Figure 2.38. Linear non-orthogonal strain definitions used by the macroscale model developed by Schirmaier [62].

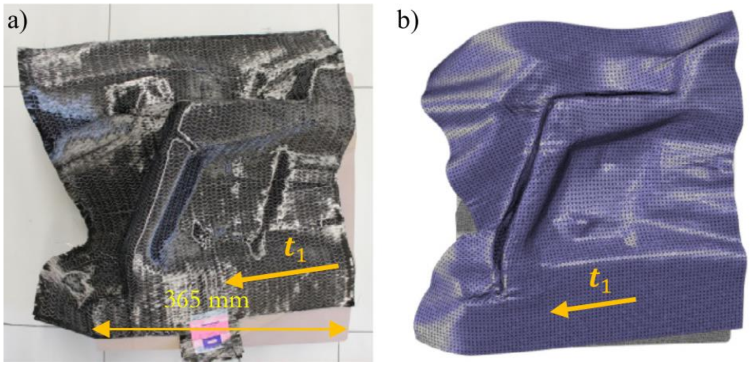

Figure 2.39. Comparison of (a) experimental and (b) numerical forming simulation results presented by Schirmaier et al. 2017 [62].

There are several commercially available finite element codes with available material constitutive models that have been also used for developing macroscale fabric draping simulation models. PAM-FORM® utilizes explicit time integration and includes MAT140 for draping of woven or unidirectional prepregs and is normally used to represent the constitutive behaviour of each separately discretized fabric layer [135]. The material model represents the fabric layers as a superposition of an elastic fiber phase, and a viscous matrix phase used for prepreg materials [31]. Another commercial software for simulating draping of fabrics is AniForm®. Currently, the code is capable of predicting forming behaviour for UD-tapes, woven and NCF dry-fabrics with either a thermoplastic, thermoset, or no matrix constituent, employing an implicit time integration scheme and a combination of elastic and viscoelastic material formulations to represent an arbitrary number of fiber families [135,136].

Other multi-purpose FE-solvers that have been used for conducting fabric draping simulations are Abaqus and LS-DYNA. Abaqus is a multi-purpose FE-solver with limited capability to execute macroscale forming simulations. Abaqus only offers one suitable built-in fabric material model (*Fabric) that was developed for a woven fabric. To enhance the capabilities of Abaqus, and taking advantage of its ability to define custom-made elastoplastic and viscoelastic material models, some researchers have developed user-defined material definitions for specific fabric draping simulations [98]. LS-DYNA includes two relevant macroscale material models for fabrics, MAT 234 and MAT 235, that incorporated crimping of fibers, shear locking, and contact force at the fiber cross-over points [137]. These material models require the input of mesoscale material parameters such as the yarn moduli and yarn-yarn interaction coefficient, which in practice require complex direct experimental characterization, and difficult and time-consuming reverse calculations [138,139]. LS-DYNA developed a thermoplastic prepreg composite material model, MAT 249, with an explicit time integration scheme that allows the definition of UD-NCF, as well as woven fabrics or NCFs. The fiber behaviour is defined by an anisotropic hyperelastic material formulation with temperature-dependent properties capabilities [135,137,140]. Dorr [135] simulated a thermoforming operation of pre-consolidated blanks of thermoplastic UD-tape using LS-DYNA MAT 249 and compared the output to experimental results. They found that LS-DYNA lacks some general features typically available in forming simulations, such as decoupled bending behaviour from in-plane deformations. However, one strength of MAT 249 is the ability to parametrize specific deformation mechanisms by means of characteristic curves [135]. Comparing the simulation to experimental results, they found that LS-DYNA was able to successfully predict wrinkling and the outer contour of a deformed surface, as shown in Figure 2.40.

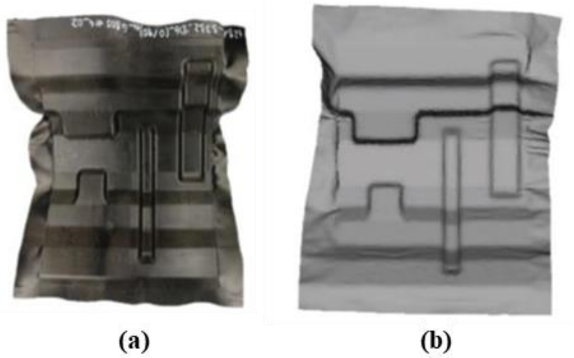

Figure 2.40. Comparison of a quasi-isotropic layup (a) experimental forming test and (b) corresponding LS-DYNA® simulation prediction [135].

2.5.3. Summary

A review of the macro and mesoscale numerical draping simulation models reported in the literature has shown the current limitations. While mesoscale models are attractive for their capacity to discretize yarn interactions, the need for high computational resources makes them unpractical for component level simulations, particularly for multi-layer fabric forming. Development efforts of the more practical macroscale models, on the other hand, have focused on woven or biaxial NCFs and few studies have been published for UD-NCFs. Additionally, macroscale fabric modelling presents important challenges, such as the ability to incorporate the potential of fabric discontinuities and coupling of the different deformation modes during draping. Although there are few commercial finite element software available for the simulation of UD-NCFs, most of these were developed and adapted from other material systems and lacked the ability to model the unique deformation characteristics of UD-NCFs.

Chapter 3: UD-NCF Material and Experimental Techniques

Details of the UD-NCF reinforcement material investigated in this study, including the fabric composition and microstructure, are first discussed (Section 3.1). The experimental techniques used to characterize the fabric deformation modes that are relevant to the fabric preforming process and required to calibrate the material constitutive model are also presented (Section 3.2). The performed draping tests that were used to validate the numerical draping simulation model are also presented (Section 3.3).

3.1. UD-NCF material

A commercially available UD-NCF, namely Zoltek^{TM} PX35-UD300, was characterized in this study (Figure 3.1). The heavy-tow fabric is comprised of 5 mm wide tows each containing 50,000 PX35 carbon fiber (CF) filaments. The tows are aligned parallel to each other and are stitched together with polyester yarn in a tricot pattern (Figure 3.2). The supporting glass fiber (GF) yarns are aligned perpendicular to the CF tows, positioned between the CFs and the polyester stitching (Figure 3.2). A light thermosetting binder powder, that is intended to cure during fabric forming, is uniformly distributed on the stitching side of the fabric. The total fabric areal density is 333 g/m^2 with the carbon fiber tows accounting for 92.8% of the total weight. A summary of the fabric characteristics measured directly from the fabric or taken from the manufacturer data sheet is presented in Table 3.1.

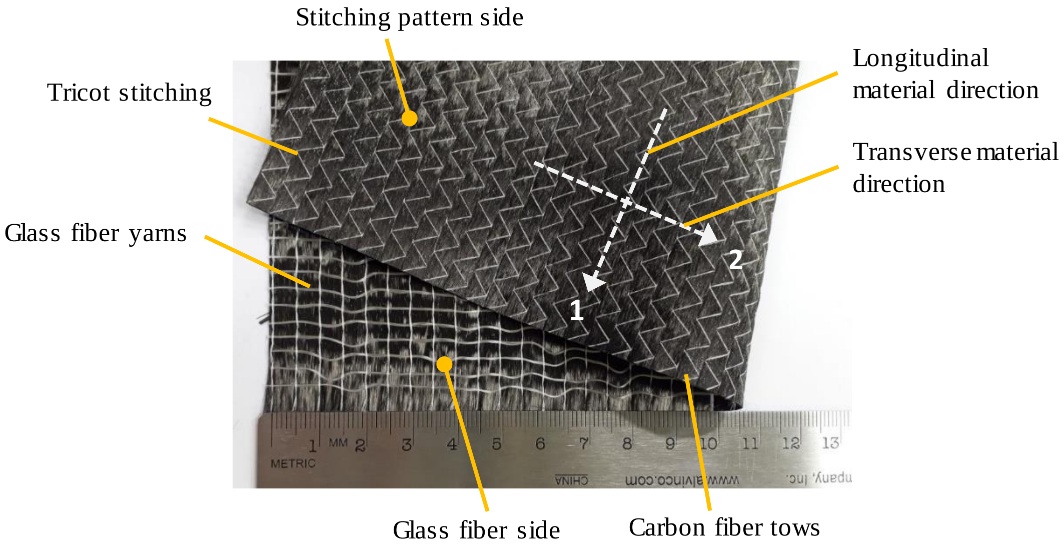

Figure 3.1. Image of ZoltekTM PX35-UD300 unidirectional non-crimp fabric with glass fiber and stitching sides indicated.

Table 3.1. ZoltekTM PX35-UD300 unidirectional non-crimp fabric characteristics [141].

Parameter	**Value**
Total fabric areal density	333 g/m^2
Carbon fiber tow weight fraction	92.8%
Glass fiber yarn weight fraction	3.0%
Glass fiber yarn linear density	34 dtex
Polyester stitch weight fraction	1.8%
Polyester stitch linear density	76 dtex
Binder resin powder weight fraction	2.4%
Nominal Carbon fiber diameter	7.2 µm
Carbon fiber tow width (measured)	5 mm
Dry fabric thickness (measured)	0.49 ± 0.02

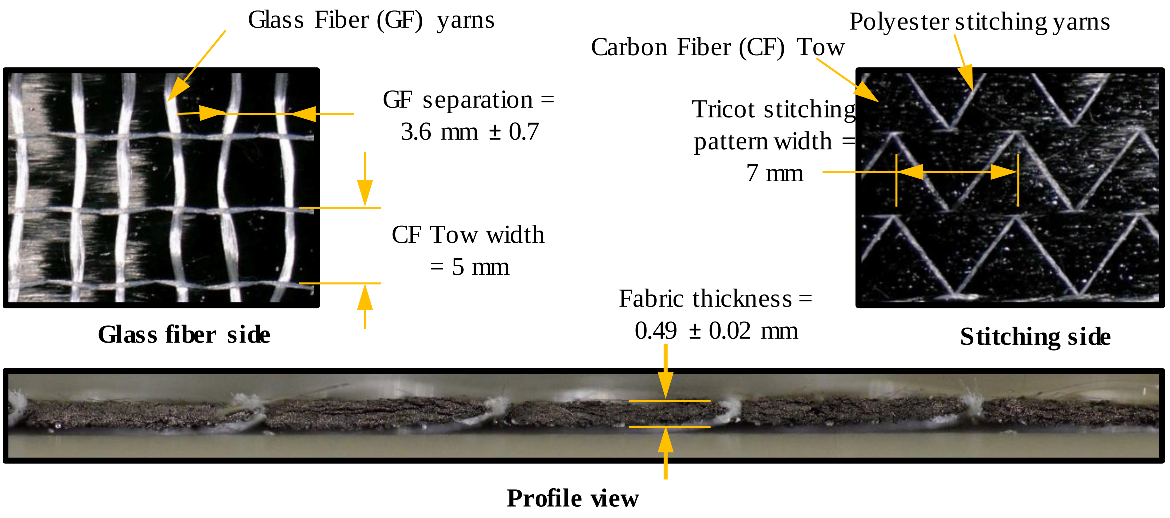

Figure 3.2. Images of ZoltekTM PX35-UD300 unidirectional non-crimp fabric illustrating the architecture of fabric components.

3.2. Characterization of UD-NCF material

A series of tests were performed on the UD-NCF to characterize in-plane extension, shear, and out-of-plane bending deformation modes (see Chapter 2), while fabric friction testing was also conducted. A summary of the performed tests is presented in Table 3.2.

Table 3.2. Summary of performed characterization tests for single layer of UD-NCF.

Test type	Specimen shape and dimensions (mm)	Measured Material Property
Longitudinal extension test	Rectangular 42 x 320 and 11 x 270	Longitudinal tensile stress-strain response
Transverse extension test	Rectangular 160 x 320	Transverse tensile stress-strain response
45° off-axis extension test	Rectangular 160 x 320	Shear stress-strain response
Picture frame test (PFT)	Square cruciform 309 x 309 overall dimensions	Shear stress-strain response
Cantilever test	Rectangular 32 x 350	Bending moduli
Friction test	Square 63.5 x 63.5	Fabric-mold friction coefficients

A small MTS servo-hydraulic test frame with a 2.22 kN (500 lbf) capacity OMEGA LC412-500 load cell, an MTS FlexTest SE controller, and custom fixtures were used for all performed tests, with the exception of the cantilever bending test, where a custom testing module was used (Section 3.2.4). All tests were conducted at room temperature under displacement control with a constant quasi-static rate of 1 mm/s. The test frame controller used a closed-loop configuration (using LabVIEW) that continuously monitored the load cell output and actuator displacement, recording data at a frequency rate of 120 Hz. Furthermore, all fabric test specimens were carefully cut using transparent acrylic templates to ensure correct fiber orientation, consistent specimen geometry, and to avoid distortion of the fabric prior to testing (Figure 3.3). A utility knife was used to cut all the fabric specimens, and a new blade was used for each specimen to provide consistent high-quality specimen edges.

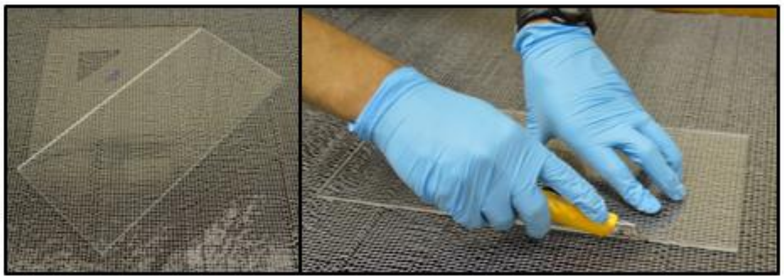
(a) **(b)**

Figure 3.3. UD-NCF specimen preparation: (a) using square rulers for alignment, and (b) acrylic templates and a utility knife for cutting.

3.2.1. Longitudinal and transverse extension tests

The UD-NCF was subjected to tensile forces in the directions parallel and perpendicular to the CF tows to extract the material response along the longitudinal and transverse directions, respectively. The dimensions of the transverse extension test specimens were chosen to ensure that there were at least 40 glass fiber yarns across their width (Figure 3.4c). The longitudinal extension test specimens were narrower due to the limited capacity of the test frame load cell, where it was ensured that there were at least 8 CF tows across their width (Figure 3.4a). A second set of test specimens were also used for the longitudinal tests to capture local deformation mechanisms (Figure 3.4b).

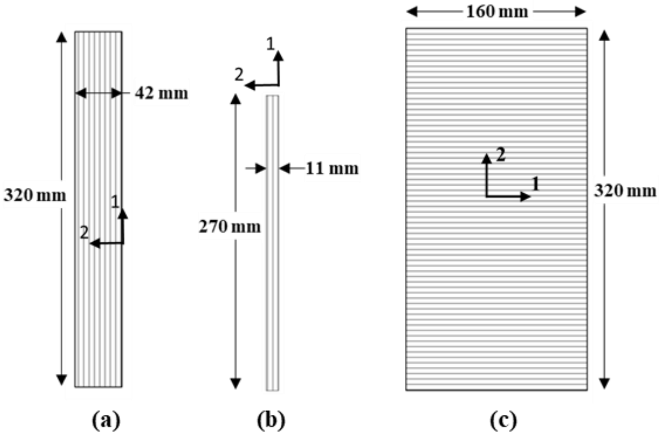

Figure 3.4. Test specimen dimensions: (a) longitudinal extension test for capturing macroscopic response, (b) longitudinal extension test for capturing deformation mechanisms, and (c) transverse extension test.

A custom set of clamping fixtures, each comprised of two bolted steel plates (Figure 3.5a), was designed to hold the fabric test specimens for the extension tests. First, an alignment fixture was used during to attach the top and bottom fabric clamps to the specimen at the right distance and orientation from each other (see Figure 3.5a). The specimen with the fabric clamps were then installed in the frame by attaching the top and bottom fabric clamps to the respective top and bottom clamping fixtures (see Figure 3.5b). During the installation of the specimen in the clamping fixture, spacers were installed in the back face of the top and bottom clamping fixtures to ensure alignment of the specimen plane with the centre of the tensile frame actuator. These spacers and clamps were secured in place using the attachment bolts shown in Figure 3.5a. Also, bolts in the front face of the top and bottom clamping fixtures (identified as clamping bolts in Figure 3.5a) were used to increase the clamping force in the middle of the specimen; these bolts were tightened to approximately 0.212 Nm.

When performing preliminary extension tests with the clamping fixture it was observed that the fixture was not able to effectively grip the fabric specimen. Specifically, the GF yarns tended to slip from the fixture when insufficient clamping force was applied to the fabric specimen or break at the clamping zone when a high clamping force was applied [65] (see Figure 3.6). A similar observation was also reported by [16] for a UD-NCF under extension loading. An investigation of the original clamp design revealed that GF breakage within the clamped area was promoted by the sharp bend in the fixture when high clamping forces were applied (Figure 3.7a). A redesigned clamp consisted of two steel plates and a PVC cylindrical rod insert with an oval cross-section, around which the fabric specimen was wrapped before placing it in a cavity formed between the two steel clamps halves (Figure 3.7b). This design eliminated GF breakage and ensured that there was no GF slippage when the steel plates were bolted together using a bolting torque of approximately 0.212 Nm. An image of a test specimen gripped in the optimized clamp within the testing frame is shown in Figure 3.5b.

For each test, the engineering stress and strain for the longitudinal and transverse fabric directions were calculated based on the initial cross-sectional area and length of the specimen.

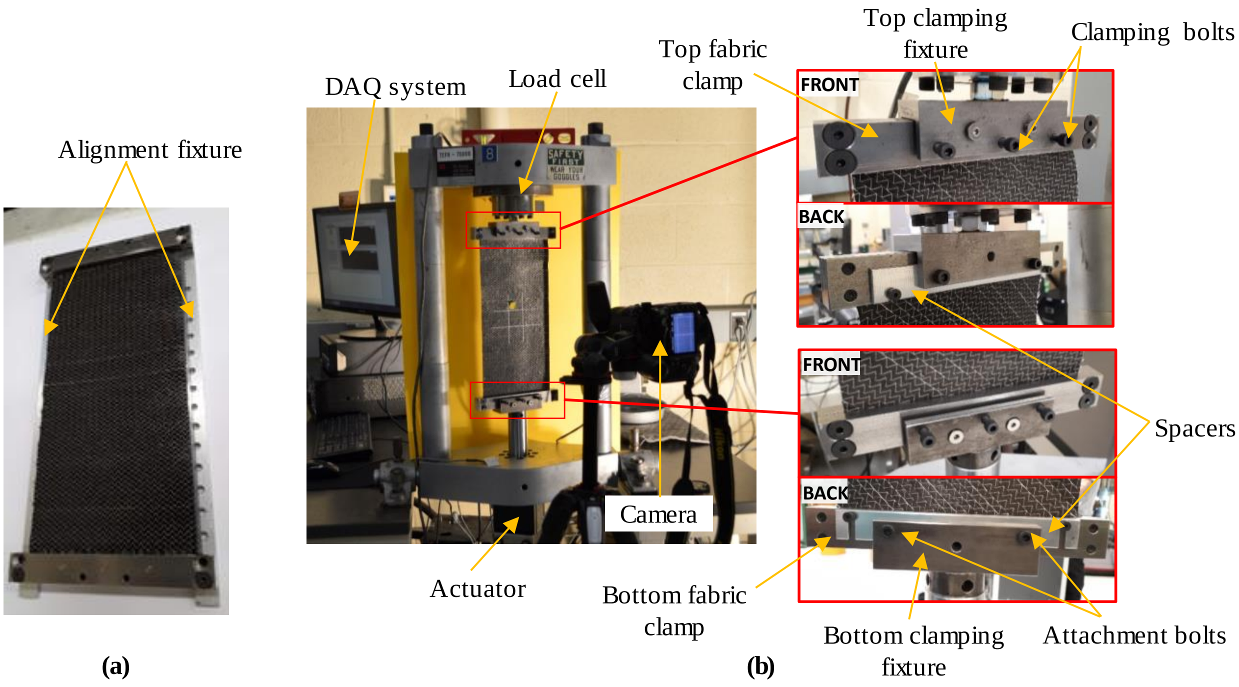

(a) **(b)**

Figure 3.5. (a) The alignment fixtures used to install the fabric clamps to the UD-NCF specimens. (b) Images of the extension test setup showing details of the top and bottom clamping fixtures.

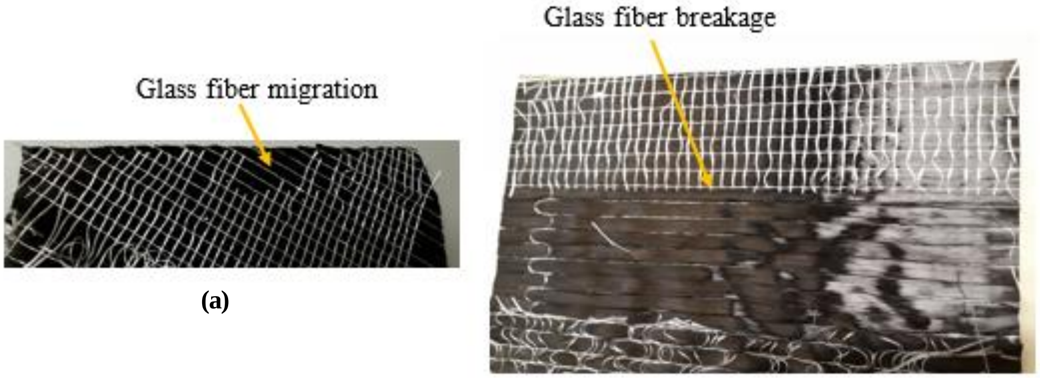

(a) **(b)**

Figure 3.6. Images of the clamped region of UD-NCF extension test specimens after test completion: (a) Glass fiber yarn migration caused by low clamping force and (b) glass fiber yarn breakage caused by high clamping forces and fabric folding.

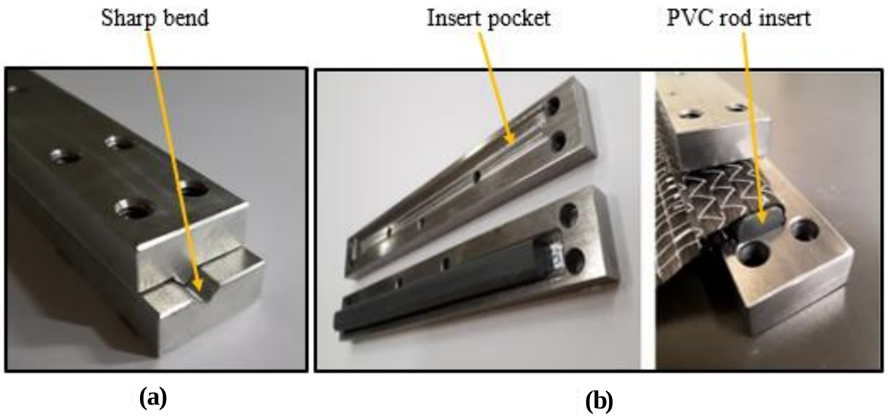

Figure 3.7. UD-NCF extension test fabric clamps: (a) original clamp design, and (b) redesigned clamping fixture with a PVC insert.

3.2.2. Picture frame test (PFT)

PFTs were performed to capture the shear stress-strain response of the fabric, under the assumption that a test specimen is subjected to a pure shear deformation. The dimensions of the PFT specimens used in this study comprised of a 170 mm by 170 mm gauge section area (Figure 3.8a).

The dimensions of the designed custom PFT fixture are shown in Figure 3.8b. The fixture consists of two parts, including a hinged square frame with four rigid arms of equal length, as well as a set of clamping mechanisms on each arm. The square frame was mounted to the test frame from the hinge points, while the clamping mechanisms were used to clamp the fabric test specimen ends and secure the specimen to the square frame. The aluminum PFT fixture was designed to fit the limited space available in the test frame and to allow for an application of a maximum shear angle of 50° on the test specimen. To eliminate undesirable GF sliding inside the clamps of the fixture, the clamping mechanisms were designed to be similar in nature to that of the extension test fixture. The fabric test specimen ends were wrapped around acrylic rods that were installed inside machined cavities within the support tabs of the clamping fixture (Figure 3.9). The surfaces of the acrylic rods were sanded with 80 grit sandpaper to increase the friction between the rod and the GF yarns.

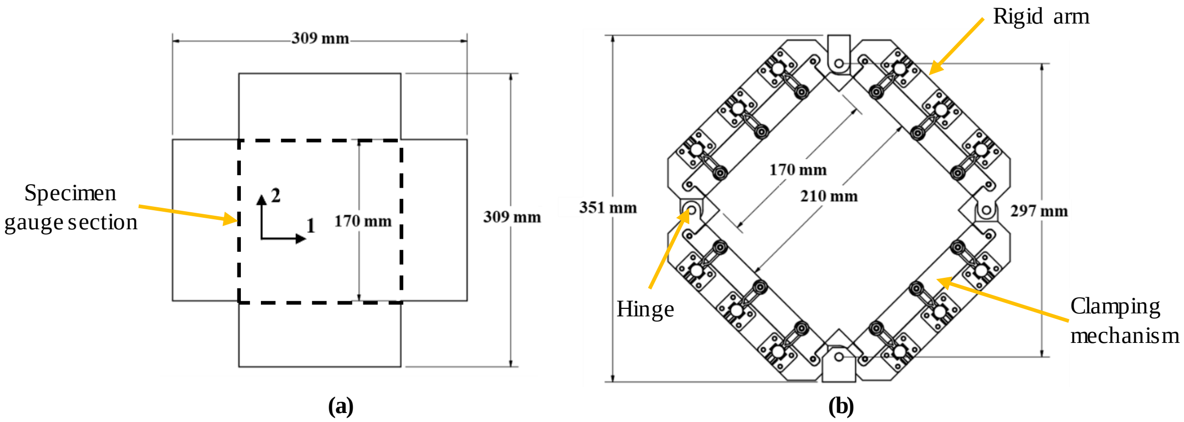

Figure 3.8. (a) PFT specimen geometry, and (b) testing fixture dimensions.

Figure 3.9. Images of the custom PFT fixture clamping mechanism illustrating the wrapped fabric specimen ends around an acrylic rod inserted into the cavity of the support tabs.

A specimen clamping process was devised to prevent fabric misalignment and pre-tensioning, both of which have been reported in the literature as common issues for PFT [51,68]. First, the four support tabs of the clamping mechanism were positioned on an aluminum alignment plate using precisely located bolt holes, and the test specimen ends were clamped (see Figure 3.10a). Then, an installation plate was bolted to the specimen-support tab assembly to allow for transport of the assembly to the testing machine (see Figure 3.10b). The specimen-support tab assembly was then installed inside precision-machined pocket cut-outs in the hinged square frame of the PFT fixture, which was pre-mounted to the test machine (Figure 3.11a). Once the assembly was accurately positioned in the fixture, toggle clamps were closed to hold down the support tabs (see Figure 3.11b). Finally, the installation plate was removed from the fixture to complete the installation process.

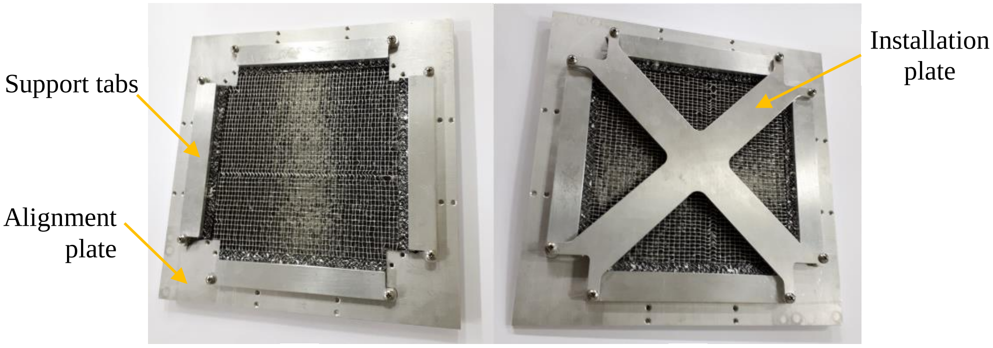

(a) **(b)**

Figure 3.10. PFT specimen clamping process: (a) Image of the specimen-support tab assembly in an alignment plate, and (b) image of the installation plate bolted to the support tabs.

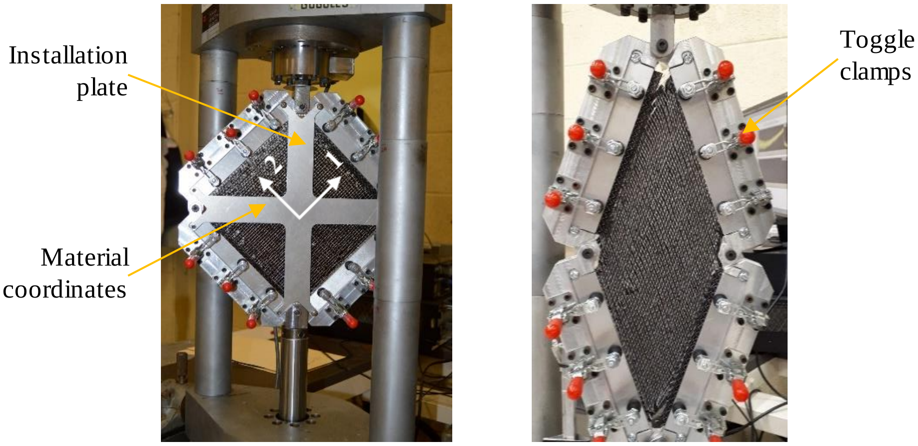

(a) **(b)**

Figure 3.11. (a) Image of a PFT specimen during installation on the testing machine, and (b) a deformed specimen during execution of a PFT.

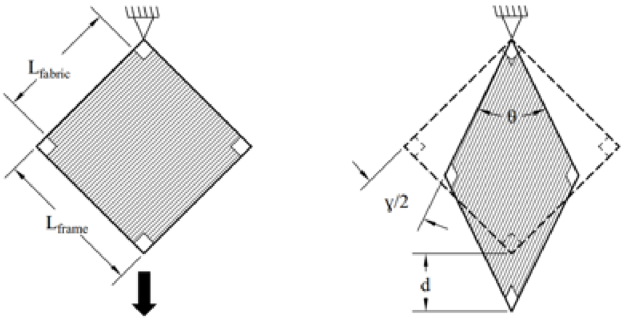

(a) **(b)**

Figure 3.12. Schematic of the pure shear deformation for a PFT specimen: (a) prior to loading, and (b) after loading.

During a PFT, a vertical displacement was applied to the lower hinge of the fixture while the upper hinge remained fixed, causing the initially square frame to deform into a rhomboid shape (Figure 3.12). Due to the pure shear assumption, the shear strain induced by the frame (γ) can be calculated from the frame arm length (L_{frame}) and frame displacement (d) or the change in the frame angle (θ) according to [49,51,142]:

$$\gamma = 90° - \theta = 90° - 2 \times \cos^{-1}\left(\frac{\sqrt{2}\times L_{frame} + d}{2\times L_{frame}}\right) \tag{3.1}$$

The corresponding shear force can be calculated as,

$$F_S = \frac{F_f}{2\cos\left(\frac{\theta}{2}\right)} \tag{3.2}$$

where F_f is the applied axial load. Based on an energy method originally proposed by Peng et al. [49] and widely adopted for the characterization of textiles [16,49,68], the normalized shear force can be defined using:

$$F_N = F_S \frac{L_{frame}}{L_{fabric}^2} \tag{3.3}$$

where L_{fabric} is the fabric side length and L_{frame} is the side length of the fixture frame. From the normalized shear force, an equivalent engineering shear stress was computed based on the cross-sectional area formed by the measured fabric thickness (0.49 mm) and the specimen side length (L_{fabric}) of 170 mm.

3.2.3. Off-axis extension test

In this study, 45° off-axis extension tests were conducted as an alternative approach to the PFTs to characterize the shear deformation of the UD-NCF material. Previous studies reported use of this test for characterizing shear deformation of UD-NCFs [96]. Also, both 30° and 60° off-axis extension tests were conducted to subject the fabric to distinct deformation modes compared to the 45° off-axis extension tests. This allowed for in-plane verification of the fabric material model.

All specimens were 160 mm in width and 410 mm in length to accommodate clamping and provide a gauge section with an area of 160x320 mm^2, shown in Figure 3.13b. For each fabric test specimen, the CF tows were aligned biased to the loading direction by either 30°, 45° or 60°. The same fixtures used for the longitudinal and transverse extension tests were used to clamp the two short sides of the specimen. In this case the specimen was only wrapped around half of the PVC rod, as illustrated in Figure 3.14.

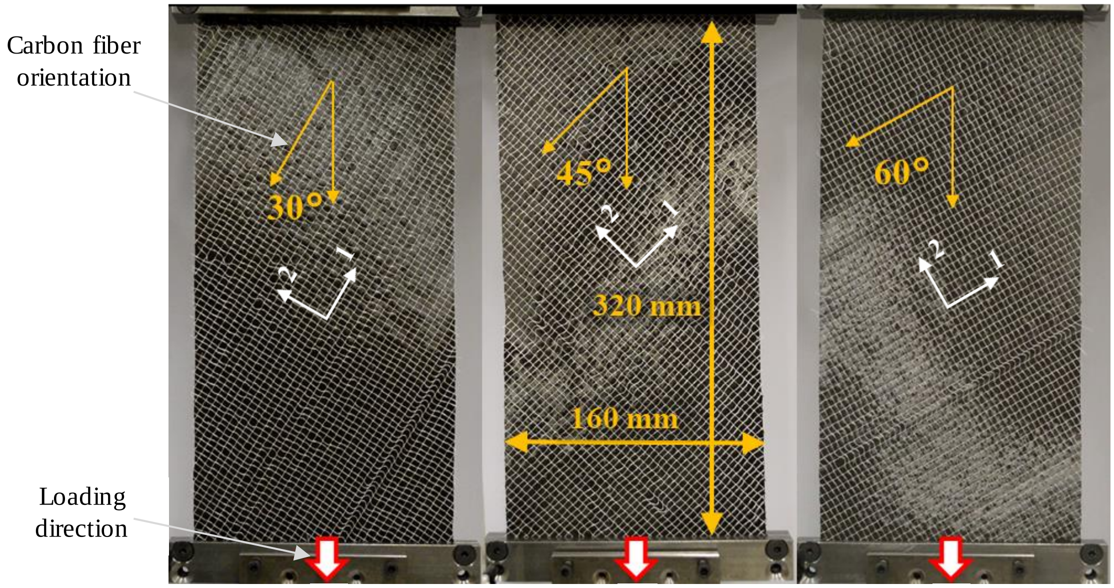

(a) (b) (c)

Figure 3.13. Images of (a) 30º, (b) 45º, and (c) 60º off-axis extension test specimens captured prior to load application.

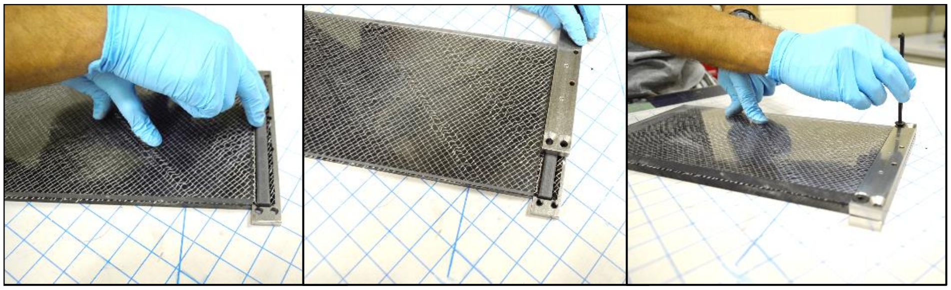

(a) (b) (c)

Figure 3.14. Images of the fabric clamp installation process for 30°, 45°, and 60° off-axis extension tests: (a) placing of PVC rod on top of the fabric specimen and half of the fabric clamp, (b) placing of the second half of the fabric clamp on top of the PVC rod, and (c) bolting of the complete fabric clamp assembly.

Poutier et al., 2019 [96] proposed a correlation of the linear displacement imposed on a 45° biased specimen and the shear deformation experienced by the specimen. By assuming simple shear deformation of the fabric specimen (Figure 3.15), with the longitudinal fabric direction oriented along the line *OP*, a correlation between an imposed displacement *D* with the angle *w* can be made per:

$$w = \sin^{-1}\left(\frac{\sqrt{2}}{2}\frac{1}{1+\frac{D}{L_0-l_0}}\right) \tag{3.4}$$

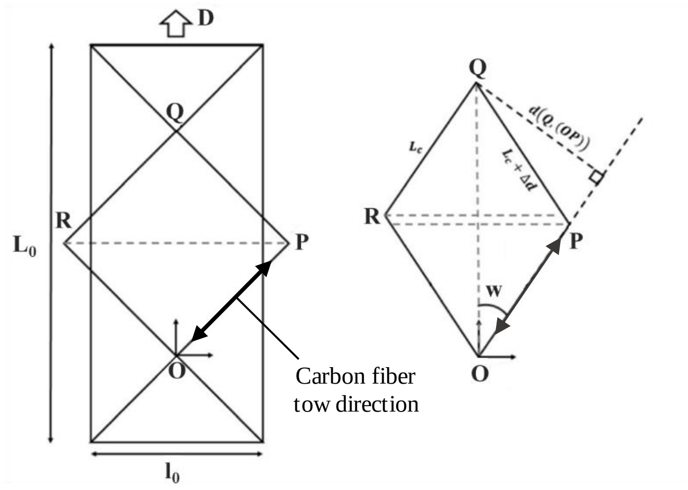

Figure 3.15. 45° off-axis extension test simple shear deformation approximation [96].

Subsequently, the shear angle can be computed as a function of the angle between the longitudinal fabric direction and the loading direction as,

$$\gamma_{ss}(w) = \frac{\pi}{2} - w - \sin^{-1}\left(\frac{\sin(w)}{\sqrt{1+\frac{1}{\sin(w)^2}-\frac{2}{\tan(w)}}}\right). \tag{3.5}$$

To compute the shear stress, the uniaxial stress generated by the imposed displacement was transformed to the material coordinate system, aligned with the direction of the CFs, from which the shear stress component of the transformed stress was extracted. The CF rotation was extracted through visual examination of the test images.

3.2.4. Bending characterization

In this investigation, the cantilever test was used to characterize the bending stiffness of the fabric in the longitudinal and transverse material directions. A linear approximation of bending stiffness was required for the calibration of the numerical material model (Chapter 4). Different variations of the cantilever test applied to fabric reinforcements have been reported in the literature [71,73,74]. Three methods were considered in this investigation: one based on ASTM standard D1388, a second one based on British standard BS EN ISO 9073, and a modified version of the British standard proposed by [73]. All three approaches were based on the cantilever test setup shown in Figure 3.16. The three considered tests variations share the same methodology, which consists of sliding a rectangular fabric specimen over a cantilever test module, effectively increasing the overhang length until the edge of the bent specimen touches a sloped surface with a constant angle of 41.5° (Figure 3.16).

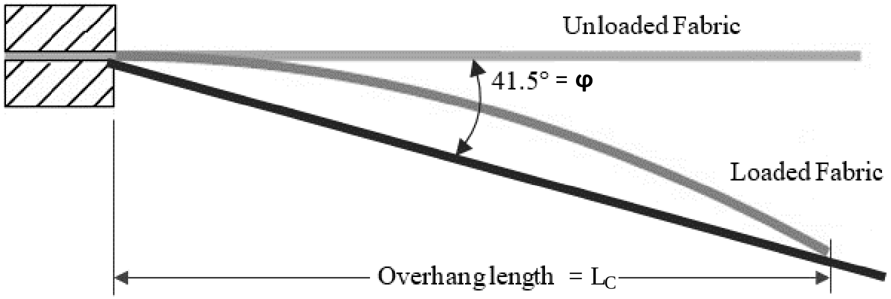

Figure 3.16. Schematic of a cantilever test setup.

In the first method considered based on ASTM D1388, the bending length (L_b) is calculated from the overhang length (L_C) per Equation 3.6, and the bending stiffness (G) is calculated from the bending length (L_b), and areal density (W), per Equation 3.7.

$$L_b = \frac{Lc}{2} \tag{3.6}$$

$$G_{ASTM} = 0.1421 \times W \times {L_b}^3 \tag{3.7}$$

The second method employed which is based on the British standard BS EN ISO 9073-7:1998 proposes Equation 3.8 for the calculation of bending stiffness, where L_C is calculated from:

$$G_{BS}(\varphi) = \frac{\cos\left(\frac{\varphi}{2}\right)}{\tan\varphi} \times W \times {L_b}^3 \tag{3.8}$$

with a surface incline angle of 41.5°; Equation 3.8 reduces to:

$$G_{BS}(\varphi = 41.5^0) = 0.1321 \times W \times {L_b}^3. \tag{3.9}$$

Harrison et al. [73] proposed an empirical correction to Equation 3.8, with an extra correcting factor calculated as a function of the bending angle:

$$G_C = G_{BS} \times f(\varphi) = \frac{\cos\left(\frac{\varphi}{2}\right)}{\tan\varphi} \times W \times {L_b}^3 \times f(\varphi) \tag{3.10}$$

Where:

$$f(\varphi) = (-3.2434387343 \times 10^{-5})\varphi^2 + (3.8717591439 \times 10^{-6})\varphi + 0.9988589066 \tag{3.11}$$

with a surface incline angle of 41.5°; Equation 3.11 reduces to:

$$G_C = 0.1319 \times W \times {L_b}^3 \tag{3.12}$$

Although all methods were considered in this study, the method proposed by [73] was chosen (Equation 3.12) since it has been previously applied to estimate the bending stiffness of fabric reinforcements.

Fabric test specimens were cut according to dimensions specified in Table 3.2. For longitudinal bending characterization the CF tows were aligned with the bending direction, while for transverse bending characterization the CF tows were aligned perpendicular to the bending direction. The test module was fabricated from machined aluminum plate and consisted of a horizontal and an inclined surface at a 41.5° angle from horizontal, as shown in Figure 3.17. A Nikon D3200 camera fitted with a Nikon DX Zoom Nikkor 28-55 MM lens was employed to capture images of the profile view of the fabric specimen.

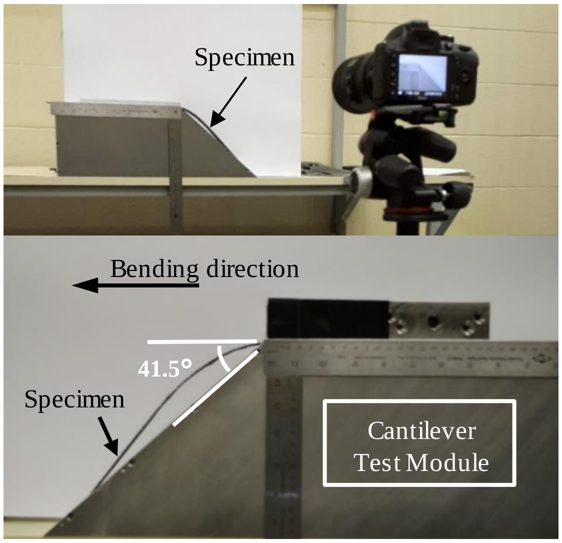

Figure 3.17. Experimental setup of the performed cantilever test.

3.2.5. Friction characterization

Friction characterization tests were performed to measure the static and dynamic friction coefficients of the UD-NCF on a steel substrate material that is representative of a preform mold surface. Currently, there is no standardized test to measure the coefficient of friction for fabrics. Nevertheless, in this study the test protocol defined in ASTM D1894 was used. This standard was originally developed to measure the static and dynamic coefficients of friction of thin plastic sheets. Five different test configurations are proposed in the standard; option C was adopted in this study (Figure 3.18).

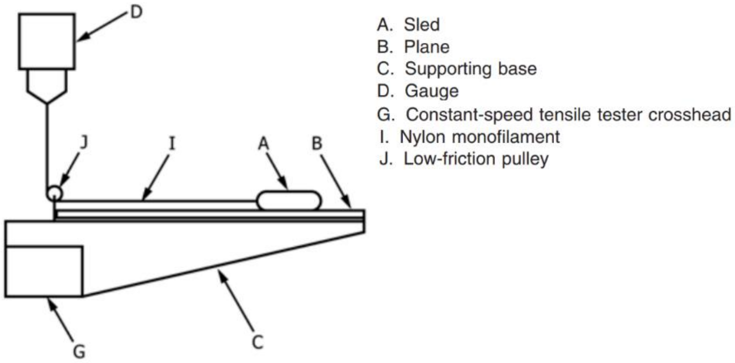

Figure 3.18. Schematic of the friction test setup presented in ASTM standard D1894 as option C and implemented in this study [143].

The contacting surface of the test specimen is indicated in Table 3.2. The specimen was wrapped around a 63.5x63.5 mm^2 steel sled and fixed in place using double-sided tape (see Figure 3.19). The bottom carbon steel plate surface was sanded with 150 grit sandpaper to achieve a surface roughness of 1 µm RA and replicate a typical steel forming tool. It should be noted that tooling provided for this project by industrial partner Laval Tool & Mould Ltd. Laval were finished by sanding with 150-grit sandpaper. A custom apparatus was designed and built to fit the same tensile frame used in previous tests, which comprised of a supporting base, pulley and upper attachment (Figure 3.19). During the test, the sled carrying the fabric specimen was pulled by a nylon wire at a displacement rate of 1 mm/s. The UD-NCF was tested on both the stitching and glass fiber sides and in the longitudinal and perpendicular material directions (see Figure 3.20). In the longitudinal direction, the CFs were aligned with the loading direction, while in the transverse direction, the CFs were aligned transverse to the loading direction.

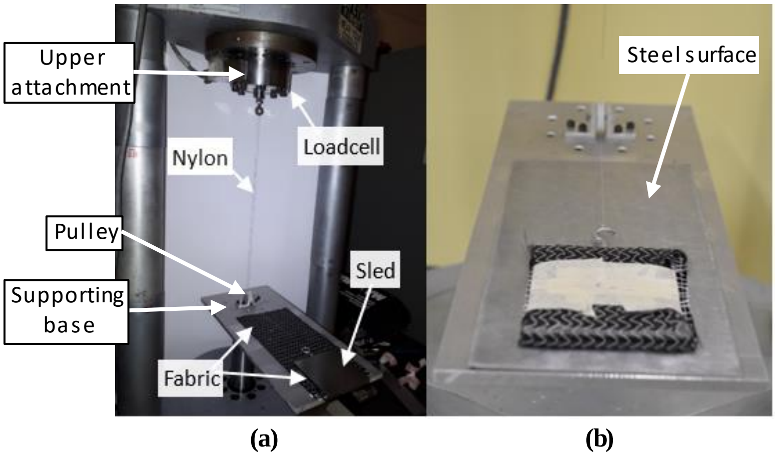

Figure 3.19. Image of the (a) friction test apparatus used to measure the static and dynamic friction coefficients of UD-NCF. (b) Image of the friction test showing the UD-NCF in contact with a steel plate surface representative of the forming tool surface.

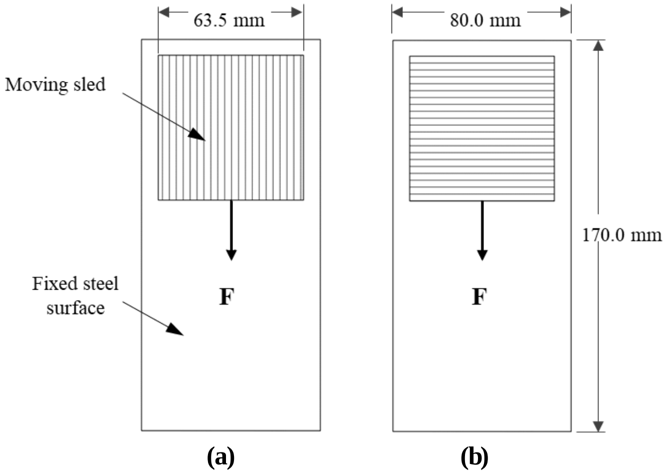

Figure 3.20. Schematic of the friction test configuration for the UD-NCF (a) longitudinal and (b) transverse directions.

The ASTM D1894 standard specifies that the coefficient of friction is defined as the ratio of the normal force applied on a surface to the pulling force required to overcome sliding resistance. The data collected was the pull force required to overcome friction and displacement of the sled. The initial force necessary to initiate sliding was denoted the peak force, F_{peak}, and was used to calculate the static friction coefficient. Following the onset of sliding, the force necessary to maintain sliding, F_{steady}, was used to calculate the dynamic friction coefficient. The static and dynamic friction coefficients were respectively calculated according to:

$$\mu_s = \frac{F_{peak}}{W_{sled}} \tag{3.13}$$

$$\mu_d = \frac{F_{steady}}{W_{sled}} \tag{3.14}$$

3.2.6. Measuring fabric strains using DIC

The two-dimensional digital image correlation (2D-DIC) software VIC-2D 2009 (Correlated Solutions Inc.) was used to process images captured during the fabric characterization tests described in Sections 3.2.1 through 3.2.3. A single Nikon D3200 camera fitted with a Nikon DX Zoom Nikkor 28-55 MM lens positioned perpendicular to the surface of the specimen was used to capture deformations throughout the full specimen surface area at 30 frames per second. It should be noted that for all the fabric characterization tests performed in this study image capturing was limited to when the test specimen deformations remained relatively planar, thus enabling the use of 2D DIC.

DIC analysis was performed on complete test specimen areas to generate strain contour plots, and in 50×50 mm^2 (200×200 pixel^2) ROIs to record average strain magnitudes. For all strain computations, a subset size of 55 pixels, a step size of 5 pixels, a decay filter size 17, and a typical resolution of 0.2646 mm/pixel were used. Also, the Gaussian weights method option was implemented for strain calculations. To increase the correlation capacity of the system given the large deformations expected, the incremental correlation option was activated.

Some challenges were encountered when texturizing the surface of the fabric. A study was conducted to evaluate the impact that surface texturization for DIC has on the response of the fabric, and also the impact of the quality of the speckle pattern for extracting strain contours. In this study, three different paint application techniques were considered: spray paint, latex paint, and oil paint (see Figure 3.21) [65]. The spray paint consisted of a base layer of white paint on the fabric specimens with black speckles on top applied from spray cans. The latex and oil paint trials consisted of applying white speckles directly to the fabric specimens using a hard bristle brush to spread the paint in small droplets. One advantage of using latex and oil paints was that a thinning agent could be used to adjust the viscosity as required. The paint viscosity was adjusted through a trial and error approach until a consistency that produced paint speckles that were small enough to minimize their influence on the mechanical properties of the fabric was achieved, were not absorbed by the fabric, and produced high contrast with the fabric background. The most effective surface texturization was achieved with a 16:1 mixture of oil-based paint to mineral spirits thinning agent ratio (see Figure 3.21c).

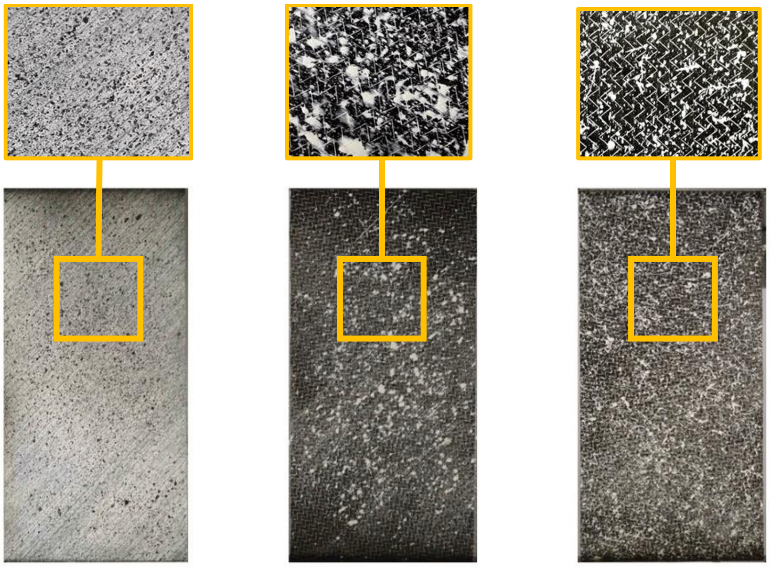

(a) **(b)** **(c)**

Figure 3.21. 45º off-axis extension test specimens texturized with (a) spray paint, (b) latex paint, and (c) oil paint [65].

3.3. Hemispherical draping tests

Hemispherical draping tests were performed to investigate the deformation of a single layer of the UD-NCF during a forming operation and to validate the developed draping simulation model (Section 4.3). Fabric specimens with dimensions of 200 mm by 200 mm were positioned with the CF tows oriented along the vertical axis of the top view (Figure 3.22a). The draping test was conducted using a servo-hydraulic MTS formability press, fitted with an MTS 407 controller and a piezoelectric 600 KN Kistler load cell (Figure 3.23). A 50 mm radius hemispherical punch was used along with a steel ring binder (125 mm inside diameter, 20 mm wide and 4 mm thick) to hold the fabric onto the die during draping (Figure 3.22b). Tests were performed at room temperature and under quasi-static conditions with a vertical punch speed of 0.25 mm/s. Initially, a 3D DIC system was used to capture and analyze deformation images of the fabric and determine the corresponding strain contours. A pair of 17 mm focal length lenses operated at a frame rate of 30 frames per second were used to capture the deformation images and Vic 3D 8 software using a step size of 5 to 11 pixels, and a subset size of 31 to 55 pixels was employed for analysis. However, due to calibration issues with the system, the captured images were not processed for this study. Instead, a Nikon D3200 camera fitted with a Nikon DX Zoom Nikkor 28-55 MM lens was used to capture the overall deformed shape of the fabric specimen at the end of the test once the fabric was fully formed.

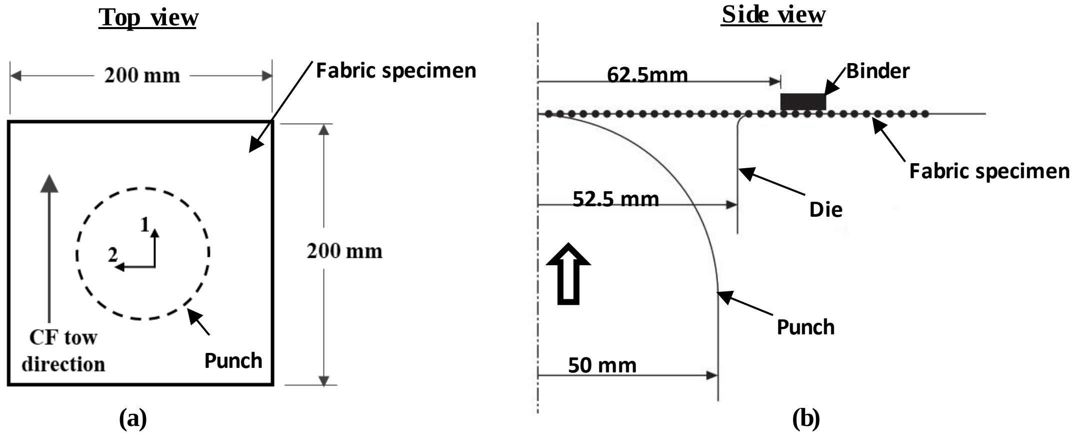

Figure 3.22. Hemispherical draping test schematic: (a) top and (b) side view.

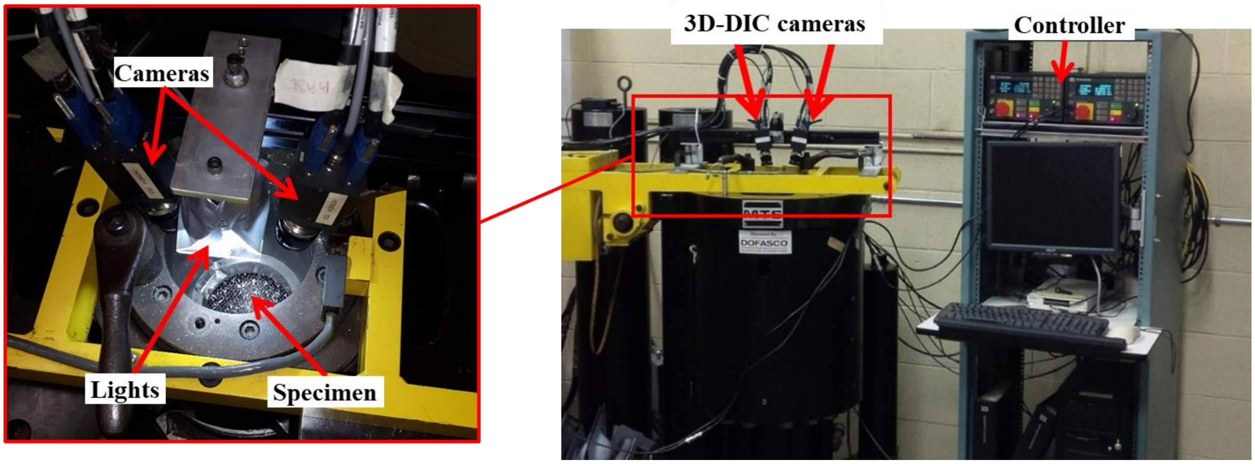

Figure 3.23. Image of the MTS formability press used for the hemispherical draping tests.

Chapter 4: UD-NCF macroscale numerical simulation models

This Chapter begins with an evaluation of relevant material models currently available in LS-DYNA (Section 4.1). The simulation models developed for the calibration of the chosen material model MAT249 (Section 4.2) and those for simulating fabric draping are also presented (Section 4.3).

4.1. Macroscopic material models – LS-DYNA®

For the purposes of the numerical simulation models developed in this study, a single layer of the UD-NCF material was treated as an effectively homogeneous continuum without regard for the discrete fabric components (Figure 4.1). Thus, a macroscale constitutive model was used to represent the response of the UD-NCF reinforcement.

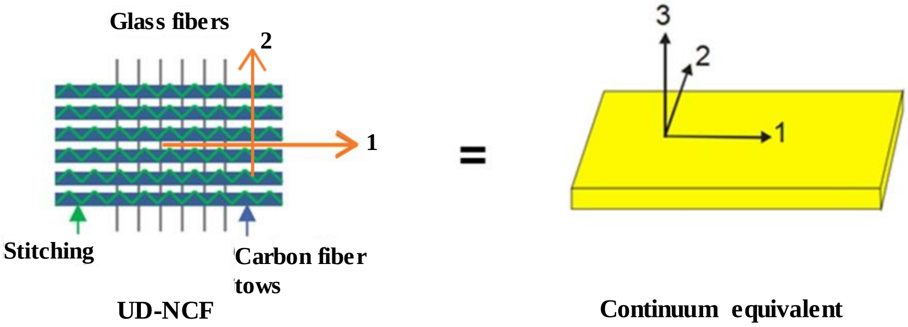

Figure 4.1. Schematic of UD-NCF fabric illustrating discrete components and equivalent homogeneous representation.

There are several material models available in the LS-DYNA material library that are compatible with shell elements and can be used for fabric reinforcements [137] (Table 4.1). A suitable material model must capture the inherent characteristics of the fabric reinforcement, including the orthotropic material characteristics and large shear strains exhibited during typical draping operations. Additionally, the material model must be able to predict local fiber orientation and fiber volume fraction for mapping to either resin infiltration models or performance models. A comparison of the available material models and the relevant selection criteria used in this study is provided in Table 4.1. Based on the assessment, MAT249 was found to be the most suitable for the UD-NCF material, providing the best combination of desirable attributes for material calibration and simulation output.

Table 4.1. Comparison of fabric reinforcement material models available in LS-DYNA® and selection criteria for UD-NCF.

Material model identifier	**MAT034**	**MAT214**	**MAT235**	**MAT249**	**MAT249 - UD**
Material model name	Fabric	Dry fabric	Micromechanics dry fabric	Reinforced thermoplastic	Reinforced thermoplastic UD fiber
Main application	Modelling of airbags and seatbelts	Propulsion engine containment systems	Inflatable structures, parachutes, body armour, blade containment	Reinforced thermoplastic composites	Unidirectional fiber-reinforced thermoplastic composites
Material constitutive behaviour	Macroscopic, orthotropic	Macroscopic, transverse orthotropic	Viscoelastic, micromechanical with homogenization	Macroscopic, hyperelastic, and anisotropic	Macroscopic, Transversely isotropic neo-Hookean
Large deformation capability	No	No	No	Yes	Yes
Input nonlinear material behaviour	Yes	No	No	Yes	No
Output fiber orientation	Yes	No	Yes	Yes	Yes
Output fiber volume fraction	No	No	No	No	Yes
Recommended for forming of unidirectional fabrics	Yes	No	No	Yes	Yes

4.1.1. Material model MAT249

MAT 249 was originally developed for simulating draping of fiber-reinforced thermoplastic composite materials, with the ability to consider a matrix phase and up to three different fiber phases. The matrix phase is represented as an isotropic hyperelastic material with temperature dependent elastic properties. Similarly, the fiber reinforcement is treated as a hyperelastic material with a predefined preferential direction based on the user-defined fiber families. Hyperelastic material formulations are suitable for fabrics because they fulfill the requirement of frame-invariance for an anisotropic material response and can be used to capture large deformations [29]. Additionally, the LS-DYNA user manual indicates that MAT249 is suitable to model woven and unidirectional dry fabrics [137].

MAT249 uses vectors stored at element integration points to represent the fiber families [137]. Every time step, an initial fiber configuration represented by $\boldsymbol{m^0}$, is updated using the deformation gradient tensor, $\boldsymbol{F}$, resulting in the current configuration $\boldsymbol{m_i}$. based on the following:

$$\overrightarrow{m_\iota} = \boldsymbol{F}\overrightarrow{m_\iota^0} \tag{4.1}$$

Elongations are computed using the fiber length from the current configuration, λ_i. The fiber strain is then computed using λ_i, from which the total Cauchy stresses are obtained from the sum of individual fiber families according to Equation 4.2 [137], where J is the determinant of the deformation gradient tensor.

$$\boldsymbol{\sigma} = \sum_{i-1}^{n} \frac{1}{J} f(\lambda_i)(\overrightarrow{m_\iota} \otimes \overrightarrow{m_\iota}) \tag{4.2}$$

The relative rotation between fiber families (i.e., the fabric shear strain) can either be defined using a constant scalar value or determined as a function of the relative angle between fibers (i.e., the shear angle). The latter was used in this study with a shear stress-strain relation, $\boldsymbol{g}$, describing the interaction between the two fiber families. Similar to normal stresses, the shear stress can then be computed as the sum of the interaction between different fiber families as specified by [137]:.

$$\boldsymbol{\tau} = \sum_{i-1}^{2} \frac{1}{J} g_{i,i+i}(\overrightarrow{m_\iota} \otimes \overrightarrow{m_{\iota+1}}) \tag{4.3}$$

Ultimately, the material behaviour is determined by the superposition of the deformation of the isotropic matrix phase and transversely isotropic fiber families.

The parameters necessary for the calibration of material card MAT249 are described in Table 4.2. A representation of the MAT249 card input from the LS-DYNA user interface, colour coded for matrix, fiber and material coordinate parameter definitions, is shown in Figure 4.2.

Table 4.2. Material parameters for LS-DYNA® material model MAT249.

Matrix Parameter	Description
EM	Young's modulus
LCEM	Young's versus temperature data (if active, EM is ignored)
PRM	Poisson's ratio
LCPRM	Poisson's ratio versus temperature data (if active, PRM is ignored)
LCSIGY	Yield stress curve

BETA	Hardening parameter
Fiber Parameter	**Description**
NFIB	Number of fiber families
THICK	Thickness change option
IDFx	Fiber family ID
ALPHx	Orientation of fiber family x
G13_x, G23_x	Through-thickness transverse shear
EFx	Young’s modulus of fiber x
LCFx	Stress-strain data for fiber family x
Gxy	Shear modulus between fiber families x and y
LCGxy	Shear stress-strain data for fiber families x an y (if active, Gxy is
METHxy	Method for shear stress calculation
ALOCKxy	Locking angle between fiber x and y
GLOCKxy	Linear shear modulus after locking angle is reached

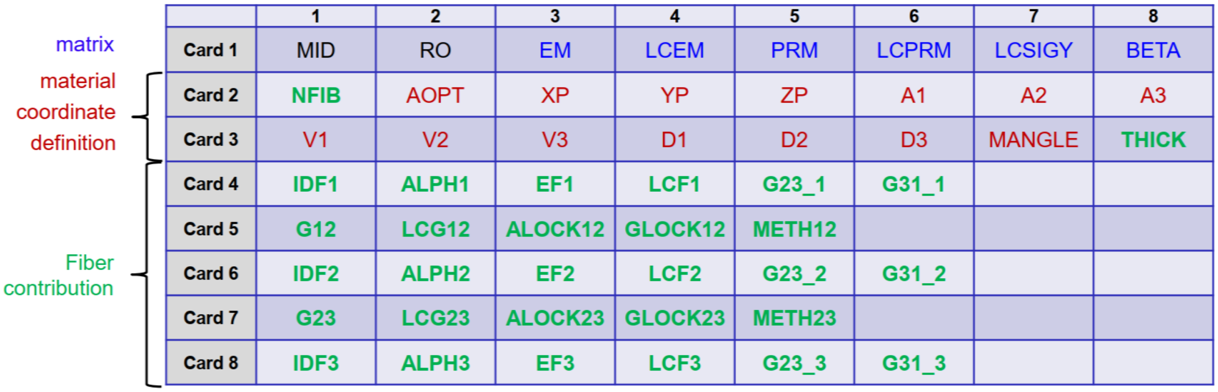

		1	2	3	4	5	6	7	8
matrix	**Card 1**	MID	RO	EM	LCEM	PRM	LCPRM	LCSIGY	BETA
material coordinate definition	**Card 2**	NFIB	AOPT	XP	YP	ZP	A1	A2	A3
	Card 3	V1	V2	V3	D1	D2	D3	MANGLE	THICK
Fiber contribution	**Card 4**	IDF1	ALPH1	EF1	LCF1	G23_1	G31_1		
	Card 5	G12	LCG12	ALOCK12	GLOCK12	METH12			
	Card 6	IDF2	ALPH2	EF2	LCF2	G23_2	G31_2		
	Card 7	G23	LCG23	ALOCK23	GLOCK23	METH23			
	Card 8	IDF3	ALPH3	EF3	LCF3	G23_3	G31_3		

Figure 4.2. MAT 249 material model parameters classified for matrix, material coordinates and fiber definitions.

4.2. Material calibration simulation models

First, single element simulations were used to evaluate the applicability of MAT249 as a material model for the studied UD-NCF material, where a series of parametric studies were performed. Subsequently, simulations of the physical characterization tests for a single layer of UD-NCF (see Chapter 3) were reproduced numerically to calibrate the material model MAT249.

A common set of material card and FE model options were retained for all simulation models developed in this study. Fully integrated shell elements, LS-DYNA type 16, with three integration points through the thickness were implemented. The double-precision explicit solver available in LS-DYNA version R10.1 was used. Two fiber families were specified to represent the behaviour of the fabric in the longitudinal and transverse directions, respectively representing the carbon fiber tows and glass fiber yarns, while the matrix phase was disregarded. The shear option METH 11, available in MAT249 to define elasto-plastic and decoupled shear behaviour between fiber families, was used to represent the shear interaction between the warp and weft fabric directions.

4.2.1. Single shell element simulation models

Three single shell element simulation models were developed for the fabric material, where deformation along the longitudinal and transverse directions, as well as in shear was considered. For each distinct simulation, the boundary conditions at the nodes of the single shell elements were adjusted accordingly to achieve the desired deformation (Figure 4.3). All four nodes were constrained from out-of-plane displacements in all simulations. For the transverse extension test, the material coordinate system was rotated to align the direction representing the CF tows perpendicular to the displacement direction (Figure 4.3b).

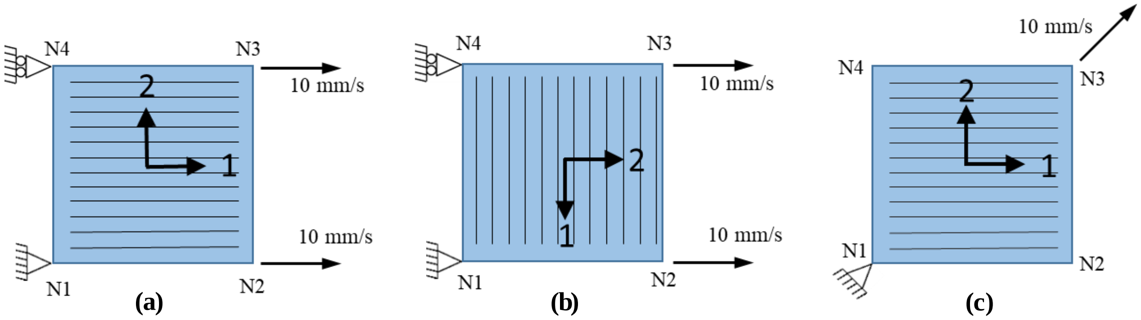

Figure 4.3. Single shell element simulation models with boundary conditions and material coordinate directions specified: (a) longitudinal extension, (b) transverse extension, and (c) shear.

4.2.2. Picture frame test simulation model

To simulate the PFT the fixture was not explicitly considered, instead, the appropriate boundary conditions were applied directly to the test specimen gauge section (see Chapter 3 for dimensions). A displacement was applied to the lower specimen corner at a rate of 10 mm/s, while the upper specimen corner was fully constrained from displacements (Figure 4.4a). To approximate the kinematics of the PFT, four rows of rigid shell elements were located around the perimeter of the fabric to represent the rigid frame of the testing fixture. All rigid element nodes were constrained from out-of-plane displacements and rotations. Additionally, the nodes around the fabric perimeter were locally constrained from displacements with the contacting nodes in the rigid frame. A mesh sensitivity study was conducted with three element sizes considered (Figure 4.4).

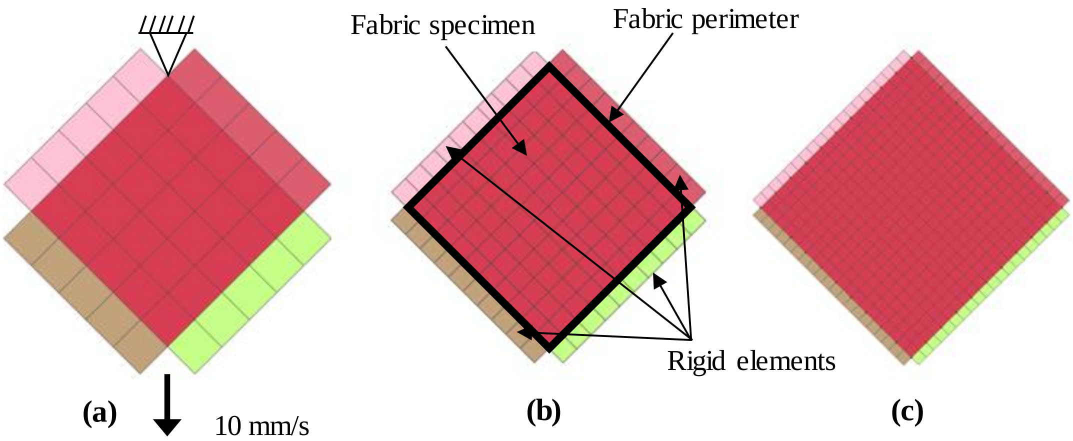

Figure 4.4. PFT simulation FE model with square element sizes of (a) 20, (b) 10, and (c) 5 mm.

4.2.3. Extension test simulation model

The extension test simulation models were developed to simulate the longitudinal, transverse, and off-axis extension tests by setting the appropriate bias angle through rotation of the local material coordinate system (Figure 4.5). The structured shell element mesh consisted of 4 mm square elements. The test clamps used were not explicitly accounted for in the FE model. One extra row of elements was added to the two short sides of the specimen to directly apply boundary conditions. The top element row had all nodes constrained from all rotations and displacements, while a vertical displacement of 10 mm/s was assigned to all the nodes in the bottom element row.

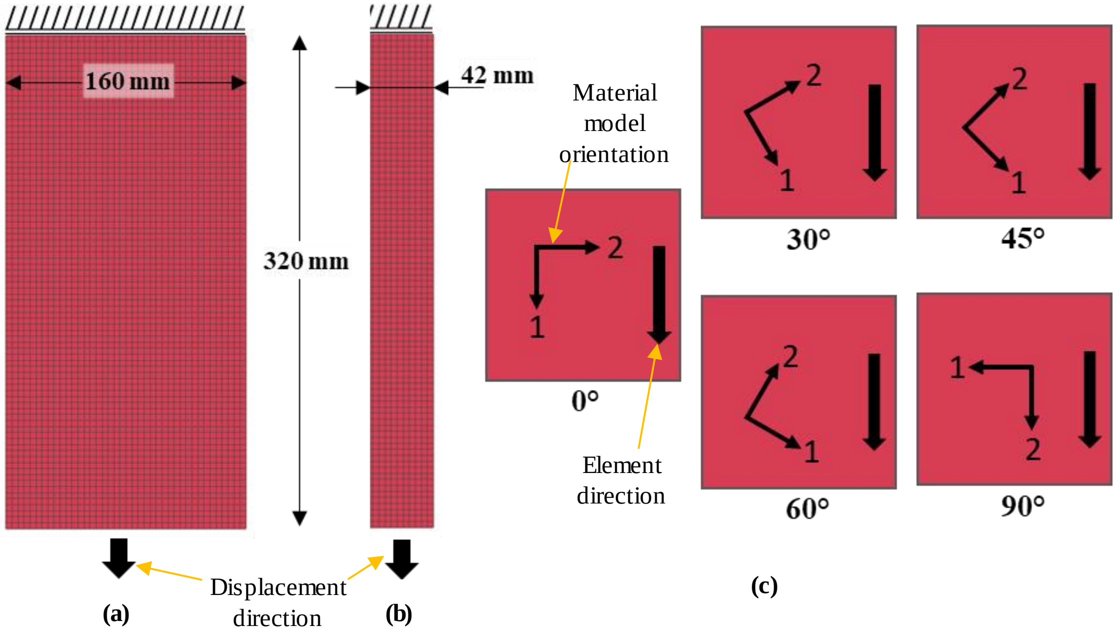

Figure 4.5. Extension test simulation configuration for (a) 30°, 45°, 60° and transverse (90°) material orientations, as well as (b) longitudinal (0°) orientation. (c) Element orientations for all off-axis extension tests, including longitudinal (0°) and transverse (90°) orientations.

4.2.4. Bending simulation model

The fabric bending simulation models consisted of two components: an inclined rigid surface representing the test module and a 32 mm wide fabric specimen. Three element sizes were considered for the fabric, as shown in Figure 4.7. Four-millimeter shell elements were used for the longitudinal cantilever bending test simulation, and 2 mm shell elements were used for the transverse cantilever test. The rigid surface was fully constrained from displacement and rotations. For the fabric specimen, the nodes that contacted the horizontal rigid surface were fully constrained while the remaining nodes were unconstrained. A constant gravitational body force was applied to the fabric component to induce bending.

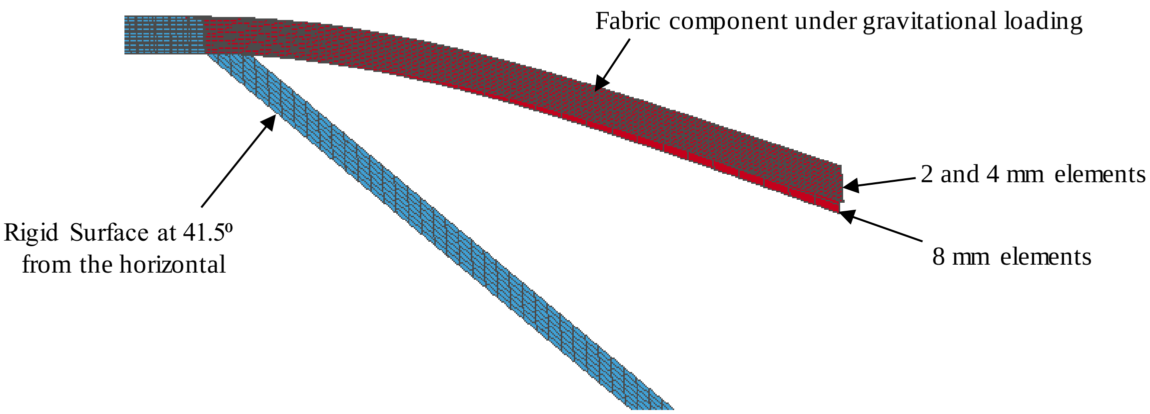

Figure 4.6. Longitudinal cantilever tests performed with 2 mm, 4 mm and 8 mm shell elements.

4.3. Hemispherical draping simulation model

A hemispherical draping simulation model was developed for a single layer of UD-NCF to replicate the physical validation tests (Section 3.3). The same physical test configuration, including specimen and tool dimensions (Figure 3.22) was used in the numerical model. Fully integrated shell elements, LS-DYNA type 16, with three integration points through the thickness were also used. The tooling and fabric specimen were meshed with 4 mm and 2 mm shell elements, respectively. The calibrated fabric material model MAT249 was used for all simulations. Similar to the calibration tests, two fiber families were specified to represent the carbon fiber tows and glass fiber yarns. MAT249, option METH11 was used to model the shear behaviour between the two fiber families. Each of the parts shown in Figure 4.7 had a unique boundary condition. The die was fully constrained, the binder and the fabric were subjected to a downward gravitational load, while the punch had a vertical upward displacement with a constant velocity of 1 mm/s. A penalty contact algorithm was used to define the contact behaviour at all contact interfaces. Friction was modelled as isotropic Coulomb friction with static and dynamic friction coefficients defined through the experimental friction tests. The simulation was explicitly solved in LS-DYNA using the double-precision option.

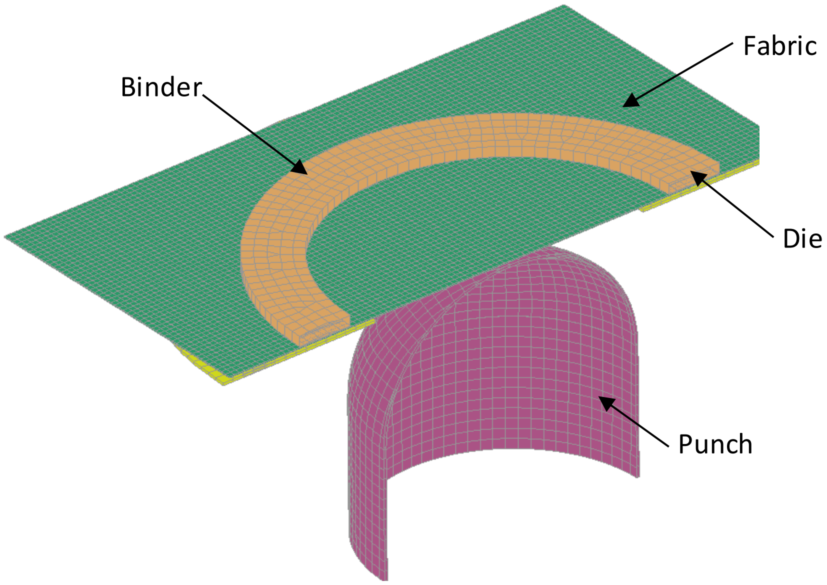

Figure 4.7. Cut-out view of the hemispherical test numerical model.

Chapter 5: Experimental and numerical results

In this chapter the results from an extensive characterization test program for the studied UD-NCF are presented (Section 5.1). The mechanical tests performed on the fabric were chosen to resemble the type of loading that a single layer of fabric may undergo during a typical draping process, namely, in-plane elongation, in-plane shear, and out-of-plane bending [31]. The details and outcomes of the calibration of the material constitutive model, Material Reinforced Thermoplastic (MAT249), in LS-DYNA are also presented (Section 5.2). Each characterized fabric deformation mode was independently calibrated and a summary of all parameters required for calibration of MAT249 is presented. Moreover, independent experiments were performed to verify the accuracy of the in-plane shear calibration for the UD-NCF, and the results are compared with corresponding simulations using the calibrated MAT249 parameters (Section 5.3). Finally, the results of a draping simulation are also presented and the model predictions are evaluated with results from independent draping tests (Section 5.3.3).

5.1. UD-NCF characterization

The fabric characterization experiments aimed to provide an understanding of the deformation response of the UD-NCF at the macroscopic level, as well as the underlying local deformation mechanisms. Extension tests along the main fabric directions, as well as along biased directions, were performed. A PFT was also utilized to capture the shear response of the fabric, while cantilever and friction tests were performed to respectively capture the bending behaviour and measure the friction coefficients of the fabric. The experimental study did not consider the effects of temperature or strain rate on the fabric deformation response; thus, all tests were performed at room temperature conditions under quasi-static loading rates. Note, all extension tests were conducted until specimens failed, while PFT were conducted until a predetermined shear angle of 35° was achieved. Given that fabric test results are highly sensitive to the imposed boundary conditions [24,55], extra care was exercised not to introduce pre-tensioning in the fabric and to prevent sliding of the CF tows, GFs and polyester yarns prior to load application. The results from the corresponding tests are presented in the following sub-sections.

5.1.1. Longitudinal and transverse extension experiments

The fabric stress-strain response along the longitudinal and transverse directions were obtained by performing corresponding quasi-static uniaxial extension tests (see section 3.3.3). A minimum of seven repetitions were performed for each test, from which data from specimen that failed prematurely or were outliers was not considered, and for each material direction to compute the average stress-strain response. It should be noted that results from a number of the initial tests performed were discarded due to specimen misalignment, premature fiber failure, or sliding at the clamps.

Figure 5.1 presents the force-displacement results of three longitudinal extension tests, as well as the average force profile with its corresponding standard deviation representing the variation in the force response. The tests were zeroed at the point during a test where a noticeable increase in the force response was observed. As seen in Figure 5.1, the results from the three specimens are similar, falling within one standard deviation from the average data plot. The initial flat portion of the force-displacement plot (prior to 0.1 mm displacement) reveals that the fabric exhibited negligible stiffness as a result of straightening of CF tows. After approximately 0.1 mm displacement the stiffness suddenly increased as the CF tows became engaged and remained almost constant until failure occurred at approximately 1.3 mm.

Forming of two-dimensional reinforcement into complexly shaped geometries is a critical process steps in manufacturing of continuously fiber-reinforced composites.

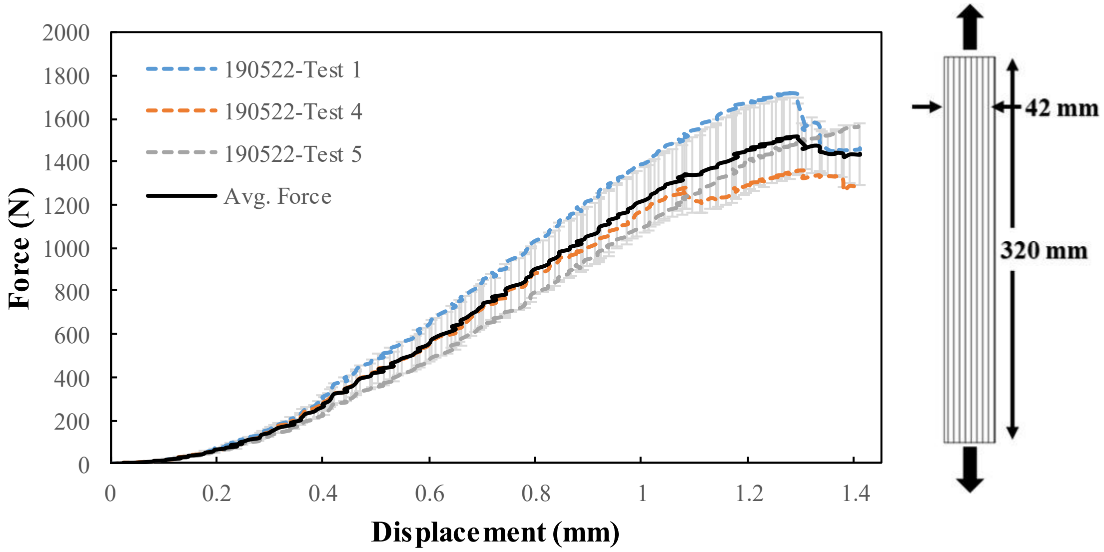

Figure 5.1. UD-NCF force-displacement response for longitudinal extension test.

A slightly different configuration of the longitudinal extension test was devised to study the corresponding local deformation mechanisms of the fabric (Figure 5.2). As seen in Figure 5.2b, which depicts the fabric at the brink of failure, there was no significant relative displacement between the fabric components. This indicates that the CF tows carried the applied load until specimen failure, and thus, the linear region observed in the force-displacement response (Figure 5.1) corresponds to the longitudinal stiffness of the CF tows.

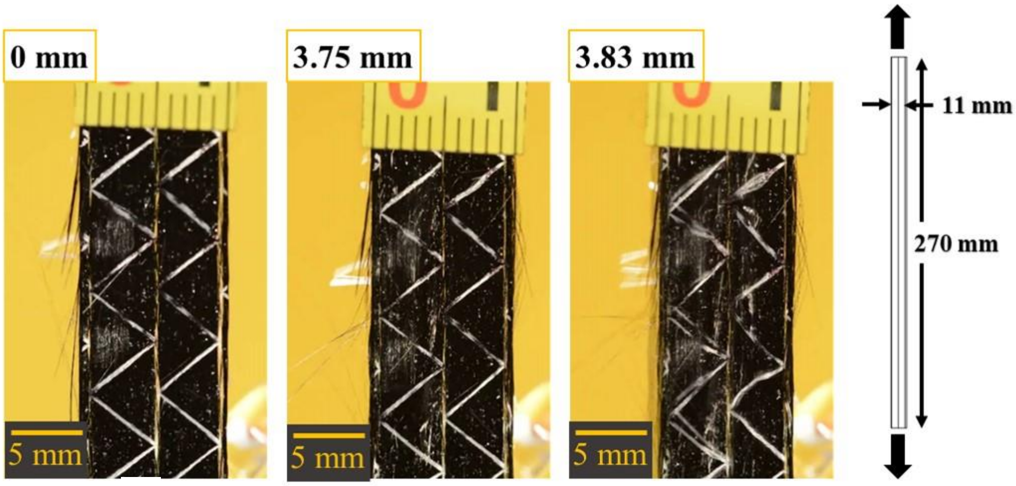

(a) (b) (c)

Figure 5.2. Images of a UD-NCF longitudinal tensile test specimen captured at different displacements during loading: (a) beginning of the test (0 mm), immediately prior to failure (3.75 mm), and (c) after failure (3.83 mm).

The uniaxial force-displacement response shown in Figure 5.1 was used to calculate the fabric stress-strain data, which was necessary for the calibration of the material constitutive model MAT249. Stress was calculated by dividing the applied force by the cross-sectional area of the fabric specimen, which had a thickness of 0.49 mm. Engineering strain was computed using the initial specimen length of 320 mm and the measured specimen displacement. The fabric stress-strain behaviour along the longitudinal direction (Figure 5.3) was analogous to the force-displacement response, where an initial region of very low stiffness until 0.05% strain was followed by a region of higher stiffness (21.8 GPa) that started at approximately 0.1% strain. At the end of the response, at approximately 0.4% strains, the CF tows suddenly failed at maximum stress of approximately 75 MPa. Although the distinct longitudinal response is nonlinear, for numerical simulation purposes, it can be reasonably described with a piecewise linear function (see Figure 5.3). This data was used to calibrate the longitudinal response of the fabric in the FE simulation model.

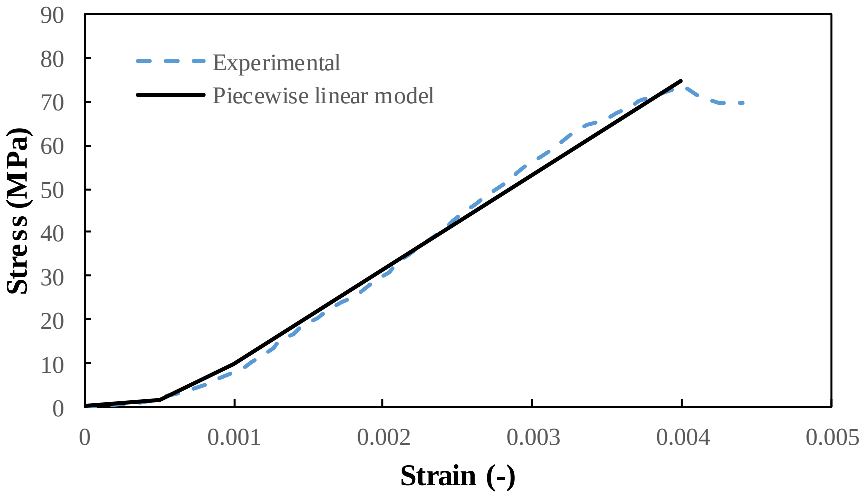

Figure 5.3. Experimental UD-NCF longitudinal extension stress-strain response and the associated piecewise linear model.

A similar process was performed for the transverse tensile response. Ten repeated transverse extension test were performed, however, data from many of the initial tests performed prior to the optimization of the original clamp were discarded due to the GFs sliding out of the clamps or failing prematurely. An average force-displacement response and corresponding standard deviation was extracted from valid test repetitions, as shown in Figure 5.4. During the first 8 mm of extension, the specimen had a negligible force due to the relaxed state of the stitching web and straightening of the initially crimped GFs (see Figure 5.5a). Beyond 8 mm of displacement, the GFs were fully straightened and carried the applied load which increased the force linearly from approximately 10 mm to 14.5 mm. After 14.5 mm of displacement, the GF began to fail progressively leading to a nonlinear response. The peak force was attained at approximately 16 mm of displacement when the GFs were fully extended (see Figure 5.5b). A complete stiffness loss occurred at approximately 20 mm when many of the GFs in the specimen had failed and could no longer hold any load (Figure 5.5c). It is important to note that the stitching appeared to remain undeformed during the execution of the test, as observed in Figures 5.5d, e and f.

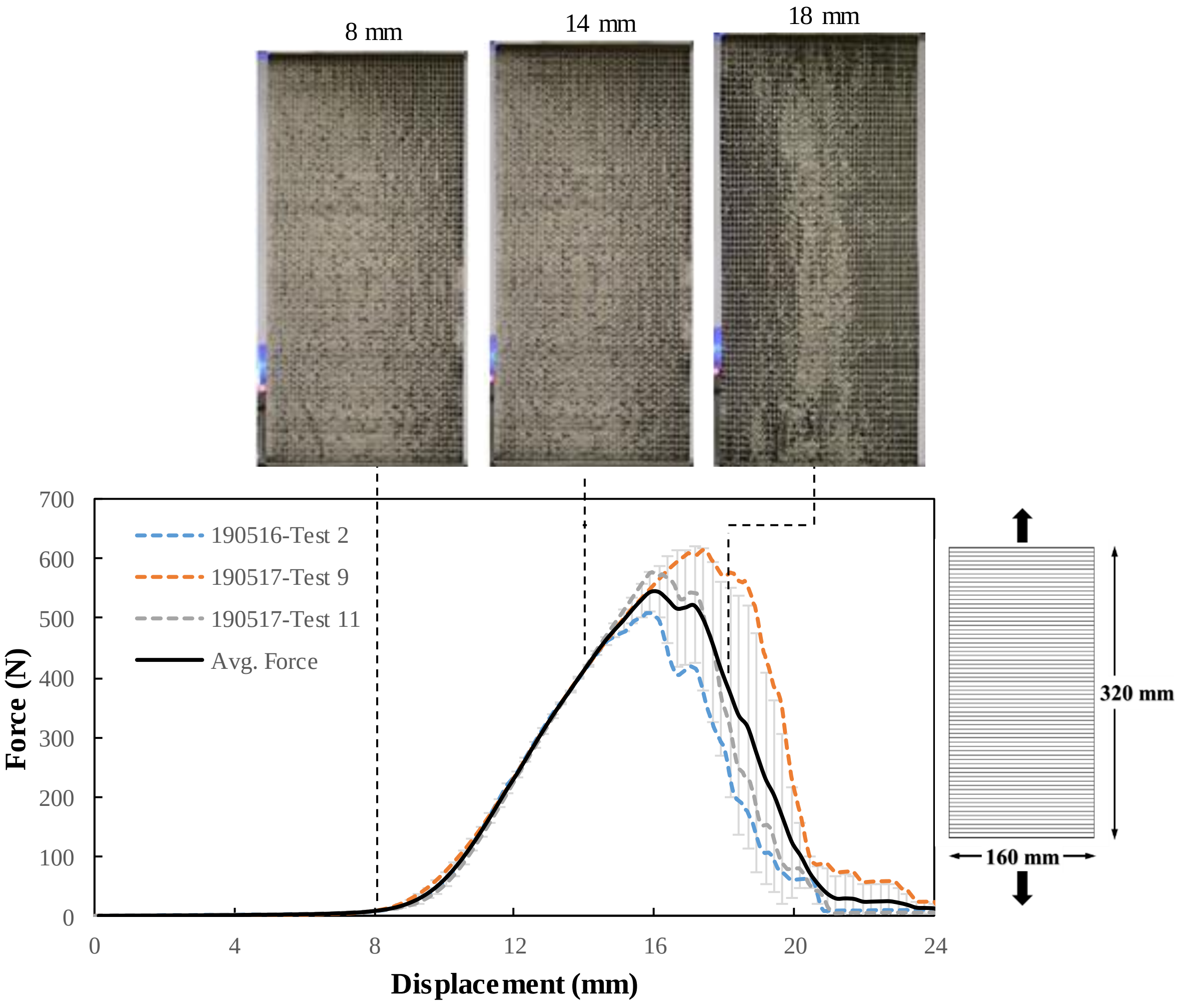

Figure 5.4. UD-NCF force-displacement response for transverse extension test, with images of overall specimen deformation captured at indicated displacements.

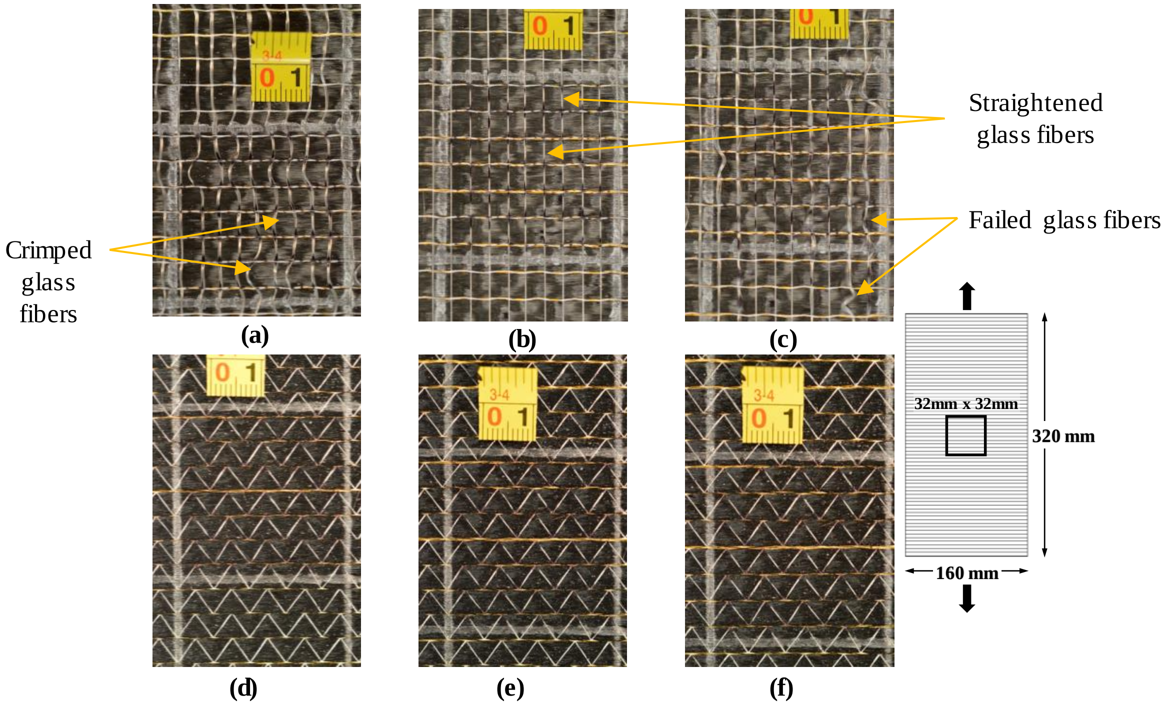

Figure 5.5. Sequential images of glass fiber and stitching sides of a UD-NCF specimen during a transverse tensile test specimen at different displacement intervals: (a and d) 0 mm, (b and e) immediately prior to failure (16 mm), and (c and f) after failure (20 mm).

Similar to the longitudinal extension tests, the fabric stress-strain response along the transverse direction was calculated using the force-displacement data in Figure 5.4. The stress-strain response was analogous to the force-displacement response with an initial region of very low stiffness that extended to approximately 2.4% engineering strain, after which the stiffness gradually increased until it reached a constant value of approximately 330 MPa (see Figure 5.6). In contrast to the sudden failure observed in the longitudinal direction, in the transverse direction, the region of constant stiffness was followed by gradual stiffness degradation starting at approximately 15 mm or 5% engineering strain. A piecewise linear function was also used to represent the transverse response of the fabric (see Figure 5.6) for implementation and calibration of the constitutive model, MAT249.

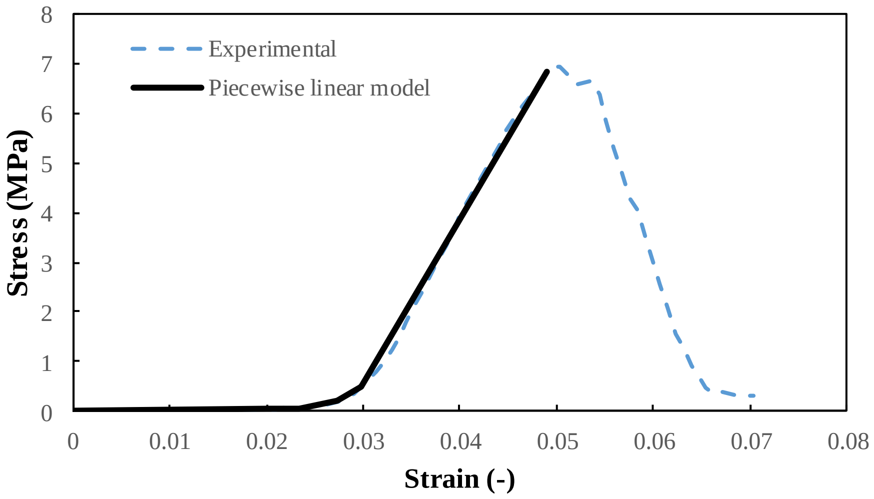

Figure 5.6. Experimental UD-NCF transverse extension stress-strain response and the associated piecewise linear model.

From the experimental results of the extension tests along the longitudinal and transverse directions, it was observed that the mechanical behaviour was remarkably different. The material stiffness during the linear portion of the response along the longitudinal direction, 21,800 MPa, is two orders of magnitude greater than that along the transverse direction, which was merely 330 MPa. This is not surprising since the carbon fiber tows, which comprise over 92% of the fabric total areal weight and have a high stiffness along their axis, carry the applied load when the fabric is extended along the CF tows. In contrast, along the transverse direction the glass fibers, which only comprise 3% of the fabric total areal weight and have a lower modulus, cannot carry significant load thus resulting in a low transverse modulus for the fabric. A similar response was observed in the study by Schirmaier et al. [16] for a different NCF.

5.1.2. Shear experiments

Next, the characterization of the fabric in-plane shear behaviour using both the PFT and the 45$^{\text{o}}$ off-axis extension test was performed. Since these tests subject the fabric to distinct shear response, i.e., pure shear or simple shear, they were both considered to determine which test is most appropriate to characterize the behaviour of the UD-NCF.

5.1.2.1. Picture Frame Test – Pure shear

Initially, the shear stress-strain response of the fabric was obtained under the assumption of ideal and homogeneous pure shear deformation through the PFT (see section 3.3.1). From the seven tests performed, four test results were discarded due to sliding of the glass fibers in the clamp. Figure 5.7 shows the applied axial force-displacement response for the three remaining tests, the average response and the corresponding standard deviation representing the variation in the data, as well as the applied shear angle from the test fixture kinematics. Good repeatability of the fabric force-displacement response was achieved for these tests. The force-displacement response has three distinct regions (Figure 5.7). The first region of high force resistance resulted from friction between the GFs, CFs and stitching components that restricted shear deformation. This was followed by a sharp drop in the shear stiffness resulting from sliding between the fabric components. Finally, after a displacement of approximately 80 mm, the force-displacement response increased as the area between the testing frame arms decreased, and the specimens were compressed. Images of the overall specimen deformation for successive shear angles during the initial portion of loading, where the pure shear approximation is valid, are shown in Figure 5.8. When the shear angle reached 5° during the test, corresponding to 13 mm of displacement, the slope of the force-displacement response began decreasing until it remained constant at a force of approximately 29 N up to a shear angle of 28°, or 63 mm displacement.

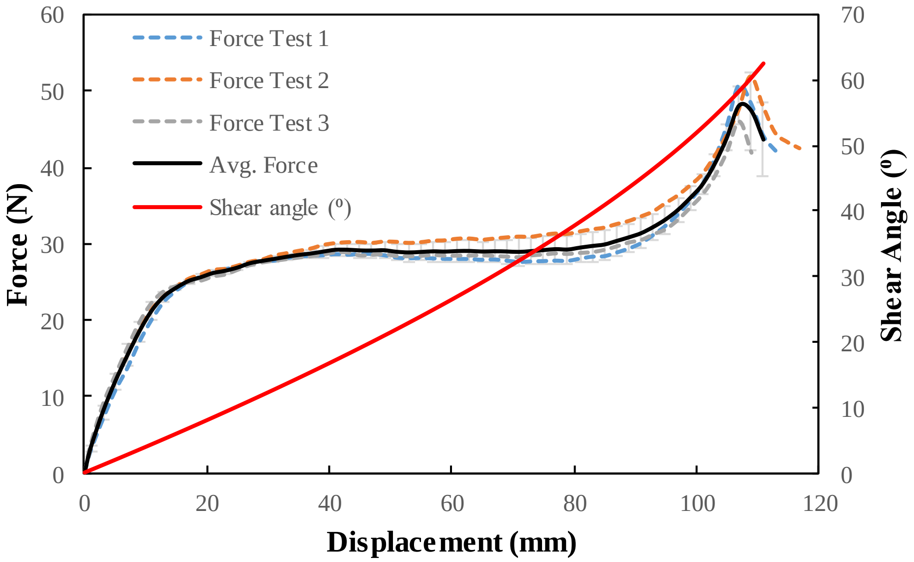

Figure 5.7. Force- and shear angle-displacement response obtained from the picture frame test.

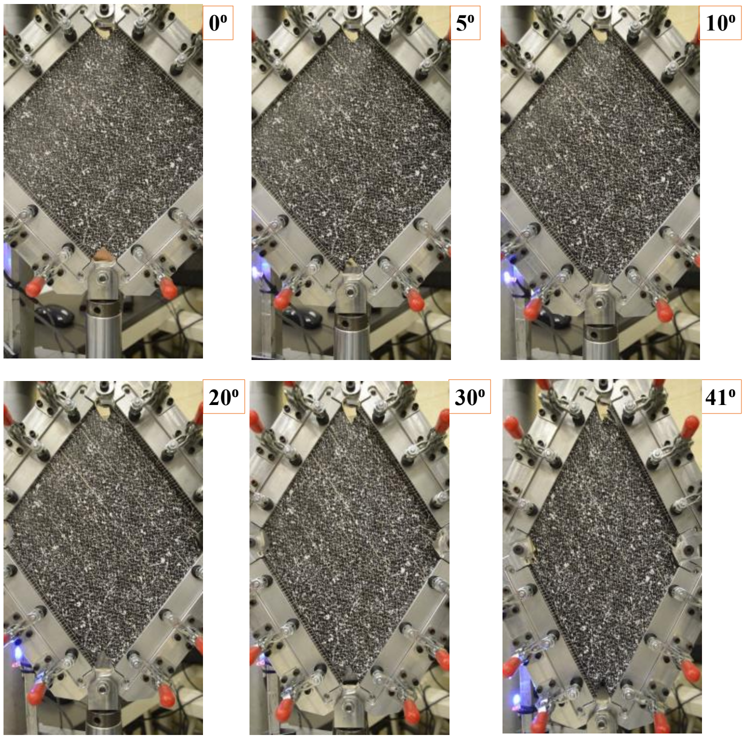

Figure 5.8. Macroscopic deformation of texturized UD-NCF picture frame test specimen indicated shear angles.

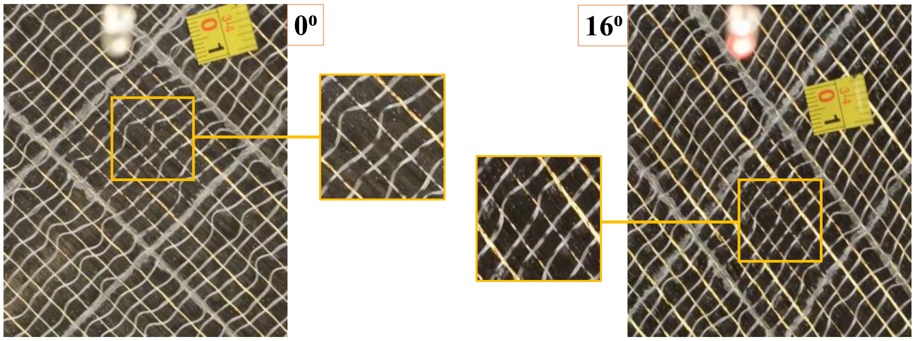

(a) (b)

Figure 5.9. Images of the glass fiber side of a UD-NCF picture frame test specimen: (a) initial state, and (b) once a shear angle of 16° was attained. The glass fiber yarns remained crimped throughout the duration of the test, and thus were loosely engaged.

When the PFT specimens were subjected to increasing load, the GFs were virtually free of loading for the duration of the test, as observed the crimped GFs at different applied displacements in Figure 5.9. Most of the resulting shear force was carried by the CF tows and the polyester tricot stitching. The stitching was severely deformed (Figure 5.10), where one segment of the tricot stitching crossing the CF tows was extended while the other adjacent segment was compressed. The tensioning of the stitching yarn segments from the onset of shear deformation explains the steep increase in force during the initial stage of loading. The compression and crimping of the CF tows caused by the stitching (see Figure 5.10), as well as the formation of gaps between the tows, which was evidenced after a shear angle of 5° was attained, explains the rapid decline in the fabric shear resistance during the second stage of loading (Figure 5.7). Once a shear angle of 35° was achieved, the rapid increase in the shear stiffness coincided with observed compression of the specimen, which began to hinder the shear deformation in the fabric. In the study by Cao et al. [68] on a plain-woven fabric, it was concluded that estimation of the shear angle from the crosshead displacement is only reasonable for shear angles below 35° when the fabric exhibits pure shear. Thus, the measured fabric response beyond a shear angle of 35° cannot be considered to be representative of the shear behaviour of the fabric [68].

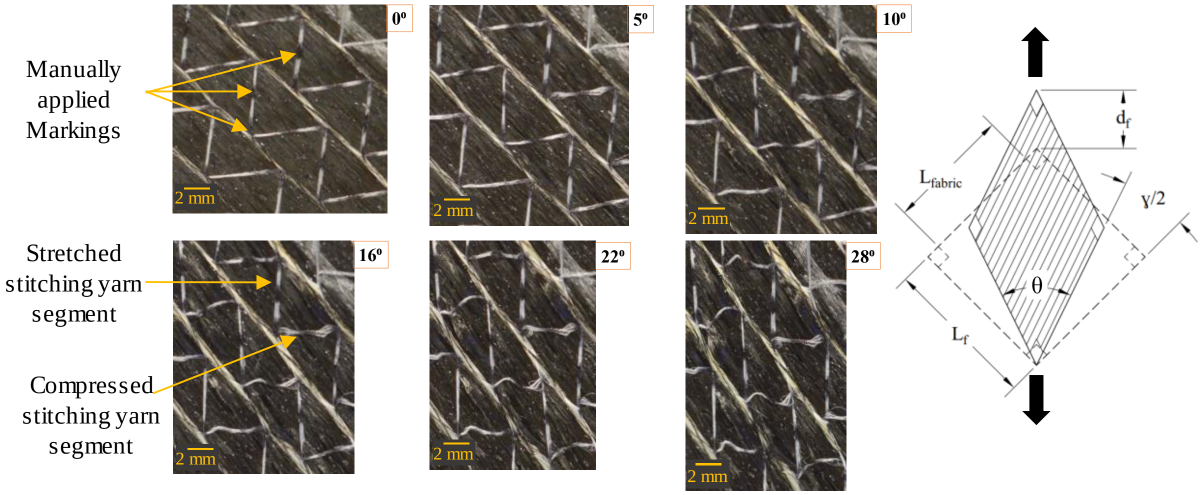

Figure 5.10. Sequential images of the stitching side of a UD-NCF picture frame test specimen at various attained shear angles (γ).

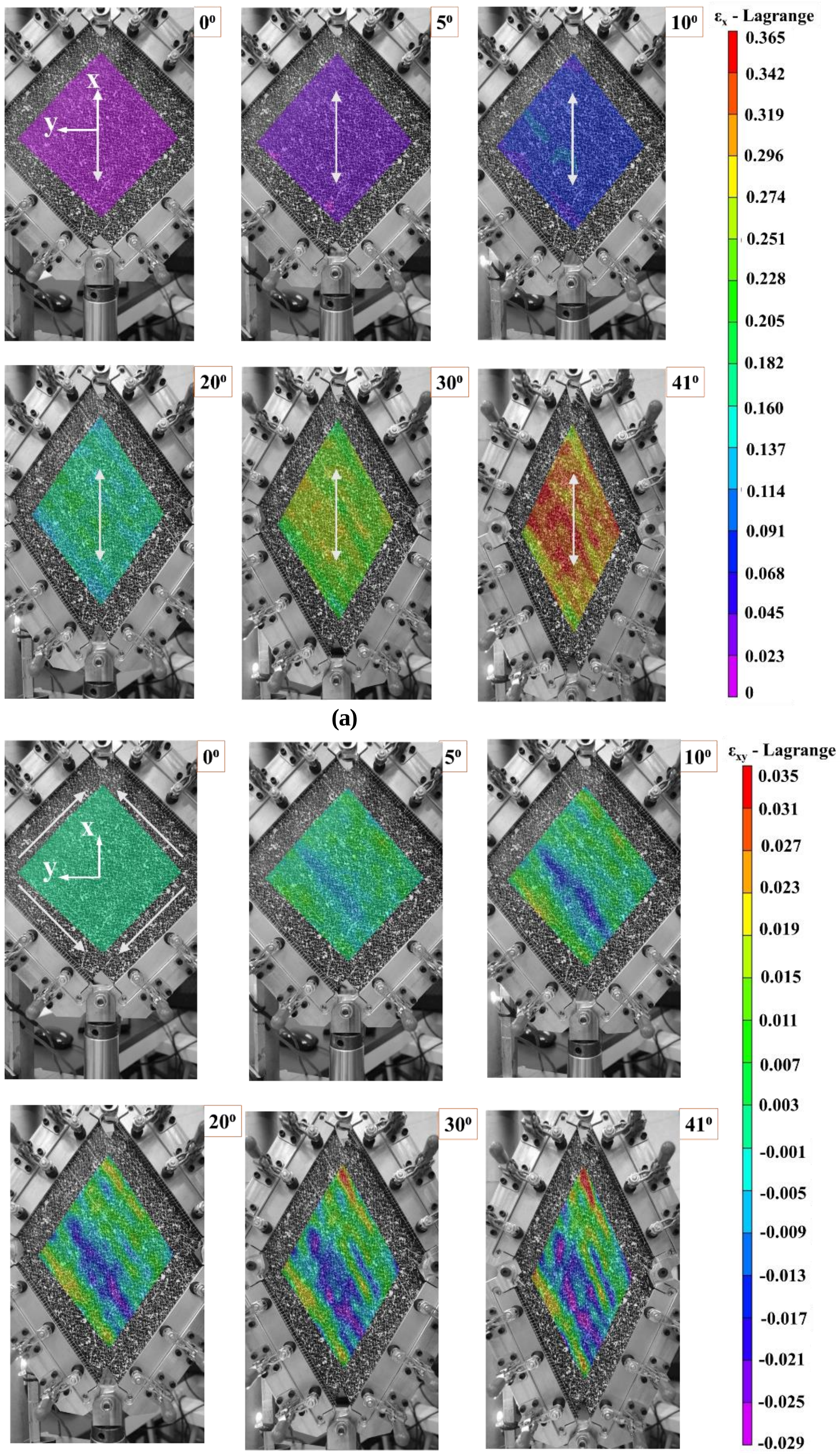

(a)

(b)

Figure 5.11. Picture frame test specimen strain contour maps captured using DIC at the indicated shear angles: (a) normal strain ε_x and (b) shear strain ε_{xy}.

DIC was used to capture strain contours for the PFT specimens. Contours of the normal strain (ε_x) along the loading direction were extracted since a positive and increasing value could be easily predicted from the motion of the frame (Figure 5.11a). On the other hand, when extracting the shear strain in a large area, close to the whole specimen surface, meaningful and consistent strain readings were not obtained. While zero shear strain was expected in the global coordinate system, the DIC system measured shear strains from -2.9% to 3.5%, as seen in Figure 5.11b. In an effort to obtain more consistent results that could be used in the calibration of the material model, a smaller region of interest was defined for DIC analysis.

Strains in the global coordinate system XY were measured in a small area (50mm x 50mm) at the centre of the specimen, minimizing the impact of undesirable edge effects, and compared to the theoretical strain values. As seen in Figure 5.12, the experimental strain closely followed the theoretical data calculated from the kinematics of the PFT fixture. The average strains were then transformed into the local coordinate system which was oriented by progressively measuring the direction of the CFs during the test (see Figure 5.13). As seen in Figure 5.13, in the material coordinates, initially, the shear strain (ε_{12})-shear angle relationship was quasi-linear, reaching a maximum value of -22% at a shear angle of 32°, confirming that the centre of the fabric specimen was subjected to a deformation close to pure shear. However, transverse and longitudinal strains also developed in the material. For example, normal compressive strains transverse to the CFs were initially negligible and slowly developed after 10° shear angle up to a compressive strain of 14% at 32° shear angle. The transverse compressive strain of individual CF tows can be explained by the effect of the stitching compacting the CF tows as the test progressed (as evidenced in Figure 5.10). Similarly, linear development of normal tensile strains longitudinal to the CF tows were seen starting from a shear angle of 4° and reaching a maximum value of 15% at a shear angle of 32°. Although the CFs were not expected to elongate, the positive strain could be the result of stretching of the stitching in the longitudinal direction, as seen in Figure 5.10.

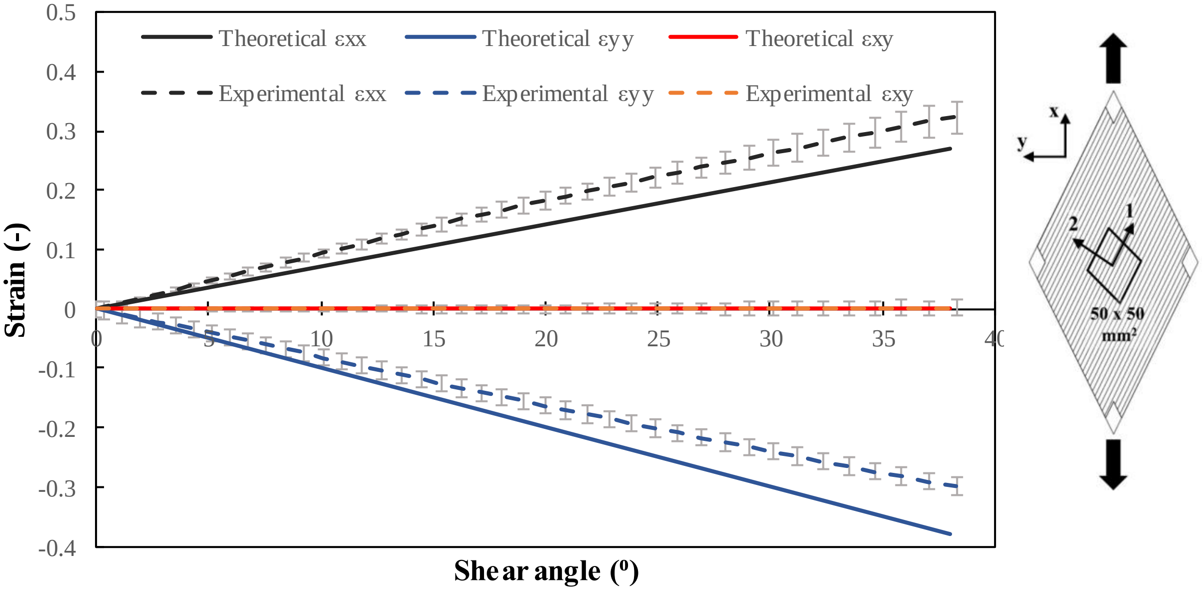

Figure 5.12. Average strain-shear angle response for three picture frame test specimens, with indicated strain components measured in the global coordinate system. Note that average strain values were extracted by DIC from a 32 mm x 32 mm area in the middle of the specimen.

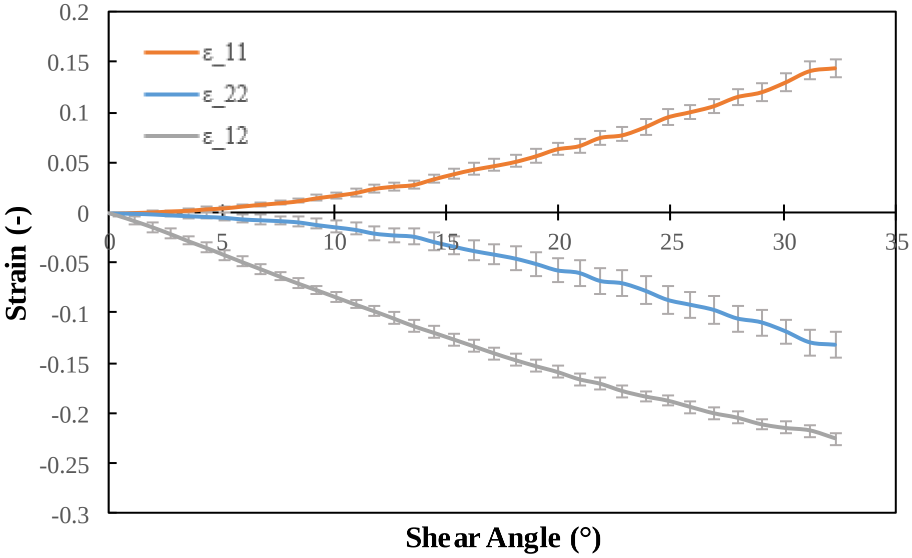

Figure 5.13. Material coordinate strain values extracted by DIC from a 50 x 50 mm^2 area in the middle of the specimen during the picture frame test.

Using the normalizing techniques of Harrison et al. [142], including the transformation of displacement to shear angles using Equation 3.1, the force-displacement response was converted to normalized shear force versus shear angle (see Figure 5.14). The response behaviour of the normalized shear force versus shear angle was similar to the force-displacement relation. From the normalized shear force-shear angle response, a shear stress-strain relation was determined under the assumption that the specimen was subjected to pure shear strain and that the strain was uniformly applied. The stress values were computed based on the measured fabric thickness of 0.49 mm. Figure 5.15 presents the average experimental data and the piece-wise linear approximation that was used to calibrate the fabric shear response for the constitutive model.

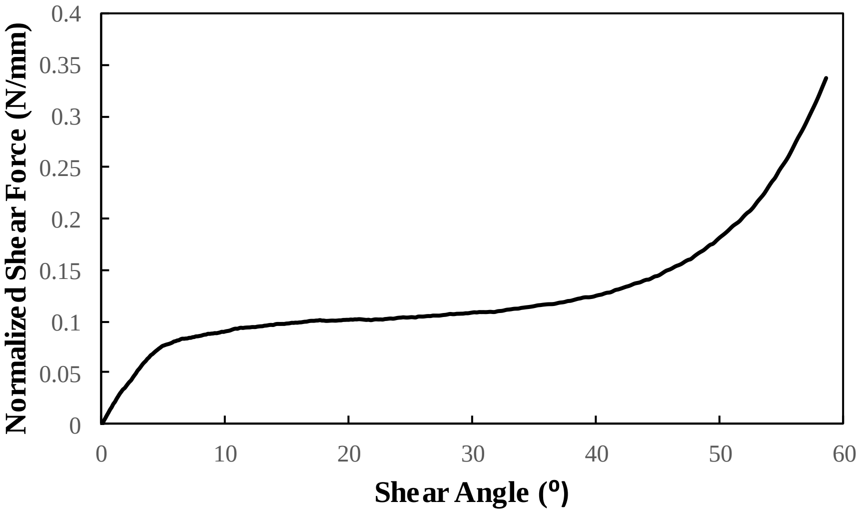

Figure 5.14. Normalized shear force-shear angle response for a picture frame test.

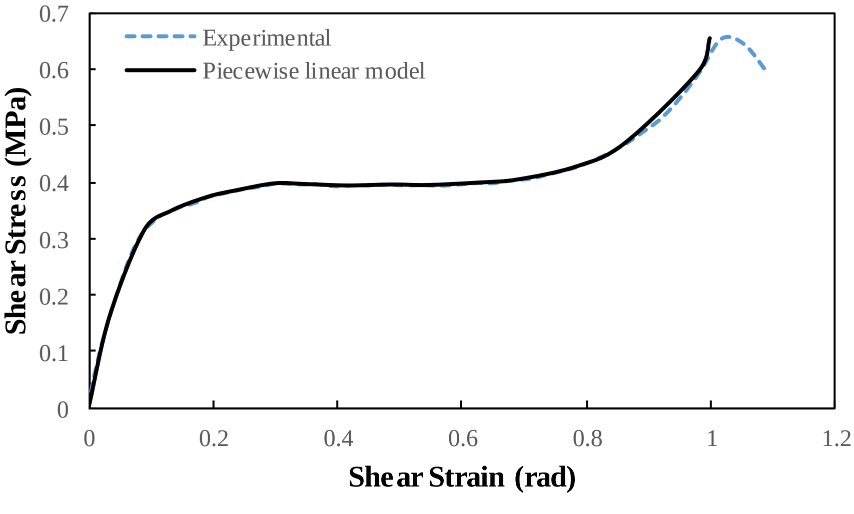

Figure 5.15. Experimental shear stress-strain response from picture frame test and associated piecewise linear model.

5.1.2.2. 45° Off-axis test - Simple shear

As an alternative to the PFT, Schirmaier et al. [16] recommended use of a 45° off-axis extension test to characterize the shear deformation of UD-NCFs, which is presented hereafter. Pourtier et al. [96] proposed that UD-NCFs subjected to 45° off-axis extension loads tend to deform under simple shear, and that under this assumption the rotating fiber direction could be predicted from the applied displacement per Equation 3.4. This assumption was verified by comparing the theoretical fiber direction variation with experimental measurements for one preliminary test specimen (Figure 5.16). The close correlation between the theoretical and experimental fiber angle profile reveals that the simple shear deformation assumption is valid for the 45° off-axis extension test.

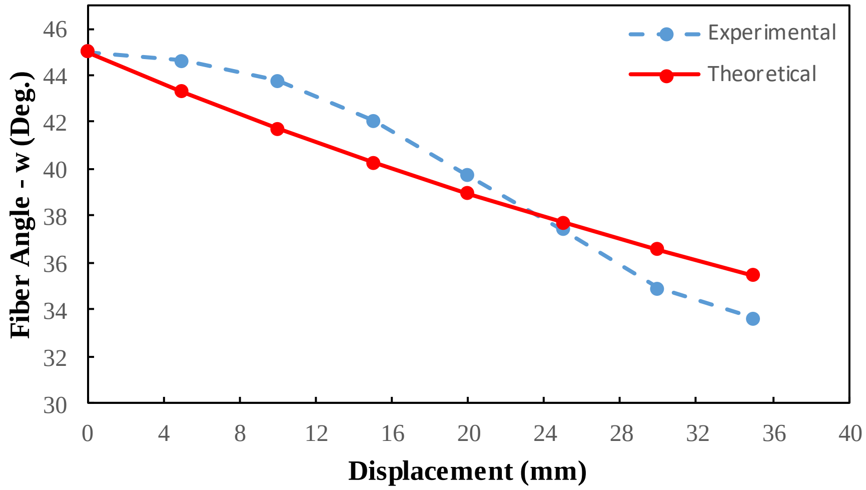

Figure 5.16. Experimental and theoretically predicted carbon fiber angle (w) during the 45° off-axis extension test.

Seven repeated off-axis extension tests were conducted, where data from four tests were discarded due to specimen misalignment, premature fiber failure or GF sliding at the clamps. Data from three tests were chosen as representative of the macroscale force-displacement response of the fabric (see Figure 5.17). The applied force increased sharply at the beginning of the test with a gradual decrease in slope for the full displacement range. The maximum force was of 16 N at the maximum applied displacement of 50 mm.

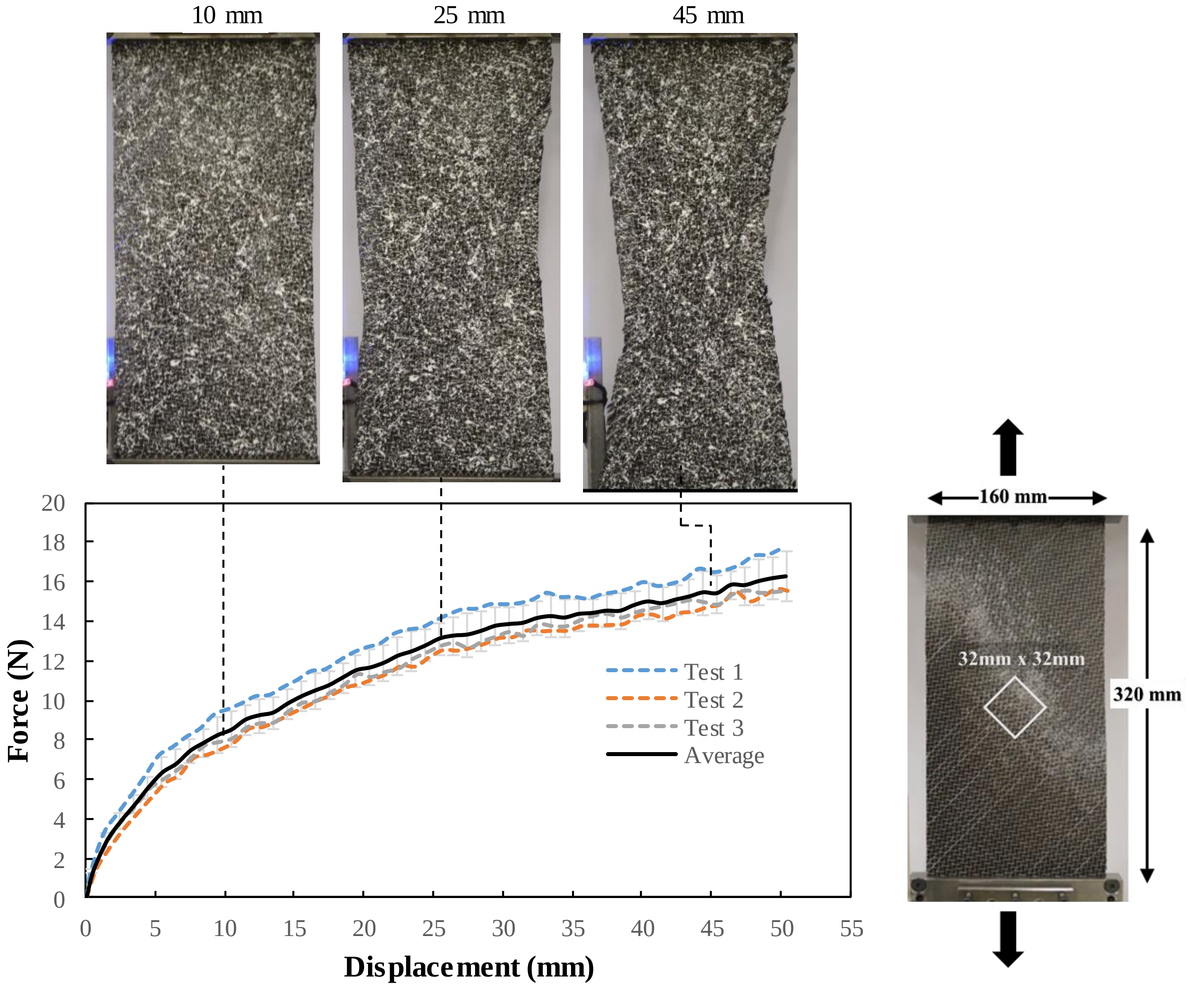

Figure 5.17. UD-NCF force-displacement response for 45° off-axis extension test, with images of overall specimen deformation captured at indicated displacements.

Figures 5.18 and Figure 5.19 show images of a 32x32 mm^2 window at the centre of a specimen at progressive displacements, respectively, for the stitching and GF sides of the fabric. Magnified images for both fabric sides of the test specimen are also presented in Figures 5.20 and 5.21. A progressive increase in the shear deformation of the fabric with increasing displacement was observed. During the initial stage of the test the stitching segments were extended (Figure 5.20) as was also observed during the PFT, which caused the initial sharp increase in the force response of the fabric. Rotation of the fabric was observed to initiate thereafter since the CF tows tended to align with the loading axis (Figures 5.20 and 5.21), which decreased the rate at which forced increased with increasing displacement. As the tension in the stitching continued to increase, at approximately 6 mm displacement, the width of the individual CF tows began decreasing due to the compression induced by the stitching. This caused gaps to form between the tows (Figure 5.20) which promoted intertow sliding at displacements beyond 10 mm (Figure 5.18), and also contributed to reducing the fabric resistance to shear deformation. Thus, the combined effect of CF tow rotation and compression, as well as intertow sliding, governed the macroscopic shear response of the fabric. Moreover, on the GF side, yarn markings reveal that the GFs do not move relative to the CF tows as the displacement increased. Also, the stretched GFs push against the compressed CF tows inducing out-of-plane deformation in the tows in the form of micro-wrinkling.

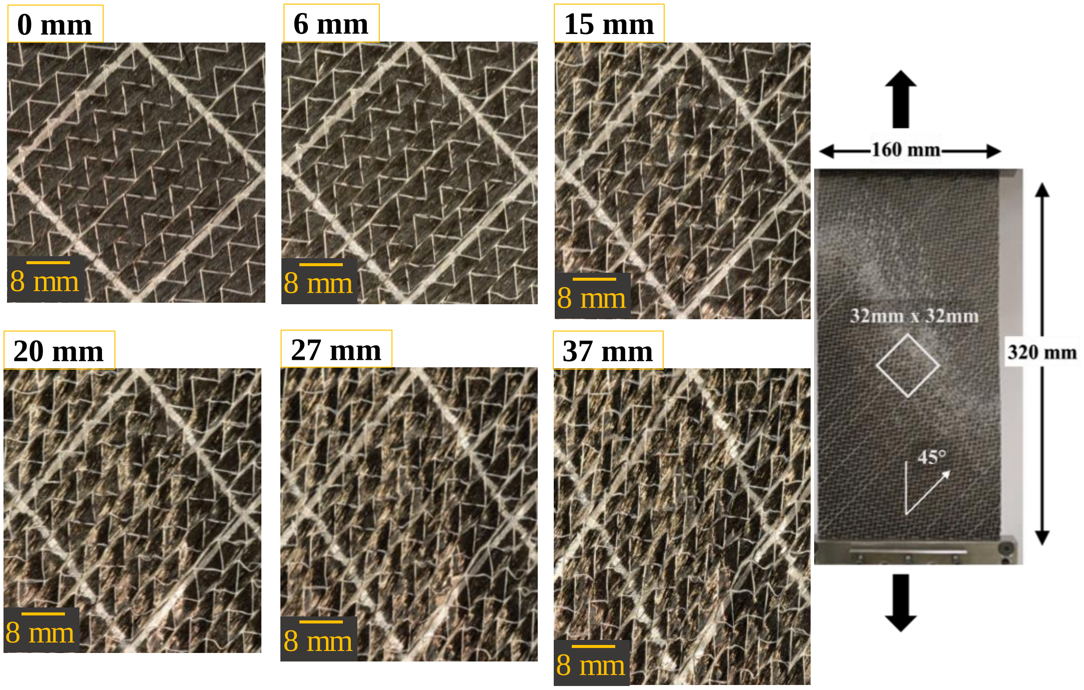

Figure 5.18. Images of the stitching side of UD-NCF fabric during the 45º off-axis extension test at different displacements: 0, 6, 15, 20, 27 and 37 mm.

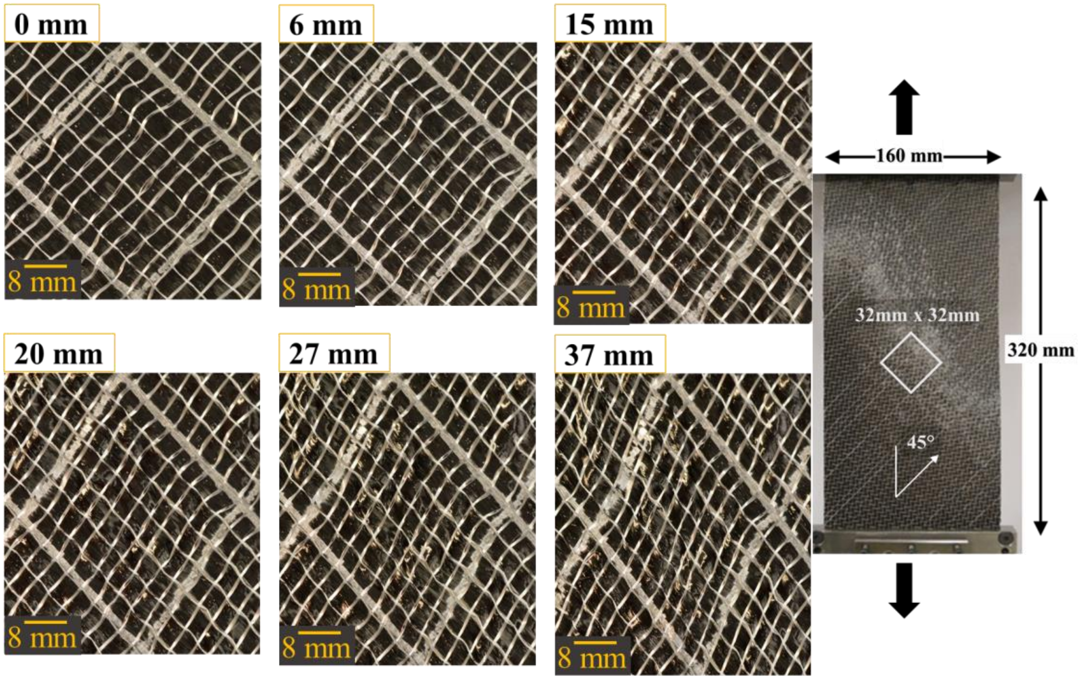

Figure 5.19. Images of the glass fiber side of UD-NCF during the 45º off-axis extension test at different displacements: 0, 6, 15, 20, 27 and 37 mm.

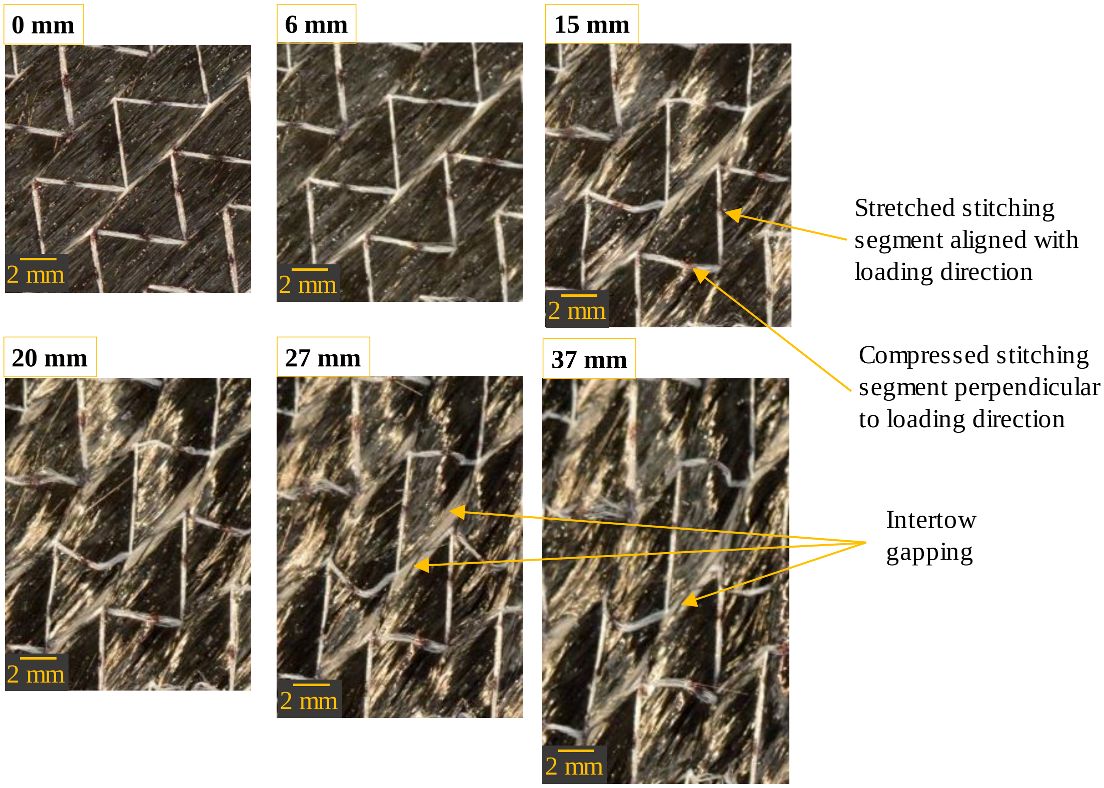

Figure 5.20. Images of the stitching side of a UD-NCF specimen during the 45º off-axis extension test captured at different displacements loading: 0 mm, 6 mm, 15 mm, 20 mm, 27 mm and 37 mm displacements.

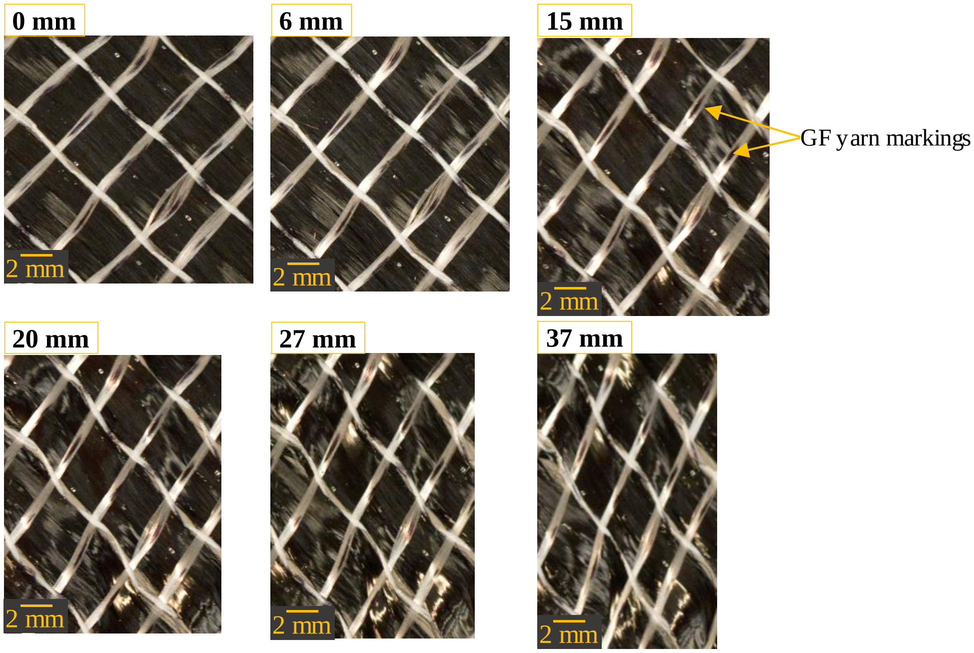

Figure 5.21. Images of the glass fiber side of a UD-NCF specimen during the 45° off-axis extension test captured at different loading displacements: 0 mm, 6 mm, 15 mm, 20 mm, 27 mm and 37 mm displacements.

To further highlight the observed deformation mechanisms, CF tow separation was investigated from another perspective. When CF tows separated, open spaces or “voids” were observed in the fabric as the displacement increased during loading. An estimate of the ratio of void area to the total surface area was calculated by post-processing the captured images from the same 32 mm by 32 mm area at the centre of a specimen. Figure 5.22 shows the original and corresponding image processing output (in black and white), where the void areas in the specimen are indicated in white.

Displacement (mm)	
0	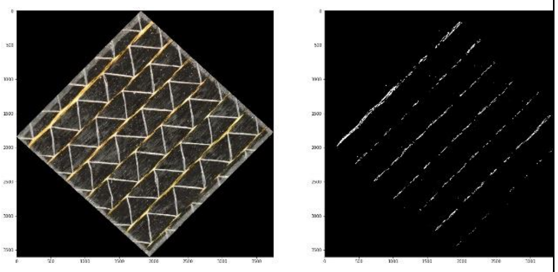
7	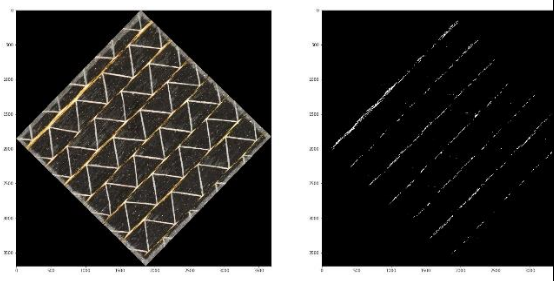
19	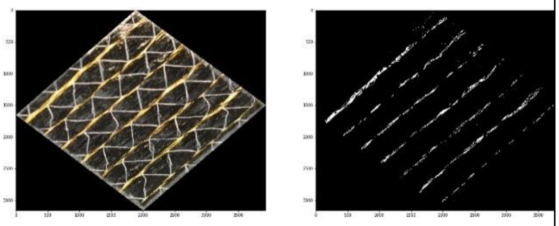
29	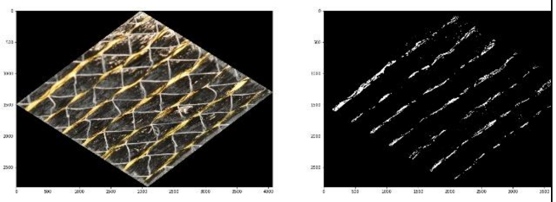
39	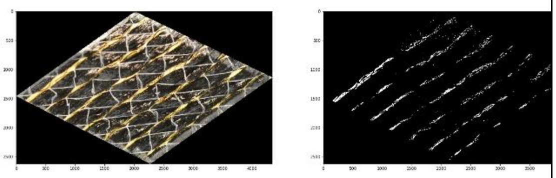
45	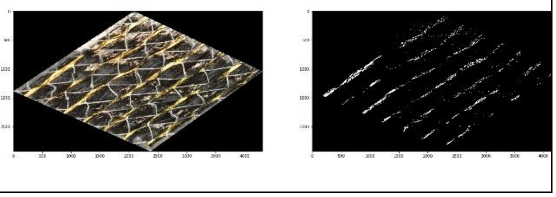

Figure 5.22. Images from a 32 mm by 32 mm area in the middle of a UD-NCF specimen, with corresponding void area represented in white in the black and white images, during the 45 off-axis extension test at different displacements during loading: 0 mm, 7 mm, 19 mm, 29 mm, 39 mm and 45 mm displacements.

Figure 5.23 presents the results of the void area content in relation to applied displacement. It is worth noting that in a relaxed state, 0 mm displacement, the fabric contained 1.6% void area which gradually increased until a displacement of around 10 mm, at which point the rate of change increased to a peak of 0.2% per mm. This displacement coincides with the loss of material stiffness previously seen in the force-displacement profile, at also approximately 10 mm, and with the tow compression seen in the mesoscale images in Figures 5.20 and 5.21. Extending the fabric in an off-axis direction applies tension to the stitching. As a result of this, the stitching web compresses the CF tows creating gaps between them that increase the void area on the fabric. The highest void content recorded was approximately 4.8% at a displacement of 30 mm, after which it decreased to 4% at complete fabric failure at 45 mm displacement. The reduction in void content before failure was most likely due to relaxation of the compression applied by the stitching on the CF tows, as the stitching progressively failed after 30 mm of applied displacement.

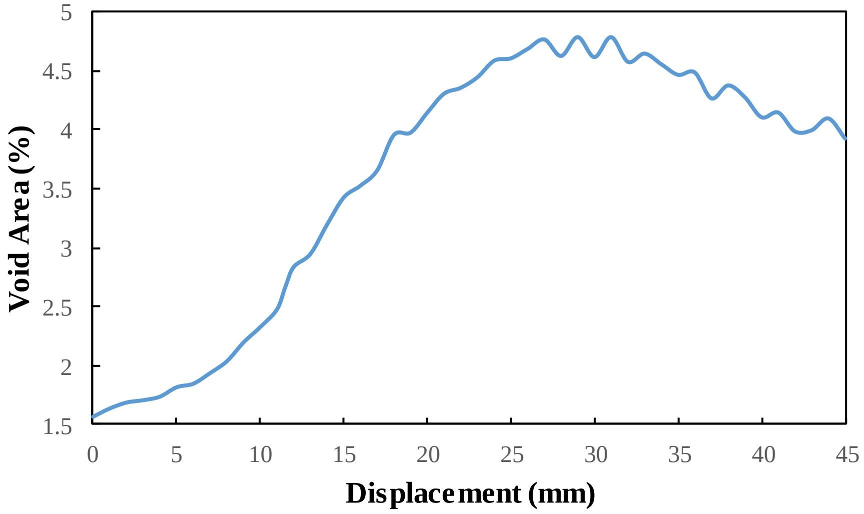

Figure 5.23. Void content in a single layer of UD-NCF during the 45º off-axis extension test.

Finally, a shear stress-strain relation was calculated from the force-displacement response of the 45º off-axis extension tests through the implementation of Equation 3.5 and CF direction data (see Figure 5.24). Due to specimen breakdown after a displacement of 35 mm, the CF direction data could not be clearly extracted from the specimen, limiting the calculated stress-strain relation used to calibrate MAT249 to a maximum shear strain of 46%.

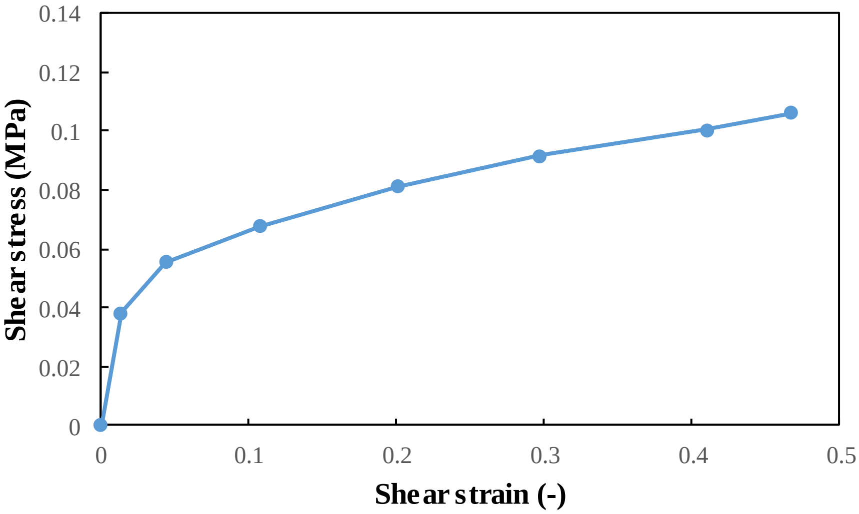

Figure 5.24. UD-NCF experimental shear stress-strain response calculated using force-displacement data gathered through the 45° off-axis extension test.

5.1.3. Cantilever bending experiments

Cantilever tests were performed to characterize the bending stiffness of the fabric along with the longitudinal and transverse directions. Representative tests along the longitudinal and transverse fabric directions are shown in Figures 5.25a and 5.25b, which define the bend length parameter. Six repeated cantilever tests were performed along each material direction and for both up-facing fabric configurations (i.e., GF side facing up and stitching side facing up).

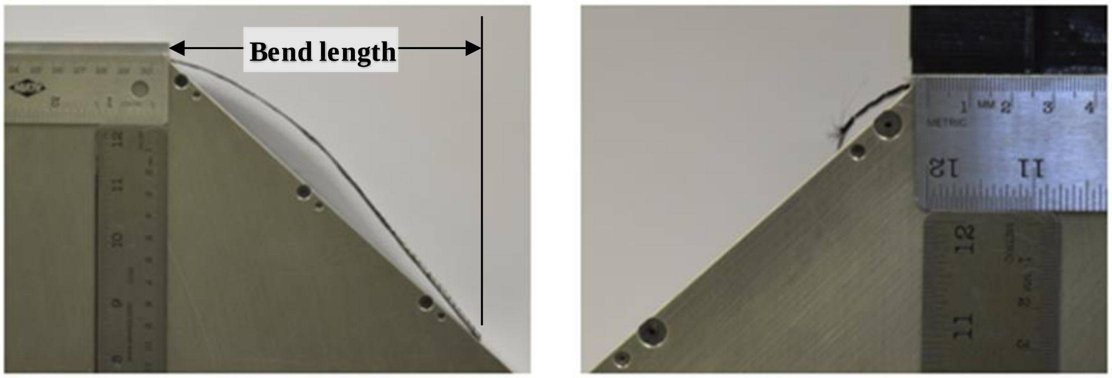

(a) (b)

Figure 5.25. Cantilever test bending response in the (a) longitudinal and (b) transverse direction.

The test results for bending along the longitudinal direction are shown in Figures 5.26 and 5.27 for both configurations. The average bend length in the longitudinal direction was 145.2±3.6 mm (see Figure 5.26) when the stitching side was convex (facing up), and 141.0±4.4 mm (see Figure 5.27) when it was concave (facing down). For both configurations, measurements of bend lengths showed excellent repeatability with standard deviation representing the data scatter of < 5%. The 2.9% decrease in bending length for the stitching side down configuration was likely due to the inadequacy of the stitching web to provide any compression resistance. In contrast, for the stitching side convex configuration, the stitching is placed in tension which increased the fabric bending stiffness. Furthermore, the resin binder present on the stitching side of the fabric may have also contributed to the increase in apparent stiffness. It should be noted that bending the fabric in the longitudinal direction completely disengaged the GFs that run perpendicular to the bending direction, leaving the bending resistance of the fabric dependent on the inter-tow sliding and the stitching web resistance to tension.

The resulting average bending stiffness in the longitudinal direction were computed according to Equation 3.12 as 0.0014 Nm and 0.0013 Nm for the stitching side convex and concave (facing down), respectively.

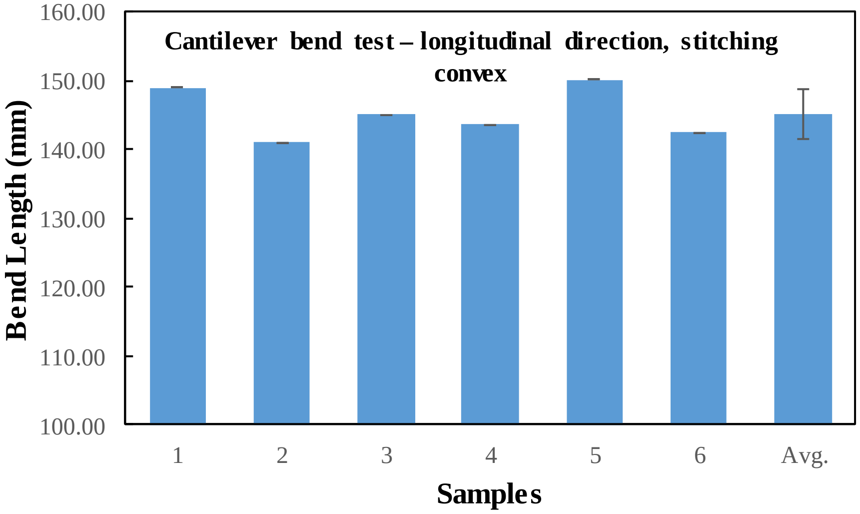

Figure 5.26. Cantilever test bend length measurements and average value with the fabric stitching side convex and oriented in the longitudinal direction.

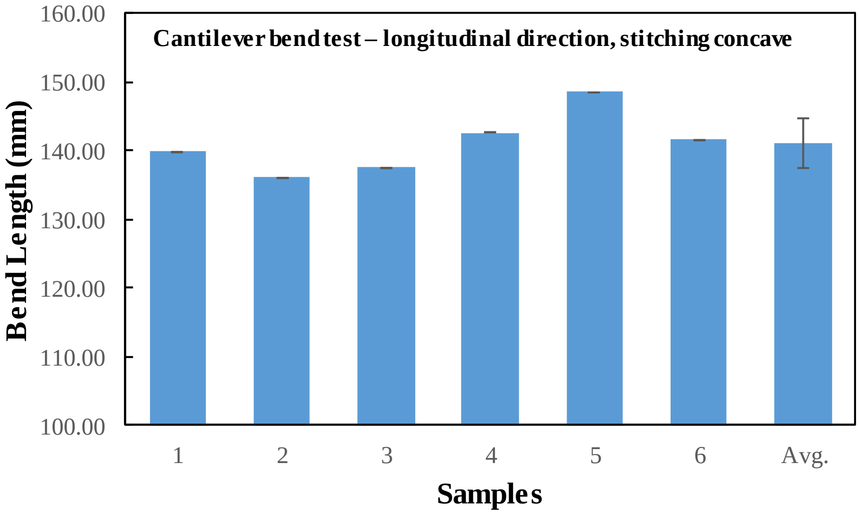

Figure 5.27. Cantilever test bend length measurements and average value with the fabric stitching side concave and oriented in the longitudinal direction.

The average bend lengths for cantilever tests performed along the transverse direction were 17.1±1.1 mm and 11.2±1.3 mm for the stitching side convex and stitching side down configurations, respectively (Figures 5.27 and 5.28). These bend lengths were significantly lower than those in the longitudinal direction as expected since the fabric stiffness along the transverse direction is much lower. Contrary to the longitudinal direction, the variations in the bend length measurements were more severe in the transverse direction for both fabric side convex configurations. With the stitching convex, the variation was 6.4%, whereas it reached 11.6% when the stitching faced down. The lack of material continuity along the transverse direction decreased the consistency of the test specimens due to variations in the stitching from specimen to specimen, potentially increasing the variability of the bending response. Additionally, the drop in bending stiffness when turning the stitching side downwards was 34.5%. Similar to the longitudinal direction, turning the stitching downward to the compression side of the bend, disengaged the stitching yarns cancelling its contribution to the bending stiffness.

The average transverse bending stiffnesses of the fabric were calculated to be 2.3E-6 Nm, and 0.65E-6 Nm for the stitching side convex and down configurations, respectively. As seen in Figure 5.30, bending stiffness in the longitudinal direction is substantially higher than in the transverse direction.

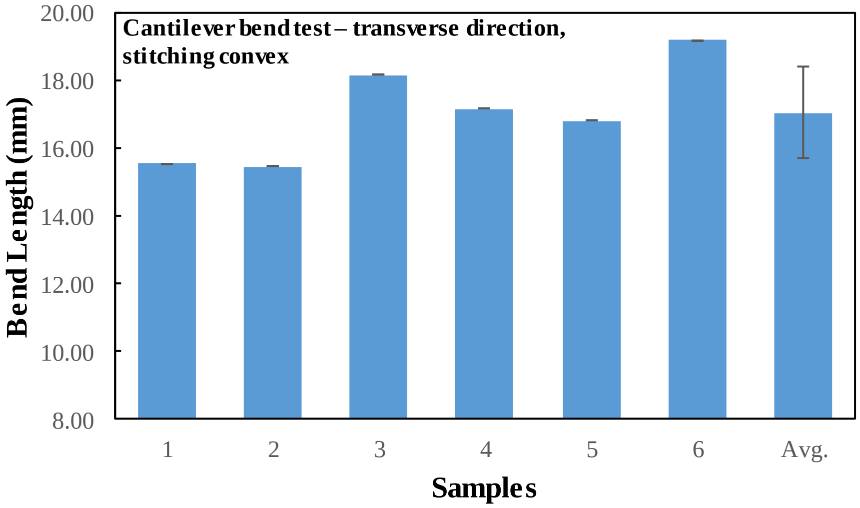

Figure 5.28. Cantilever test bend length measurements and average value with the fabric stitching side convex and oriented in the transverse direction.

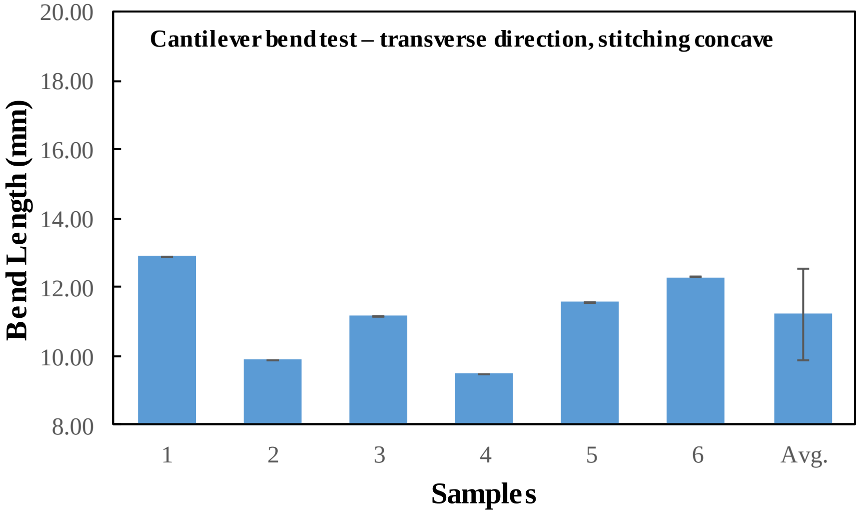

Figure 5.29. UD-NCF cantilever test bend length measurements and average value with the fabric stitching side concave and oriented in the transverse direction.

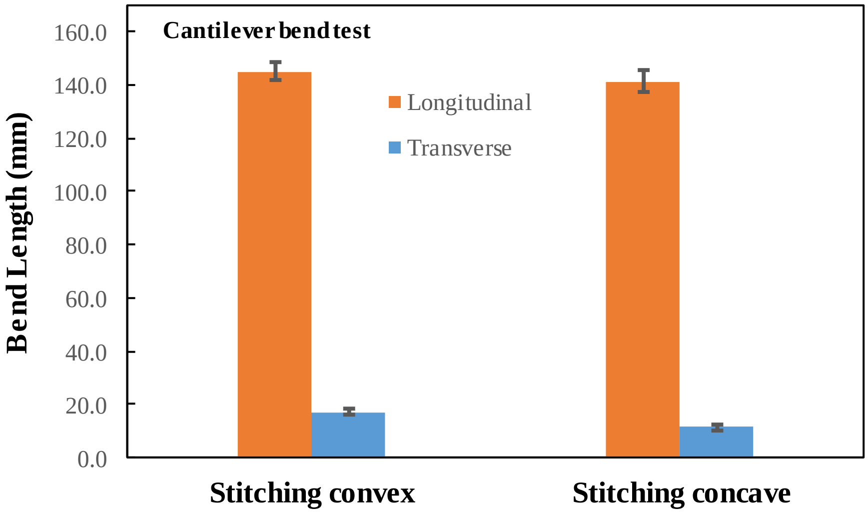

Figure 5.30. UD-NCF cantilever bend test length measurements in the longitudinal and transverse directions.

5.1.4. Fabric-tooling friction experiments

The friction response of the fabric when in contact with a steel surface, which resembles the tooling surface used for a preforming operation, was investigated. The friction coefficients of the fabric along the two principal directions and both fabric sides were determined per the procedure explained in section 3.25. The steel surface was sanded with 150 grit sandpaper to simulate the surface condition of the forming tool that would be used to preform the fabric, with an approximated average surface roughness of 1 µm.

Figures 5.31 and 5.32 illustrate the average sliding force response of the fabric along the longitudinal direction when the GF side and stitching side were in contact with the steel substrate surface, respectively. The average responses and scatter were calculated from at least three test repeats for each configuration. Note that the resistance friction forces determining the static and dynamic friction coefficient are specified on the graph by the two horizontal lines.

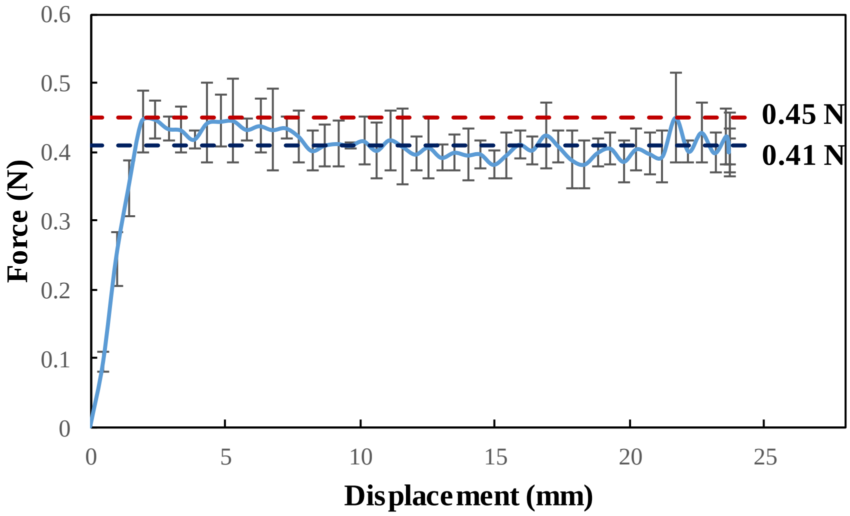

Figure 5.31. UD-NCF friction force response of the fabric glass fiber side oriented in the longitudinal direction when contacting a steel surface conditioned to simulate a forming tool.

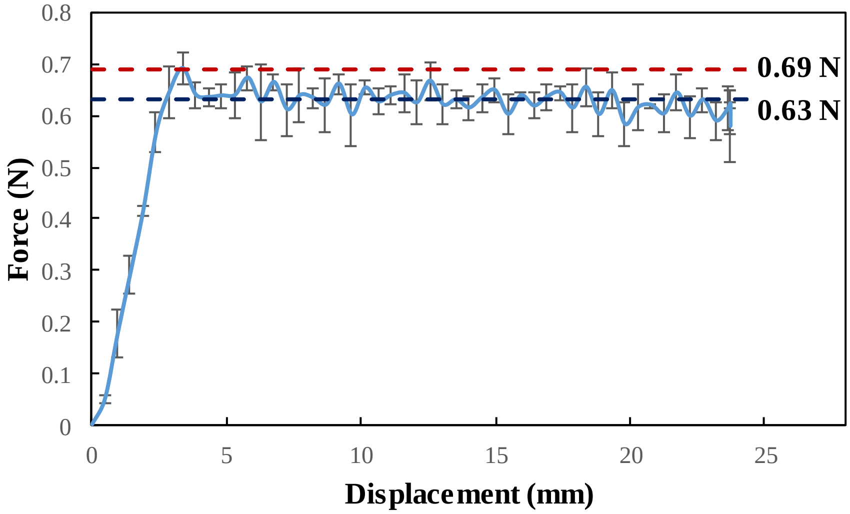

Figure 5.32. UD-NCF friction force response of the fabric stitching side oriented in the longitudinal direction when contacting a steel surface conditioned to simulate a forming tool.

Figures 5.33 and 5.34 respectively illustrate the average sliding force response of the fabric along the transverse direction when the GF and stitching side and in contact with the steel surface. At least three repeats were conducted for each test and the corresponding standard deviation error bars are shown.

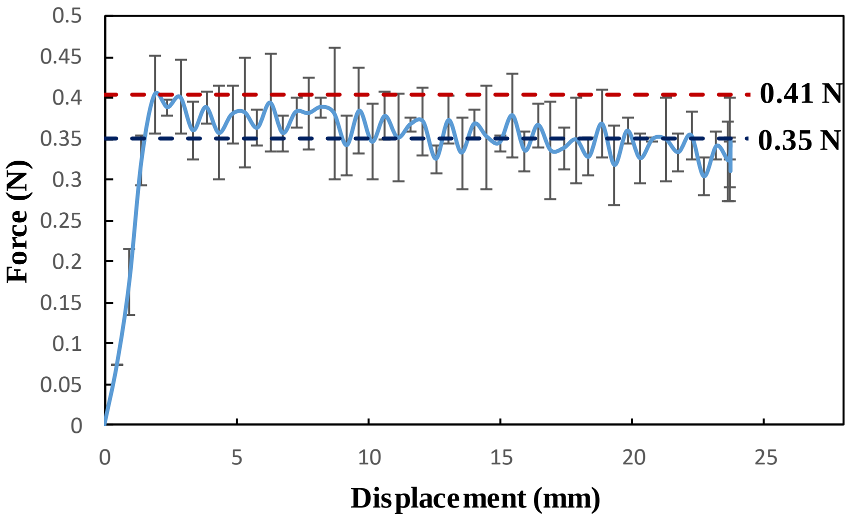

Figure 5.33. UD-NCF friction force response of the fabric glass fiber side oriented in the transverse direction when contacting a steel surface conditioned to simulate a forming tool.

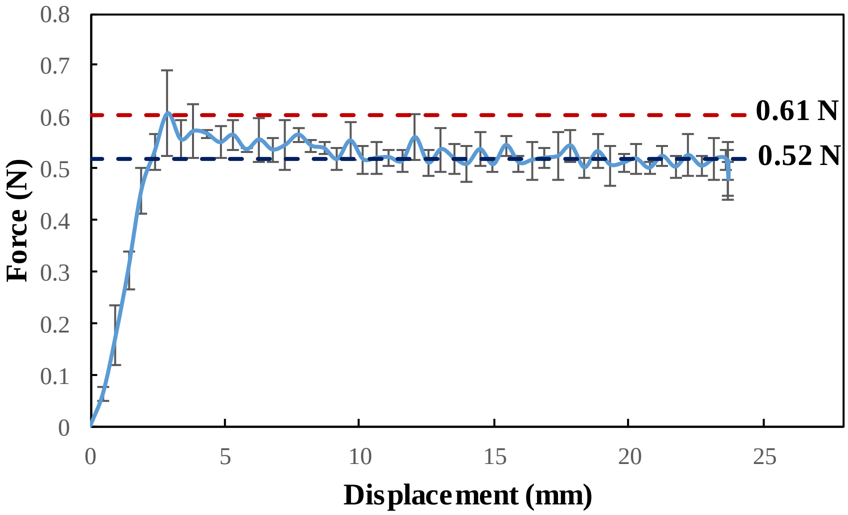

Figure 5.34. UD-NCF friction force response of the fabric stitching side oriented in the transverse direction when contacting a steel surface conditioned to simulate a forming tool.

Using the equations presented in Section 3.3.6 and considering the weight of the sled of 200 g, the static and dynamic friction coefficients were calculated from the recorded peak and sliding forces, respectively (see Table 5.1).

Table 5.1. UD-NCF static and dynamic friction coefficients.

Bending Direction	Fabric side	Static friction coefficient	Dynamic friction coefficient
Longitudinal	Glass fiber	0.23±0.03	0.21±0.02
	Stitching	0.35±0.02	0.32±0.01
Transverse	Glass fiber	0.21±0.02	0.18±0.02
	Stitching	0.31±0.04	0.27±0.01

In the longitudinal direction, the static and dynamic friction coefficients of the stitching side were 39% and 52% higher than the GF side correspondingly. Likewise, in the transverse direction, the stitching side static and dynamic friction coefficients were 48% and 50% higher than the GF side. A possible cause of the higher friction response of the stitching side is that more fabric components are present on this surface than on the GF side. In other words, the stitching segments that connect tows and the binding agent are both on the stitching side of the fabric. Consequently, contact with the stitching surface generates more interactions between the fabric components and the contacting surface, resulting in higher coefficients of friction.

It is also important to note that turning the fabric from the longitudinal to the transverse orientation decreases the static and dynamic friction coefficients. On the GF side, the static and dynamic friction coefficients decrease by approximately 9% and 14%, respectively. On the other hand, a decrease of approximately 11% and 16% was recorded for the stitching side of the fabric. This decline in friction coefficient in relation to orientation may be owing to the oval cross-sectional shape of the CF tows, which reduces the amount of contact points interaction when the sliding occurs in the direction perpendicular to the CF tows.

The calculated friction coefficients reported in this section were implemented as input parameters in the material model. Since only one static and one dynamic coefficient of friction were needed in the numerical material model, an average value from the two fabric surfaces was calculated.

5.2. Calibration of material constitutive model - MAT249

The purpose of the experimental tests presented in Section 5.1 was to capture the stress-strain response of the fabric material in the warp and weft directions, the in-plane shear response, as well as to estimate transverse shear and the friction response of the fabric. The experimental data was subsequently used to calibrate the material constitutive model MAT249 (see section 4.1.1 for more details).

Some simplifying assumptions were made during the model calibration to isolate and fully capture the stress-strain behaviour in the principal material directions. The fabric was assumed to have negligible stiffness in the thickness direction; hence corresponding material properties were set to zero or negligible values. Also, the fabric characterization was performed under the assumption that the fabric behaves as a continuum. Once the extracted fabric material properties were implemented in the numerical model, the experimental tests were simulated and the results compared to confirm the proper calibration of the material model. The corresponding details are provided in the following sub-sections for each deformation mode studied.

5.2.1. Longitudinal and transverse extension response calibration

Single shell element simulations were initially performed to verify the predicted response of the fabric along with the longitudinal and transverse directions. See section 4.2.1 for model details. The stress-strain relations from Section 5.1 (see Figures 5.3 and 5.6) were used as input for MAT249. The predicted stress-strain response was compared to experimental data. Also, the experimental extension tests were also simulated by considering the full test specimen geometry as per the model described in section 4.2.3. These predicted results were also compared to experimental data.

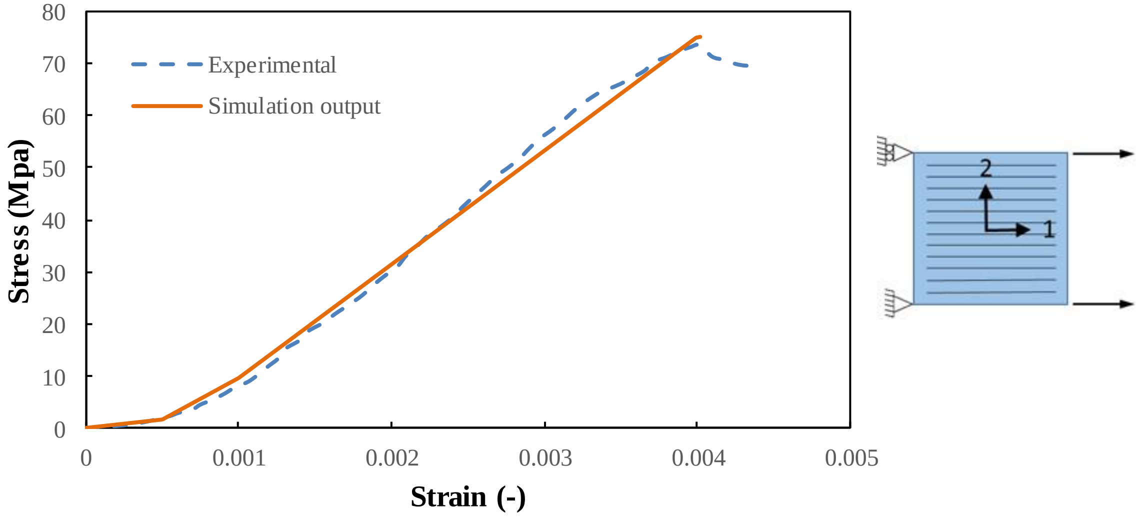

Figure 5.35. Stress-strain data of the UD-NCF longitudinal extension experimental test and a single shell element simulation with material model MAT249 subjected to tensile loading in the longitudinal direction.

For the UD-NCF longitudinal extension response, there was a good correlation between the numerically predicted and experimentally obtained stress-strain response (Figure 5.35). When simulating the experimental longitudinal extension test, the predictions of force-displacement (Figure 5.36) and stress-strain response (Figure 5.37) were also in very good agreement with the experimentally obtained data.

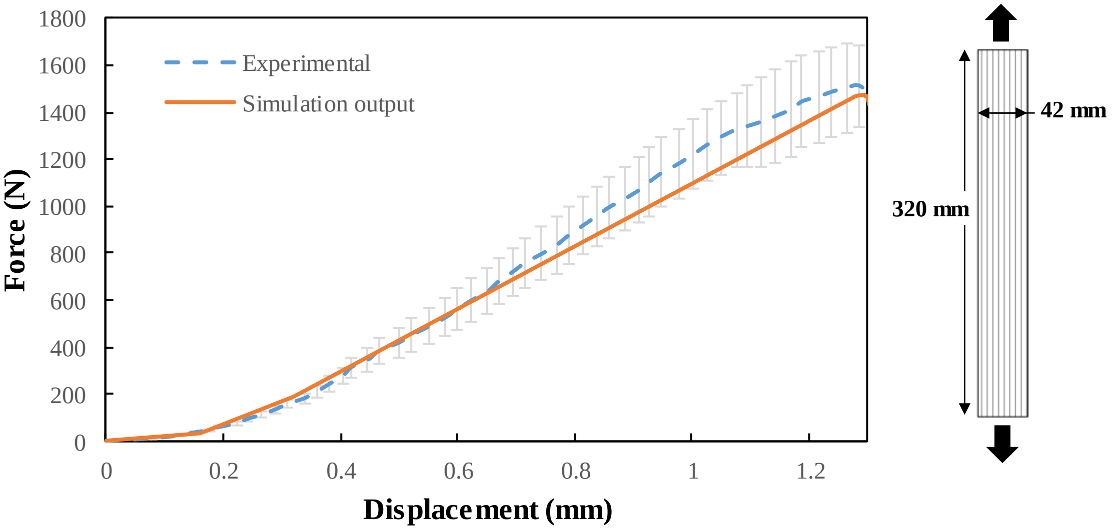

Figure 5.36. Longitudinal extension test force-displacement experimental data and corresponding output data from numerical simulation employing material model MAT249.

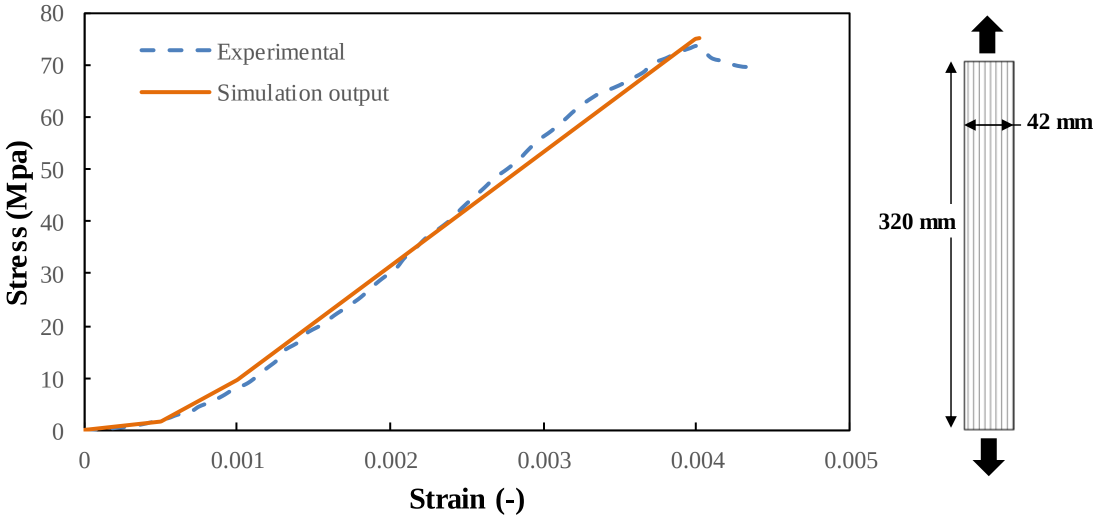

Figure 5.37. Longitudinal extension test stress-strain experimental data and corresponding output data from numerical simulation employing material model MAT249.

For the UD-NCF transverse extension response, the stress-strain response predicted using a single shell element simulation correlated well with the experimental values (Figure 5.38). When simulating the experimental transverse extension test, the predictions of force-displacement (Figure 5.39) and stress-strain response (Figure 5.40) also agreed well with experimental data.

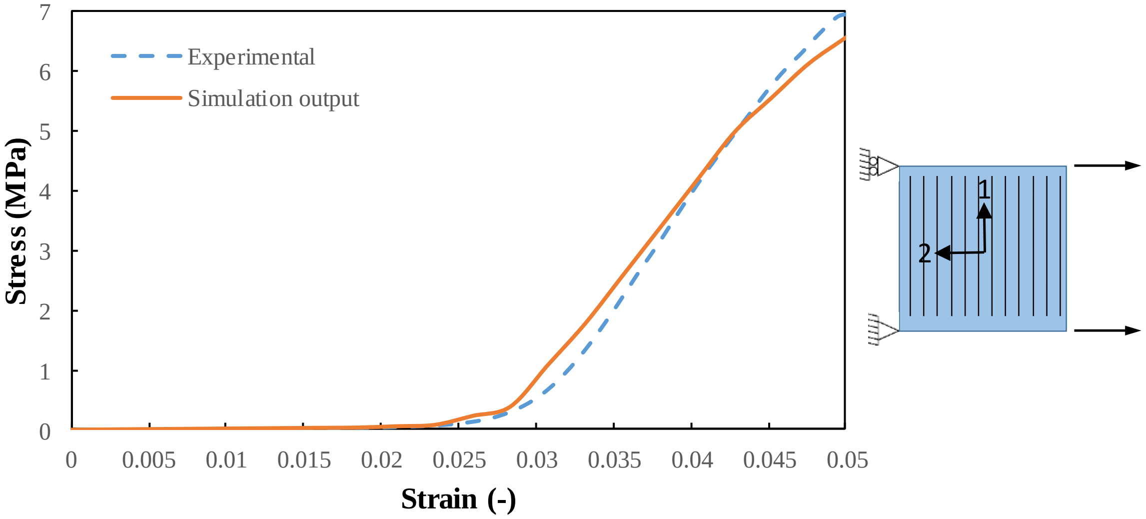

Figure 5.38. Stress-strain data of the UD-NCF transverse extension experimental test and a single shell element simulation with material model MAT249 subjected to tensile loading in the transverse direction.

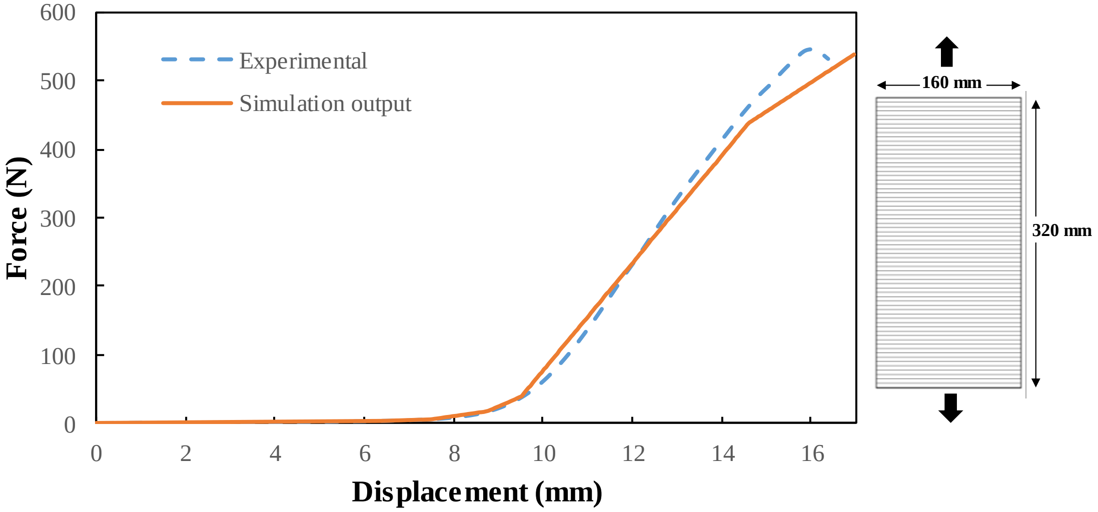

Figure 5.39. Transverse extension test force-displacement experimental data and corresponding output data from numerical simulation employing material model MAT249.

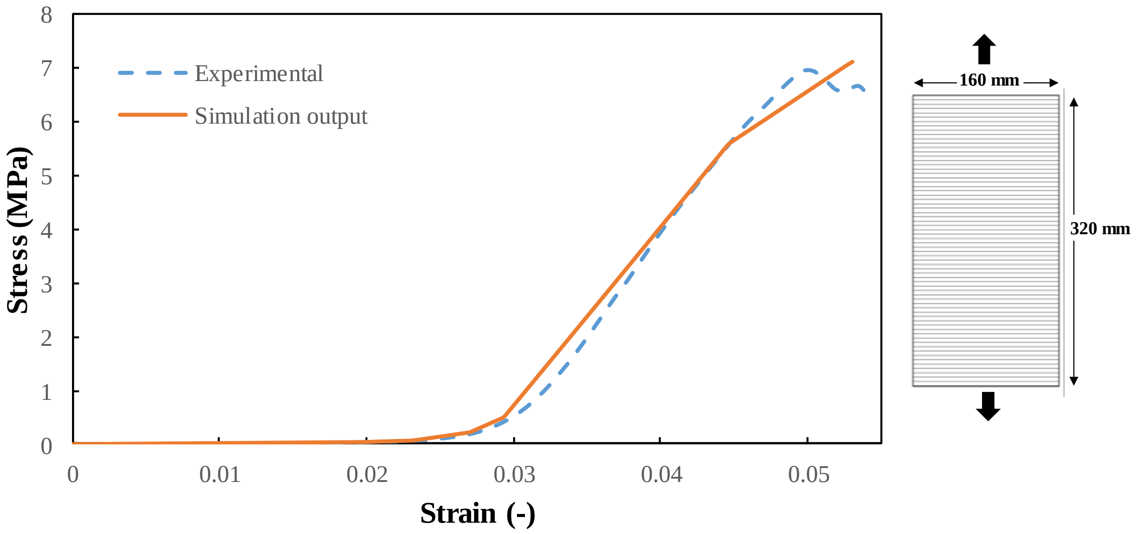

Figure 5.40. Transverse extension test stress-strain experimental data and corresponding output data from numerical simulation employing material model MAT249.

5.2.2. Shear response calibration

The shear response of the fabric was calibrated using two sets of data, the PFT and the 45° off-axis extension test. Before starting the calibration process, a series of single element simulations were performed to investigate the parameters that influence the shear behaviour for the material constitutive model (MAT249). These simulations were performed according to recommendations from the Institute for Aircraft Design for calibration of shear behaviour of fabric constitutive models [144] as described in section 4.2.1.

The first parameter evaluated was *Em* which represents the modulus of the resin phase when simulating fiber-reinforced composites using MAT249 [137]. In this study *Em* was varied from 0.04 MPa to 5 MPa. As observed in Figure 5.41, as the magnitude of *Em* increased the shear stress-strain response of the fabric stiffness. For example, at a shear strain of 50%, the shear stress response approximately tripled by increasing *Em* from 1 MPa to 5 MPa. The value of *Em* was set to 0.04 MPa in all subsequent simulations.

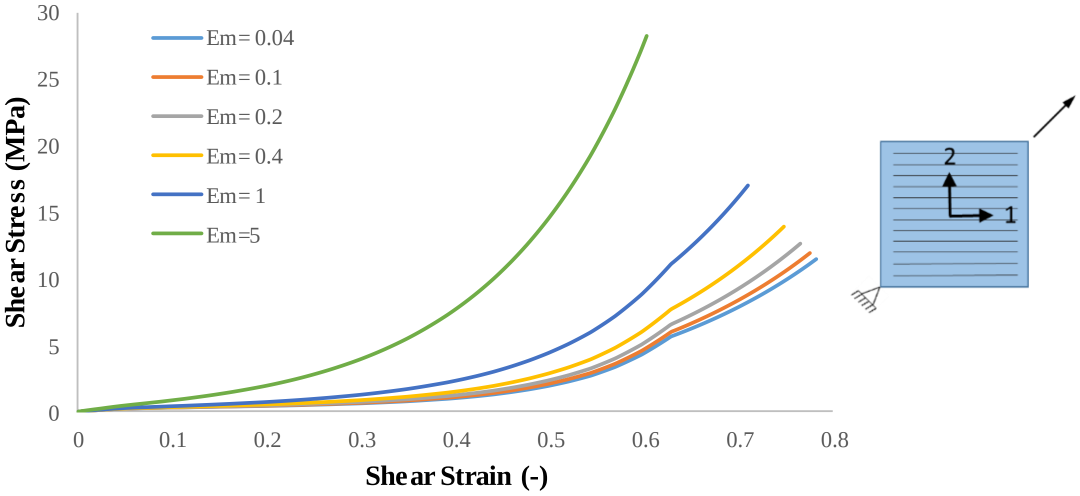

Figure 5.41. Shear stress-strain data resulting from a single element parametric study of MAT249 parameter Em. Em is used to represent the resin phase when modelling fiber-reinforced composites.

Next, the effect of material model MAT249 parameters E1 (longitudinal modulus) and E2 (transverse modulus) on the fabric shear response were examined. In MAT249, E1 and E2 can be specified as stiffness constants or stress-strain data points. As seen in Figure 5.42, E1 was introduced as a constant elastic value and had no impact on the shear response of the shell element over a wide range of values. Likewise, the stress data of the transverse normal stiffness input, depicted in Figure 5.6, were scaled by factors of 2, 10, 20 and 100 (see Figure 5.43) showing no influence on the predicted shear response of the material model.

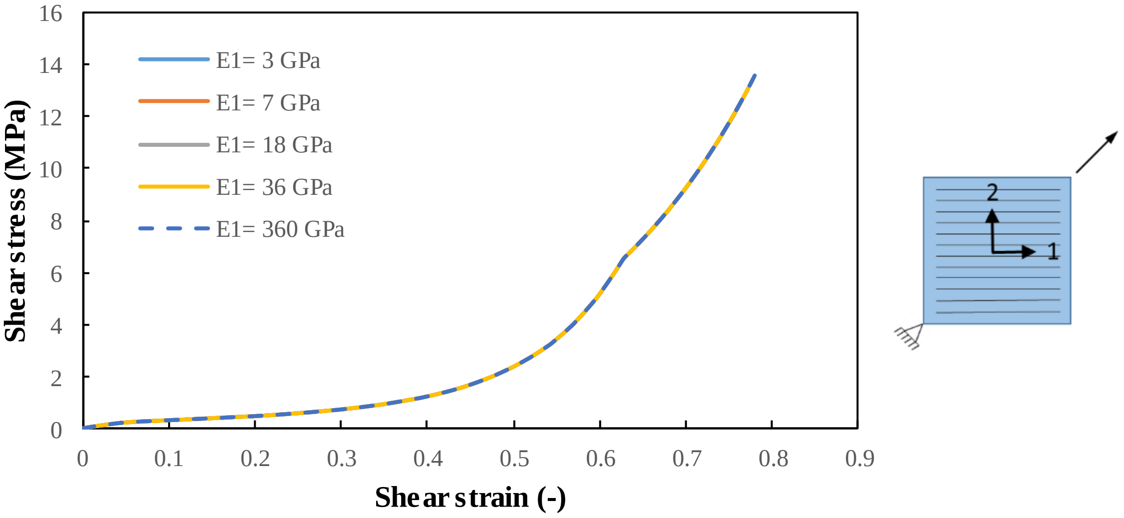

Figure 5.42. Shear stress-strain data resulting from a single element parametric study of MAT249 parameter E1, which represents the Young's Modulus of the fabric in the carbon fiber direction.

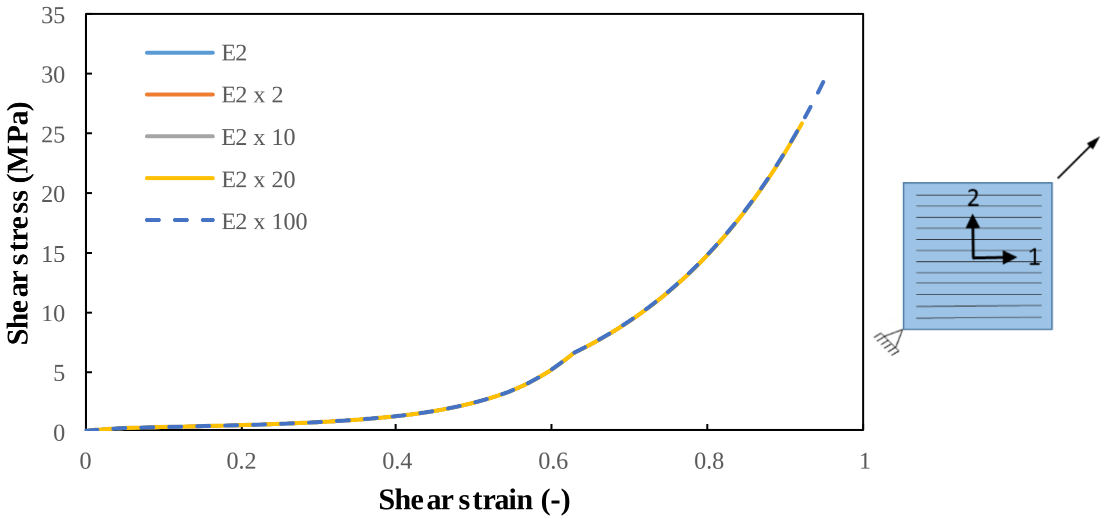

Figure 5.43. Shear stress-strain data resulting from a single element parametric study of MAT249 parameter E2, which represents the fabric stiffness transverse to the carbon fiber direction. A non-linear shear stress-strain data set was implemented as E2, which was scaled by factors of 2, 10, 20 and 100.

As seen in Figure from 5.41 to 5.43 a discontinuity is seen in the predicted shear stress-strain profile at approximately a shear strain of 62%. The discontinuity is suspected to be caused by the fact that the applied boundary condition only provides a state of pure shear at relatively low shear strains. At larger shear strains, the shell element deformation lost symmetry with respect to the direction of loading (45° diagonal) required to maintain a state of pure shear, entering a state of combined shear and tension that likely produced the observed discontinuities. Having determined that the shear response of MAT249 is not influenced by the in-plane material stiffness, calibration of the shear behaviour of MAT249 was first performed through the PFT.

5.2.2.1. Pure shear calibration approach – Picture frame test

Initially, the shear response of the fabric model was calibrated using PFT data, which was calculated under the assumption that the specimen deformed in pure shear. A simulation that replicated the kinematics of the PFT frame test was developed and an element mesh sensitivity study was performed with the model described in section 4.2.2. The shear stress-strain data presented in Figure 5.15 was used to calibrate the model. Up to a shear strain of 80% the predicted shear response was not significantly influenced by element size (Figure 5.44). While the simulation model using a 5 mm element size provided the best correlation with the experimental data, it took over ten times more computational time than the 10 mm element size simulation, which took 5 minutes to complete. The 20 mm shell element took the shortest time with a computational time of only 2 minutes. Regardless of element size, the numerical model was able to correctly predict the shear stress-strain response of the fabric under pure shear deformation. Images of the PFT and corresponding simulation at the start of the test and at a shear angle of 38° are shown in Figure 5.45. As observed in this Figure, the model was also able to accurately capture the overall deformation of the specimen.

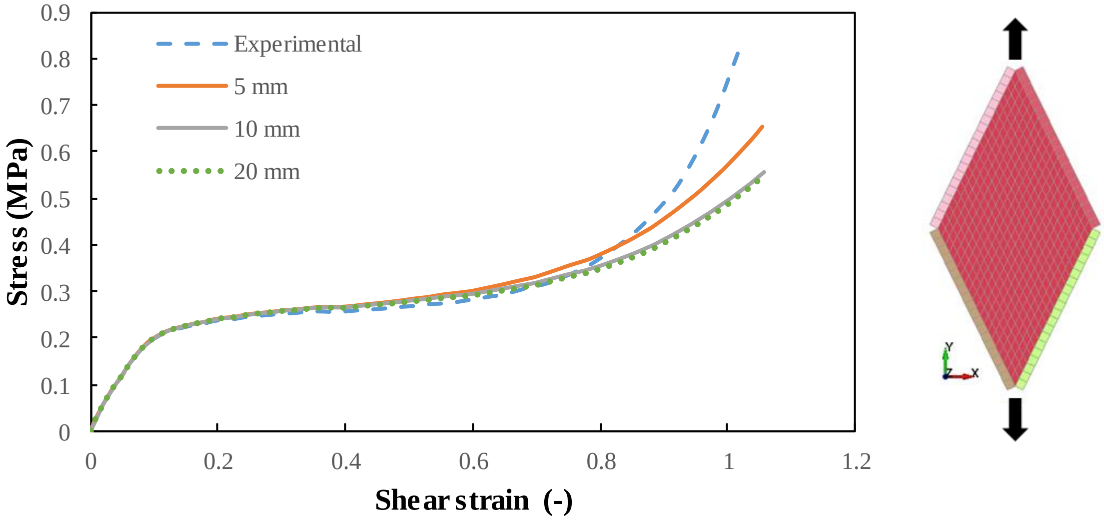

Figure 5.44. Picture frame test stress-strain data and corresponding data from numerical simulation employing material model MAT249 with different shell element sizes: 5mm, 10 mm and 20 mm.

DIC was used to compute local strain measurements, from a 32 mm by 32 mm region at the centre of the specimen, that were transformed to the material coordinates using CF orientations manually measured from test images. For all specimens, the DIC system was able to compute strains up to a shear angle of 38°. Thereafter, correlation was lost in part due to fibers originally on the fabric surface moving under the surface, effectively disappearing from the digital images. Another possible explanation is that the large deformation induced during the test could have exceeded the computational capacity of the system.

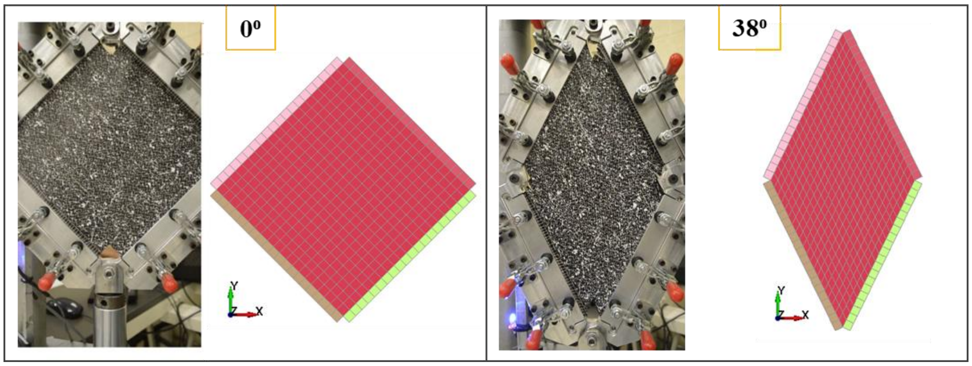

(a) (b)

Figure 5.45. Images of the PFT specimen and the corresponding FE simulation: (a) prior to loading, and (b) once a shear angle of 38° is achieved.

As seen in Figure 5.46, the numerical model was able to accurately predict the shear and transverse strains up to a shear angle of 15°, after which the simulation underpredicted the transverse strain and overpredicted the shear strain. Interestingly, in the case of the longitudinal strain, no correlation was obtained between the experimental and predicted data. The DIC system consistently produced a positive normal strain reading in the longitudinal direction; this was somewhat counterintuitive since no fiber extension was seen during the tests. However, this may be explained by the fact that the PFT fixture applies a bending moment to the fabric at the boundaries, as seen in Figure 5.47a, potentially stretching the CF tows. This has also been reported in prior studies on fabric shear deformation [86,93,145]. On the other hand, in the numerical simulation, the boundary of the specimen was defined by rotational friction-free nodes that apply no bending on the specimen, aligning with the theoretical pure shear deformation assumptions underlining the analysis of the PFT. Another possible explanation is that some of the local fabric deformations generated during the test, as seen in Figure 5.47b, were not taken into consideration in the computation of deformation by the 2D DIC system. The mathematical algorithm used by the 2D DIC system assumes no out-of-plane deformation takes place, and that surface continuity is maintained throughout the deformation [99].

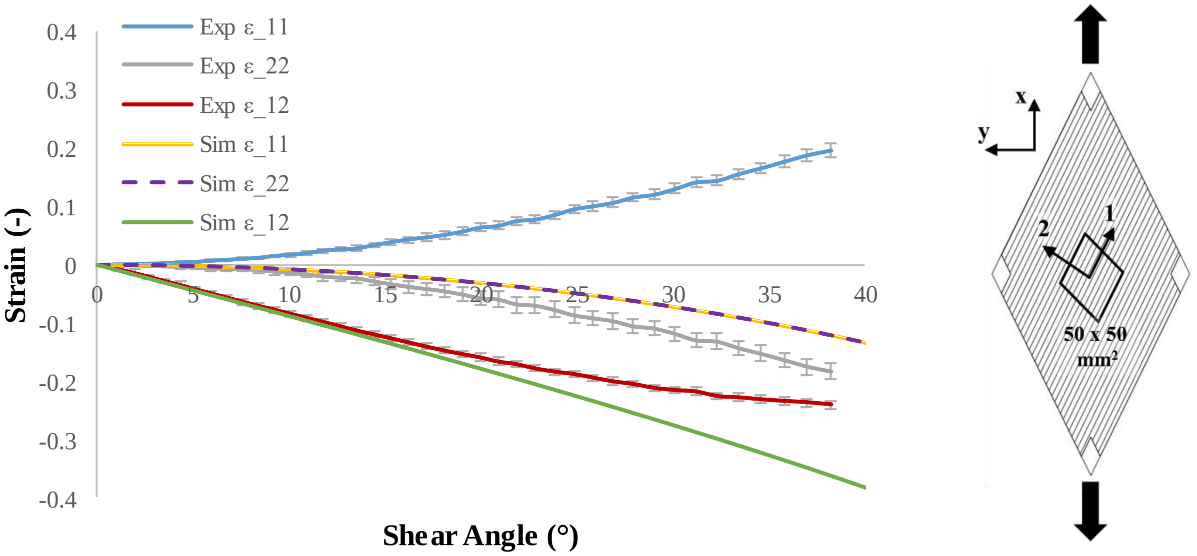

Figure 5.46: Experimental and simulation strain versus shear angle data of the PFT. The strains are reported in the material coordinates with ε11, ε22, and ε12 representing the longitudinal, transverse and shear strains, respectively.

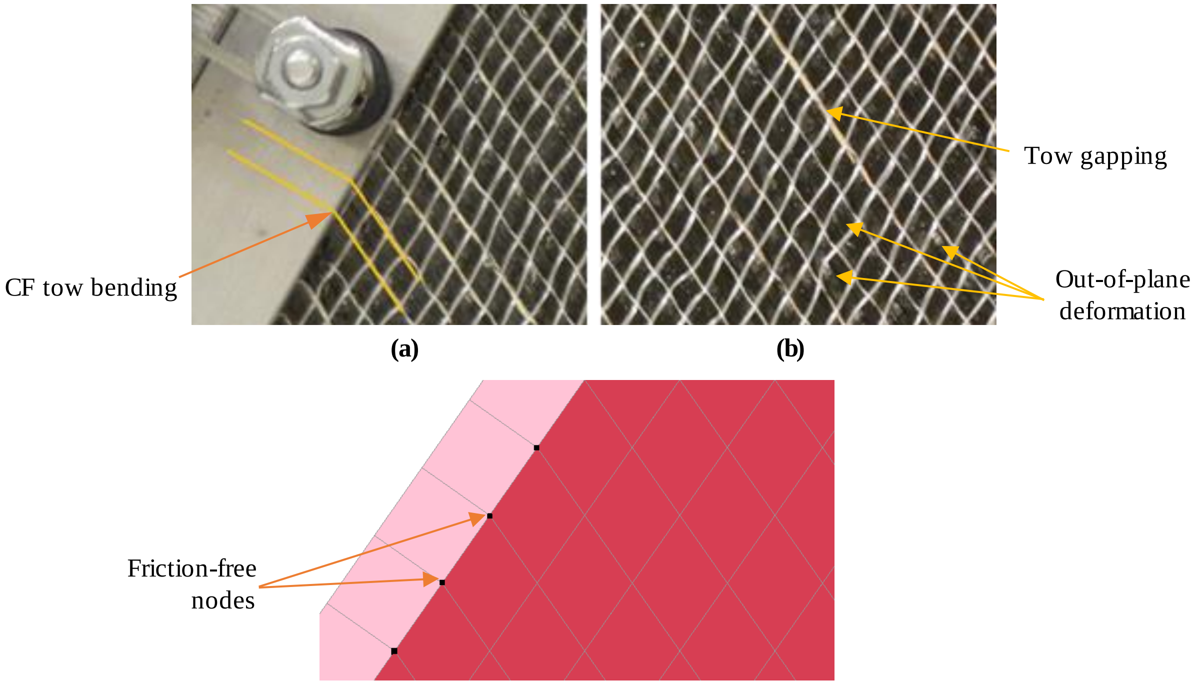

(a) (b)

(c)

Figure 5.47. (a) Local bending of carbon fiber tows close to the clamped boundaries. (b) UD-NCF deformations seen during the PFT not considered in the numerical simulation. (c) Friction-free nodes defined at the boundary of the PFT numerical simulation.

As shown in Figure 5.48, the numerical model overpredicted the fabric force-displacement response. The weak correlation motivated the search for an alternative approach. Thus, the 45° off-axis test was subsequently considered to model the fabric shear response.

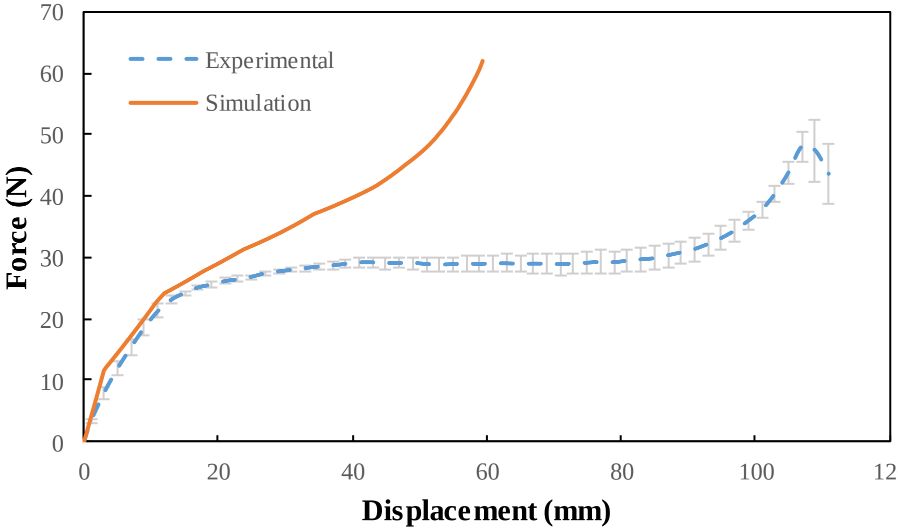

Figure 5.48. Experimental and simulation prediction of the force response during the picture frame test.

5.2.2.2. Simple shear calibration approach – 45°-off-axis extension test

The simulation results using the simple shear approach introduced by Pourtier et al. [96] and the 45° off-axis extension test data for calibration are presented here. The model described in section 4.2.3 was used.

First, a mesh sensitivity analysis was conducted to examine the most efficient shell element size for the simulation. As seen in Figure 5.49, up to 6 mm of applied displacement, there were no significant differences between the force predictions for element sizes in the range of 3 to 6 mm, with all the predictions falling within the scatter of the experimental data. Beyond 6 mm of applied displacement, the predictions began to diverge with a tendency of the simulations with larger elements to over predict the force-displacement response the most. The 5 mm and 6 mm shell elements originally became unstable as the displacement approached 32 mm displacement. After incorporating mass damping, with a Rayleigh damping coefficient of 0.03, the simulation was stabilized. The 4 mm element size was chosen for all subsequent simulations since it yielded an appropriate force prediction with reasonable processing time and a stable simulation. The tendency of the simulation model to overpredict the force-displacement response could be explained, among other factors, by the inability of the model to account for sliding of the GFs that are clamped at one end of the specimen and free at the other end.

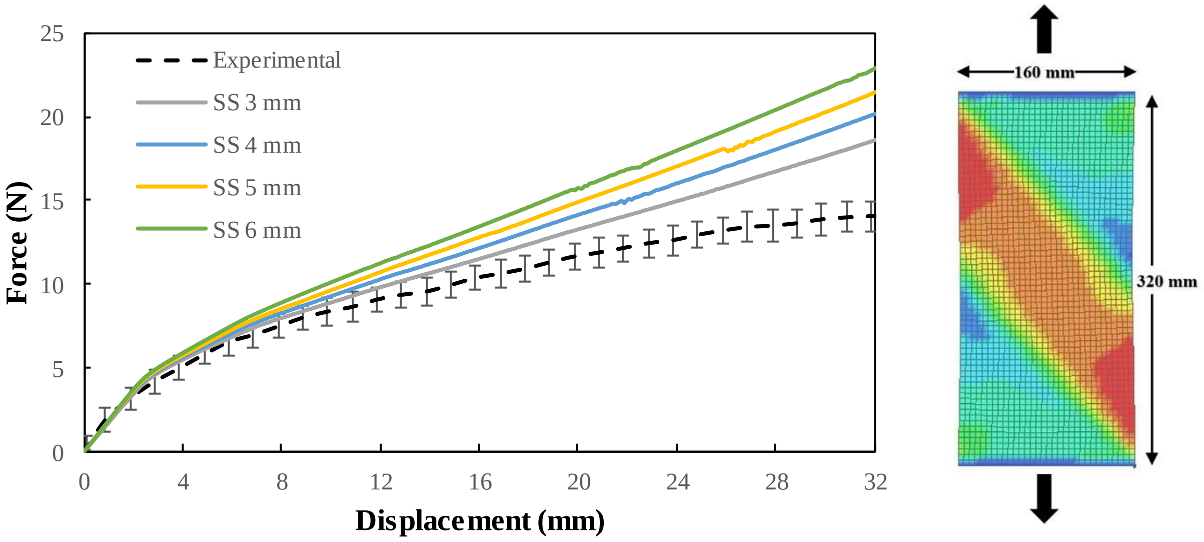

Figure 5.49. Experimental and simulation force-displacement results and mesh sensitivity analysis of 45° off-axis extension test simulation using 3 mm, 4 mm, 5 mm, and 6 mm mesh sizes.

The strain contours with respect to the global coordinate system measured during experiments using DIC and the corresponding simulation predictions for a displacement of 20 mm are presented in Figure 5.50. Significant differences were found between the strain measured by the DIC system and the predictions of the simulation. Broadly speaking, the numerical model underpredicted the magnitude of most in-plane strains. As evidenced in Figure 5.50, the predicted shear strain near the centre of the specimen was only 6%

of the experimental value. The normal strain predictions were slightly better with the numerical model predicting 35% of the experimental normal strain parallel (ε_{xx}) and perpendicular (ε_{yy}) to the loading direction. The reasons for the variations between the experimental and simulation strain maps may be similar to the ones examined in the study of the PFT. As shown in Figure 5.20, there were local deformation modes, such as stitching distortions and intertow gapping that were observed during the 45° off-axis extension test and were not considered in the numerical simulation, while the same local deformation modes increased the amount of decorrelation in the DIC images potentially causing errors in measuring strain during the tests. Nonetheless, as observed in Figure 5.50, the model was able to predict the different strain zones along the length of the specimen, as well as the overall deformation of the specimen.

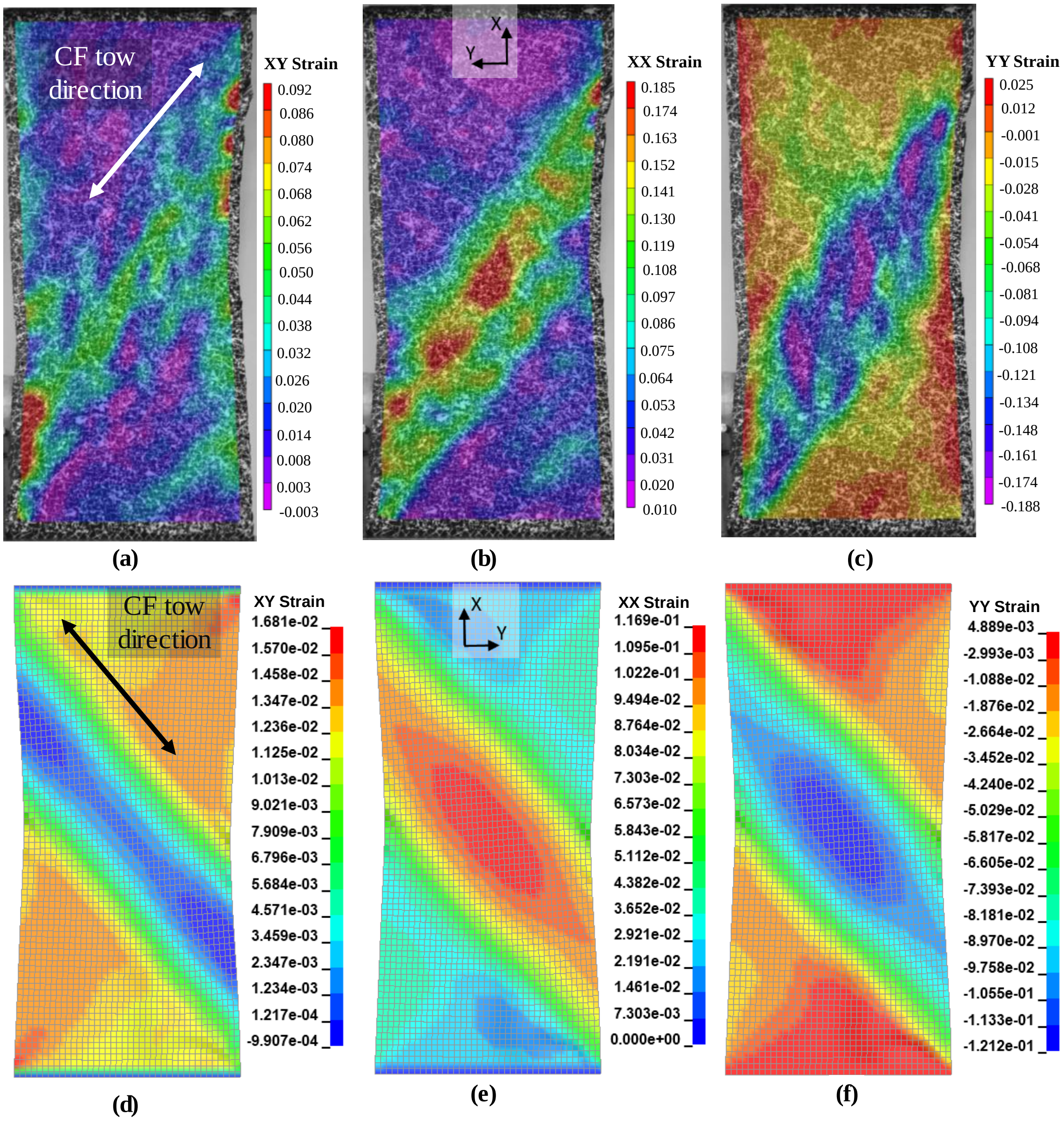

Figure 5.50. Experimental and simulation strain contour plots of the 45° off-axis extension test at a displacement of 20 mm, where (a and d) show the shear strain (ε_{xy}), (b and e) the normal strain in the loading direction (ε_{xx}) and (c and f) the normal strain transverse to the loading direction (ε_{yy}).

Average strain values from three experimental tests were extracted using DIC from a 32 mm by 32 mm area in the middle of the 45° off-axis extension test specimens. The experimentally obtained and predicted normal strains parallel to the loading direction, transverse to the loading direction and shear strains are respectively compared in Figures 5.51, 5.52 and 5.53. When averaging the strain values at the centre of the specimen it was found that the numerical simulation was able to more accurately predict the normal strain in the direction of loading, ε_{xx}. On the other hand, the normal strain perpendicular to the loading direction, ε_{yy}, did not correlate as closely but still fell within the standard deviation of the experimental results, as seen in Figure 5.52. Regarding the shear behaviour, shown in Figure 5.53, a good correlation was observed up to approximately 10 mm, after which the simulation largely underpredicted the shear behaviour of the fabric. This finding was unexpected since the previous force-displacement prediction matched rather well with the experimental data over the same applied displacement range. This reveals that the calibrated model is able to predict macroscale in-plane fabric deformation; however, it has limitations when predicting the local deformation of the fabric. Also, as previously indicated the accuracy of the measured strains using DIC during the tests should be considered.

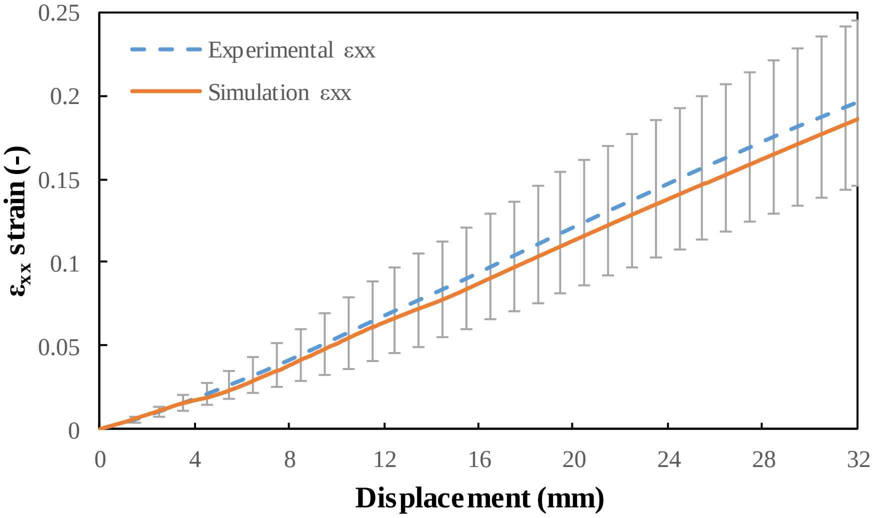

Figure 5.51. Strain ε_{xx}-displacement response for 45° off-axis extension tests and corresponding simulation prediction. Note that ε_{xx} corresponds to the normal strain in the direction of loading.

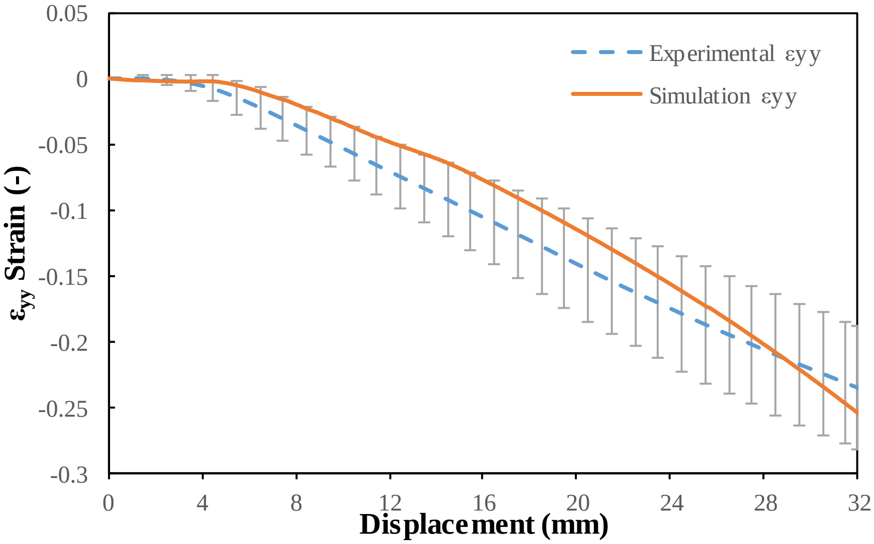

Figure 5.52. Strain ε_{yy}-displacement response for 45° off-axis extension tests and corresponding simulation prediction. Note that ε_{yy} corresponds to the normal strain parallel to the direction of loading.

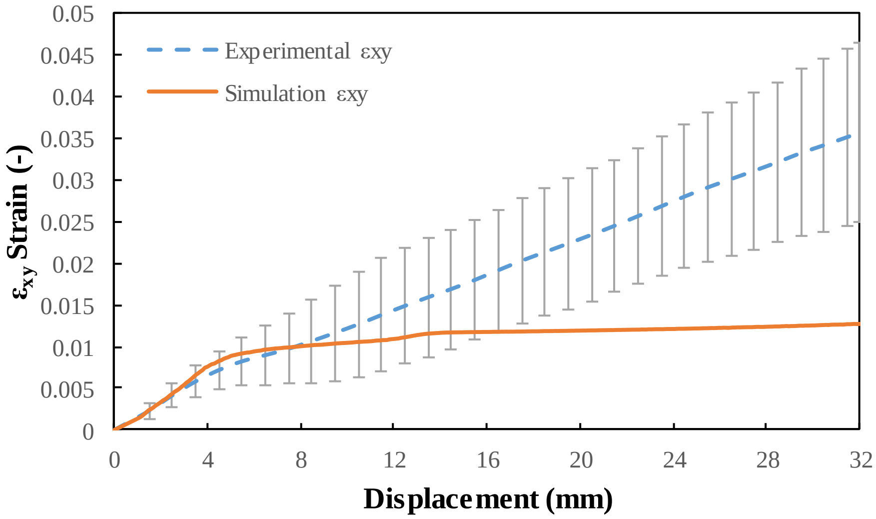

Figure 5.53. Strain ε_{xy}-displacement response for 45° off-axis extension tests and corresponding simulation prediction. Note that ε_{xy} corresponds to the shear strain in the global coordinate system.

According to the LS-DYNA manual [137], the material properties of each fiber family are defined independently, and the interaction between the fiber families is defined through the shear input properties. To confirm the ability of the model to predict the interaction between the CF and GF fiber families, the predicted shear angle and shear stress were compared to experimental results, as seen in Figure 5.54 and 5.55. Although the simulation was able to accurately predict the shear angle between the two fiber families, thus adequately capturing the fabric shear deformation response, it overpredicted shear stress. Similar to the force response prediction shown in Figure 5.48, the higher stress prediction could be the result of the inability of the material model to account for localized fabric component interactions observed during the physical testing, such as sliding of GFs that are unclamped at one of their ends. It should be noted that previous studies typically report calibration of constitutive models based on the fabric macroscopic deformations and do not report local strains [16,51,73].

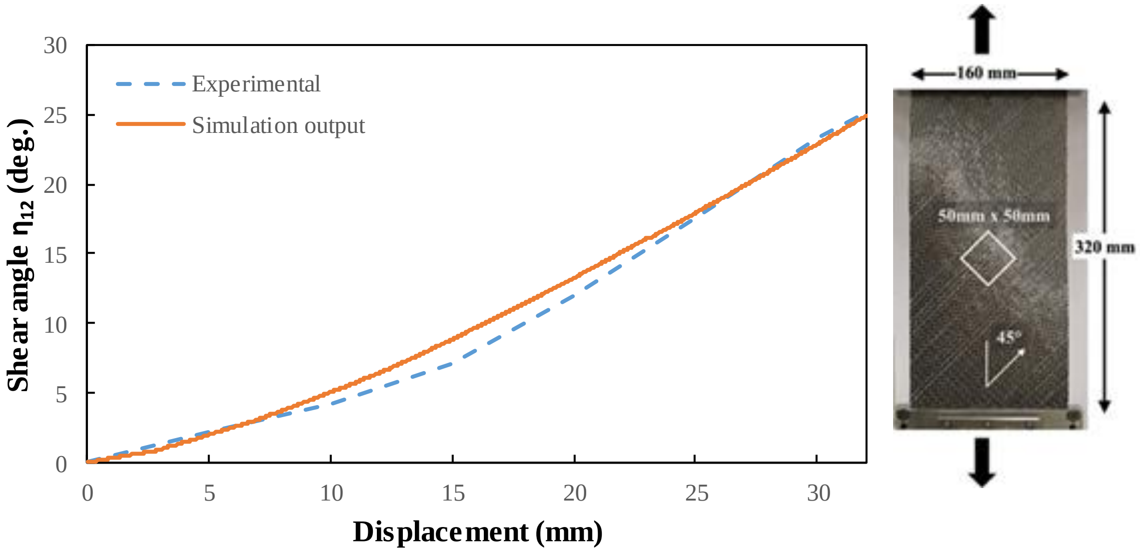

Figure 5.54. 45° off-axis extension test relationship between shear angle, between the fiber families 1 and 2, and displacement for an experimental test and corresponding simulation prediction.

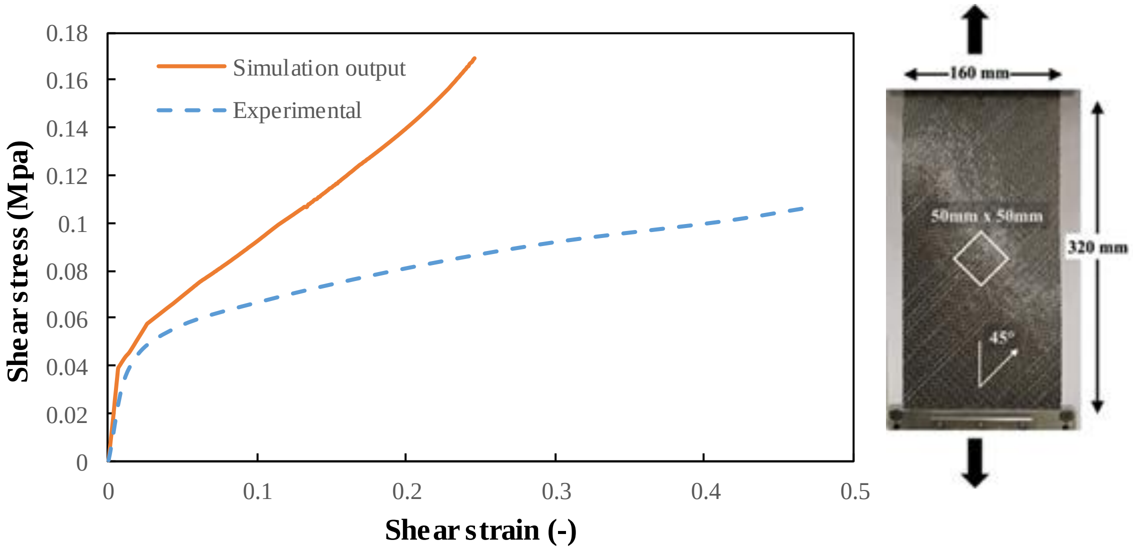

Figure 5.55. Shear stress-strain response for a 45° off-axis extension test and corresponding simulation prediction.

5.2.3. Bending Calibration – Cantilever bending test

The material model bending behaviour can be controlled in the simulation model by adjusting the transverse shear modulus, G_t [29]. The model described in Section 4.2.4 was used. Initially, an average of the bending modulus of the fabric with the stitching side up and with the stitching side down was used to calibrate the model. Using this experimentally obtained value, the model predicted bending stiffness was overestimated for both, the longitudinal and transverse directions (Figure 5.56). Using the experimentally obtained values, the through-thickness transverse shear modulus in the longitudinal direction, G_{31}, was set to 93.9 MPa. As seen in Figure 5.56, using the shell element default configuration with three integration points across the thickness and even weight distribution (1/3, 1/3 and 1/3) among the integration points resulted in an overprediction of the bending stiffness in the longitudinal direction. It was evidenced that as the weight distribution shifted towards the middle, the bending stiffness decreased. The weight balance of the three through-thickness integration points was modified to 2/9, 5/9 and 2/9 each to adjust the stiffness of the predicted bending behaviour to match experimental results. Additionally, to the weight distribution, varying the location of the integration points through the shell element thickness also altered the bending response of the material model. In LS-DYNA, the integration point location is based on a local coordinate system where the bottom and top surfaces have respective coordinates of -1 and +1, and the element centreline is the reference location. Figure 5.57 shows the effect that varying the location of the integration points with respect to the centreline, using variables y_1, y_2 and y_3 to adjust the bending response of the material. Finally, regarding computational times, the 2 mm element size simulation took 108 minutes to complete, while the 4 mm and 8 mm element size simulations were processed in 14 and 2 minutes, respectively. An element size of 4 mm was chosen as a good compromise between accuracy and computational speed for the cantilever test.

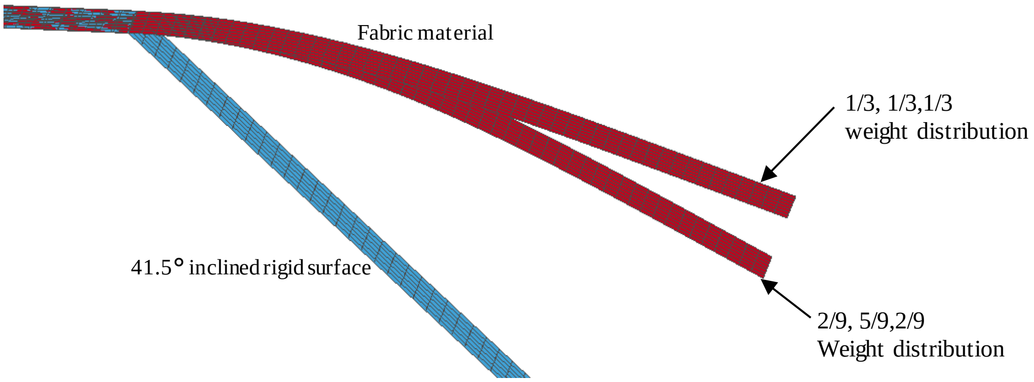

Figure 5.56. Prediction of the cantilever test simulation in the longitudinal fabric direction showing the effect of changing the weight distribution of the through-thickness integration points on the bending response of the fabric material model.

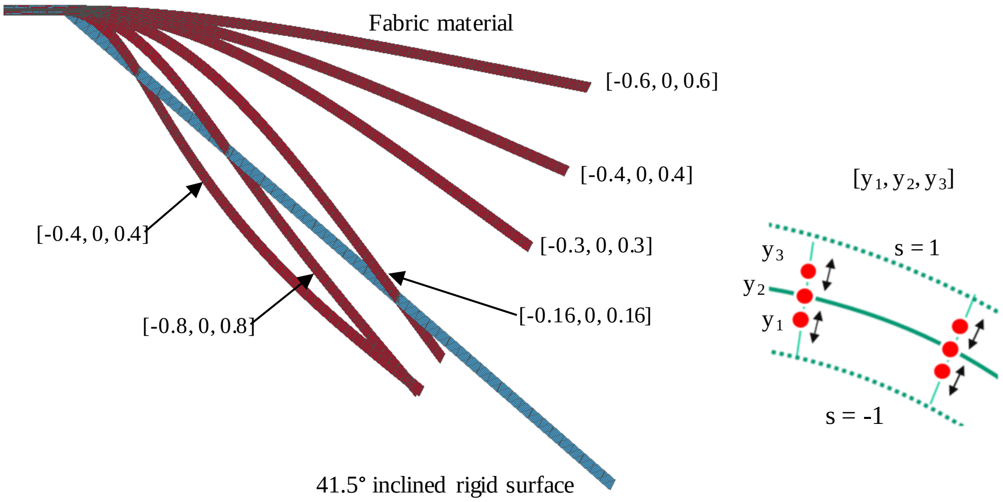

Figure 5.57. Prediction of the cantilever test simulation in the longitudinal direction showing the effect of changing the location of the through-thickness integration points on the bending response of the fabric material model.

Balancing the integration point weight distribution and location to find a suitable combination that matches the physical cantilever experiments is an approach for calibration of out-of-plane deformation recommended in [146]. Some advantages of this approach include the ability to define a fixed ratio between and in-plane and out-or plane stiffness, as well as ease of implementation [146]. A satisfactory correlation between the cantilever test and simulation result was found using an integration point weight distribution of [21/50, 8/50, 21/50] and integration point local coordinates of [-0.2, 0, 0.2] (Figure 5.58). Figure 5.59c compares images of the experimental and numerical results of the cantilever tests in the longitudinal direction. Overlaying their corresponding images shows a close match between the experimental and numerical responses.

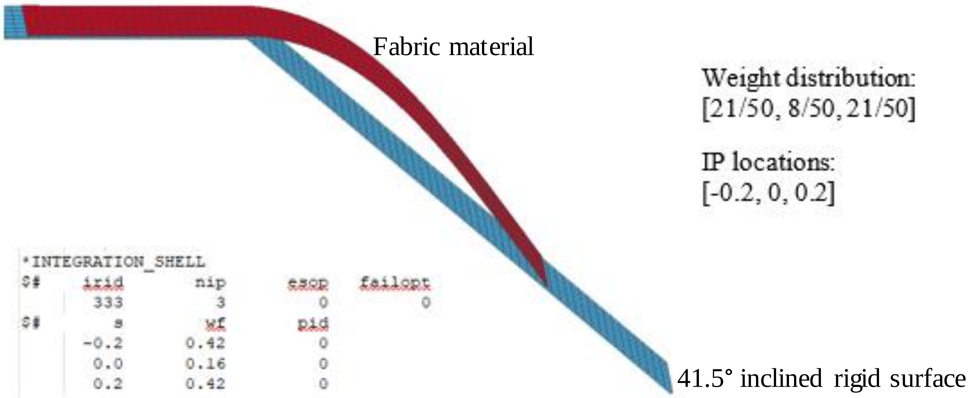

```
*INTEGRATION_SHELL
$#      irid         nip         esop   failopt
         333           3            0         0
$#         s          wf          pid
        -0.2        0.42            0
         0.0        0.16            0
         0.2        0.42            0
```

Figure 5.58. Bending stiffness calibration results by modifying the through-thickness properties of shell element integration points using LS-DYNA 'integration shell' function.

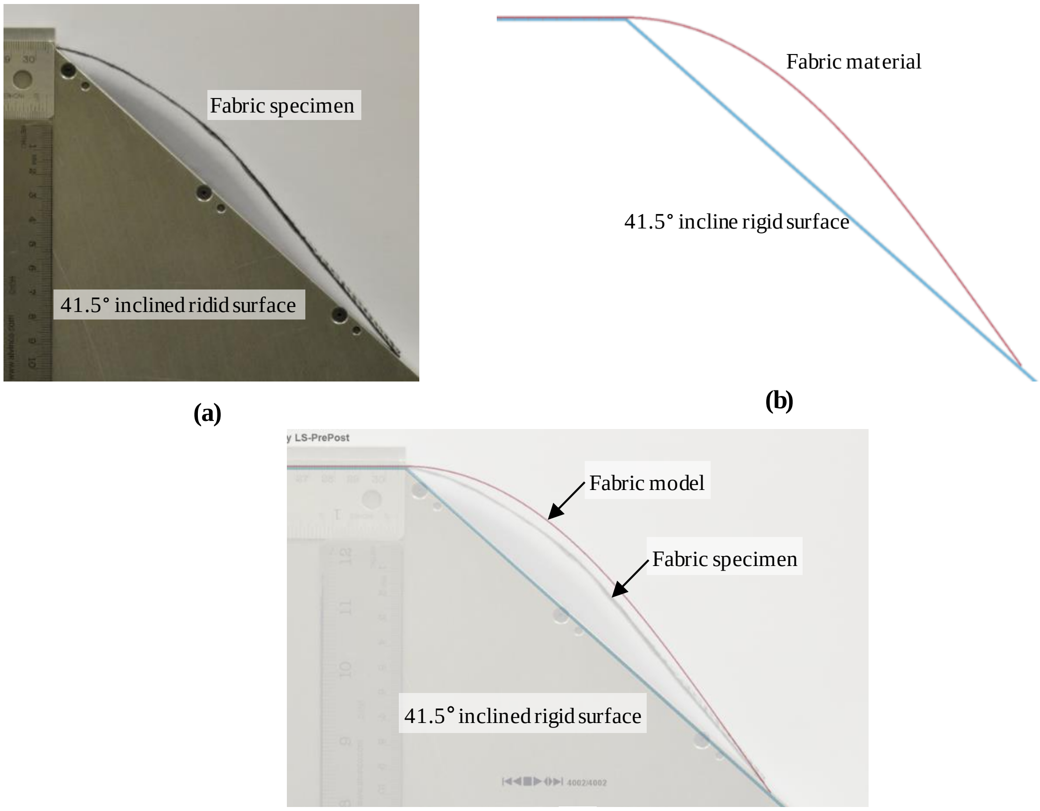

(a)

(b)

(c)

Figure 5.59. Images of (a) experimental and (b) numerical simulation results of the cantilever test in the longitudinal fabric direction. Image (c) shows an overlay of both images for visual comparison.

Similar to the longitudinal direction, the bending stiffness in the transverse direction was adjusted by setting the through-thickness transverse shear modulus, G_{23}, to a suitable value to achieve a good correlation with the experimental behaviour. The most suitable value of G_{23} was 1.0 MPa, which produced the behaviour observed in Figure 5.60b while keeping the same configuration of integration points previously achieved through the calibration of the longitudinal bending behaviour. As shown in Figure 5.60c, a good agreement was obtained between the experimental and simulation response.

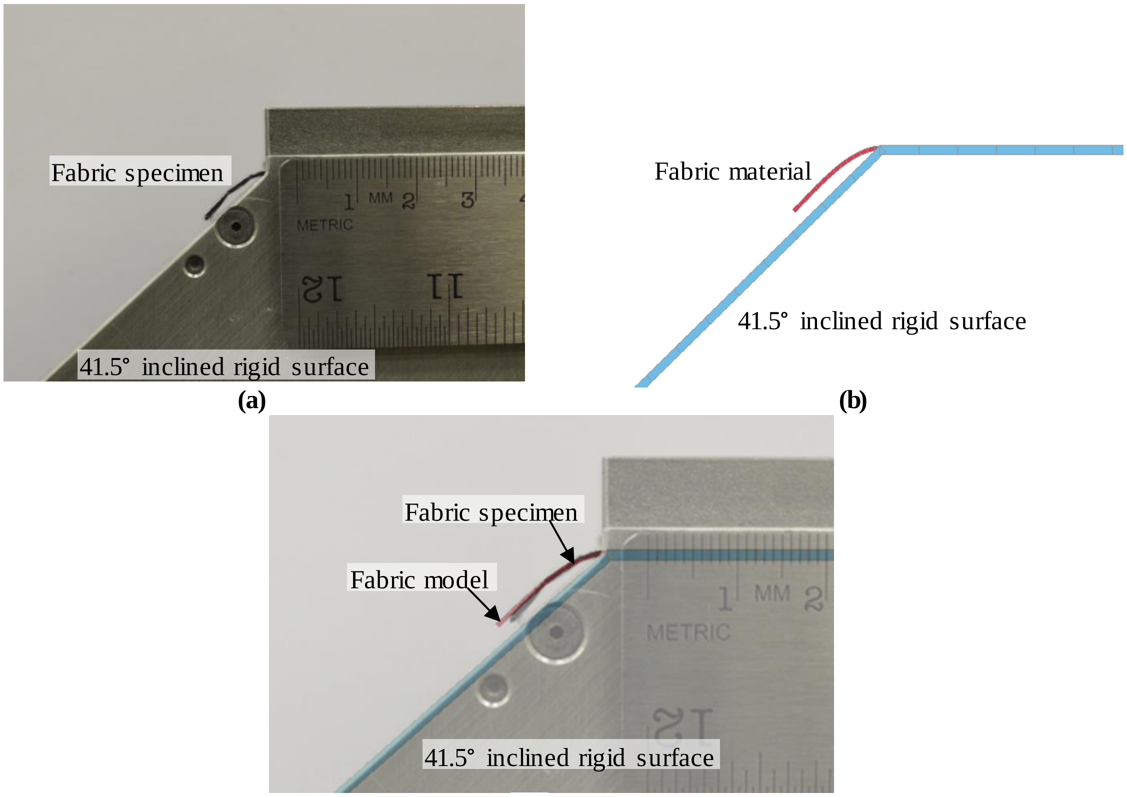

(a) (b)

(c)

Figure 5.60. Images of (a) experimental and (b) numerical simulation results of the cantilever test in the transverse fabric direction. Image (c) shows an overlay of both images for visual comparison.

5.2.4. Summary of calibration parameters

The calibration verification presented in the previous sub-sections led to the final calibration parameters required for MAT249, which were based on experimental data used in the predictions presented in Figures 5.37, 5.40, 5.44, 5.55, and 5.58. A summary of the material model parameters used for subsequent simulations is presented in Tables 2 – 6. It should be noted that the shear response of the fabric was calibrated using the 45° off-axis extension test since it produced force-displacement predictions closer to experimental values than the PFT calibration.

Table 5.2. Longitudinal normal tensile stress-strain data implemented in the calibration of MAT249.

Strain (-)	Stress (MPa)
0	0
0.0005	1.61
0.001	9.60
0.004	75.00
0.104	620.00

Table 5.3. Transverse normal tensile stress-strain data implemented in the calibration of MAT249.

Strain (-)	Stress (MPa)
0	0
0.02	0.039
0.02341	0.06707
0.02738	0.21873
0.02977	0.4977
0.04565	5.5858
0.04962	6.27361
0.14962	23.6

In-plane shear behaviour was modeled using option METH11 in MAT249. This option requires to set an initial linear shear stiffness, followed by a data-defined non-linear region and a final linear response specified after a certain locking angle. Tables 4, 5 and 6 present the calibrated values implemented to describe shear behaviour of the material model.

Table 5.4. In-plane shear parameters used in the calibration of MAT249, METH11 formulation.

In-plane shear properties	
Initial linear stiffness:	4.82 MPa
Non-linear region initial stress:	0.064328 MPa
Locking angle:	1 rad
Locking stiffness:	0.232 Mpa

Table 5.5. Shear stress-strain data implemented to describe the non-linear region required in MAT249 option METH11.

Non-linear Shear Response

Normalized Strain (-)	Shear Stress (MPa)
0	0.064328
0.031285	0.092892
0.095783	0.112095
0.189673	0.127294
0.287926	0.140337
0.401932	0.153712
0.460073	0.167044
1	0.290851

Table 5.6. Transverse shear stiffness implemented in MAT249.

Transverse shear stiffness	
G_{13}	93.9 MPa
G_{23}	1.0 MPa

5.3. Evaluation of the Constitutive Model

The ability of the calibrated material model MAT249 to predict the behaviour of the UD-NCF was investigated. Two independent off-axis extension tests with 30° and 60° fabric biases were conducted and simulated (Sections 5.3.1 and 5.3.2). As a final step, hemispherical tests were performed on the fabric and used to validate the corresponding draping simulation FE model (Section 5.3.3).

5.3.1. 30° off-axis extension test and numerical simulation results

The simulation model developed for the 30° off-axis extension test was the same as the one used for the 45° off-axis-extension test with an adjusted bias fabric angle (see model details in section 4.2.3). The experimental and predicted force-displacement response are shown in Figure 5.61. One simulation prediction corresponds to the material model whose shear response was calibrated using the 45° off-axis-extension test data and the other using the PFT test. Both predictions overestimated the force magnitude when compared to experimental force values. Also, as seen in Figure 5.61b, the fabric wrinkled significantly in the out-of-plane direction producing non-physical instabilities in the simulation that manifested in the force-displacement data as noise.

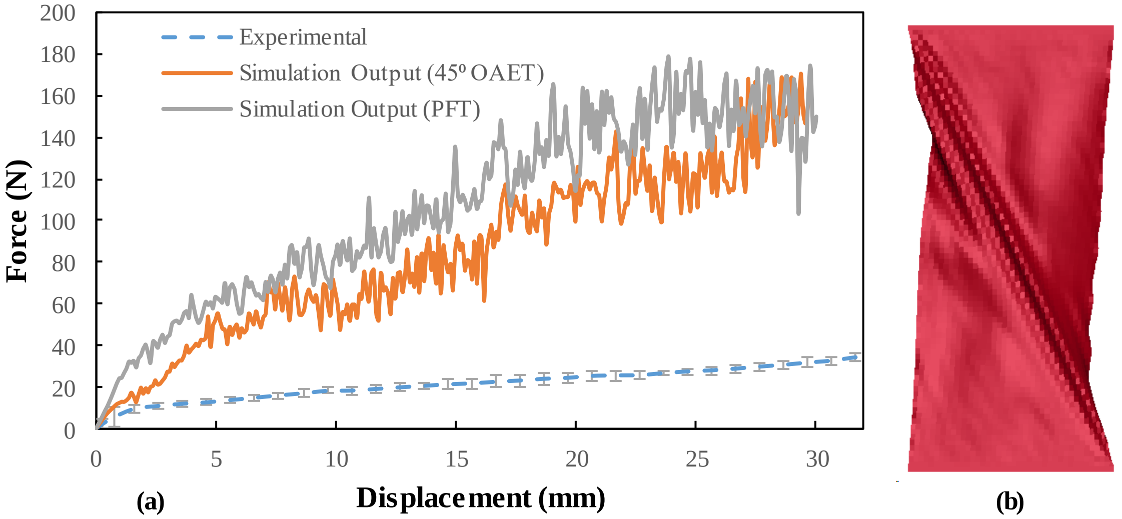

(a) (b)

Figure 5.61. (a) 30° off-axis extension test force-displacement experimental data and corresponding output data from numerical simulation employing two different shear behaviour calibration methods: the 45 off-axis extension test and the PFT shear calibration. (b) Wrinkling observed in the simulation specimen at 20 mm displacement.

As revealed by the deformation of the square geometry printed on the fabric shown in Figure 5.62, during the 30° off-axis extension test, the fabric endured a combination of macroscopic transverse compressive and shear deformations. It was also observed that decreasing the biased angle from 45° to 30° increased the extent of intertow sliding and compression. Figure 5.63 provides a closer look into the deformation of the stitching, revealing that similar to the 45º off-axis extension test, intertow sliding stretches the stitching inducing individual CF tow compression that results in intertow gapping. Figure 5.64 and Figure 5.65 show the GF side of the fabric during the 30º off-axis extension test, showing a similar macroscopic deformation as seen on the 45º off-axis extension test, except with more intertow sliding. Examining the GF side more closely in Figure 5.65 shows that the CFs on the surface of the fabric tended to bulge and crimp out-of-plane more than on the stitching surface of the fabric. The main reason for this seems to be the compression force applied by the stitching combined with a lack of tension on the transverse GFs. These local deformations were more severe than in 45º off-axis extension tests due to more pronounced intertow sliding, especially in the middle of the specimen or area demarked by the white square. These local deformation modes were not accounted for in the macroscopic material model, therefore, generating the discrepancies between the experimental results and the numerical predictions.

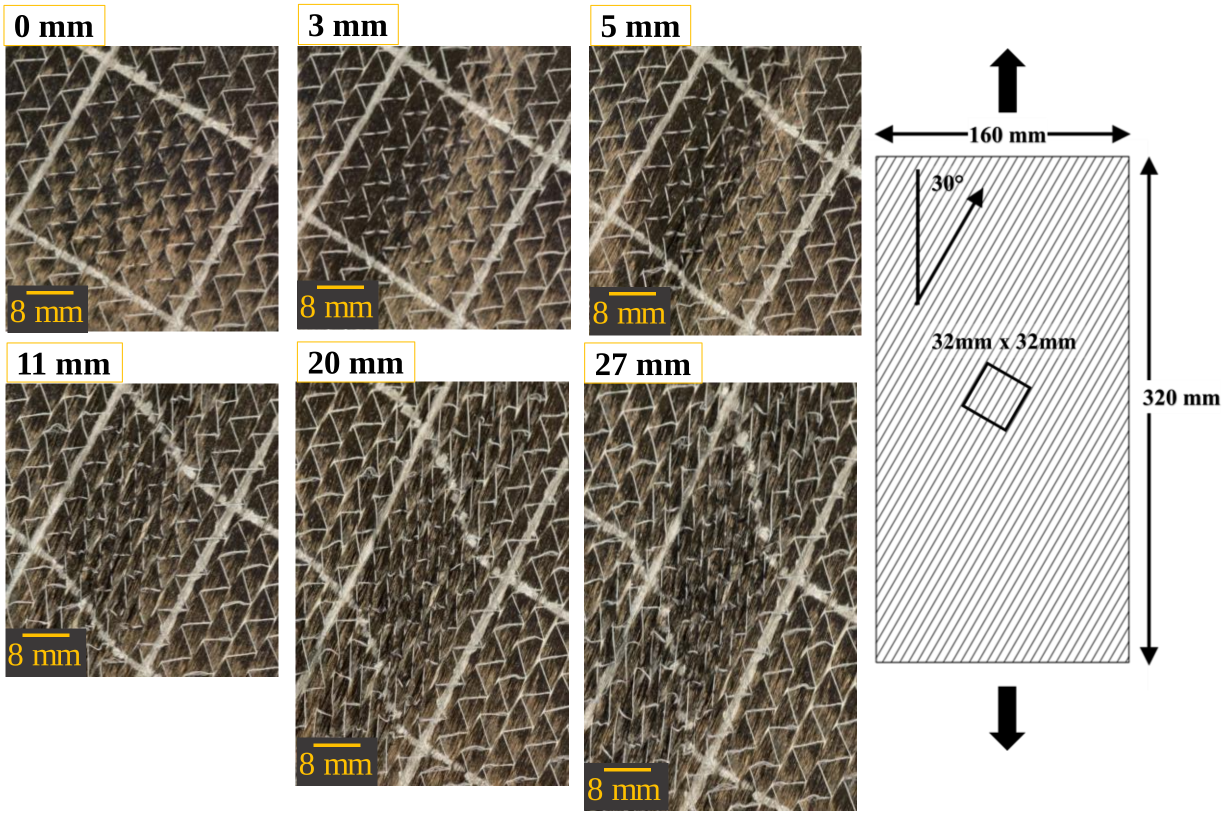

Figure 5.62. 30º off-axis extension test images of the fabric stitching side at progressive displacements: 0, 3, 5, 11, 20 and 27 mm.

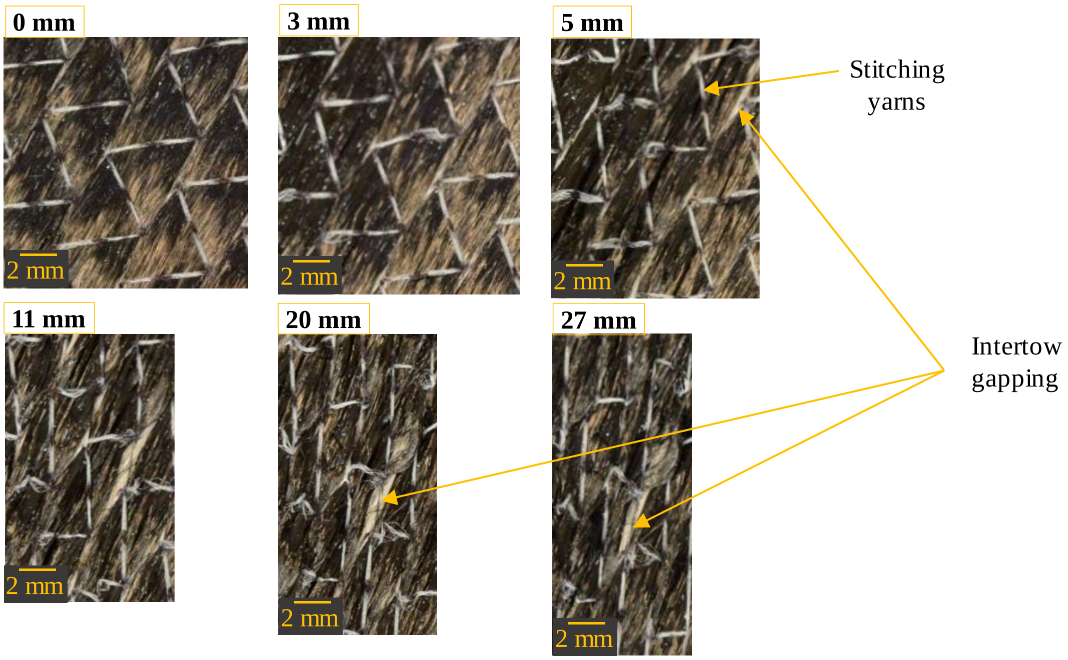

Figure 5.63. 30º off-axis extension test close-up images of the fabric stitching side at progressive displacements: 0, 3, 5, 11, 20 and 27 mm.

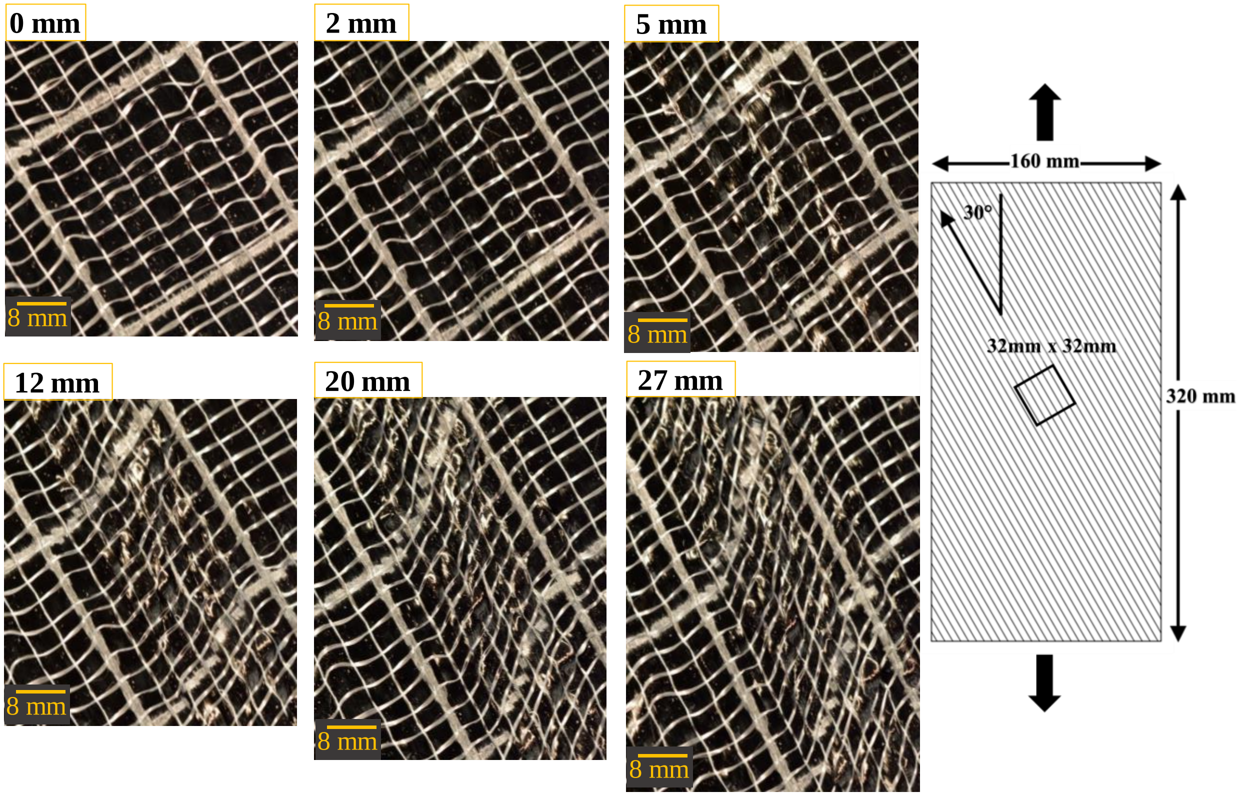

Figure 5.64. 30º off-axis extension test images of the fabric glass fiber side at progressive displacements: 0, 2, 5, 12, 20 and 27 mm.

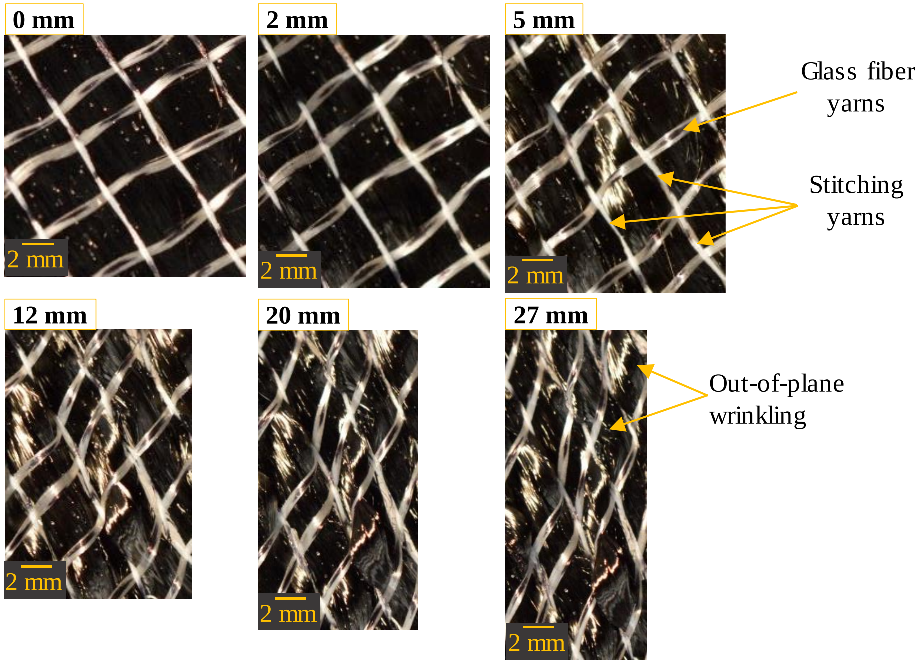

Figure 5.65. 30º off-axis extension test close-up images of the fabric glass fiber side at progressive displacements: 0, 2, 5, 12, 20 and 27 mm.

Figure 5.64 shows the strain contour plots during the 30º off-axis extension test, gathered through DIC, and their corresponding simulation predictions. The numerical model was able to predict the different strain zones seen in the experimental results, including the concentration of deformations in the diagonal parallel to the CF fibers. However, significant differences were found between the strains reported by the DIC system and the predictions of the simulation. The simulation underpredicted the two normal strains, with respective values of, 52% and 63% of the experimental results for ε_{xx} and ε_{yy}. In contrast, 20% of the magnitude of shear strain, ε_{xy}, was predicted by the model. The underprediction was caused by the inability of the simulation to represent intertow sliding and compression of the CF tows by the stitching, as evidenced in Figure 5.20 and 5.21. As shown in Figure 5.62, wrinkling transverse to the CFs was present during the experimental test, however, to a lower degree than in the simulations. This may be due to the bending stiffening effect that in-plane tensile strains had in the real fabric and was not incorporated into the material model. It is important to note that in the 30º off-axis extension test the magnitude of shear strains increased compared to the 45º off-axis extension test, suggesting that fabric shear response directly correlates with intertow sliding in the fabric. The inability to account for this interaction between shear and extensional strains is another limitation of the numerical model. One potential reason for the strain underprediction by the model is its inability to represent inter-tow sliding, which was observed during physical experiments (Figure 5.18).

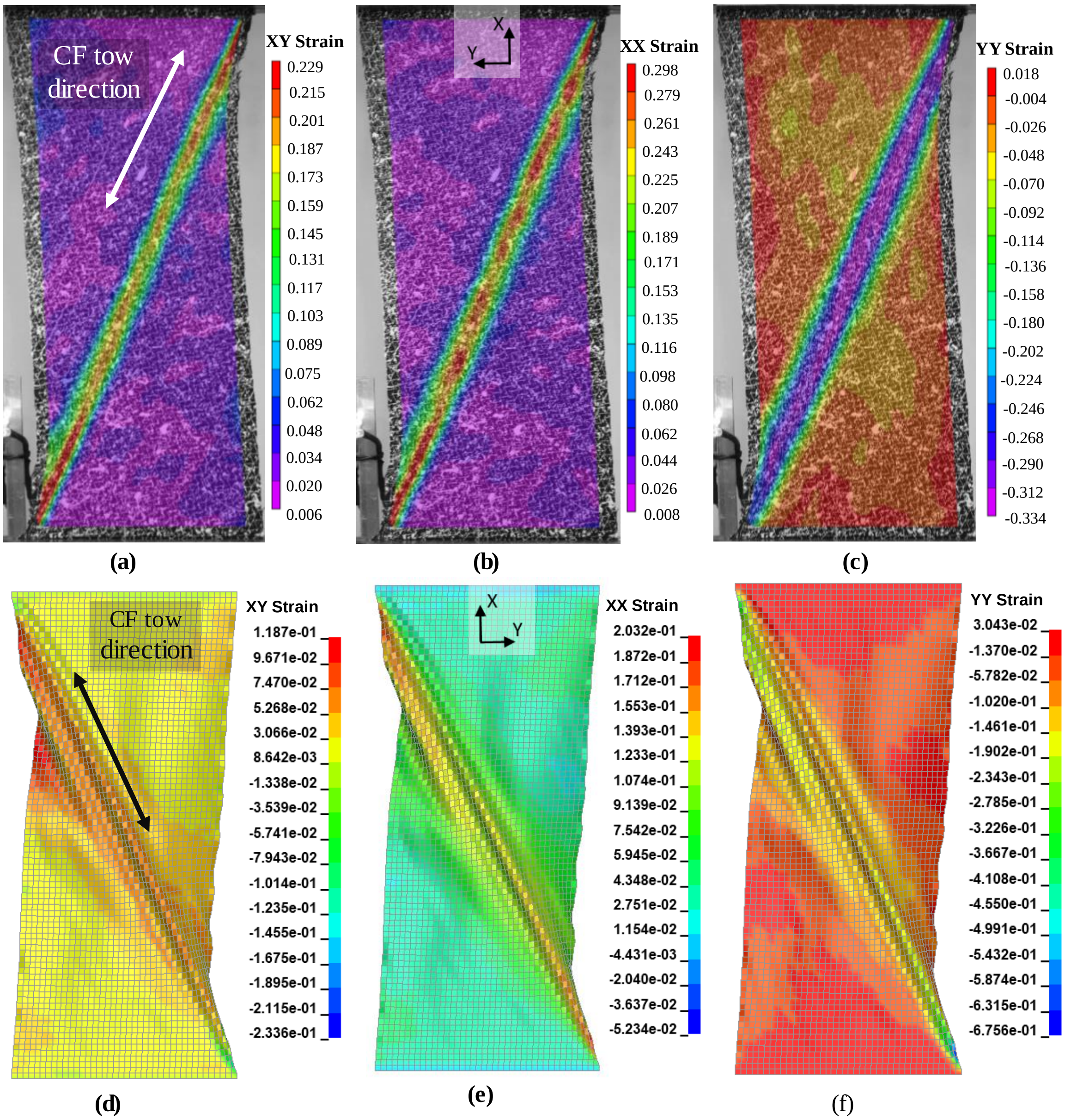

Figure 5.66. Experimental and simulation strain contour plots of the 30º off-axis extension test at a displacement of 20 mm, where (a and d) shows the shear strain (ε_{xy}), (b and e) the normal strain in the loading direction (ε_{xx}) and (c and f) the normal strain perpendicular to the loading direction (ε_{yy}).

5.3.2. 60° off-axis extension test and numerical simulation results

The simulation model developed for the 60° off-axis extension test was the same as the one used for the 45° off-axis-extension test with an adjusted bias fabric angle. The experimental and predicted force-displacement response are presented in Figure 5.67. The two predicted profiles correspond to the material model calibrated using 45° off-axis-extension test data and the PFT. The simulation calibrated with the 45°

off-axis extension test was able to accurately predict the force-displacement response up to a displacement of approximately 12 mm. In contrast, the PFT calibrated model satisfactorily predicted force-displacement up to an imposed displacement of 5 mm. Afterwards, the response was largely overestimated by both simulations compared to the experimental data.

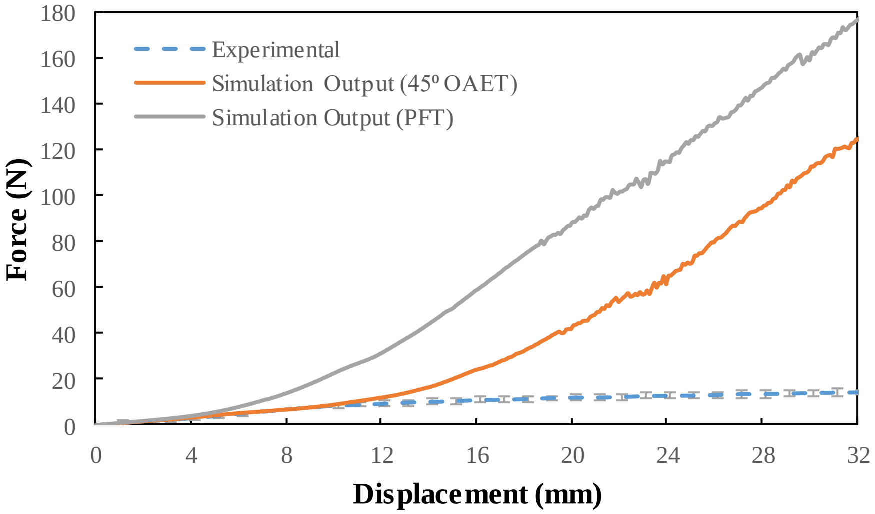

Figure 5.67. Average experimental results of 60° off-axis extension test and simulation prediction.

Figures 5.68 and 5.69 show the fabric deformation in a 32 mm by 32 mm square marked in the centre of the specimen. Tracking of the deformation as applied displacement increases reveals that the macroscopic deformation of the fabric is characterized by transverse tensile, longitudinal compression and shear superimposed deformation modes. Compared to the local deformations seen in the 45° off-axis extension test, there was less intertow sliding but more intertow gapping due to the larger transverse extension component and strong tensioning of the stitching. Intertow gapping was another deformation mode that was not accounted for in the macroscale numerical model.

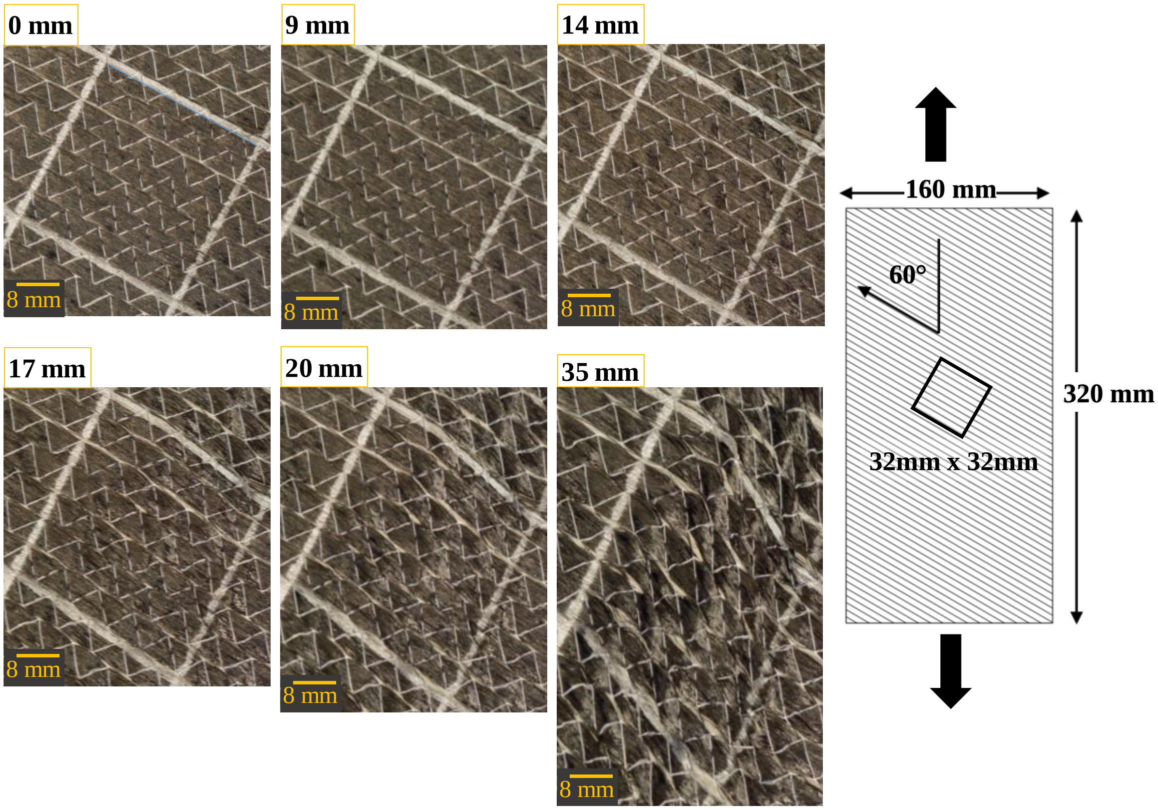

Figure 5.68. 60º off-axis extension test images of the fabric stitching side at progressive displacements: 0, 9, 14, 17, 20 and 35 mm.

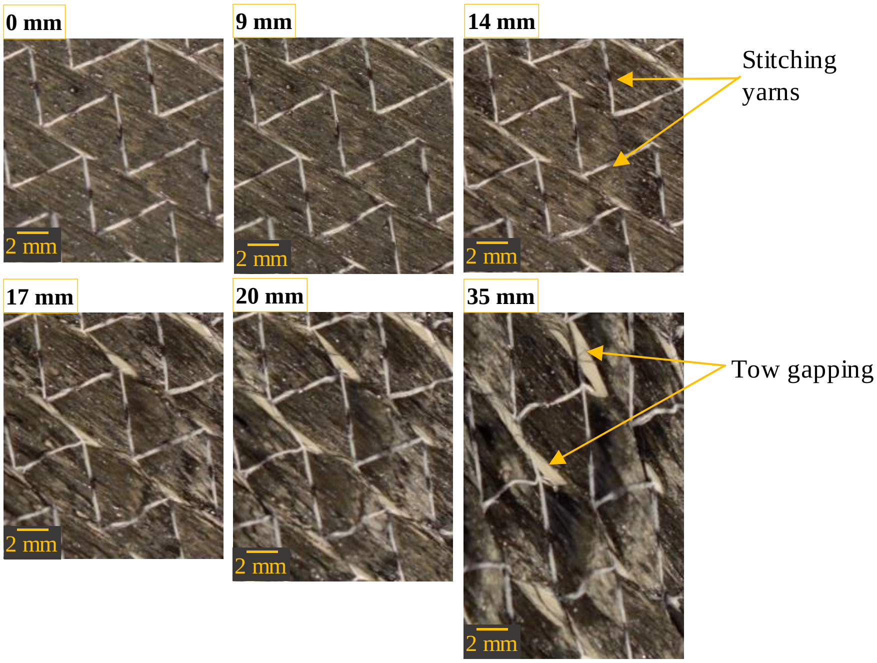

Figure 5.69. 60º off-axis extension test close-up images of the fabric stitching side at progressive displacements: 0, 9, 14, 17, 20 and 35 mm.

Figure 5.70 shows the fabric normal and shear strains during the 60º off-axis extension test extracted with DIC at a displacement of 20 mm and the corresponding simulation predictions. Once more, the numerical model underpredicted all strains; however, this time, the predictions were closer to the experimental values. Focusing on the centre of the specimen, the simulation predicted 90%, 65% and 87% of the experimental strains ε_{xx}, ε_{yy}, and ε_{xy}, respectively. Likewise, the numerical model accurately predicted the different strain zones, including the location and orientation of the regions of large strains, which was not found the 30° off-axis extension tests. The improved prediction ability of the numerical model, compared to the previous two off-axis extension tests with distinct fabric biased angles, may be explained by the fact that intertow sliding was less pronounced in the 60° off-axis extension angle since the specimen deformation was more closely associated with the transverse tensile deformation, which was independently calibrated. In contrast to the 30º off-axis extension test, the magnitude of shear strain decreased compared to the 45º off-axis extension test, representing further evidence that the shear response of UD-NCFs is coupled to extensional deformation.

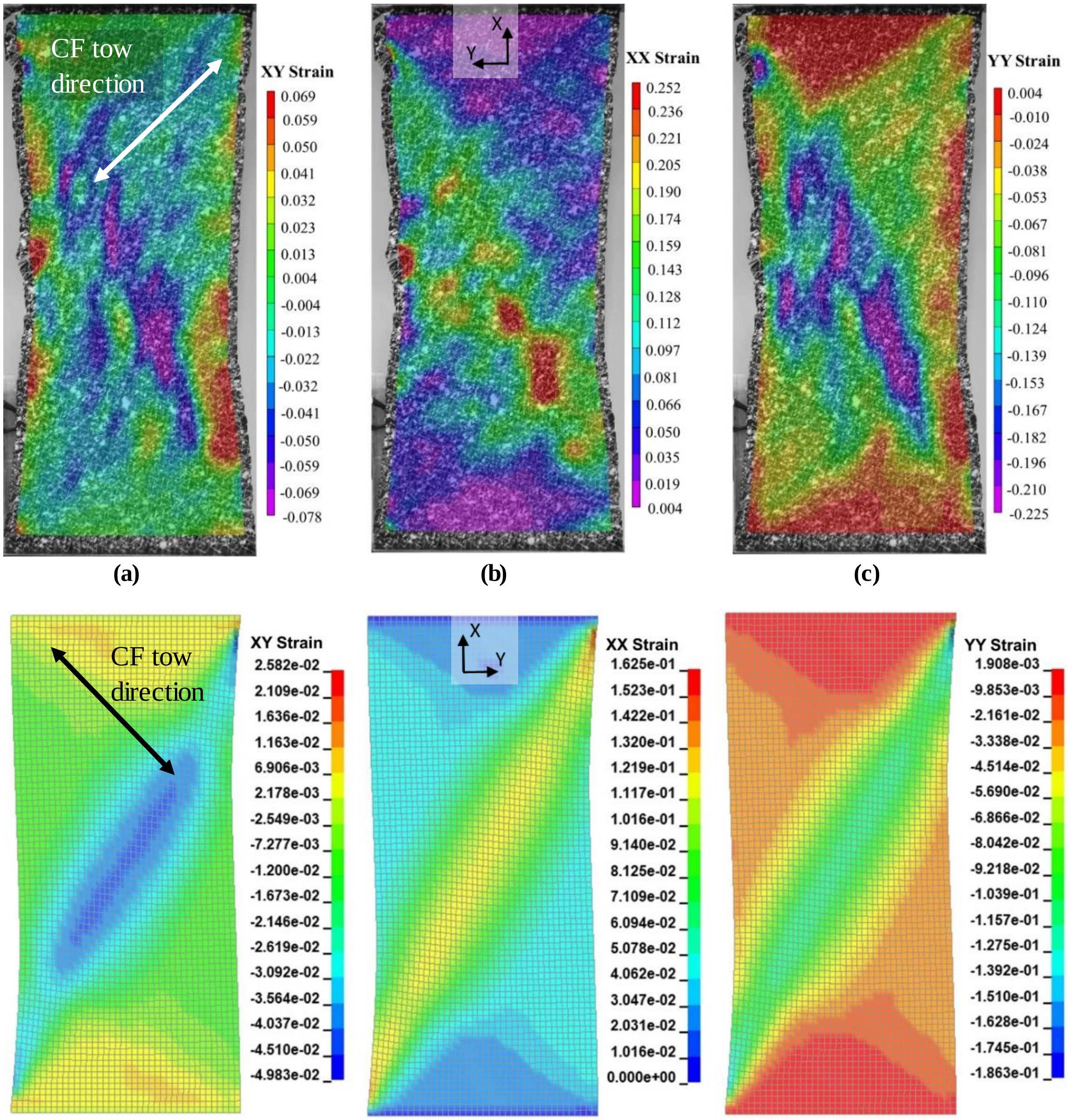

(a) **(b)** **(c)**

(d) **(e)** **(f)**

Figure 5.70. Experimental and simulation strain contour plots of the 60º off-axis extension test at a displacement of 20 mm, where (a and d) shows the shear strain (ε_{xy}), (b and e) the normal strain in the loading direction (ε_{xx}) and (c and f) the normal strain perpendicular to the loading direction (ε_{yy}).

The initial force-displacement correlation, seen in Figure 5.67, could be explained by the fact that the first phase of the deformation was characterized by GF de-crimping and stitching deformation, which was captured during the transverse tensile test, therefore incorporated in the calibration of the transverse deformation mode. The similarity of the 60° off-axis extension test to the transverse extension test is also seen in the improved correlation levels shown in the strain contour plots shown in Figure 5.70. One aspect of this test that was not captured in the model is the sliding of the GFs that are unclamped at one of their ends. The sliding of unclamped GFs reduces the force response of the fabric, and therefore, the stress response of the material model. The inability to account for GF sliding is another critical limitation of MAT249.

5.3.3. Hemispherical test results and draping simulation validation

Data from a hemispherical test (see Section 3.3.7) was compared to the numerical simulation of the test, described in section 4.2.5, that implemented the calibrated material model MAT249. The intention of the hemispherical preforming test was to extract strain measurements using 3D DIC; however, due to decorrelation issues, it was not possible to extract consistent strain maps from multiple test repeats. The problems were mainly associated with the coarse speckle pattern applied on the specimen surfaces and the large deformation experienced by the material during the test. Also, due to the meagre punch forces needed to deform the fabric, the load cell installed in the testing machine was oversized and was not able to record punch loads. Nonetheless, validation of the model was performed by comparing overall fabric deformations, i.e. specimen contour shape and specimen macroscale wrinkling, as seen in Figure 5.71 and Figure 5.72. Figure 5.71 show images of the experimental hemispherical test at 10 mm, 20 mm and 30 mm punch displacements captured by the VIC-3D® system camera, and the corresponding simulation predictions. From the experimental images, it was difficult to visually extract relevant information regarding local and global deformation modes during preforming. As an alternative, a picture of one of the hemispherical tests was taken with a DSLR digital camera at a 30 mm punch displacement to compare the macroscopic and local deformation seen in the experimental data to the simulation predictions. As seen in Figure 5.72, local stretching of the fabric test specimens along the longitudinal and transverse directions was observed in regions A and B. The draping simulation model, as shown in the contour plots in Figure 5.73, also predicted this behaviour. In regions C and D, indicated in Figure 5.72, local compression along the transverse direction and associated wrinkling were observed in the experimental results and predicted by the numerical model. In terms of macroscopic deformations, the model was able to accurately predict overall fabric deformation, as evidenced by the resemblance between the fabric specimen contour of the experimental and numerical simulation.

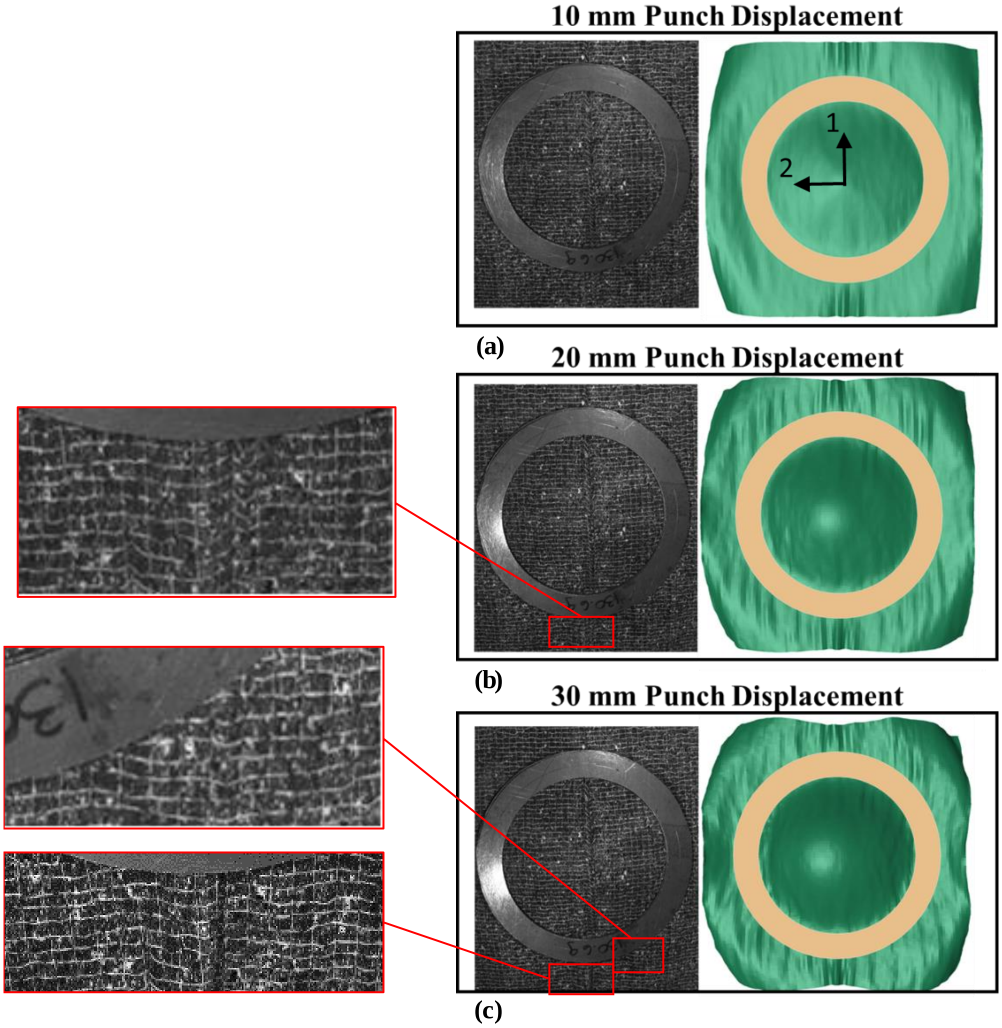

Figure 5.71. Experimental images (capture with VIC-3D DIC system camera) and simulation predictions of the hemispherical test at punch displacements of (a) 10 mm, (b) 20 mm and (c) 30 mm.

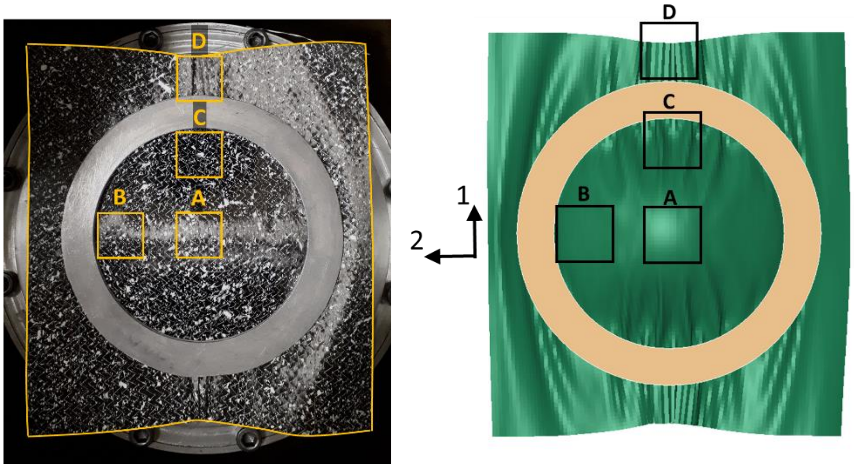

(a) **(b)**

Figure 5.72. Hemispherical test (a) experimental specimen image (capture with DSLR camera), and (b) numerical simulation prediction at a punch displacement of 30 mm.

From the strain contour plots presented in Figure 5.73, it is observed that the largest values of normal strains were seen at the top of the punch, i.e. in the centre of the specimen. In this location, the longitudinal strain, ε_{11}, remained relatively low until reaching approximately 1% at 30 mm punch displacement. In the transverse direction, tensile strains of approximately 2% were observed near the apex of the punch, remaining relatively constant with displacement. The shear strain developed steadily with punch displacement in different quadrants of the specimen. In two diagonally opposite quadrants, positive shear strain increased from approximately 1% to 14%, while in the other two quadrants, it decreased from approximately -1% to -15 from 10 to 30 mm punch displacement.

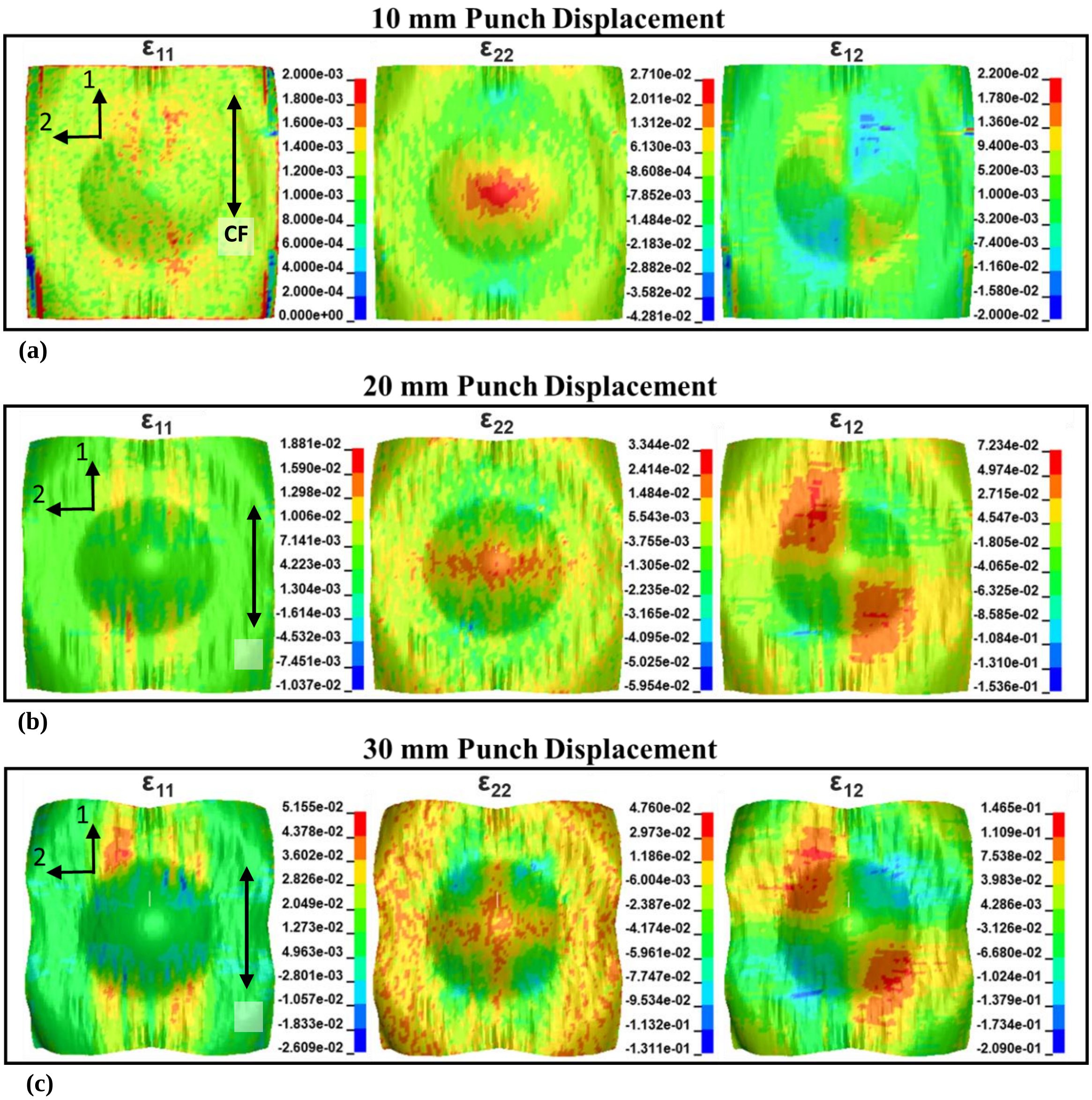

Figure 5.73. Contour plots of simulation predictions of in-plane strains for the hemispherical test at punch displacements of 10 mm, 20 mm, and 30 mm. Note that the carbon fiber tows are aligned with the Z direction.

Finally, Figure 5.74 shows the punch force-displacement relation predicted by the numerical model. The punch forced increased unevenly from the beginning of the test to approximately 1.1 N at 12 mm punch displacement. From 12 mm to 30 mm punch displacement the punch force varied unsteadily from 0.7 N to 1.3 N. The variations in force may be associated with the development of wrinkles in the specimen from 10 mm to 30 mm punch displacement, as evidenced in Figures 5.71 and 5.72.

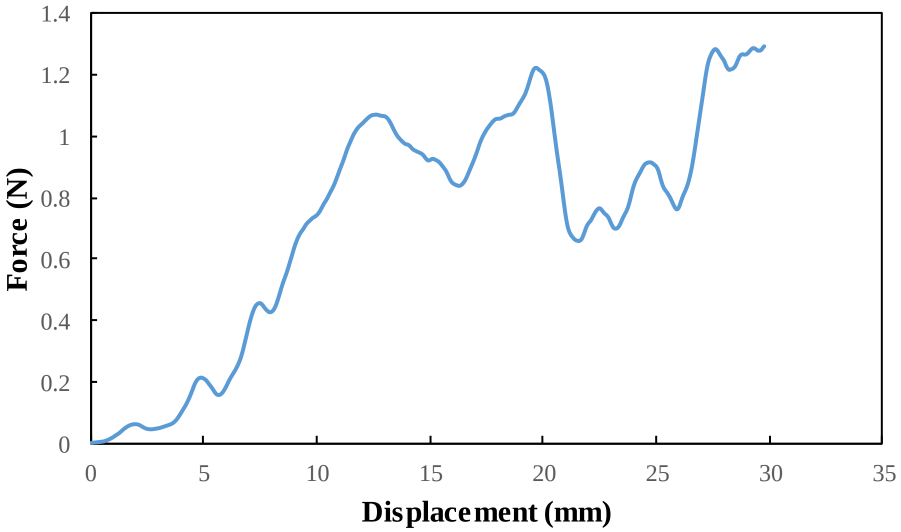

Figure 5.74. Numerical simulation punch force versus displacement prediction for the hemispherical test.

Chapter 6: Discussion

In-plane deformation mechanisms observed in UD-NCFs when subjected to off-axis loading were found not to correspond with the modes of deformation associated with woven and biaxial fabrics, as reported in the literature [16]. When loaded at an angle biased to the fiber tow axes, biaxial fabrics tend to deform predominantly in shear [77,147], while UD-NCFs undergo a combination of shear and transverse extension deformation activated at low force magnitudes [16,73], as seen in Figures 5.49, 5.61 and 5.67. The resistance of the studied UD-NCF to in-plane extension was found to be lowest at a biased loading angle of 45º (see Figures 5.1, 5.4, 5.61 and 5.67). The relation between shear and transverse deformation of the fabric was mainly influenced by the interactions between the stitching and the CF tows, as well as the direction of applied loading.

The shear resistance of the fabric was weak, highly sensitive to boundary conditions, and dependent on the stitching kinematics. The shear stress required to overcome friction among the fabric components during the picture frame test was approximately four times greater than that during the 45º off-axis extension test (see Figures 5.15 and 5.24). Such a difference was presumed to be caused by greater than expected pre-tensioning of the fabric specimen during the PFT as well as normal strains along and transverse to the CF tows, revealing that the macroscopic shear response of the fabric was coupled to the amount of deformation present in the fabric. The main factor influencing the shear response of the fabric was observed to be the deformation and changing geometry of the polyester stitching, as well as the interaction between the stitching and the CF tows. A key interaction was the lateral compression of the tows by the stitching as the imposed shear deformation increased. As shown in Figure 5.20 and 5.21, this shear-induced compression introduced inter-tow gapping (revealed by increasing surface area void content; see Figure 5.23) and out-of-plane tow undulations. Also, as evidenced by the development of shear during the 30º, 45º and 60º off-axis extension tests, the macroscopic shear response of the fabric was coupled to the amount of extension in the fabric. During the 30º and 45º off-axis extension tests, shear deformation was triggered first and dominated the macroscopic fabric deformation as the fabric rotated to align itself with the loading direction. On the contrary, during the 60º off-axis extension test, transverse extension dominated as the carbon fiber tows rotated in the opposite direction to align themselves perpendicular to the direction of loading (see Figure 6.1). As the biased angle increased from 30º to 60º the balance between shear and transverse macroscale deformations transferred from the former to the latter. Common between the three loading cases was the generation of gaps between the CF tows, with the 60º CF tow orientation generating the most severe gapping.

Although UD-NCFs have been reported not to exhibit tow crimping [148], a small degree of negligible stiffness that is characteristic of tow decrimping was observed during longitudinal testing (see Figure 5.1). The longitudinal tensile stiffness of the fabric was negligible up to a tensile strain of approximately 0.05% (see Figure 5.3). On the other hand, transverse extension was observed to be highly dependent on the state of the transversely oriented supporting GFs. In unloaded conditions, the GFs were relaxed and tended to exhibit a noticeable level of crimping (Figure 5.5). The transverse extension stress-strain response of the fabric showed two distinct stages prior to specimen failure, an initially negligible stiffness stage characterized by GF decrimping, which extended until approximately 2.5%, and a constant stiffness stage that extended until the GFs began to fail progressively. Beyond the GF failure stage, out-of-plane CF tow undulations and inter-tow gapping developed as the stitching began to support the load. Shortly after the load was completely transferred to the stitching, and the fabric structure deteriorated as the stitching rapidly failed.

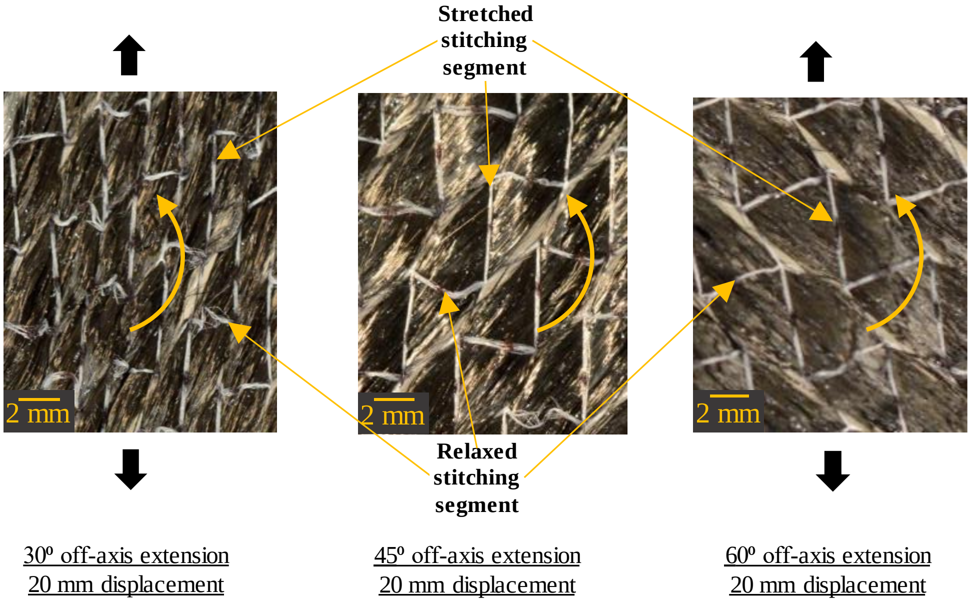

Figure 6.1. Deformation of the stitching web during the 30°, 45° and 60° off-axis extension tests captured at an applied displacement of 20 mm.

Some techniques used to characterize the shear deformation of woven fabrics were found to be not entirely applicable for UD-NCFs. Particularly, the methods used to analyze PFT and BET data are distinct for UD-NCF [16]. This was corroborated by the significant differences between the macroscopic strain state observed during the 45° off-axis extension test and those reported in the literature for woven fabrics. As seen in Figures 5.51-53, the 45° off-axis extension test induced a combination of transverse normal and shear strains in the fabric, which are the intrinsic deformation modes of UD-NCF [16]. On the other hand, it was found difficult to clamp UD-NCF specimens to the PFT fixture without introducing pre-tensioning that inevitable affects the shear response of the fabric. This is especially true for UD-NCFs given their low shear stiffness compared to, for example, woven fabrics [16]. Due to this difference, the 45º off-axis extension test, analyzed under the approximation of simple shear [96], was found to be most appropriate to study the shear response of the UD-NCF.

In terms of out-of-plane deformations, the bending stiffness response of the fabric was remarkably distinct for bending along the longitudinal and transverse directions, as revealed by the cantilever test results shown in Figures 5.26-5.30. While the longitudinal direction exhibited a moderate level of bending stiffness, in the transverse direction, the bending stiffness was found to be negligible. This explains the proliferation of transverse wrinkling observed during the hemispherical draping test. Given this negligible transverse bending stiffness, the fabric was expected to wrinkle during off-axis extension testing, however, this was not the case. As a result, the bending response of the fabric is anticipated to be coupled to the magnitude of in-plane normal strain present in the fabric.

Similar to the bending response, the friction response of the fabric varied with fabric orientation, with slightly higher static and dynamic friction coefficients obtained in the longitudinal direction. This may be attributed to the topography of the fabric having the highest points aligned in the direction of the CF tows, increasing the number of surface interactions between the fabric and the rough surface when the sliding was parallel to the carbon fiber tows. Out-of-plane CF tow undulation caused by compression forces applied by the stitching were observed on the fabric with the application of transverse and shear deformations [14], as seen in Figure 5.20. These deformations altered the surface conditions of the fabric and are anticipated to cause changes in the friction response.

A high level of variability was observed in the force response data from the different extension tests. Possible sources of scatter include fabric-manufacturing defects such as tow misalignment or slight variability in the stitching pattern, and inconsistent pre-tensioning of the fabric test specimens.

Some challenges were encountered with the application of DIC to characterize surface deformations. The discrete nature of the fabric made it difficult to apply a speckle pattern on the fabric surface without affecting the mechanical properties of the material [65,102]. In addition to the mechanical sensitivity of the fabric to any surface treatment, the fabric surface was rough and highly reflective, thus a significant amount of diffused reflections affected the quality of the images captured for DIC analysis. Also, as previously discussed, the fabric developed out-plane undulations in individual CF tows, challenging the assumption of material continuity required for DIC analysis, potentially affecting the accuracy of the DIC results.

Moreover, the predictive capabilities of the material model MAT249 was evaluated through single element analyses and simulations of the characterization tests. These revealed that the material model was able to successfully predict all individual deformation modes, i.e., tensile, shear, and bending, as demonstrated by the data presented in Figures 5.35-5.44 and 5.59. However, limitations were encountered when the model was used to predict fabric deformation under multiaxial loading conditions, such as for the simulation of the 45° off-axis extension test. Specifically, the model was not able to accurately predict the development of combined normal and shear deformations and their inter-dependency, as evidenced in Figure 5.49. The inability of the model to accurately predict this coupled behaviour was also demonstrated by the overprediction of the force response seen in Figures 5.61 and 5.67 for the 30º and 60º off-axis extension test, respectively. This is clearly shown in Figures 5.42 and 5.43, where changes in the fabric in-plane moduli did not impact the shear response. It should be noted that this limitation may partially stem from the fact that the material model did not account for potential normal and shear stiffness losses during the multi-axial loading, which is a characteristic of the fabric. A distinct approach to characterize and model this complex characteristic may be required for UD-NCFs. Also, the method by which the out-of-plane shear moduli, G13 and G23, were calculated and the scheme used to calibrate the bending response of the fabric may have led to inaccurate predictions of wrinkling during the 30° off-axis extension test simulation. This supports the likelihood that the bending deformation of the fabric is coupled to the degree of fabric extension. In addition, use of a macroscopic constitutive model did not allow capturing of the observed local deformation mechanisms, which were dependent on the off-axis angle of the fabric. Notwithstanding, simulations of the 30º and 60º off-axis extension tests revealed that calibration of the material model using the 45° off-axis extension test data led to improved force-displacement response predictions compared to when the PFT data was used (Figures 5.61 and 5.67). This further supports the fact that calibration of the UD-NCF shear response should be performed using the 45° off-axis extension test data.. Despite the limitations of MAT249, during the hemispherical draping simulation, the material model was able to accurately capture the overall deformation of the fabric and the macroscopic wrinkling observed during the hemispherical draping test.

Chapter 7: Conclusions

The overall goal of this investigation was to develop a computational approach for predicting defects associated with preforming of heavy-tow unidirectional non-crimp fabrics (UD-NCFs). The main research objectives comprised of characterizing the deformation behaviour of the carbon fiber UD-NCF PX35-UD300 (Zoltek Corporation), calibrating an available macroscale material constitutive model, and developing a computational fabric draping simulation model using the commercial finite element software LS-DYNA.

Longitudinal and transverse extension tests as well as off-axis extension tests and a picture frame test were conducted to characterize the different membrane deformation modes of the UD-NCF, and the results were used to calibrate the material constitutive model MAT249 in LS-DYNA. Also, cantilever tests were performed to capture the bending deformation modes of the fabric along both the longitudinal and transverse material directions. The interaction between the fabric and a surface representative of a typical steel forming tool was also captured through friction characterization tests, ultimately providing required boundary conditions for the developed computational draping simulation model. All custom fixtures used to perform the characterization tests were designed and procured through this study. Two-dimensional digital image correlation (DIC) was also used to capture fabric strains during fabric membrane characterization tests. To prepare the experiments for DIC analysis three paint techniques were evaluated for optimal texturization of speckle pattern application. The fabric characterization tests captured the macroscopic response as well as the associated local deformation mechanisms, providing an improved understanding of the complex behaviour of the UD-NCF.

One of the main findings of this work was that the behaviour of the investigated UD-NCF was notably different from that of more widely studied woven fabrics or biaxial NCFs reported in the literature. First, woven fabrics or biaxial NCFs are typically tested using the picture frame test to impose pure shear deformation on the test specimen. For UD-NCFs, it was found that the picture frame test did not strictly impose a pure shear deformation state on the fabric specimens, where instead combined shear and extension were observed which may be due to pretensioning of the specimen and/or the characteristic response of the fabric. The 45° off-axis extension test was also used to characterize the UD-NCF where the expected shear-extension coupling was observed. The coupling between shear and extension deformation modes was highly influenced by the complex interactions between the stitching and the carbon fiber tows, and was dependent on the degree of tension acting on the fabric. Furthermore, the bending properties of the fabric exhibited a high level of anisotropy with negligible bending stiffness in the direction transverse to the carbon fiber tows. This behaviour is distinct from woven fabrics where the fabric bending stiffness would be notable along the primary material directions.

In addition, the calibrated material constitutive model (MAT249) was first used to simulate the conducted characterization tests. It was found that the model was able to predict the response of the fabric for cases when individual modes of deformation were imposed. However, predictions were less accurate when combined shear and extension were imposed on the fabric, which revealed that the model was unable to accurately capture the variability in the shear extension coupling of the fabric. Nonetheless, simulation of the hemispherical draping test revealed that the draping simulation model was able to accurately capture the overall deformed shape of the fabric and the wrinkling observed during the experiments.

7.1. Recommendations for Experimental Characterization of Mechanical Properties

The outcomes of the investigation provided relevant data for understanding the behaviour of the UD-NCF and for developing a computational draping simulation model. However, there are some recommendations related to the performed characterization tests which are detailed here.

- Minor fluctuations were observed in the force data captured using the 2.2 kN load cell for the off-axis extension tests. To further improve the quality of the experimental data it is recommended that a load cell with a smaller capacity, on the order of 500 N, is used for off-axis extension tests.
- Also, some difficulties were encountered when capturing close-up images of the fabric caused by light reflections and low camera resolution. As such, a diffuse light source is recommended when filming or photographing the fabric, especially at close proximity, as well as a video camera with a resolution of at least 10 megapixels on video mode.
- As an improvement for the picture frame tests, it is recommended to bond the fabric outside of the gauge area of the specimen using a resin or an adhesive. This is expected to eliminate pre-tensioning that may have been introduced at the boundaries when clamping the fabric.
- For DIC surface texturization, application of a non-binding ink is recommended to further minimize the effect it has on the response of the fabric response. Alternatively, texturizing the fabric can be eliminated and the features of the fabric, such as the stitching locations, can be used to track deformation; albeit this may require the development of a custom algorithm.
- To capture macroscopic deformations during the hemispherical test, it is recommended to use a square grid applied with white or silver marker instead of DIC analysis. Also, for the hemispherical test it is recommended to use a smaller load cell in order to gather force-displacement data.

7.2. Recommendations for Future Work

There are several recommendations for future studies to build on the results from the current study.

- Due to the complex shear-extension coupling exhibited by the UD-NCF, a more in-depth characterization of the fabric can be conducted through additional experiments. For example, to better understand the dependency of shear deformation on extension, the fabric can be subjected to a pretension prior to conducting an off-axis extension test. Similarly, to characterize the dependency of bending on extension, the fabric can be subjected to a pretension prior to conducting a cantilever test. This may lead to an improved calibration of the material model MAT249 or the identification of the need to develop a custom user-defined material model for the UD-NCF. Furthermore, meso-scale computational models can be used in conjunction with tests to better inform the macroscale constitutive model for the fabric.
- In general, fabric preforming operations are conducted at various pressing rates. Therefore, it is assumed that the deformation rate may have an effect on the deformation response of the fabric. As such, it is advised to conduct the characterization tests on the fabric at higher deformation rates.
- Fabric preforming operations are conducted in preheated tools to activate the binder and allow the preform to retain shape. The binder on the stitching side of the fabric may alter the friction response at elevated temperatures. Therefore, it is recommended to investigate the impact that temperature has on the friction response of the fabric.
- Fabric forming is normally performed using multiple layers of fabric where inter-ply friction may play an important role in the deformation behaviour. Therefore, to inform future multi-layered draping simulations, it is recommended to conduct fabric-fabric friction characterization tests along different fabric directions.
- Finally, the draping simulation model can be expanded and used to conduct multi-layer draping simulations for the hemispherical and other part geometries. Corresponding validation tests can also be conducted.

References

[1] "Obama Administration Finalizes Historic 54.5 MPG Fuel Efficiency Standards," The White House Office of the Press Secretary, Aug. 28, 2012. Accessed: May 06, 2020. [Online]. Available: https://obamawhitehouse.archives.gov/the-press-office/2012/08/28/obama-administration-finalizes-historic-545-MPG-fuel-efficiency-standard

[2] U. Dutta and M. Ghosh, "The road ahead," National Highway Traffic Safety Administration, Report, 2016.

[3] F. Lum, Canada to copy Obama's fuel efficiency rules, The Globe and Mail, Aug. 30, 2012. Accessed: May 06, 2020 [Online]. Available: https://www.theglobeandmail.com/report-on-business/industry-news/energy-and-resources/canada-to-copy-obamas-fuel-efficiency-rules/article4508608/

[4] G. Gardiner, BMW 7 Series Plant: Dingolfing, Germany, CompositeWorld, 2016. Accessed: May 06, 2020 [Online]. Available: https://www.compositesworld.com/articles/bmw-7-series-plant-dingolfing-germany

[5] S. Das, D. Graziano, V. Upadhyayula, E. Masanet, M. Riddle, J. Cresko, "Vehicle lightweighting energy use impacts in U.S. light-duty vehicle fleet," Sustainable Materials and Technologies, vol. 8. pp. 5-13, 2016.

[6] A. T. Mayyas, A Qattawi, A. R. Mayyas, M. A. Omar, "Life cycle assessment-based selection for a sustainable lightweight body-in-white design," *Energy*, vol. 39, no. 1, pp. 412–425, 2012.

[7] J. C. Kelly, J. L. Sullivan, A. Burnham, and A. Elgowainy, "Impacts of Vehicle Weight Reduction via Material Substitution on Life-Cycle Greenhouse Gas Emissions," *Environmental Science and Technology*, vol. 49, no. 20, pp. 12535-12542, 2015.

[8] G. Zhu, G. Sun, H. Yu, S. Li, Q. Li, "Energy absorption of metal, composite and metal/composite hybrid structures under oblique crushing loading," *International Journal of Mechanical Sciences*, vol. 135, pp. 458-483, 2018.

[9] A. Cherniaev, C. Butcher, and J. Montesano, "Predicting the axial crush response of CFRP tubes using three damage-based constitutive models," *Thin-Walled Structures*, vol. 129, pp. 349–364, Aug. 2018.

[10] ArcelorMittal Technical Staff, New Audi A8 follows recent trend of automakers to increase the use of advanced steels, ArcelorMittal. Accessed: May 06, 2020. [Online]. Available: https://automotive.arcelormittal.com/news_and_stories/cases/2017AudiA8comebacktosteel

[11] H. Singh, "Mass Reduction for Light-Duty Vehicles for Model Years 2017-2025 - Final Report," National Highway Traffic Safety Administration, Report, Auburn Hills, MI, 2012.

[12] P. Rosenberg, B. Thoma, and F. Henning, "Characterization of Epoxy and Polyurethane Resin Systems for Manufacturing of High - Performance Composites in High - Pressure RTM Process" In Proc. *Automotive Composite Conference and Exhibition*, 2015, pp. 1–18.

[13] M. Graf, E. Fries, J. Renkl, F. Henning, R. Chaudhari, and B. Thoma, Topic: "High pressure resin transfer molding - Process advancements." in Society of Plastics Engineers - 10th Annual

Automotive Composites Conference and Exhibition 2010, Troy, MI, Sep. 2010.

[14] S. Galkin, E. Kunze, L. Kärger, R. Böhm, and M. Gude, “Experimental and Numerical Determination of the Local Fiber Volume Content of Unidirectional Non-Crimp Fabrics with Forming Effects,” *Journal of Composites Science*, vol. 3, no. 1, p. 19, 2019.

[15] L. Kärger, A. Bernath, F. Fritz, S. Galkin, D. Magagnato, A. Oeckerath, “Development and validation of a CAE chain for unidirectional fibre reinforced composite components,” *Composite Structures*, vol. 132, pp. 350–358, 2015.

[16] F. J. Schirmaier, K. A. Weidenmann, L. Kärger, and F. Henning, “Characterisation of the draping behaviour of unidirectional non-crimp fabrics (UD-NCF),” *Composites Part A: Applied Science and Manufacturing*, vol. 80, pp. 28–38, Jan. 2016.

[17] P. K. Mallick, Fiber- Reinforced Composites: Materials, Manufacturing, and Design, 3rd ed., Boca Raton, FL: CRC Press, 2007.

[18] K. K. Chawla, Composite Materials: Science and Engineering, 3rd ed., New York, NY: Springer-Verlag, 2012.

[19] C. T. Herakovich, Mechanics of Fibrous Composites, 1st ed., New York, NY: Wiley, 1997.

[20] M. Inagaki, New Carbons: Control of Structure and Functions. Kidlington, Oxford: Elsevier Science, 2000.

[21] A. B. Strong, Fundamentals of Composites Manufacturing Materials, 2nd ed., Dearborn, MI: Society of Manufacturing Engineers, 2007.

[22] A. K. Kaw, Mechanics of Composite Materials. Boca Raton, FL: CRC Press, 1997.

[23] S. V. Lomov, C. Truong, I. Verpoest, “Mechanical properties of non-crimp fabric (NCF) based composites: stiffness and strength” in *Non-crimp fabric composites: Manufacturing, properties and applications*, S. V. Lomov, Ed. Cambridge, MA: Woodhead Publishing, 2011, pp. 1–523.

[24] P. Boisse, Editor, Composite reinforcements for optimum performance. Sawston, Cambridge: Woodhead Publishing, 2011.

[25] K. Vanclooster, S. V. Lomov, and I. Verpoest, “Experimental validation of forming simulations of fabric reinforced polymers using an unsymmetrical mould configuration,” *Composites Part A: Applied Science and Manufacturing*, vol. 40, no. 4, pp. 530–539, Apr. 2009. [26] Horrocks AR, Anand SC. Handbook of technical textiles. 2000. doi:10.1533/9781855738966.

[27] B. L. Lee, J. W. Song, and J. E. Ward, “Failure of Spectra polyethylene Fiber-Reinforced Composites under Ballistic Impact Loading,” *Journal of Composite Materials*, vol. 28, no. 13, pp. 1202-1226, 1994.

[28] A. Margossian, M. Ding, L. A. Gray, S. Bel, and R. Hinterhölzl, “Flexural Characterisation of Unidirectional Thermoplastic Tapes using a Dynamic Mechanical Analysis system,” in *Proc. European Conference on Composite Materials*, 2014, pp. 22–26.

[29] T. Senner, S. Kreissl, M. Merklein, M. Meinhardt, A. Lipp, and M. Merklein, “Bending of unidirectional non-crimp-fabrics: experimental characterization, constitutive modeling and application in finite element simulation,” *Production Engineering*, vol. 9, no. 1, pp. 1–10, 2015.

[30] S. V. Lomov, Editor, Non-crimp fabric composites: Manufacturing, properties and applications. Cambridge, MA: Woodhead Publishing, 2011.

[31] A. Mallach, F. Härtel, F. Heieck, J.-P. Fuhr, P. Middendorf, and M. Gude, “Experimental comparison of a macroscopic draping simulation for dry non-crimp fabric preforming on a complex geometry by means of optical measurement,” *Journal of Composite Materials*, vol. 51, no. 16, pp. 2363–2375, 2017.

[32] S. Mazumdar, Composites Manufacturing, 1st ed., Boca Raton: CRC Press, 2002.

[33] S. V. Lomov et al., “Meso-FE modelling of textile composites: Road map, data flow and algorithms,” *Composites Science and Technology,* vol. 67, no. 9, pp. 1870–1891, Jul. 2007.

[34] O. Döbrich, T. Gereke, and C. Cherif, “Modeling the mechanical properties of textile-reinforced composites with a near micro-scale approach,” *Composite Structures*, vol. 135, pp. 1–7, Jan. 2016.

[35] P. Šimáček and S. G. Advani, “Desirable features in mold filling simulations for liquid composite molding processes,” *Polymer Composites,* vol. 25, no. 4, pp. 355–367, 2004.

[36] A. Cherniaev, Y. Zeng, D. Cronin, J. Montesano, “Quasi-static and dynamic characterization of unidirectional non-crimp carbon fiber fabric composites processed by HP-RTM,” *Polymer Testing*, vol. 76, pp. 365–375, 2019.

[37] R. Arbter, J. M. Beraud, C. Binetruy, L. Bizet, J. Bréard, S. Comas-Cardona, “Experimental determination of the permeability of textiles: A benchmark exercise,” *Composites Part A: Applied Science and Manufacturing*, vol. 42, pp. 1157-1168, 2011.

[38] E. Schmachtenberg, J. Schulte zur Heide, and J. Töpker, “Application of ultrasonics for the process control of Resin Transfer Moulding (RTM),” *Polymer Testing,* vol. 24, no. 3, pp. 330–338, May 2005.

[39] L. Fong and S. G. Advani, “Resin Transfer Molding,” in *Handbook of Composites,* S. T. Peters, Ed. Boston, MA: Springer, 1998, pp. 433–455.

[40] S. Laurenzi and M. Marchetti, “Advanced Composite Materials by Resin Transfer Molding for Aerospace Applications,” in *Composites and Their Properties,* 1st ed., N. Hu, Ed. Rijeka: Intech, 2012, pp. 197–226.

[41] Chaudhari R, Karcher M, Elsner P, Henning F. Characterization of high pressure RTM processes for manufacturing of high performance composites. ECCM 2012 - Composites at Venice, Proceedings of the 15th European Conference on Composite Materials 2012;m:24–8.

[42] R. Chaudhari, P. Rosenberg, M. Karcher, S. Schmidhuber, P. Elsner, and F. Henning, “High-pressure RTM process variants for manufacturing of carbon fiber reinforced composites,” *ICCM International Conferences on Composite Materials*, pp. 1560–1568, July 2013.

[43] D. Magagnato and F. Henning, “RTM molding simulation for unidirectional fiber reinforced composite components considering local fiber orientation and fiber volume fraction,” *Journal of the Scientific Alliance of Plastics Technology,* vol. 12, no. 2016, pp. 136–156, 2016.

[44] M. Devillard, K.-T. Hsiao, A. Gokce, and S. G. Advani, “On-line Characterization of Bulk Permeability and Race-tracking During the Filling Stage in Resin Transfer Molding Process,” *Journal of Composite Materials,* vol. 37, no. 17, 2003.

[45] P. Boisse, M. Borr, K. Buet, and A. Cherouat, “Finite element simulations of textile composite forming including the biaxial fabric behaviour,” *Composites Part B: Engineering*, vol. 28, no. 4, pp. 453–464, Jan. 1997.

[46] D. Jauffrès, J. A. Sherwood, C. D. Morris, and J. Chen, “Discrete mesoscopic modeling for the simulation of woven-fabric reinforcement forming,” *International Journal of Material Forming*,

vol. 3, pp. 1205–1216, 2010.

[47] P. Boisse, “Simulations of Woven Composite Reinforcement Forming,” in *Woven Fabric Engineering*, P. Dubrovski Editor, pp. 978–953, 2010.

[48] T. Senner, S. Kreissl, M. Merklein, J. Meinhardt, A. Lipp, and S. Kreissl, “A modular modeling approach for describing the in-plane forming behavior of unidirectional non-crimp-fabrics,” *Production Engineering - Research and Development*, vol. 8, pp. 635–643, 2014.

[49] X. Q. Peng, J. Cao, J. Chen, P. Xue, D. S. Lussier, and L. Liu, “Experimental and numerical analysis on normalization of picture frame tests for composite materials,” *Composites Science and Technology*, vol. 64, no. 1, pp. 11–21, Jan. 2004.

[50] S. V. Lomov et al., “Full-field strain measurements in textile deformability studies,” *Composites Part A: Applied Science and Manufacturing*, vol. 39, no. 8, pp. 1232–1244, Aug. 2008.

[51] P. Harrison, M. J. Clifford, and A. C. Long, “Shear characterisation of viscous woven textile composites: a comparison between picture frame and bias extension experiments,” *Composites Science and Technology*, vol. 64, no. 10–11, pp. 1453–1465, Aug. 2004.

[52] C. K. Chan, X. Y. Jiang, K. L. Liew, L. K. Chan, W. K. Wong, and M. P. Lau, “Evaluation of mechanical properties of uniform fabrics in garment manufacturing,” *Journal of Materials Processing Technology*, vol. 174, no. 1–3, pp. 183–189, 2006.

[53] P. Boisse, N. Hamila, E. Vidal-Sallé, F. Dumont, “Simulation of wrinkling during textile composite reinforcement forming. Influence of tensile, in-plane shear and bending stiffnesses,” *Composites Science and Technology*, vol. 71, pp. 683-692, 2011.

[54] W. R. Yu, M. Zampaloni, F. Pourboghrat, K. Chung, and T. J. Kang, “Analysis of flexible bending behavior of woven preform using non-orthogonal constitutive equation,” *Composites Part A: Applied Science and Manufacturing*, vol. 36, no. 6, pp. 839–850, Jun. 2005.

[55] A. Rashidi and A. S. Milani, “A multi-step biaxial bias extension test for wrinkling/de-wrinkling characterization of woven fabrics: Towards optimum forming design guidelines,” *Materials & Design*, vol. 146, pp. 273–285, May 2018.

[56] N. D. Chakladar, P. Mandal, and P. Potluri, “Effects of inter-tow angle and tow size on carbon fibre friction,” *Composites Part A: Applied Science and Manufacturing*, vol. 65, pp. 115–124, Oct. 2014.

[57] S. Chen, “Fabric Forming Simulation and Process Optimisation for Composites,” PhD thesis, University of Nottingham, Nottingham, UK, 2016.

[58] G. Hivet and P. Boisse, “Consistent mesoscopic mechanical behaviour model for woven composite reinforcements in biaxial tension,” *Composites Part B: Engineering*, vol. 39, no. 2, pp. 345–361, 2008.

[59] P. Boisse, Editor, *Advances in Composites Manufacturing and Process Design*, 1st ed. Cambridge: Woodhead Publishing, 2015.

[60] P. Harrison, M. F. Alvarez, and D. Anderson, “Towards comprehensive characterisation and modelling of the forming and wrinkling mechanics of engineering fabrics,” *International Journal of Solids and Structures*, vol. 154, pp. 2–18, 2018..

[61] J. I. Kim, Y. T. Hwang, K. H. Choi, H. J. Kim, and H. S. Kim, “Prediction of the vacuum assisted resin transfer molding (VARTM) process considering the directional permeability of sheared woven fabric,” *Composite Structures*, vol. 211, pp. 236–243, Mar. 2019.

[62] F. J. Schirmaier, D. Dörr, F. Henning, and L. Kärger, "A macroscopic approach to simulate the forming behaviour of stitched unidirectional non-crimp fabrics (UD-NCF)," *Composites Part A: Applied Science and Manufacturing*, vol. 102, pp. 322-335, 2017.

[63] Ž. Penava, D. Š. Penava, and Ž. Knezić, "Determination of the elastic constants of plain woven fabrics by a tensile test in various directions," *Fibres and Textiles in Eastern Europe*, vol. 104, no. 2, pp. 57–63, 2014.

[64] L. Li, Y. Zhao, H. gia nam Vuong, Y. Chen, J. Yang, and Y. Duan, "In-plane shear investigation of biaxial carbon non-crimp fabrics with experimental tests and finite element modeling," *Materials and Design*, vol. 63, pp. 757–765, 2014.

[65] E. A. Trejo, M. Ghazimoradi, C. Butcher, and J. Montesano, "Assessing strain fields in unbalanced unidirectional non-crimp fabrics," *Composites Part A: Applied Science and Manufacturing*, vol. 130, pp. 105758, Mar. 2020.

[66] P. Boisse, N. Hamila, and A. Madeo, "Modelling the development of defects during composite reinforcements and prepreg forming," Philosophical Transactions of the Royal Society A: Mathematical, *Physical and Engineering Sciences*, vol. 374, no. 2071, 2016.

[67] G. Lebrun, M. N. Bureau, and J. Denault, "Evaluation of bias-extension and picture-frame test methods for the measurement of intraply shear properties of PP/glass commingled fabrics," *Composite Structures*, vol. 61, no. 4, pp. 341–352, Sep. 2003.

[68] J. Cao et al., "Characterization of mechanical behavior of woven fabrics: Experimental methods and benchmark results," *Composites Part A: Applied Science and Manufacturing*, vol. 39, no. 6, pp. 1037–1053, Jun. 2008.

[69] A. Hosseini, M. H. Kashani, F. Sassani, A. S. Milani, and F. K. Ko, "Identifying the distinct shear wrinkling behavior of woven composite preforms under bias extension and picture frame tests," *Composite Structures*, vol. 185, pp. 764–773, Feb. 2018.

[70] S. Chen, O. P. L. McGregor, L. T. Harper, A. Endruweit, and N. A. Warrior, "Defect formation during preforming of a bi-axial non-crimp fabric with a pillar stitch pattern," *Composites Part A: Applied Science and Manufacturing*, vol. 91, pp. 156–167, Dec. 2016.

[71] E. De Bilbao, D. Soulat, G. Hivet, and A. Gasser, "Experimental Study of Bending Behaviour of Reinforcements," *Experimental Mechanics*, vol. 50, pp. 333–351, 2010.

[72] B. Liang, N. Hamila, M. Peillon, and P. Boisse, "Analysis of thermoplastic prepreg bending stiffness during manufacturing and of its influence on wrinkling simulations," *Composites Part A: Applied Science and Manufacturing*, vol. 67, pp. 111–122, 2014.

[73] P. Harrison, "Modelling the forming mechanics of engineering fabrics using a mutually constrained pantographic beam and membrane mesh," *Composites Part A: Applied Science and Manufacturing*, vol. 81, pp. 145–157, Feb. 2016.

[74] S. V. Lomov, I. Verpoest, M. Barburski, and J. Laperre, "Carbon composites based on multiaxial multiply stitched preforms. Part 2. KES-F characterisation of the deformability of the preforms at low loads," *Composites Part A: Applied Science and Manufacturing*, vol. 34, no. 4, pp. 359–370, 2003.

[75] K. A. Fetfatsidis, J. A. Sherwood, J. Chen, and D. Jauffres, "Characterization of the tool/fabric and fabric/fabric friction for woven-fabric composites during the thermostamping process," *International Journal of Material Forming*, vol. 6, pp. 209–221, 2013.

[76] "Kes-Fb4-A Surface Tester," Accessed on: Mar. 20, 2020. [Online]. Available: http://electrotekintl.com/kes-fb4-a-surface-tester/.

[77] M. H. Kashani, A. Hosseini, F. Sassani, F. K. Ko, and A. S. Milani, "Understanding different types of coupling in mechanical behavior of woven fabric reinforcements: A critical review and analysis," *Composite Structures*, vol. 179, pp. 558-567, 2017.

[78] X. Zeng, A. Endruweit, L. P. Brown, A. C. Long. "Numerical prediction of in-plane permeability for multilayer woven fabrics with manufacture-induced deformation," *Composites Part A: Applied Science and Manufacturing,* vol. 77, pp. 266-274, 2015.

[79] P. Jearanaisilawong, "Investigation of Deformation and Failure Mechanism in Woven and Nonwoven Fabrics under Quasi-Static Loading Conditions," PhD thesis, Massachusetts Institute of Technology, Cambridge, MA, 2004.

[80] P. Harrison, F. Abdiwi, Z. Guo, P. Potluri, and W. R. Yu, "Characterising the shear–tension coupling and wrinkling behaviour of woven engineering fabrics," *Composites Part A: Applied Science and Manufacturing*, vol. 43, pp. 903-914, 2012.

[81] F. Abdiwi, P. Harrison, I. Koyama, W. R. Yu, A. C. Long, N. Corriea. "Characterising and modelling variability of tow orientation in engineering fabrics and textile composites," *Composites Science and Technology*, vol. 72, pp. 1034-41, 2012.

[82] B. Zhu, T. X. Yu, and X. M. Tao, "An experimental study of in-plane large shear deformation of woven fabric composite," *Composites Science and Technology*, vol. 67, no. 2, pp. 252-261, 2007.

[83] A. Willems, S. V. V. Lomov, I. Verpoest, and D. Vandepitte, "Drape-ability characterization of textile composite reinforcements using digital image correlation," *Optics and Lasers in Engineering*, vol. 47, no. 3–4, pp. 343–351, Mar. 2009.

[84] T. Gereke, O. Döbrich, M. Hübner, and C. Cherif, "Experimental and computational composite textile reinforcement forming: A review," *Composites Part A: Applied Science and Manufacturing*, vol. 46, pp. 1–10, Mar. 2013.

[85] M. J. J. King, P. Jearanaisilawong, and S. Socrate, "A continuum constitutive model for the mechanical behavior of woven fabrics," *International Journal of Solids and Structures*, vol. 42, no. 13, pp. 3867–3896, Jun. 2005.

[86] M. H. Kashani, A. Hosseini, F. Sassani, F. K. Ko, and A. S. Milani, "The Role of Intra-Yarn Shear in Integrated Multi-Scale Deformation Analyses of Woven Fabrics: A Critical Review," *Solid State and Materials Sciences*, vol. 43, no. 3, pp. 213-232, 2018.

[87] S. Allaoui, G. Hivet, A. Wendling, P. Ouagne, and D. Soulat, "Influence of the dry woven fabrics meso-structure on fabric/fabric contact behavior," *Composite Materials*, vol. 45, no. 6, pp. 627–639, 2012.

[88] H. Lin, J. Wang, A. C. Long, M. J. Clifford, and P. Harrison, "Predictive modelling for optimization of textile composite forming," *Composites Science and Technology*, vol. 67, no. 15–16, pp. 3242–3252, Dec. 2007.

[89] S. V Lomov, A. Willems, I. Verpoest, Y. Zhu, M. Barburski, and T. Stoilova, "Picture Frame Test of Woven Composite Reinforcements with a Full-Field Strain Registration," *Textile Research Journal Article Textile Research Journal*, vol. 76, no. 3, pp. 243–252, 2006.

[90] S. B. Sharma and M. P. F. Sutcliffe, "A simplified finite element model for draping of woven material," *Composites Part A: Applied Science and Manufacturing*, vol. 35, no. 6, pp. 637–643,

2004.

[91] A. Willems, S. V. Lomov, I. Verpoest, D. Vandepitte. “Optical strain fields in shear and tensile testing of textile reinforcements,” *Composites Science and Technology*, vol. 68, pp. 807-819, 2008.

[92] L. Liu, J. Chen, X. Li, and J. Sherwood, “Two-dimensional macro-mechanics shear models of woven fabrics,” *Composites Part A: Applied Science and Manufacturing*, vol. 36, no. 1, pp. 105-114, 2005.

[93] F. Nosrat-Nezami, T. Gereke, C. Eberdt, and C. Cherif, “Characterisation of the shear–tension coupling of carbon-fibre fabric under controlled membrane tensions for precise simulative predictions of industrial preforming processes,” *Composites Part A: Applied Science and Manufacturing*, vol. 67, pp. 131–139, Dec. 2014.

[94] K. Bilisik and G. Yolacan, “Experimental determination of bending behavior of multilayered and multidirectionally-stitched E-Glass fabric structures for composites,” *Textile Research Journal*, vol. 82, no. 10, pp. 1038–1049, 2012.

[95] F. Nosrat Nezami, T. Gereke, and C. Cherif, “Analyses of interaction mechanisms during forming of multilayer carbon woven fabrics for composite applications,” *Composites Part A: Applied Science and Manufacturing*, vol. 84, pp. 406–416, May 2016.

[96] J. Pourtier, B. Duchamp, M. Kowalski, P. Wang, X. Legrand, and D. Soulat, “Two-way approach for deformation analysis of non-crimp fabrics in uniaxial bias extension tests based on pure and simple shear assumption,” *International Journal of Material Forming*, vol. 12, no. 6, pp. 995–1008, 2019.

[97] F. Härtel, P. Harrison, “Evaluation of normalisation methods for uniaxial bias extension tests on engineering fabrics,” *Composites Part A: Applied Science and Manufacturing*, vol. 9, pp. 61-69, 2014.

[98] S. Ropers, “Bending Behavior of Thermoplastic Composite Sheets: Viscoelasticity and Temperature Dependency in the Draping Process,” 1st Ed., New York, NY: Springer, 2017.

[99] M. A. Sutton, J. J. Orteu, and H. Schreier, “Image Correlation for Shape, Motion and Deformation Measurements,” 1st Ed., New York: Springer US, 2009.

[100] Correlated Solutions Technical Staff, Vic-2D V6 Manual, Correlated Solutions, 2009.

[101] M. Tekieli, S. De Santis, G. de Felice, A. Kwiecień, and F. Roscini, “Application of Digital Image Correlation to composite reinforcements testing,” *Composite Structures*, vol. 160, pp. 670–688, Jan. 2017.

[102] J. Li, D. Zeng, X. Zhu, W. Xu, B. Zhang, and L. Yang, “Property and Fiber Orientation Determination for Carbon Fiber Composite,” In *Proc. WCX World Congress Experience*, Apr. 2018, pp. 1–7.

[103] S. Dridi, F. Morestin, A. Dogui, and C. S. Dridi, “Use of Digital Image Correlation to Analyse the Shearing Deformation in Woven Fabric,” *Experimental Techniques*, vol. 36, pp. 46-52, 2012.

[104] K. Vanclooster, S. V. Lomov, and I. Verpoest, “Simulating and validating the draping of woven fiber reinforced polymers,” *International Journal of Material Forming*, vol. 1, pp. 961–964, Apr. 2008.

[105] C. Mack and H. M. Taylor, “The fitting of woven cloth to surfaces,” *Journal of the Textile Institute Transactions*, vol. 47, no. 9, pp. T477–T488, 1956.

[106] F. Van Der Weeën, "Algorithms for Draping Fabrics on Doubly-curved Surfaces," *Internatinal Journal for Numerical Methods in Engineering*, vol. 31, pp. 1415-1426, 1991.

[107] L. Dong, C. Lekakou, and M. G. Bader, "Processing of composites: simulations of the draping of fabrics with updated material behaviour law," *Journal of Composite Materials*, vol. 35, no. 2, pp. 138–163, 2001.

[108] P. Badel, S. Gauthier, E. Vidal-Sallé, and P. Boisse, "Rate constitutive equations for computational analyses of textile composite reinforcement mechanical behaviour during forming," *Composites Part A: Applied Science and Manufacturing*, vol. 40, no. 8, pp. 997–1007, Aug. 2009.

[109] W. R. Yu, P. Harrison, and A. Long, "Finite element forming simulation for non-crimp fabrics using a non-orthogonal constitutive equation," *Composites Part A: Applied Science and Manufacturing*, vol. 36, no. 8, pp. 1079–1093, Aug. 2005.

[110] P. Boisse, B. Zouari, and J.-L. Daniel, "Importance of in-plane shear rigidity in finite element analyses of woven fabric composite preforming," *Composites Part A: Applied Science and Manufacturing*, vol. 37, no. 12, pp. 2201–2212, Dec. 2006.

[111] P. Boisse, B. Zouari, and A. Gasser, "A mesoscopic approach for the simulation of woven fibre composite forming" *Composites Science and Technology*, vol. 65, pp. 429-436, 2005.

[112] B. A. Behrens et al., "Automated Stamp Forming of Continuous Fiber Reinforced Thermoplastics for Complex Shell Geometries," *Procedia CIRP*, vol. 66, pp. 113–118, 2017.

[113] X. Peng and J. Cao, "A dual homogenization and finite element approach for material characterization of textile composites," *Composites Part B: Engineering*, vol. 33, no. 1, pp. 45–56, Jan. 2002.

[114] H. Lin, A. C. Long, M. Sherburn, and M. J. Clifford, "Modelling of mechanical behaviour for woven fabrics under combined loading," *International Journal of Material Forming*, vol. 1, no. 1, pp. 899–902, 2008.

[115] A. Cherouat and H. Bourouchaki, "Numerical Tools for Composite Woven Fabric Preforming," *Advances in Materials Science and Engineering*, vol. 2013, 2013.

[116] O. Erol, B. Powers, and M. Keefe, "Development of a non-orthogonal macroscale material model for advanced woven fabrics based on mesoscale structure," *Composites Part B: Engineering*, vol. 110, pp. 497–510, Feb. 2017.

[117] D. Dörr, F. J. Schirmaier, F. Henning, and L. Kärger, "A viscoelastic approach for modeling bending behavior in finite element forming simulation of continuously fiber reinforced composites," *Composites Part A: Applied Science and Manufacturing*, vol. 94, pp. 113–123, Mar. 2017.

[118] J. Bonet and A. J. Burton, "A simple orthotropic, transversely isotropic hyperelastic constitutive equation for large strain computations," *Computer Methods in Applied Mechanics and Engineering*, vol. 162, no. 1–4, pp. 151–164, Aug. 1998.

[119] A. Aridhi et al., "Textile composite structural analysis taking into account the forming process," *Composites Part B: Engineering*, vol. 166, pp. 773–784, Jun. 2019.

[120] W. R. Yu, F. Pourboghrat, K. Chung, M. Zampaloni, and T. J. Kang, "Non-orthogonal constitutive equation for woven fabric reinforced thermoplastic composites," Composites Part A: Applied Science and Manufacturing, vol. 33, no. 8, pp. 1095–1105, Aug. 2002.

[121] E. Guzman-Maldonado, N. Hamila, N. Naouar, G. Moulin, and P. Boisse, "Simulation of

thermoplastic prepreg thermoforming based on a visco-hyperelastic model and a thermal homogenization," *Materials & Design*, vol. 93, pp. 431–442, Mar. 2016.

[122] Y. Aimène, E. Vidal-Sallé, B. Hagège, F. Sidoroff, and P. Boisse, "A hyperelastic approach for composite reinforcement large deformation analysis," *Journal of Composite Materials*, vol. 44, no. 1, pp. 5–26, 2010.

[123] X. Peng, Z. Guo, T. Du, and W. R. Yu, "A simple anisotropic hyperelastic constitutive model for textile fabrics with application to forming simulation," *Composites Part B: Engineering*, vol. 52, pp. 275–281, Sep. 2013.

[124] P. Badel, E. Vidal-Sallé, and P. Boisse, "Large deformation analysis of fibrous materials using rate constitutive equations," *Computers & Structures*, vol. 86, no. 11–12, pp. 1164–1175, Jun. 2008.

[125] M. A. Khan, T. Mabrouki, E. Vidal-Sallé, and P. Boisse, "Numerical and experimental analyses of woven composite reinforcement forming using a hypoelastic behaviour. Application to the double dome benchmark," *Journal of Materials Processing Technology*, vol. 210, no. 2, pp. 378–388, Jan. 2010.

[126] A. S. Milani and J. A. Nemes, "An intelligent inverse method for characterization of textile reinforced thermoplastic composites using a hyperelastic constitutive model," *Composites Science and Technology*, vol. 64, no. 10–11, pp. 1565–1576, 2004.

[127] T. Belytschko, W. K. Liu, and B. Moran, *Nonlinear Finite Elements for Continua and Structures*, 2nd ed. Chichester: John Wiley & Sons, Ltd, 2014.

[128] X. Peng and F. Ding, "Validation of a non-orthogonal constitutive model for woven composite fabrics via hemispherical stamping simulation," *Composites Part A: Applied Science and Manufacturing*, vol. 42, no. 4, pp. 400–407, Apr. 2011.

[129] W. Lee, and J. Cao, "Numerical simulations on double-dome forming of woven composites using the coupled non-orthogonal constitutive model" *International Journal of Material Forming*, vol. 2, no. 145, pp. 145-148, 2009.

[130] M. Duhovic and D. Bhattacharyya, "Simulating the deformation mechanisms of knitted fabric composites," *Composites Part A: Applied Science and Manufacturing*, vol. 37, no. 11, pp. 1897–1915, Nov. 2006.

[131] G. Scarlat, R. Ramgulam, P. Martinsson, K. Kasper, and H. Bayraktar, "Material characterization of a 3D-woven carbon fiber preform at macro-scale level for manufacturing process modeling," in *Proc. 11th European LS-DYNA Conference*, Salzburg, Austria, 2017.

[132] P. Boisse, N. Hamila, and A. Madeo, "The difficulties in modeling the mechanical behavior of textile composite reinforcements with standard continuum mechanics of Cauchy. Some possible remedies," *International Journal of Solids and Structures*, vol. 154, pp. 55–65, Dec. 2018.

[133] E. Guzman-Maldonado, N. Hamila, P. Boisse, and J. Bikard, "Thermomechanical analysis, modelling and simulation of the forming of pre-impregnated thermoplastics composites," *Composites Part A: Applied Science and Manufacturing*, vol. 78, pp. 211–222, Nov. 2015.

[134] S. D. Rajan, B. Mobasher, Z. Stahlecker, S. Bansal, and D. Zhu, "Explicit Finite Element Modeling of Multilayer Composite Fabric for Gas Turbine Engine Containment Systems: Part 3: Model Development and Simulation of Experiments," U.S. Department of Transportation Federal Aviation Administration, Tempe, AZ, USA, Final Report, Nov. 2004.

[135] D. Dörr, W. Brymerski, S. Ropers, T. Joppich, L. Kärger, and F. Henning, "A Benchmark Study of

Finite Element Codes for Forming Simulation of Thermoplastic UD-Tapes," *Procedia CIRP*, vol. 66 pp. 101-106, 2017.

[136] "AniForm Suite's key," Accessed on: Mar. 20, 2020. [Online]. Available: https://aniform.com/features

[137] LS-DYNA keyword user's manual Volume II - Material Models, Livermore Software Technology, Livermore, CA, 2018.

[138] L. J. Deka, S. D. Bartus, and U. K. Vaidya, "Damage Evolution and Energy Absorption of FRP Plates Subjected to Ballistic Impact Using a Numerical Model," in *Proc. 9th International LS-DYNA Users Conference*, no. 4, pp. 49–60, 2006.

[139] W. Zhang et al., "A non-orthogonal material model of woven composites in the preforming process," *CIRP Annals – Manufacturing Technology*, vol. 66, no. 1, pp. 257–260, Jan. 2017.

[140] M. Grubenmann et al., "Influence of temperature on in-plane and out-of-plane mechanical behaviour of GFRP composite," *Journal of Physics: Conference Series*, vol. 1063, no. 1, p. 012146, 2018.

[141] Zoltek Corporation Technical Staff, Panex 35 Uni-directional Fabrics, Zoltek Corporation, 2018.

[142] P. Harrison, J. Wiggers, and A. C. Long, "Normalization of shear test data for rate-independent compressible fabrics," *Journal of Composite Materials*, vol. 42, no. 22, pp. 2315–2344, 2008.

[143] Test Method for Static and Kinetic Coefficients of Friction of Plastic Film and Sheeting, ASTM International, D1894-14, 2014.

[144] A. Pickett, Composites material model 140 for draping simulation, Institute for Aircraft Design, Sep. 2012. Accessed on: May 1, 2020. [Online]. Available: http://www2.ifb.uni-stuttgart.de/fem/Ex_Materials/CompositesDraping_Mat140/CompositeForming_Mat140_V2.pdf

[145] A. A. Hosseini, "Multiscale Analysis of Forming Induced Wrinkles in Woven Composite Preforms," PhD thesis, The University of British Columbia, Vancouver, BC, 2018.

[146] T. Klöppel and A. Haufe, Topic: "Simulation of Draping with LS-DYNA - New material model *MAT_249 for thermoplastic pre-pregs and dry fabrics", Stuttgart, Mar. 2016.

[147] P. Boisse, N. Hamila, E. Guzman-Maldonado, A. Madeo, G. Hivet, and F. dell'Isola, "The bias-extension test for the analysis of in-plane shear properties of textile composite reinforcements and prepregs: a review," *International Journal of Material Forming*, vol. 10, no. 4, pp. 473–492, 2017.

[148] A. R. Horrocks and S. C. Anand, *Handbook of Technical Textiles: Technical Textile Applications*, 2nd ed. Woodhead Publishing, 2016.